Doctoral theses at NTNU, 2022:36

Mohammed Mostafa Adnan

In situ nanocomposites for high voltage insulation

Doctoral thesis

NTNU
Norwegian University of Science and Technology
Thesis for the Degree of
Philosophiae Doctor
Faculty of Natural Sciences
Department of Materials Science and Engineering

NTNU
Norwegian University of
Science and Technology

Mohammed Mostafa Adnan

In situ nanocomposites for high voltage insulation

Thesis for the Degree of Philosophiae Doctor

Trondheim, February 2022

Norwegian University of Science and Technology
Faculty of Natural Sciences
Department of Materials Science and Engineering

NTNU
Norwegian University of
Science and Technology

NTNU
Norwegian University of Science and Technology

Thesis for the Degree of Philosophiae Doctor

Faculty of Natural Sciences
Department of Materials Science and Engineering

ISBN 978-82-326-6253-1 (printed ver.)
ISBN 978-82-326-5861-9 (electronic ver.)
ISSN 1503-8181 (printed ver.)
ISSN 2703-8084 (online ver.)

Doctoral theses at NTNU, 2022:36

Printed by NTNU Grafisk senter

Preface

This thesis has been submitted to NTNU Norwegian University of Science and Technology in partial fulfilment of requirements for the academic degree of *Philosophiae Doctor*.

The doctoral study was performed in the Functional Materials and Materials Chemistry Research Group (FACET), Department of Materials Science and Engineering (DMSE), NTNU, Trondheim from September 2017 to January 2022. The work was supervised by Professor Mari-Ann Einarsrud, and co-supervised by Associate Professor Julia Glaum and Dr. Marit-Helen Glomm Ese, SINTEF Energy Research, Trondheim.

The work has been funded by The Research Council of Norway through the project "Stipendiatstillinger til SINTEF Energi AS" (project number 259866).

Mohammed Mostafa Adnan
Trondheim, January 16, 2022

Author contributions

All of the experiments were performed by the author of this thesis at DMSE in NTNU, except for the following.

The transmission electron microscopy images were taken by Dr. Ragnhild Sæterli (Department of Physics, NTNU) and MSc Inger-Emma Nylund (DMSE, NTNU).
The molecular dynamics simulations and the preparation of the various scripts and programs used were performed by MSc Arpenik Kroyan (DMSE, NTNU) and Associate Professor Sondre Kvalvåg Schnell (DMSE, NTNU), with some contributions from the author.
The nuclear magnetic resonance measurements were taken by Dr. Aleksander Jaworski (Department of Materials and Environmental Chemistry, Stockholm University).
The COMSOL simulations of the electrical field were performed by Dr. Torbjørn Andersen Ve (SINTEF Energy Research).
The small angle X-ray scattering measurements were performed by the author at the University of Oslo (UiO) under the Norwegian national resource centre for X-ray diffraction and scattering (RECX), with assistance from Associate Professor Reidar Lund (Department of Chemistry, UiO).
The dynamic mechanical analysis was performed by the author at the Department of Manufacturing and Civil Engineering, NTNU Gjøvik, with assistance from Professor Sotirios Grammatikos and MSc Chaman Srivastava.
The epoxy-Al_2O_3 nanocomposites were prepared by Antoine Claude Demange, under the supervision of the author. The *ex-situ* epoxy-SiO_2 nanocomposites were prepared by Alexander Svalheim Lien, under the supervisior of the author.

Parts of this thesis have been published. The author of this thesis has been the main contributor to these works, and all the co-authors have been involved in the preparation of the manuscripts. The following works are included in this thesis and are shown in Appendix A:

1. **Adnan, M.M.**, Tveten, E.G., Miranti, R., Hvidsten, S., Ese, M.-H. G., Glaum, J., Einarsrud, M.-A. In situ synthesis of epoxy nanocomposites with hierarchical surface-modified SiO_2 clusters. *Journal of Sol-Gel Science and Technology* 95, 783-794, 2020.
   Contributions: Performed experiments, analyzed the data, and wrote the first draft of the manuscript. Participated when the TEM images were recorded by Dr. Ragnhild Sæterli.

2. **Adnan, M.M.**, Nylund, I.-E., Jaworski, A., Hvidsten, S., Ese, M.-H. G., Glaum, J., Einarsrud, M.-A. The structure, morphology, and complex permittivity of epoxy nanodielectrics with in situ synthesized surface-functionalized SiO_2. *Polymers* 13(9), 1469, 2021.
   Contributions: Performed experiments, analyzed the data, and wrote the first draft of the manuscript. Participated during the NMR measurements taken by AJ, and when the TEM images were recorded by IEN.

The following papers/manuscripts are not included in the thesis since they are either still in preparation, or review papers written by the author:

1. **Adnan, M.M.**, Tveten, E.G., Glomm, W., Hvidsten, S., Ese, M.-H. G., Glaum, J., Einarsrud, M.-A. Epoxy-based nanocomposites for High-Voltage Insulation: A Review. *Advanced Electronic Materials* 5(2), 1800505, 2018.
   Contributions: Performed the literature review and wrote the first draft of the manuscript.

2. **Adnan, M. M.**, Dalod, A.R.M., Balci, M.H., Glaum, J., Einarsrud, M.-A. In Situ Synthesis of Hybrid Inorganic-Polymer Nanocomposites. *Polymers* 10(10), 1129, 2018.
   Contributions: Performed the literature review and wrote the first draft of the manuscript.

3. **Adnan, M.M.**, Ve, T.A., Hvidsten, S., M.-H. G., Glaum, J., Einarsrud, M.-A. Electrical treeing and partial discharge behaviour in epoxy nanocomposites with in situ synthesized SiO_2. In preparation (2021).
   Contributions: Performed experiments, analyzed the data, and wrote the first draft of the manuscript.

4. **Adnan, M.M.**, Kroyan, A., Schnell, S.K., Einarsrud, M.-A. Theoretical and experimental determination of thermomechanical properties of epoxy-SiO_2 nanocomposites. In preparation (2021).
   Contributions: Performed the experimental measurements. Discussed and provided feedback for the theoretical simulation work to AK and SKS. Wrote the first draft of the paper.

Acknowledgements

It has now been a bit over ten years since I started as a student in Trondheim, which has now culminated in this PhD thesis. Along the way I've met many wonderful people who have helped me develop into the person I am today, both professionally and personally.

First and foremost, of course, is my supervisor Mari-Ann Einarsrud. I remember attending your inorganic chemistry class in my very first year, and soon after knocking on your door to ask for an idea of what I would have to do if I wanted to do a PhD. You remain as open, welcoming, helpful and supportive today as you were on that first day, and I am truly grateful for having you as one of my mentors through the last four and a half years. I was also lucky enough to have the support of a couple of excellent co-supervisors. While Mari-Ann advised me on the chemistry side of things, I had Julia Glaum to help me understand the electrical behaviour of my materials. Thank you Julia for your time whenever I needed to pop by and ask silly questions, and for our discussions on the challenges of understanding things as a researcher, which helped put things into perspective for me at times. To my other co-supervisor Marit-Helen Glomm Ese, thank you for always making time for me when I needed feedback, and for facilitating the help I needed when performing electrical measurements. I think the most valuable guidance I received from all my supervisors is not only the advice and suggestions on the project I worked on, but also that on the profession of being a researcher, and for that I am very grateful to all of you!

The work reported in this thesis has been, as most things in life, a collaborative effort. I would like to thank both Sondre Kvalvåg Schnell and Arpenik Kroyan for their time and efforts in performing the molecular dynamics work, for their valuable feedback on the writing, and for introducing me to a new and different tool of research. I also greatly appreciate the help from Inger-Emma Nylund in taking the TEM images of my nanocomposite materials - I imagine my thesis would be less interesting to look at without those images! I have been assisted by a team of scientists from SINTEF Energy in performing a lot of the electrical characterization of the materials, and would like to thank Erlend Grytli Tveten, Torbjørn Andersen Ve, Hans Helmer Sæternes, and Knut Brede Liland for their help and advice in setting up the casting equipment, the (not-so-succesful) dielectric breakdown setups, and the (successful) electrical treeing setups. In addition, thank you very much Sverre Hvidsten for our discussions, on all things related to the electrical properties of these materials. I would also

like to thank Reidar Lund at the University of Oslo for his help in performing the SAXS measurements, and Aleksander Jaworski at Stockholm University for performing the solid-state NMR experiements - these experiments provided a lot of valuable data for me, and I appreciate the opportunity that was given to perform them. In addition, thank you to Professor Sotirios Grammatikos and Chaman Srivastava for helping me perform DMA measurements at Gjøvik.

A lot of this work would have been much more difficult without the help of our excellent engineers and technicians at our department. Pei Na Kui, Johannes Ofstad, Elin Albertsen, Eva Rise, and Anita Storsve, thank you all for your prompt help whenever I needed it in the labs! I have also had the pleasure of co-supervising several Master's and project students during my PhD - to Morten Steinsmo Dybdahl, Katharina Zürbes, Antoine Claude Demange, and Alexander Svalheim Lien, thank you for the wonderful experience and for our collaborations which have also been very helpful for me and my work. And finally on the research side of things, thank you to my supervisor during my Master's degree, Sverre Magnus Selbach, for encouraging me to always remain curious. And for being cool enough to Rick-roll our entire class before exams.

As most reasonable people will inform you, one needs a lot of emotional support as well throughout the PhD. And in that respect I have been truly lucky to be in a very open, friendly, and supportive work environment. There are too many to name here sadly, but to all my present and former colleagues in the FACET group (as well as the rest of IMA), you guys are awesome. Whether it be a chill barbecue session, going bowling or playing laser tag, game nights of AoE, or the group camping, hiking, and skiing trips (which involved more riding on my butt than skiing for me) - they have always been fun and a good way to remind myself of the more important things in life away from the work. I will miss our extended lunches with talks about anything and everything.
I've also been lucky enough to have friends who I can always count on, and with whom I've shared many memories and experiences throughout the ten years here in Trondheim, as well as back home in Bangladesh. To Oskar, Kristian, Petter, Frida, Veronica, Fredrik (R), Hanne, Carl, Fredrik (L), Asle - thank you all for welcoming an awkward and shy teenager from Bangladesh when he was still getting used to things around here, for introducing me to your families, and inviting me in to share all the quintessential Norwegian experiences. To Sanjid (H), Sanjid (S), Abrar, Ridwan, Tahsin, Samiul - you guys are the OG, and I hope to see you all again together soon. To Shukh, thanks for asking me to visit Sanjid (S) a day earlier, which ended up in a very fishy affair!
I would also like to thank the Bangladeshi community in Trondheim, especially Hossain uncle, Amin uncle, and their families, for always inviting me over and

providing me the occasional relief from homesickness via company or some excellent home cuisine.

Finally, a few words for my family. My grandparents, Nanu and Dadabhai, have always been around me and my brother as we grew up, and have always taken care of us and prayed for us in many ways. We are both very lucky to have had them around us for so long, and are grateful for their love and affection.
To Maa and Abbu, thank you both for your encouragement, support, and prayers, especially through the final stage of writing my thesis.
To my brother, Irfan - you have become an inspiration not only to me but to many others. Thank you for listening to my rants from time to time, for the subsequent advice and support, and most of all for opening me up to different perspectives on life.
To my parents, Ammu and Baba. I don't know where to begin even. Thank you both so much for everything you have given me in life, and for the sacrifices you've made for me and Irfan. I could not have asked for more from you. I only hope to make you as proud of me as I am of you both.
And finally, to Swapno, my ador. Your patience, love, and strength of will have been my inspiration through the last few years, and I thank you for everything we've experienced through this time. But most of all, thank you for your leap of faith. I look forward to so much more in the years we will share together ahead.

Alhamdulillah.

Summary

The rapid technological development and the expanding scope of human activity in the present era has significantly increased the energy demand. This huge demand for electrical power results in the need for improved insulation systems with low dielectric losses and high dielectric strength. Other important properties for electrical insulation materials include low permittivity, high thermal conductivity and stability, and high mechanical strength and resistance to chemical corrosion. Polymers have long been employed as electrical insulation due to low costs, high thermal and chemical resistances, flexibility, and ease of processing. More recently, the development of inorganic-organic hybrid nanocomposite materials has attracted attention for application as dielectric materials in high voltage electrical insulation. The inclusion of inorganic nanoparticles as fillers has demonstrated potential in improving the dielectric, mechanical, and thermal properties of the polymer. Complete realization of that potential requires a deeper understanding of the interfacial interactions between the organic and inorganic components, and of the structure-property relations in these hybrid materials. The state of dispersion of the nanoparticles is known to be an important factor determining the properties of nanocomposites, thus necessitating improved control over the preparation of these materials. The synthesis of inorganic oxides directly in the polymer resin can unlock the challenges faced with traditional *ex-situ* approaches in the preparation of nanocomposites. Therefore, the use of *in-situ* synthesis routes was investigated in this work. The effects of variations in the synthesis conditions on the resulting structure and morphology of the nanoparticles, and on the properties of the nanocomposites, were investigated. Nanocomposites containing three types of inorganic oxides, SiO_2, TiO_2, and Al_2O_3, were prepared in this work. Pure epoxy was used as a reference material for the various properties of the nanocomposites that were investigated.

Silicon dioxide (SiO_2) nanoparticles were synthesized *in situ* in an epoxy resin (diglycidyl ether of bisphenol-A). Surface functionalization of the particles with the silane coupling agent 3-(aminopropyl) triethoxysilane (APTES) resulted in the formation of well-dispersed SiO_2 clusters between 10 and 150 nm. Poorly dispersed and agglomerated SiO_2 formed when no coupling agent or 3-(glycidyl oxypropyl) trimethoxysilane was used for surface functionalization. The state of dispersion (cluster size, agglomeration, and free space length) was controlled by altering the amount of APTES or the SiO_2 content. Small-angle X-ray scattering (SAXS) demonstrated the formation of a hierarchical structure of the SiO_2

clusters, consisting of both mass and surface fractal features. The use of 5 wt% SiO_2 in the epoxy reduced the real relative permittivity at room temperature. The dielectric losses (tan δ) in the nanocomposites were decreased at frequencies above 10^3 Hz, and increased at 1-100 Hz due to the emergence of a new relaxation. The nanocomposites demonstrated improved thermal stability, and the glass transition temperature exhibited an initial decrease followed by an increase with increasing SiO_2 content (up to 92 °C). Above the glass transition temperature, the nanocomposites exhibited significant low frequency dispersion and electrode polarization effects, possibly caused by the addition of ions and by-products from the *in-situ* synthesis route. The epoxy-SiO_2 nanocomposites demonstrated improved resistance to electrical tree growth when the SiO_2 was synthesized with sufficient amount of APTES, as the growth speed decreased by ~30 %. However, the tree initiation voltage decreased by ~20-60 % in the nanocomposites, compared to pure epoxy. The tree channels became conductive over the duration of the tree growth, as revealed from partial discharge measurements. The ultimate tensile strength of the nanocomposites decreased with increasing SiO_2 content. The nanocomposites exhibited an increased tensile elastic modulus, and larger plastic deformation and strain prior to failure.

Pre-synthesized SiO_2 nanoparticles (0.5 wt%) were mixed with epoxy in an *ex-situ* preparation route to compare the the dispersion of SiO_2 and the properties of the *ex-situ* nanocomposite with the *in-situ* nanocomposites. The SiO_2 was poorly dispersed, forming agglomerates from 200 nm to 2 µm. The dispersion was improved slightly when the particles were functionalized with APTES, forming 250 nm - 500 nm sized agglomerates. The permittivity was decreased below, and increased above, 10^4 Hz for the *ex-situ* nanocomposites. This change was attributed to the differences in the morphology of the SiO_2 particles compared to those present in the *in-situ* nanocomposites.

To improve the understanding of the effects of particle morphology, molecular dynamics (MD) simulations were performed using two different models for the SiO_2 in the nanocomposites. In the first model, the SiO_2 was constructed as uniformly dispersed particles with a defined size. In the second model, the SiO_2 was represented by molecular O-Si-O units dispersed randomly in the epoxy. The calculated elastic moduli and glass transition temperatures corresponded well with the experimental measurements. Both models exhibited the same trends in the glass transition temperature with increasing SiO_2 content. The second model overestimated the thermal conductivity of the nanocomposites. An amalgamation of both models is likely to be more representative for the nanocomposite system.

Titanium dioxide (TiO_2) and aluminium oxide (Al_2O_3) nanoparticles were also synthesized *in situ* in epoxy, using APTES for surface functionalization. The TiO_2 nanoparticles (10-50 nm) were discrete, possessed a defined shape, and were dispersed. The presence of titanium oxo-alkoxy clusters, which precipitate to form larger particles, was proposed due to the discrepancy between the results from SAXS and transmission electron microscopy (TEM). The epoxy-TiO_2 nanocomposites exhibited increasing thermal stability with increasing TiO_2 content, and a higher glass transition temperature than pure epoxy (up to 105 °C). The real relative permittivity decreased with increasing TiO_2 content. However, at 5 wt% TiO_2 the profile of the permittivity changed, similar to that observed in the *ex-situ* epoxy-SiO_2 nanocomposites. The new relaxation at 1-100 Hz was more prominent, resulting in a higher tan δ at below 10^3 Hz than pure epoxy and the epoxy-SiO_2 nanocomposites. The epoxy-TiO_2 nanocomposites demonstrated a significant increase in the resistance to electrical tree growth at both 10 and 15 kV. The tensile elastic modulus and ultimate tensile strength increased in the epoxy-TiO_2 nanocomposites with increasing TiO_2 content. However, the strain at failure decreased significantly before increasing slightly with increasing TiO_2 content.

The inorganic structures formed in the epoxy-Al_2O_3 nanocomposites were most probably not Al_2O_3, but a pseudo-Al_2O_3 structure resembling amorphous boehmite (but are still referred to as Al_2O_3). The Al_2O_3 particles formed diffuse clusters (~250 nm) that appeared close together. SAXS confirmed the formation of surface fractal structures in these particle clusters. The epoxy-Al_2O_3 nanocomposites exhibited higher glass transition temperatures than pure epoxy. The permittivity decreased with increasing Al_2O_3 content, and the profile of the permittivity was unchanged. Unlike the other nanocomposites in this work, the epoxy-Al_2O_3 nanocomposites exhibited a weak tan δ peak for the new relaxation emerging at low frequencies. The electrical treeing resistance was significantly higher in the epoxy-Al_2O_3 than the epoxy-TiO_2 nanocomposites when trees were grown at 10 kV. At 15 kV, however, the epoxy-Al_2O_3 nanocomposites exhibited rapid tree growth, comparable to that of trees grown in pure epoxy at 15 kV. In addition, the electrical trees in the epoxy-Al_2O_3 nanocomposites initiated at the same voltage as in the pure epoxy.

The *in-situ* synthesis approach was demonstrated to be successful in the preparation of epoxy nanocomposites for high voltage insulation. The results highlight the importance of the inorganic oxide filler morphology, the filler composition, and the degree of dispersion in determining the properties of the nanocomposites. All three types of *in-situ* nanocomposites exhibited lower permittivities and increased glass transition temperatures, compared to pure epoxy, when 5

wt% of filler was used. The resistance to electrical tree growth was generally increased, and was largest for the epoxy-TiO_2 and epoxy-Al_2O_3 nanocomposites. The epoxy-TiO_2 nanocomposites showed the highest tensile strength and glass transition temperatures. From the findings, structure-property relations were proposed that can explain the changes observed in the properties of the nanocomposites. The *in-situ* synthesis method used is versatile, and the improved understanding of the structure-property relations can be used to adjust the procedure as required to achieve the desired properties for different applications.

Contents

List of important abbreviations

AC	Alternating current
AIP	Aluminium isopropoxide
APTES	3-(aminopropyl) triethoxysilane
BET	Brunauer-Emmett-Teller
CTE	Coefficient of thermal expansion
DBS	Dielectric breakdown strength
DC	Direct current
DGEBA	Diglycidyl ether of bisphenol-A
DMA	Dynamic mechanical analysis
DSC	Differential scanning calorimetry
EDS	Energy dispersive X-ray spectroscopy
FFT	Fast-Fourier transform
FTIR	Fourier-transform infrared spectroscopy
GPTMS	3-(glycidyl oxypropyl) trimethoxysilane
LFD	Low frequency dispersion
MD	Molecular dynamics
NMR	Nuclear magnetic resonance
PD	Partial discharge
POPDA	Poly (oxypropylene) diamine, AKA Poly(propylene glycol) bis(2-aminopropyl ether), AKA Jeffamine D230
PRPD	Phase-resolved partial discharge
QDC	Quasi-direct current
RDF	Radial distribution function
SAXS	Small-angle X-ray scattering
SCA	Silane coupling agent
STEM	Scanning transmission electron microscopy
TEM	Transmission electron microscopy
TEOS	Tetraethyl orthosilicate
TGA	Thermogravimetric analysis
TIP	Titanium (IV) isopropoxide
UTS	Ultimate tensile strength
XRD	X-ray diffraction

1 Background

1.1 Motivation

Dielectrics are pervasive, especially in today's technological society where everyone is carrying, using, or is in some way connected to multiple electronic appliances. Every single piece of electrical equipment is reliant on the various dielectrics present in its components, among which are electrical insulators. Although the field of electrical insulation is considered as a "mature" science, due to relatively few changes in the types of electrical insulation employed industrially in the last few decades, any gain in the properties can potentially have a large impact, especially in the field of electric power transmission [1]. Until the late 1920s only natural materials were used in insulation systems, typically composites based on fibers such as cellulose, silk, cotton, and wool, or inorganic minerals such as mica, sand or quartz [2, 3]. With the advent of alternating current (AC), electrical insulation for much higher voltages became necessary. Dried paper impregnated with mineral oil was used for transformers and underground cables, and is still used today in many places. Since 1925, alkyd and phenolic resins were introduced as the first synthetic insulators, followed shortly by polyvinylchloride (PVC). More recently, cross-linked polyethylene (XLPE), ethylene-propylene-rubber (EPR) and epoxy resins have replaced many of the natural materials used as electrical insulation in different applications [2]. Figure 1.1 shows some applications of epoxy resins as insulation materials in e.g. transformers, printed circuit boards, rotating machines, and electric aircraft, alongside other applications such as adhesives or coatings and packaging materials.

As the demands on insulating materials increase further with the increasing variety and functionality of various electrical apparatus (such as transformers, switchgear, and motors), the necessity of new types of "functional materials" becomes increasingly evident. The electrical properties are no longer the only factor determining the performance of these materials as electrical insulation, as thermal and mechanical properties may also play a role depending on the specific applications. This has led to the development of "new" insulation systems that consist of polymers with additives, or composites of different types of materials. Various inorganic fillers, with particles in the micron size range, such as TiO_2, SiO_2, Al_2O_3, SiC, BN, and Si_3N_4 have been used to reinforce the mechanical properties of plastics since the 1970s [2]. However, the fillers may

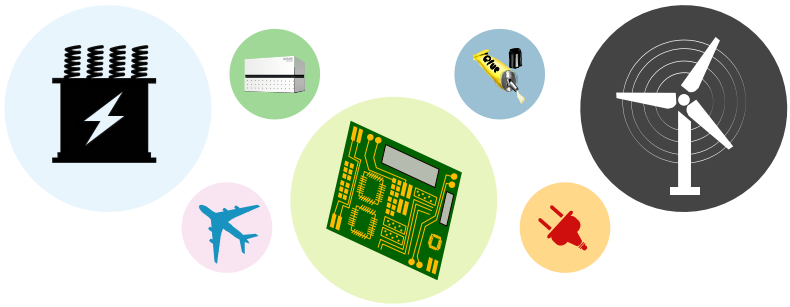

Figure 1.1. Applications of epoxy in various equipment and components, such as electrical insulation in power transformers, printed circuit boards, cables and rotating machines, as structural materials in aeronautical parts and wind turbine blades, or as packaging and encapsulation materials, coatings and adhesives.

deteriorate the electrical properties [1, 4, 5]. Further developments have led to the application of nanocomposites, a class of hybrid organic-inorganic materials consisting of inorganic nanoparticles dispersed in an organic polymer matrix, as electrical insulation. These nanocomposites, often interchangeably referred to as nanodielectrics in the literature, have occasionally displayed improvements in the electrical, thermal and mechanical properties compared to conventional polymer composites [6]. The dispersion and morphology of the nanoparticles affect the interfacial regions between the organic and inorganic components, and are suspected to play a critical role in determining the final properties of the material. Therefore, the procedures used in the fabrication of the nanocomposites, which can affect the dispersion and subsequently the properties, should be considered carefully, and is often a significant challenge in the production of well-dispersed nanocomposites [7]. Additionally, it is still not well understood how these interfacial regions, and the interactions between the polymer chains and the inorganic nanoparticles in these regions, alter the dielectric properties of the base polymer [6]. Questions remain regarding the mechanisms for how the complex permittivity is reduced in nanocomposites, despite the filler materials often having far larger intrinsic permittivities, and regarding how far the dielectric breakdown strength may be improved. An improved understanding of the structure-property relations of these complex systems will allow one to potentially tailor the properties as desired by manipulating the structure, content, or dispersion of the organic and inorganic components.

While various polymer composite systems have been investigated for diverse applications [8–13], epoxy resins and epoxy-based composite materials have been of interest in the dielectrics and electrical insulation field due to their ver-

satility (e.g. good thermal and mechanical properties and resistance against chemical corrosion, in addition to its excellent dielectric properties). The motivation of this work is therefore to first establish a robust fabrication process for epoxy nanocomposites containing different types of inorganic oxide fillers, with improvements in the dielectric, thermal and mechanical properties. While the majority of electrical engineers have exclusively used pre-synthesized nanoparticles that were mechanically mixed into the epoxy, chemists have used an alternative route for developing hybrid materials, namely synthesizing the inorganic particles *in situ* within the epoxy. This approach has not yet been used in the preparation of epoxy nanocomposites for electrical insulation applications. The dielectric properties of nanocomposites prepared in this way are therefore yet to be investigated, which harbours the potential for further improvements in these properties when combined with the new synthesis techniques.

1.2 Aim of the thesis

The primary objective of the work was to prepare epoxy nanocomposites suitable for use as high voltage insulation materials. This was achieved by preparing nanocomposites with a high quality of dispersion of the inorganic nanoparticles, with strong interfacial interactions between the particles and the polymer matrix.

An *in-situ* synthesis route was employed for producing surface-functionalized nanoparticles of SiO_2, TiO_2, and Al_2O_3 by using the sol-gel process [14], with metal alkoxides as precursors and a silane coupling agent for the surface functionalization. The structure and dispersion of the nanoparticles in the epoxy was characterized, and changes in these with various parameters (e.g. choice of coupling agent, pH of the reaction, and filler content) were investigated.

Selected thermal, mechanical, and dielectric properties of the prepared nanocomposites were investigated. The correlations between the structure and morphology of the materials with these properties are discussed. The electrical treeing resistances of the nanocomposites were measured and compared to that of pure epoxy to assess their applicability as high voltage insulation.

In addition, a structural model for the epoxy and epoxy-SiO_2 nanocomposite system was built and used for molecular dynamics simulations. The calculated thermal and mechanical properties of the epoxy and the nanocomposites were then compared to the experimental results obtained, and the applicability of the models was discussed.

2 Introduction

2.1 Polymers

Polymers are macromolecules that consist of long chains of repeating subunits or monomers. Polymers can be homopolymers (with the same monomer unit) or heteropolymers (with more than one type of monomer unit), and can be linear or branched. The branching depends on the conditions during the polymerization and the type of monomer(s) used. Due to the variations in the lengths of the chains present in a polymer, an average molecular weight for the polymer chains (M_n) is used to describe them.

Polymers can also be classified as thermoplastics or thermosets, depending on the behaviour above the glass transition. The glass transition is a reversible transition in amorphous or semi-crystalline materials from a hard and brittle glassy phase to a viscous, rubbery state as the temperature is increased. This transition, however, is not considered a phase transition, although it is similar to second-order phase transitions [15]. Thermoplastics, such as polyethylene (PE), polypropylene (PP), polyvinyl chloride (PVC), and polytetrafluoroethylene (PTFE, commonly known as Teflon), have high molecular weight and retains some amorphous characteristics in the glassy state. Above the glass transition temperature (T_g) the physical properties change without an associated phase change, and the polymer becomes softer and more flexible, allowing them to be reshaped. Thermosets on the other hand do not become soft and flexible above the glass transition (although they do become more rubbery) and therefore cannot be reshaped. This is due to the presence of covalent cross-links between the chains that form when the polymer is hardened by curing. The cross-links are irreversible and produce an insoluble polymer network that does not melt, but decomposes when heated sufficiently. Commonly used thermosets include epoxy resins, polyimides (PI), polyester, vulcanized rubber, and polyurethanes (PU) [16]. Polyethylene can also be cross-linked to form a thermoset.

Polymers have been used for electrical insulation since 1908 when phenol-formaldehyde resins were used in different electrical applications, but their usage boomed significantly with the introduction of PVC, PE, PU and other resins between the 1920s and 1940s [2]. These days cross-linked polyethylene (XLPE) is primarily used for high voltage AC and DC cables. Low density PE (LDPE) in general is a good option for power cables due to its excellent dielectric properties and the possibility of extrusion. Epoxy resins and other thermosets

are generally used as insulation in machines and dry transformers due to their toughness and improved thermal resistances, making them more suitable for hasher environments and higher service temperatures.

2.1.1 Epoxy resins

Epoxy is one of the most widely used thermosetting polymers, with a diverse range of applications as adhesives, laminates, encapsulation, coatings, aerospace components, and as electrical insulation in electronic devices and power transmission equipment [8]. Epoxy resins consist of low-weight monomers or oligomers (pre-polymers) containing epoxide structures as end groups. The structures of some of the most commonly used epoxy resins are shown in Figure 2.1.

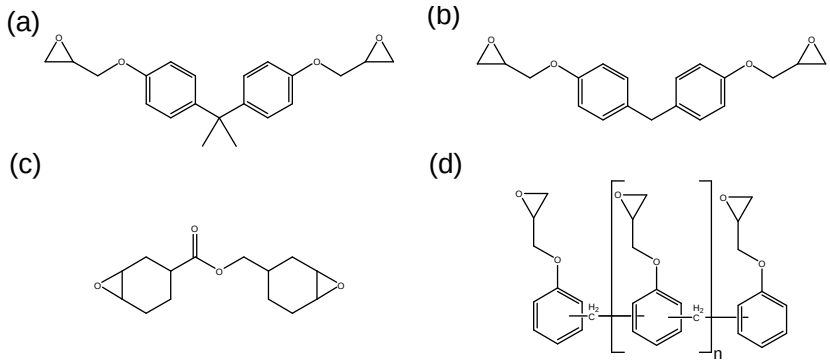

Figure 2.1. Selected examples of various types of epoxy monomers. **(a)** Diglycidyl ether of bisphenol A (DGEBA). **(b)** Diglycidyl ether of bisphenol F (DGEBF). **(c)** 3',3'-epoxycyclohexylmethyl 3,4-epoxycyclohexanecarboxylate. **(d)** Glycidyl ethers of phenolic novolac.

These resins are cured via the use of curing agents (or hardeners) that form cross-links between the pre-polymer units, resulting in the formation of a thermoset heteropolymer. The curing agents used are typically amines, acid anhydrides, phenols, thiols, and alcohols [8]. Curing reactions are initiated either via a nucleophilic addition or copolymerization reaction [13], or through cationic polymerization with the aid of initiators that promote homopolymerization of the epoxide groups [17]. A simplified curing reaction between an epoxy resin and a primary amine is shown in Figure 2.2. The properties of epoxy resins therefore can vary greatly depending on, among other factors, the type of monomer and curing agent used, the lengths of the monomer chains, the degree of cross-linking, and the conditions of the cure (temperature, photocuring, etc.) [13].

Aromatic epoxy resins, such as the diglycidyl ethers of bisphenol A (DGEBA) and F (DGEBF) (Figure 2.1a,b), are produced the most for industrial applications [8], as these can be prepared with large variations in molecular weight. Cycloaliphatic epoxy resins (such as that shown in Figure 2.1c) are also attractive in high-temperature applications due to excellent thermal stability [13]. Novolac epoxy resins (Figure 2.1d) possess high cross-linking densities due to the numerous epoxide groups present along the backbone (compared to the two present for DGEBA and DGEBF), resulting in good thermal properties and increased solvent resistance [13].

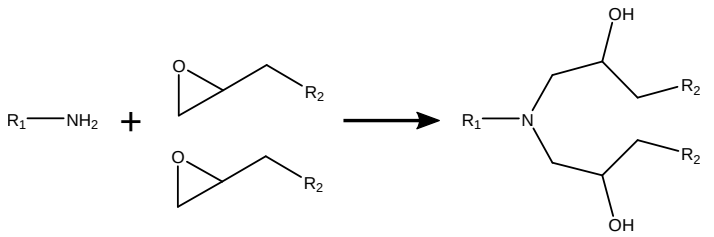

Figure 2.2. A cross link formed between two epoxy resin monomers via an amine group in the curing agent.

As a thermosetting polymer, epoxy resins cannot be shaped after curing. This results in most epoxy resins, especially those that are highly cross-linked, being brittle with poor resistance to crack initiation and growth in its glassy state [13, 18]. The glass transition region is dependent on multiple factors, such as the the presence of bulky side groups of the polymer chain, the types of intermolecular forces and cross linking, or the molecular weight of the chains. Additionally, epoxy systems that cure at higher temperatures have higher glass transition temperatures [8].

DGEBA is among the most studied epoxy resins for applications as high voltage insulation [6]. Cured DGEBA resins typically exhibit a real relative permittivity (ϵ_r') of 3-5 at 50 Hz and conductivities of 10^{-16}-10^{-15} S cm^{-1} at room temperature. The thermal conductivity varies between 0.1 and 0.5 W m^{-1} K^{-1} [6]. The glass transition of DGEBA-based epoxy is within the temperature range between 40 and 150 °C [18–21], depending on the curing agent and temperature used. The low permittivity, high thermal stability, and high glass transition temperature make epoxy resins an attractive option for application as electrical insulation materials.

2.2 Hybrid materials and nanocomposites

Composite materials are multiphase and possess properties that may be unique to the specific composite, resulting from the interactions between the various phases in the material. Hybrid materials are one type of composite material, and consist of a combination of organic and inorganic components [22, 23]. Hybrid materials are particularly interesting as organic and inorganic materials generally display opposing properties, and so the resulting composites can exhibit a unique blend of these properties that may be tuned for specific applications and requirements. The organic component allows the material to be easily shaped or processed and keeps the material light, while the inorganic component can provide mechanical, chemical and thermal stability in addition to new functionalities that depend on the structure, size, crystallinity, etc. of the component [11]. The properties of hybrid materials are, however, not only the sum of the individual contributions from each phase but also the interfaces between them, which can result in synergistic effects from the coexistence of two phases. Due to the importance of the interfaces, these materials are classified based on the different types of interactions between the organic and inorganic phases, as shown in Figure 2.3. Class I contains materials with weak physical bonds between the organic and inorganic components (e.g. van der Waals bonds, hydrogen bonds, dipole interactions), while Class II contains materials with strong covalent or iono-covalent chemical bonds (e.g. alkoxy or organometallic bonds) [24].

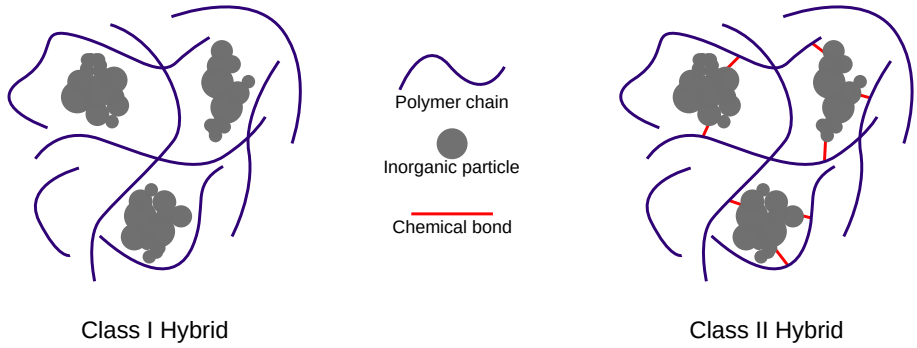

Figure 2.3. An illustration of the two classes of hybrid materials.

When one of the components in a composite material is at the nanoscale, the term nanocomposite is often used. In hybrid nanocomposites, it is usually the inorganic component that is present in the nanoscale (either as nanoparticles, nanorods, or nanotubes) and is dispersed as a filler material in an organic polymer matrix. Nano-sized fillers, in contrast to micron-sized fillers, result in a larger interfacial region that is available for interactions between the polymer chains and the particles due to the larger surface area to volume ratio of smaller particles. This means that it is possible to achieve properties similar to those of a traditional composite (containing micron-sized filler particles) with a much lower weight or volume fraction of particles. Additionally, while composites were originally developed as structural materials with a focus on reinforcing the mechanical properties, the advent of nanotechnology has allowed nanocomposites to be employed as functional materials with novel optical, electronic, magnetic and chemical properties [25]. Hybrid nanocomposites therefore have potential in optical applications, biomaterials, protective coatings and encapsulations, microelectronics, photovoltaics, flame-retardant materials, and fuel cell membranes [11].

Although inorganic micron-sized particles are used to reinforce the mechanical properties of epoxy-based composites, this often came at the cost of deteriorations in the electrical properties [1,4,6,7]. The use of nanoparticles instead have therefore attracted increasing attention in the electrical engineering community in the past two decades, as the resulting nanocomposite materials can potentially exhibit improved dielectric properties, in contrast to epoxy reinforced with micron-sized particles (hereby referred to as microcomposites).

2.2.1 Nanomaterials

Nanomaterials are defined as materials that contain particles or structures (internal or surface) with at least one dimension in the nanoscale (1-100 nm) [26]. Most nanomaterials can be classified into different categories [27], such as carbon-based (e.g. fullerenes, carbon nanotubes and nanofibers, carbon black, and graphene), inorganic (e.g. metals, metal oxides, clays, and ceramics), and organic (organic matter organized into structures such as micelles, liposomes, dendrimers, etc.). Among these, metal oxides, ceramics, mineral clays, and carbon nanotubes have been investigated extensively in various polymer systems for application in high voltage insulation systems [2].

The surface area to volume ratio of particles at the nanoscale increases drastically with decreasing size. As a result, the chemical and physical properties of nanomaterials are determined by the properties of and the interactions at the surfaces. Since the surfaces are so important, it is not only the size but

also the shape (and aspect ratio) of the nanomaterials that can affect the properties. The shape becomes more significant the smaller the particles become. Figure 2.4 displays examples of the various morphologies of nanomaterials that can be produced, from spherical and cubic particles to rods and wires, or even core-shell structures and tubes. Nanomaterials are well known for exhibiting finite size effects on the cell parameters [28], structure [29], phase transition temperatures [30], and band gaps and optical properties [31].

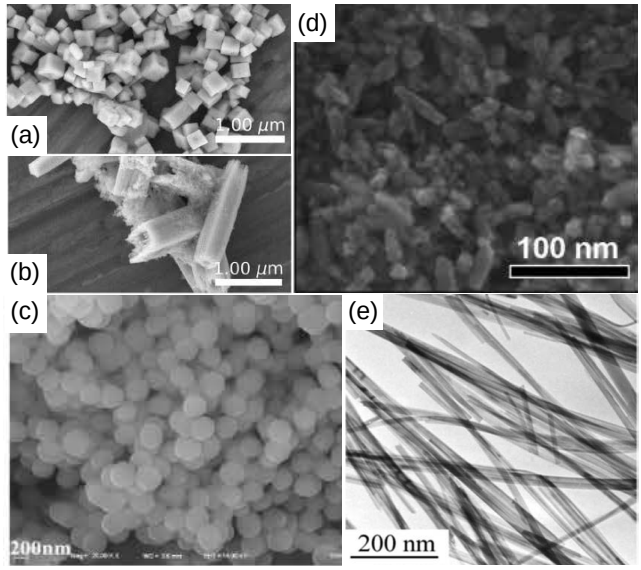

Figure 2.4. Nanomaterials with different morphologies: **(a)** cubic nanoparticles, and **(b)** hollow nanotubes of $Sr_xBa_{1-x}Nb_2O_6$, reprinted with permission from [32]; **(c)** spherical SiO_2 nanoparticles, reprinted from [33] with permission from Elsevier; **(d)** elongated rodlike nanoparticles of TiO_2, reprinted with permission from [34], Copyright 2021 American Chemical Society; **(e)** MnO_2 nanowires, reprinted with permission from [35], Copyright 2021 American Chemical Society.

Nanomaterials are synthesized either in top-down or bottom-up processes. In the former, micro- or macroscopic materials are successively cut and sliced or etched down to obtain nano-sized particles. This is commonly performed using techniques such as photolithography (with ultraviolet or X-ray radiation), electron beam lithography (EBL), or with a focused ion beam (FIB). In bottom-up processes, the nano-sized particles are built up from smaller units such as atoms and molecules. The process involves designing a synthesis route that allows the building blocks to self-assemble as desired. Physical deposition techniques such

as pulsed laser deposition (PLD) or atomic layer deposition (ALD) may be used to deposit atoms onto a substrate in a bottom-up process. An alternative would be to use chemical solution methods, such as sol-gel, hydrothermal synthesis, or spray pyrolysis, to synthesize the nanomaterials using reactions in chemical solutions instead.

In the following subsections, a brief description of the inorganic oxide nanoparticles that are used in this work is given.

2.2.1.1 Silicon dioxide

Silicon dioxide, SiO_2, also known as silica, can exist in a variety of crystalline and amorphous phases. Many of these phases consist of O atoms in a tetrahedral array around Si atoms, forming the orthosilicate anion. Silicate anions have the general formula $[SiO_{4-x}^{(4-2x)-}]_n$ and $0 \leqslant x < 2$. Silica and other silicate materials are found in nature as sand, or minerals such as quartz and montmorillonite. Naturally occurring crystalline polymorphs of silica include, among others, α- or β-quartz and α- or β-cristobalite [36]. Synthesized silica however tends to form amorphous and nanostructured powders, primarily by two main routes - either via high temperature flame pyrolysis to form *fumed* silica, or via hydrolysis and condensation reactions in the sol-gel process to form *colloidal* silica [37].

Amorphous silica lacks the long-range order present in crystalline silica, and the structures formed are dependent on kinetic and environmental factors due to the flat energy landscape [37]. This can result in a wide variety of amorphous structures forming with differences in the siloxane framework, built up from a network of silicate groups that can arrange themselves randomly or in rings, ladders, cages, and other shapes. Figure 2.5 shows an orthosilicate anion and possible arrangements of the anions in random or cage-like structures. Amorphous silica can also form branched structures characterized by a *mass fractal dimension*, or smooth colloidal particles that are non-fractal, or colloidal agglomerates characterized by rough *surface fractals*.

2.2.1.2 Titanium dioxide

Titanium dioxide, TiO_2, or titania, is a wide band gap semiconductor. Like silica, it can also exist in several crystalline polymorphs or amorphous nanostructures, although the crystalline forms of titania have attracted far more interest from the scientific community for applications in pigments, cosmetics, sunscreen, photocatalysis, photovoltaics, and optics [15]. Eleven crystalline polymorphs of titania are known, of which rutile, anatase and brookite (Figure 2.6) are the most common as they occur naturally. Rutile and anatase have tetragonal unit cells,

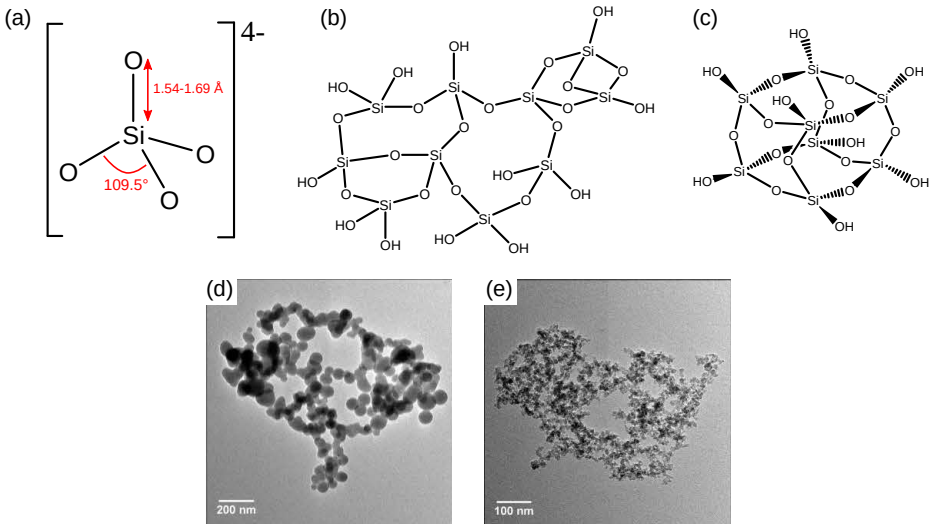

Figure 2.5. **(a)** Structure of the orthosilicate (SiO_4^{4-}) ion. **(b)** A randomly organized silica structure. **(c)** A cage-like silica structure. **(d)** Fumed silica with large, discrete particles arranged in a mass fractal structure. **(e)** Fumed silica with smaller particles organized in a surface fractal arrangement. The images in **(d)** and **(e)** were reprinted from [38], with permission from Elsevier.

while brookite has an orthorhombic unit cell [39]. The thermodynamically stable form in bulk titania is rutile at room temperatures, while anatase and brookite are metastable with higher lattice energies due to the smaller Ti-Ti distances as a result of the increased number of edges shared between the TiO_6 octahedra [39]. For titania nanoparticles however, anatase is observed more frequently. Amorphous titania is metastable, and heat treatment is used to achieve the transformation to a crystalline structure. The amorphous phase is described generally by a partial loss of octahedral coordination, with a certain amount of Ti ions with 5- or 7-fold coordination (instead of 6-fold) [40]. While there is disorder in the long range atomic structure, which is typical for amorphous materials, the local structure may be similar to anatase or rutile [41].

TiO_2 nanoparticles are generally synthesized by chemical solution methods (e.g. sol-gel or hydrothermal synthesis) with alkoxide or chloride precursors [44]. The synthesis conditions and additives used can greatly influence the morphology and crystal structure of the particles formed, although anatase is the preferred structure in most cases for nano-sized particles [15].

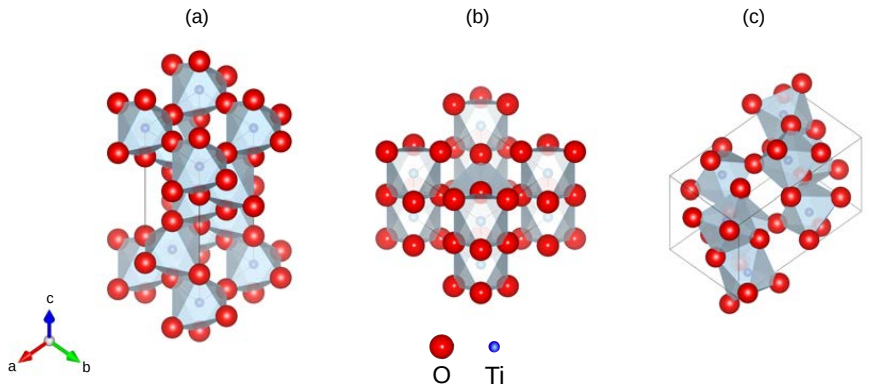

Figure 2.6. The unit cell structures of **(a)** anatase, **(b)** rutile, and **(c)** brookite. Represented using VESTA [42] with crystallographic data from [43].

2.2.1.3 Aluminium oxide and boehmite

Aluminium oxide, Al_2O_3, or alumina, is an electrically insulating ceramic with a relatively high thermal conductivity (compared to SiO_2 and TiO_2) [45]. The thermodynamically stable phase at room temperature is α-Al_2O_3 (corundum), with the crystal structure shown in Figure 2.7a. Alumina can be found in a multitude of metastable crystalline phases (e.g. the cubic γ and η phases, the monoclinic θ phase) [46]. Alumina is used in industry as absorbents, catalysts, coatings, or abrasives, but has also been employed as a filler material for epoxy resins to improve the thermal conductivity [1].

Aluminium oxide monohydroxide, also known as boehmite (γ-AlO(OH)), can be used as a precursor for various Al_2O_3 polymorphs [46]. Boehmite can also be formed using chemical solution methods, such as sol-gel or hydrothermal synthesis from aluminium alkoxide precursors. The structure of boehmite is shown in Figure 2.7b. Upon heating boehmite to above 420 °C it transforms to γ-Al_2O_3. Further heating to 513, 1069 and 1183 °C results in phase transformations to δ-Al_2O_3, θ-Al_2O_3 and α-Al_2O_3, respectively [49, 50]. Boehmite nanoparticles have been used to reinforce the mechanical properties of epoxy resins, such as shear strength and modulus, compressive strength, and fracture toughness [51].

2.2.2 The organic-inorganic interface in composite materials

Composite materials containing micron-sized filler particles are, compared to nanocomposites, more easily understood. The properties of the composite can

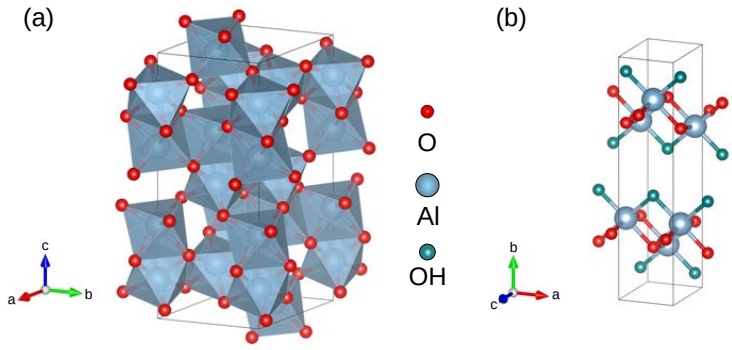

Figure 2.7. Crystal structures of **(a)** α-Al_2O_3, and **(b)** boehmite. Represented using VESTA [42] with crystallograhic data from [47] for Al_2O_3 and [48] for boehmite, respectively. The sizes of the atoms are not representative of the actual atomic radii.

be predicted based on the properties of the individual components. For example, the Lichteneker-Rother logarithmic law of mixing can be used to estimate the permittivity of dielectric composites [5, 52]. With nanocomposites however, the interfacial regions between the organic and inorganic components is significantly larger, assuming that the nanoparticles are dispersed homogeneously in the matrix. At the interfaces between the polymer chains and the inorganic nanoparticles, the interactions between them in the form of chemical and physical bonds will affect the mobility, conformations, and perhaps even the crystallinity of the chains in the region [53]. Raetzke and Kindersberger [54] consider the regions of polymer close to or around the interfaces as a third phase in the composite due to the structure of the chains and the properties of the region being different from both the bulk polymer and the inorganic filler. These regions are therefore referred to as an *interphase*. The *interphase* can be considered to be a layer between 1 and 10 nm surrounding the nanoparticles [55]. As seen in Figure 2.8, for a given filler content in volume fraction, a reduction in filler particle size results in a significantly larger volume fraction of this *interphase*. Based on the graph in Figure 2.8b, with a filler content of only 20 vol%, particles as small as 15 nm will result in the entirety of the polymer being comprised of interphase volume. Hence, all of the polymer chains will have some interaction with the dispersed particles.

Due to the significance of interfaces in nanocomposites, several models and theories have been proposed to understand and explain the properties and behaviour of nanodielectrics, some of which are shown in Figure 2.9. One of the earliest models was proposed by Lewis in 1994 [56], which was based

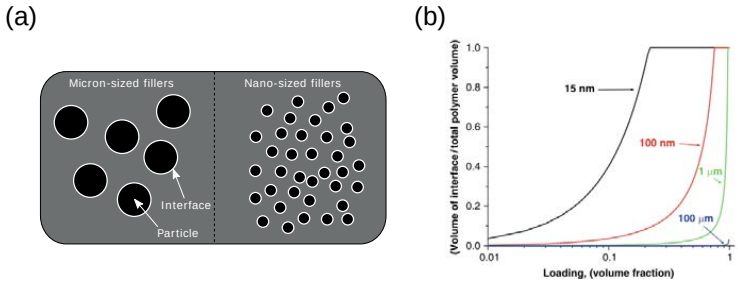

Figure 2.8. (a) An illustration of the increased area of the interfaces for nano-sized fillers compared to micron-sized filler particles. **(b)** Interphase volume per total polymer volume as a function of filler content (loading in volume fraction) for different filler particle sizes. Adapted with permission from Springer Nature Customer Service Centre GmbH: Springer Nature, Dielectric Polymer Nanocomposites by J. Keith Nelson, 2010.

on the established electrical double layer model that was used to visualize the ionic environment around a charged surface. Afterwards, Tsagaropoulos and Eisenberg [57] and Tanaka et al. [53] proposed variants of models describing a layered or "multi-core" structure of the interface. Several other models, often based on the aforementioned models, have been proposed to explain the various effects observed from experiments, such as the water-shell model by Zou et al. [58], the polymer chain alignment model by Andritsch et al. [59], or the interphase volume model by Raetzke and Kindersberger [54]. More recently, Alhabil et al. [60] proposed a *particle interphase* model, where the interphase layer is extended to inside the particle in addition to the polymer.

2.2.2.1 The electrical double layer at the interfaces

In his model, Lewis defined the interface as the region in which the forces associated to a selected property are different from the bulk in each phase (where the respective forces are constant) [56]. Additionally, the interface was characterized based on the organization of the charges at and around the nanoparticle surface. If the surface of the nanoparticle is charged, the surrounding polymer will establish a screening counter charge.

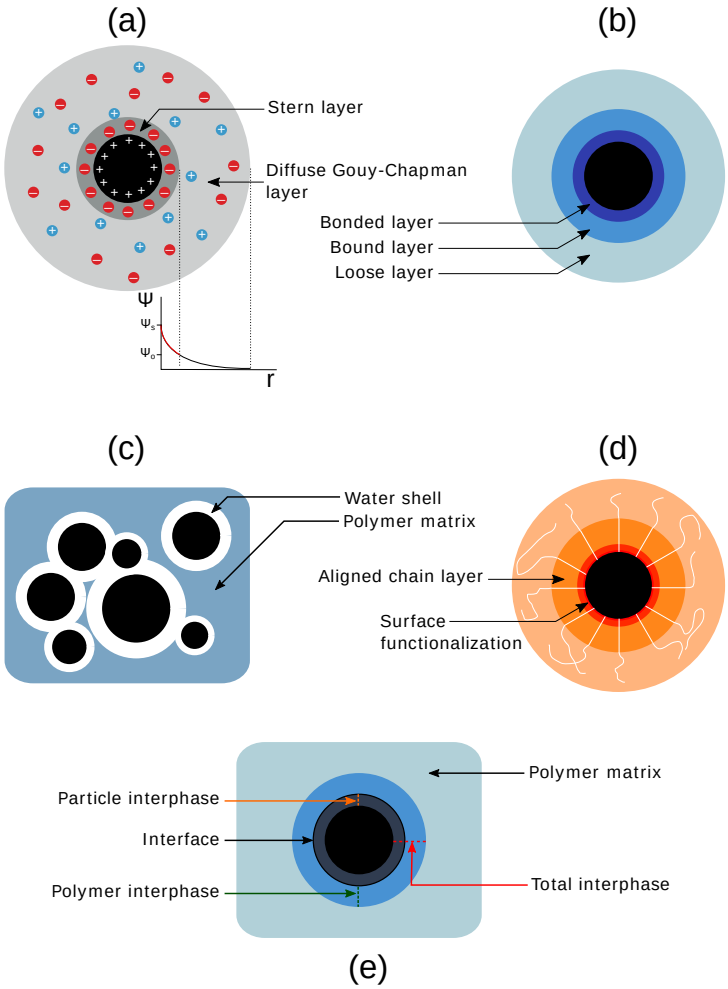

Figure 2.9. Schematic of the various models for the interfaces in polymer-inorganic nanocomposites: **(a)** The Lewis model for a positively charged nanoparticle, showing the electrical double layer and the resulting electrical potential distribution (ψ) at distance r from the surface. **(b)** The Tanaka multi-core model with three layers. **(c)** The water-shell model, showing a layer of adsorbed water on the nanoparticle surface. **(d)** The polymer chain alignment model, showing the aligned chains in the middle layer. **(e)** The particle interphase model, showing the interphase regions in both the particle and the polymer matrix. In each figure the inorganic nanoparticle is represented by the black circle.

The screening charge may occur in two ways - either by polarization of the organic phase via electronic polarization and reorganization of permanent dipoles, or by the migration of mobile ions in the organic phase to establish an electrical double layer around the nanoparticle, as shown in Figure 2.9a. The double layer consists of a counterion layer bound to the surface, forming the Stern (Helmholtz) layer, and a thermally activated fluctuating distribution of counter- and co-ions, forming the diffuse Gouy-Chapman layer. The Coulombic interaction between the charges is expressed by a potential distribution function (ψ) that simultaneously satisfies the Poisson and Boltzmann equations. The potential at the surface (ψ_s) drops linearly to ψ_o across the Stern layer. ψ then drops exponentially in the diffuse layer with increasing distance (r) from the surface. The Debye length (κ^{-1}) defines the extent of the exponential decay of the double layer. The characteristics of the electrical double layer can therefore determine the homogeneity of the distribution of inorganic nanoparticles in a polymer matrix. Due to the incompatibility between organic and inorganic materials and the large surface area of nanomaterials, there will be a large tendency for the nanoparticles to form agglomerates to reduce the surface area exposed to the organic phase. This is facilitated by the attractive inter-particle van der Waals forces but may be hindered by the screening double layer if the particles are charged. This balancing of the attractive polarization and repulsive double layer forces, which was described for colloidal systems by the Derjaguin, Landau, Verwey and Overbeek (DLVO) theory [61], results in an energy minimum at a certain distance between the charged particles. A large Debye length is preferred for maintaining the separation of the charged nanoparticles.

It is important to also consider the steric effects from the polymer chains at the interfaces. This depends on the strength of the bonds formed between the particle surface and the polymer chains, which may also improve the compatibility between the materials and aid in the dispersion of the particles. The models by Tsagaropoulos and Tanaka look further into the nature of the polymers at the interface, in contrast to Lewis' model which focuses on the electrostatics at the particle surface.

2.2.2.2 Multi-layered interfaces

Tsagaropoulos and Eisenberg [57] proposed a multi-layered interface depending on the strength of the interactions between the particles and the polymer. In the first layer of this interface, the polymer chains in the vicinity of the nanoparticles appear to be immobile in the temperature and frequency regimes, based on the low spin-spin relaxation time from nuclear magnetic resonance (NMR) measurements, and do not participate in the polymer's glass transition [57].

There is an additional layer beyond this immediate layer of immobilized chains where the polymer chains have restricted mobility, the so-called "loosely bound" layer. These chains are capable of participating in a second glass transition (typically at higher temperatures) that is distinct from the regular glass transition observed in the bulk polymer. This second transition becomes prominent when the regions of restricted mobility overlap below a critical distance between the filler particles. The model also postulates that the immobilized polymer chains do not restrict the mobility of the chains in the loosely bound layer as efficiently as the particles do. Additionally, the thermal history of the composite may affect the transformation between loosely bound to tightly bound/immobilized polymer, as the behaviour of the second glass transition changes with repeated measurements [57].

Tanaka et al. [53] proposed a similar model containing an additional layer, forming a multi-core structure around the nanoparticle. In this model, the multi-core structure (shown in Figure 2.9b) consists of a bonded layer, a bound layer, and a loose layer. The bonded layer is defined generally as any polymer that is chemically bonded to the particle surface, which does not always occur in nanocomposites. A coupling agent or surface functionalization on the particle is often required to facilitate a chemical bond with the polymer chains. The second layer is a region consisting of polymer chains that interact with the chains in the first layer or the nanoparticle surface, and may be "bound" with restricted mobility. The third layer consists of polymer chains with loose coupling and interaction to the second layer, and with different chain conformations and mobility. In addition to the chemical interactions, Tanaka's model also includes Coulombic interactions by superimposing a Gouy-Chapman diffuse layer over the other three for charged nanoparticles, assuming there are mobile ions in the polymer. The free volume, defined as the regions not occupied by the polymer chains [62], is also an important parameter as the behaviour and properties of the polymer chains in the bulk polymer will vary significantly when compared to the chains in the different interfacial layers. A collaborative effect is also expected, similar to Tsagaropoulos' model, when the interfacial layers of neighbouring nanoparticles overlap [53].

Other models that also describe the interface as layers share similarities with the models proposed by Tsagaropoulos and Tanaka. One of these is the water shell model [58], which assumes that water molecules are adsorbed around the nanoparticles creating water layers. The first layer is formed by tightly bound water molecules, while the second layer consists of water molecules held loosely by van der Waals forces and is a conductive layer. As a result, when a large amount of water is absorbed into the composite, percolative pathways

are formed through overlapping water shells (Figure 2.9c). The model is used to explain the degradation of the electrical properties of insulating epoxy nanocomposites in humid environments or when using nanoparticles with no surface modifications. In the case where the nanoparticle surfaces are functionalized, Andritsch et al. [59] proposed the polymer chain alignment model. This model states that with the correct functionalization, the polymer chains will be bonded to the particle surface and form a rigid inner layer where the chains are aligned, as shown in Figure 2.9d, resulting in increased crystallinity. An outer layer also forms between this rigid layer and the bulk polymer, where the polymer chains are affected (in contrast to the bulk polymer) but not aligned.

Raetzke and Kindersberger's *interphase* model postulates that understanding how the structure of the polymer chains in the interphase is different from the bulk polymer may shed light on the different mechanical, thermal and electrical properties. A more recent development of the interphase model was proposed by Alhabil et al. [60], which stipulates that it is not only the polymeric regions around the nanoparticles that are different from the rest of the polymer matrix. The atoms in the particles that are at, or just under, the particle surface should also be affected by the interactions with the polymer, and therefore are different from the atoms in the bulk of the particle. Hence, the interphase region consists of both polymer and particle interphases, although the particle interphase may be significantly narrower than the polymer interphase. This is illustrated in Figure 2.9e, which also highlights the sharp interface at the nanoparticle surface between the two interphases.

2.2.2.3 Challenges in understanding the interface

The models described above share certain assumptions, such as the shape of the particle (spherical) or the formation of layers in the interface, or that the model is independent of the type of particle or polymer in the system. Lewis' model can explain the electrical and electromechanical features of interfaces, but disregards any chemical interactions between the polymer and the particles. Tsagaropoulos' model on the other hand investigates just the chemical and physical features instead, and can explain the occurrence of a second glass transition in some nanocomposite systems, but does not explain why this second glass transition is not always observed. Tanaka's model is more universal, but still has limitations in that it fails to explain contradictory results (e.g. why the glass transition sometimes decreases with increasing filler content [4]). The aforementioned models can explain variations in the electrical and thermal properties of nanocomposites in several cases, but there are many instances of contradictory results by different researchers even with repeated measurements and similar

preparation and characterization procedures [1,6,60]. This does not necessarily mean that the models presented are wrong, but rather that their verification is difficult, and that there is still much that is not understood about the interface chemistry. Even small variations in each synthesis or preparation step may be responsible for different effects on the properties of the material, as seen in the review by Alcoutlabi and McKenna [63] which investigated reports of changes in the glass transition temperature. However, despite the limitations, these models still represent a significant effort towards improving our understanding of the interfaces in hybrid nanocomposites, and may yet contribute to the development of a universal model in the future.

2.3 Preparation of epoxy nanocomposites

Nanocomposites are generally prepared using *ex-situ* methods that involve physically mixing pre-synthesized filler particles into the polymer (blending or intercalation), or into a monomer that is subsequently polymerized [64]. This approach is currently the most practical for large or industrial scale production. The physical mixing is typically performed using mechanical mixers with high shear rates, although ultrasonication and centrifugation (or both) have been employed. In the case of epoxy nanocomposites, the mixing must be done prior to the addition of the curing agent. Afterwards the samples may be cast in molds and cured. The presence of the nanoparticles, depending on the filler content, may increase the viscosity of the epoxy resin [65], leading to difficulties in casting. In many cases the nanoparticle surfaces are functionalized prior to dispersal in the epoxy. The surfaces are modified using organic molecules to improve the compatibility between the hydrophilic inorganic particles and the hydrophobic organic resin, which may improve the dispersion. Figure 2.10a shows the general steps in the *ex-situ* processes for nanocomposite production with surface-functionalized nanoparticles.

The functionalization of the nanoparticle surfaces may be achieved using physical interactions (e.g. when surfactants or macromolecules are adsorbed on the surface as ligands), resulting in the formation of Class I hybrids. Alternatively, the functionalization may be achieved using chemical interactions (such as when silane coupling agents are used), forming a bridge between the organic and inorganic components via chemical bonds, resulting in a Class II hybrid [9]. Physical modifications, however, may be thermally and solvolytically unstable due to the weak forces involved (e.g. hydrogen bonds or van der Waals forces) compared to the chemical bonds formed during chemical modification. In the case of epoxy nanocomposites, silane coupling agents

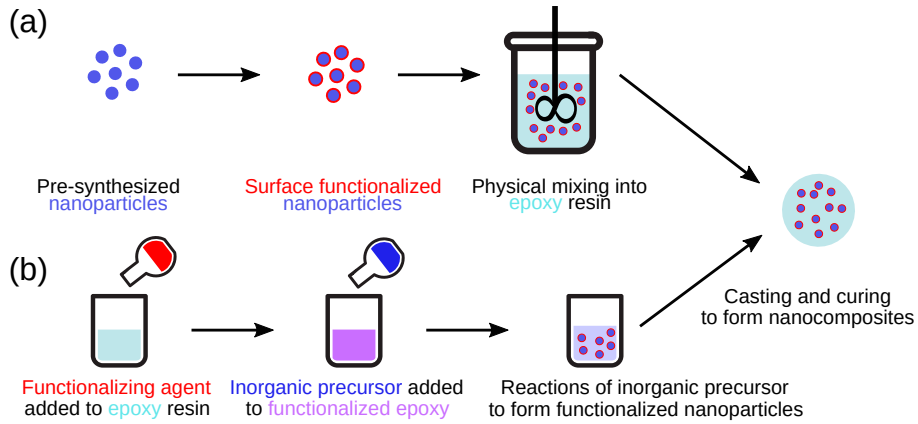

Figure 2.10. General schematic of the **(a)** *ex-situ* and **(b)** *in-situ* pathways used in the preparation of epoxy nanocomposites.

(SCAs) are commonly used for functionalizing the surfaces of inorganic oxide nanoparticles [66–68]. SCAs are organosilicon compounds with the general formula $Y(CH_2)_nSiZ_3$, where Y is a functional organic group (which can bond to the polymer chains) and Z is a hydrolysable group (which can attach to the surface of the particles). Commonly used SCAs include 3-(aminopropyl) triethoxysilane (APTES), 3-(glycidyl oxypropyl) trimethoxysilane (GPTMS), 3-(isocyanatopropyl) triethoxysilane (IPTES), among others [9]. Certain organic molecules (e.g. self-assembled monolayers of organophosphates [69]) or polymer brushes (e.g. thiocene or anthracene molecules on a poly(glycidyl methacrylate) backbone [70]) have also been employed as ligands that are grafted onto the nanoparticle surfaces, and provide steric repulsion.

An alternate approach that has also been employed in the preparation of nanocomposites with well-dispersed fillers is to use a bottom-up *in-situ* method, where the inorganic nanoparticles are synthesized and grown directly inside the polymer (or monomer). Several different synthesis techniques can be used in this approach, including (but not limited to) the sol-gel method [71, 72], reverse microemulsion [73], hydrothermal or solvothermal synthesis [74], or other non-aqueous reaction pathways [75]. The surface modification may be performed simultaneously with or after the particle synthesis. Figure 2.10b shows an *in-situ* process for the production of nanocomposites (in this case the sol-gel method), with the epoxy being functionalized first prior to synthesis of the particles from the precursor. The main advantage of using these *in-situ* methods is that it allows greater control over the structure of the nanocomposite,

enabling the possibility to then tailor specific properties. As the particle generation, surface modification, and incorporation in the polymer is integrated into a single process, the organic groups on the monomer or polymer chains can have a passivating effect on the particles to limit the agglomeration and control their growth [76]. The disadvantage of the *in-situ* synthesis procedure for preparation of nanocomposites is the possible presence of by-products or unreacted material, which may have a detrimental influence on the properties of the final nanocomposite. Additionally, such procedures are not necessarily suitable for upscaling to industrial production.

2.3.1 The sol-gel method

The sol-gel method is an extensively used process in the preparation of inorganic materials, typically ceramic oxides and glasses, but is also one of the most common processes used for preparing hybrid materials *in situ* at low temperatures [24,77–79]. The method consists of two fundamental reactions: first, a molecular precursor, usually a metal alkoxide, is hydrolysed; in the second step, polycondensation reactions occur between the hydrolysed molecules [80]. As the polycondensation reactions proceed, the "sol" of inorganic nanoparticles in a colloidal solution is converted into a viscous gel, consisting of a continuous inorganic network containing the solvent. Drying of the gel will result in removal of the liquid phase, and a subsequent thermal treatment (e.g. calcination or firing) may be used to obtain the synthesized nanoparticles. Figure 2.11 shows the outline of the hydrolysis and condensation reactions.

These reactions can be summarized in total as:

$$\mathrm{M(OR)_n} + m\mathrm{XOH} \rightarrow \left[\mathrm{M(OR)_{n-m}(OX)_m}\right] + m\mathrm{ROH} \tag{2.1}$$

where M is a metal, R is an alkyl group, and X is H during hydrolysis and M during condensation [81]. Figure 2.11 shows both an oxolation condensation reaction, where two metal hydroxyl (M-OH) groups react to form an M-O-M bond with water as a leaving group, and an alkoxolation condensation reaction, where a hydroxyl group reacts with an alkoxo (M-OR) group, with the alcohol (R-OH) as a leaving group. Successive condensation reactions between hydrolysed molecules will form longer M-O-M chains that eventually build up the inorganic oxide network.

One of the most attractive features of the sol-gel method is the ability to control the size, structure, and morphology of the materials formed by controlling the rate and progression of the hydrolysis and condensation reactions. For example, the choice of metal alkoxide precursor can affect the hydrolysis rate. Hydrolysis

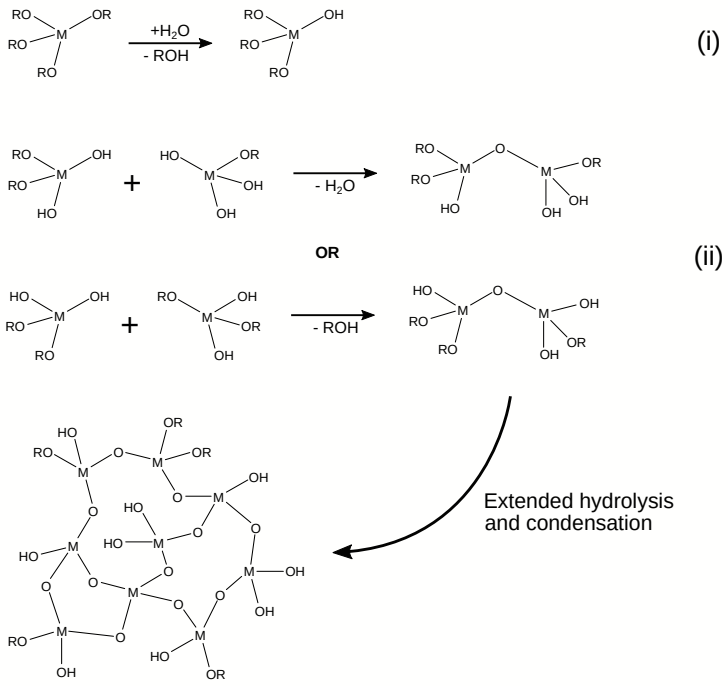

Figure 2.11. Simplified representation of the **(i)** hydrolysis and **(ii)** condensation (both oxolation and alkoxolation) reactions occurring in a metal (IV) alkoxide ($M(OR)_4$), and the formation of an amorphous network of M-O-M bonds.

is faster for metal cations with high electrophilicity and high degree of unsaturation (*N-Z*, where N is the coordination number and Z is the oxidation state of the metal cation) [24]. As a result, transition metal alkoxides are typically very reactive, as $N\text{-}Z > 0$, and hydrolyse easily in the presence of moisture. Silicon alkoxides, however, are more stable due to the lower electrophilicity of Si [24], and may require a catalyst to increase the hydrolysis rate [22, 82]. The length and branching of the alkoxide chains will also affect the hydrolysis, as these chains provide steric hindrance that reduces the reactivity of the metal alkoxide. The choice of solvent is another important parameter, not only for the control of the reaction rates, but also to control polymer solubility or preventing phase separations when the sol-gel process is used for synthesizing nanocomposites [80]. The pH of the solution will affect the reaction rates. Acidic conditions will protonate the alkoxide groups, thereby enhancing the reaction kinetics by producing good leaving groups [14], catalysing the hydrolysis. Condensation

in acidic conditions will result in extended, less branched and more polymer-like networks as the condensation will occur preferentially on the ends of the chains due to the greater ease of protonation on metal cations with more alkoxy groups [14]. Conversely, basic conditions will catalyse the condensation reactions, as it encourages the deprotonation of hydroxyl groups. This reaction occurs preferentially on the middle of the chains, resulting in a highly branched, more compact structure. The development in structure with pH for aqueous silica prepared from alkoxides is shown in Figure 2.12.

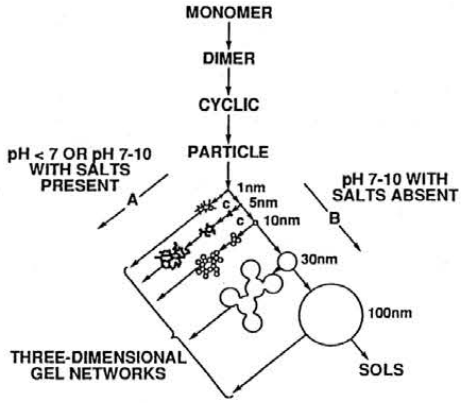

Figure 2.12. Differences in the polymerization behaviour and final structure in silica prepared from silicon alkoxide precursors in basic and acidic solutions, with and without flocculating salts, respectively. Reprinted from [14], with permission from Elsevier.

The sol-gel process may also be non-hydrolytic (or non-aqueous). This process can be solvent-free since water is not required for hydrolysis. A non-aqueous sol-gel route requires an oxygen donor (e.g. alkoxide, ether, alcohol, carboxylate) to react with the metal precursor under non-aqueous conditions [83] with a ligand exchange mechanism catalysed by Lewis acids [84]. This route can be useful where the aqueous route may be suboptimal or discouraged, and is also easier to control as the reactions proceed more slowly [84].

2.3.2 Synthesis of inorganic oxides *in situ* in epoxy

The sol-gel method has been employed extensively in the synthesis of inorganic fillers, particularly SiO_2, in polymer nanocomposites [9]. In the case of epoxy, the majority of literature report the use of either a one-step or a two-step hydrolytic sol-gel process. In the one-step process, the reactants are combined and allowed to react simultaneously prior to casting and curing [71,85]. The two-step process

has several variants: in a *'simultaneous'* procedure, the alkoxide precursor is pre-hydrolysed in the first step, followed by mixing with the epoxy resin and curing agent in the second step where the polymerization of the epoxy monomers and the formation of the inorganic network occurs simultaneously [71, 85]. In a *'sequential'* procedure, the epoxy is cured first, followed by swelling with the inorganic precursors in the second step [86, 87]. In a *'chronological'* procedure, the epoxy is first functionalized using a surface modifier (typically SCAs), followed by addition of the precursors and other reactants [88, 89]. The non-hydrolytic sol-gel process has also been used in the preparation of *in-situ* nanocomposites, with boron trifluoride monoethylamine (BF_3MEA) [21, 90, 91] or benzyl alcohol (BzOH) [92] as the catalysts. TiO_2 can also be synthesized *in situ* in epoxy using similar one-step or two-step hydrolytic processes [20, 93, 94], or a non-hydrolytic process with formation of titania nanoparticles in a sol first, which is subsequently mixed with the epoxy [92]. Table 2.1 summarizes various procedures using both aqueous and non-aqueous sol-gel in the preparation of epoxy-SiO_2 and epoxy-TiO_2 nanocomposites, and shows the variety of morphologies and structures that can be obtained with different precursors, procedures, catalysts and surface modifiers.

In the synthesis of SiO_2, tetraethyl orthosilicate (TEOS) is the most common alkoxide precursor. However, SCAs such as GPTMS have also been used as the precursor, and not only as surface functionalizing agents, due to their compatibility with epoxy. In earlier works, *p*-toluenesulfonic acid monohydrate (TSA) was used as a catalyst for the hydrolysis of TEOS [71, 85–87]. In the absence of an acidic catalyst, the use of an amine curing agent (e.g. polypropylene glycol diamine) may have a catalytic effect as the amine groups can serve as an effective nucleophile [71]. Other studies have used dibutyltindilaurate (DBTDL) or inorganic acids (e.g. HCl) as catalysts [18, 88], despite some indications that DBTDL is less effective than TSA at hydrolyzing TEOS, which would result in more compact SiO_2 structures [86]. The effects of a catalyst for the hydrolysis is quite evident in the resulting morphology of the SiO_2. Matejka et al. [71] demonstrated this in a one-step synthesis with no catalyst, where the SiO_2 formed 100-300 nm compact agglomerates with high fractal dimension (D_m = 2.7), and in a two-step simultaneous procedure with TSA which resulted in more 50-100 nm open structures with a lower fractal dimension (D_m = 1.7). For epoxy-TiO_2 nanocomposites, various titanium alkoxides have been used, such as titanium (IV) isopropoxide (TIP), titanium (IV) butoxide (TBO), or tetraethyl orthotitanate (TEOT) [9]. Non-aqueous routes for TiO_2 can use $TiCl_4$ as a precursor [92]. The choice of catalyst does not appear to affect the morphology of the *in-situ* prepared TiO_2, where the formation of more defined particles is more common than branched and diffuse clusters.

Surface functionalization has been used to control the size and dispersion of the inorganic oxide particles. Generally, improvements in the state of dispersion of the nanoparticles have been reported when surface modifiers are used. Jiao et al. [95] and Nazir et al. [89] both observed a less distinct phase boundary between the epoxy and the SiO_2 when APTES was incorporated, indicating an improved mixing and interfacial interaction between the components. Wu and Hsu [20] also demonstrated phase separation in epoxy-SiO_2 nanocomposites without GPTMS. Apart from conventional SCAs, ionic liquids have also been employed in the synthesis procedure. These can act as molecular templates (resulting in different matrix-filler interface characteristics [96]), as catalysts, or as an alternative to volatile solvents, and can improve the dispersion and reducing the size of the agglomerates [91,97,98].

From Table 2.1, the variations in the morphologies of the synthesized nanoparticles observed with small differences in the synthesis procedures highlights the versatility of the sol-gel process and the tools it provides to tailor the inorganic oxide particles formed. However, it should also be noted that the inorganic precursors, catalysts, and coupling agents (or other surface modifiers) are only one part of the hybrid system. The final morphology and organization of the *in situ* synthesized particles will also be affected by the organic components, which are not necessarily accounted for in Table 2.1. The length and types of the epoxy monomers, as well as the curing agents that are used, will also determine the kinetics of the sol-gel processes. For example, the use of an amine-based curing agent can result in basic conditions even in the presence of an acidic catalyst (if the curing agent is in excess), thereby resulting in the formation of larger colloidal particles, as evidenced in the works of Matejka et al. [71]. In their work, a one-step procedure (with all of the precursors mixed together) resulted in large agglomerates forming, whereas a two-step procedure with pre-hydrolysis of the TEOS prior to mixing with the epoxy and the curing agent resulted in smaller SiO_2 structures.

Table 2.1. Selected sol-gel processes employed in the synthesis of SiO_2 and TiO_2 *in situ* in epoxy nanocomposites, including the morphologies of the inorganic structures formed.

Inorganic material	Precursor	Sol-gel procedure	Catalyst	Surface modification	Morphology	Ref.
SiO_2	TEOS	Aqueous, two-step simultaneous	-	-	10 nm domains	[85]
SiO_2	TEOS	Aqueous, one-step	TSA	-	100-300 nm aggregates with high fractal dimension	[71]
SiO_2	TEOS	Aqueous, two-step simultaneous	TSA	-	50-100 nm structures with low fractal dimension	[86]
SiO_2	TEOS	Aqueous, two-step chronological	-	APTES	Bicontinuous phases with APTES, distinct 100 nm SiO_2 clusters without APTES	[89]
SiO_2	GPTMS	Aqueous, one-step	DBTDL	-	15-60 nm branched, interconnected fractal structures	[18]
SiO_2	GPTMS	Aqueous, two step simultaneous	DBTDL	-	5 nm particles in larger (unspecified) clusters	[99]
SiO_2	TEOS	Aqueous, two-step simultaneous	DBTDL	GPTMS	Hierarchical clusters consisting of siloxane nanostructured domains with 0.5-1 nm primary particles	[100]
SiO_2	TEOS	Non-aqueous, two-step process	BF_3MEA	-	20 nm branched, interconnected structures	[21]
SiO_2	TEOS	Non-aqueous, two-step process	BF_3MEA	Ionic liquids [1]	10-100 nm clusters	[91]

Continued on next page

Table 2.1. continued

Inorganic material	Precursor	Sol-gel procedure	Catalyst	Surface modification	Morphology	Ref.
SiO_2	TEOS	Aqueous, two-step sequential	BF_3MEA	Ionic liquids and GPTMS	Silsesquioxane domains smaller than 20 nm	[98]
SiO_2	TEOS	Aqueous, two-step chronological	Unspecified acid	GPTMS	Not reported	[88]
SiO_2	TEOS	Aqueous, two-step chronological	-	IPTES	15-60 nm particle clusters	[101]
SiO_2	TEOS	Aqueous, one-step	DBTDL	IPTES	40 nm particles	[102]
SiO_2	TEOS	Aqueous, two-step chronological	-	APTES	Particle clusters below 100 nm with APTES, and between 100-300 nm without APTES	[95]
TiO_2	TBO	Aqueous, one-step	-	AEAPTMS [2]	Branched, fractal structures of unknown size	[93]
TiO_2	TEOT	Aqueous, one-step	HCl	-	22 nm spherical particles	[20]
TiO_2	$TiCl_4$	Non-aqueous, two-step with TiO_2 sol	BzOH		10-20 nm particles	[72]
TiO_2	TIP	Aqueous, two-step chronological	-	GPTMS	50-100 nm clusters	[103]
TiO_2	$TiCl_3$	Aqueous, one-step	-	-	2-10 nm TiO_2 particles	[104]
TiO_2	TIP	Aqueous, two-step sequential	Orthophosphoric acid	-	40 nm particles in larger (> 200 nm) aggregates	[94]
TiO_2	TBO	Aqueous, two-step simultaneous	-	TCTMTEA [3]	TiO_2 domains with average size < 100 nm	[105]

[1] Carboxylic (CH_2CO_2HMImCl and $C_3H_6CO_2$HMImCl) and ether (C_7O_3MImMeS) ionic liquids
[2] *N*-(2-aminoethyl)-3-aminopropyltrimethoxysilane
[3] Triethoxysilane-capped trimercaptothioethylamine

2.4 Dielectric materials

A dielectric material is an electrical insulator that is polarized in an applied electric field. The polarizability of the material is often represented by its relative permittivity (or dielectric constant), ϵ_r, which is a ratio of the absolute permittivity (ϵ) of the material to the vacuum permittivity (ϵ_0). There are four mechanisms of polarization in a dielectric material, shown in Figure 2.13. Electronic polarization is caused by the displacement of electrons within the atoms, resulting in a temporary induced dipole. This mechanism is very rapid (time scale of 10^{-15} s) and vanishes when the electric field is removed. Ionic polarization is also a rapid mechanism ($10^{-12} - 10^{-13}$ s) caused by the displacement of ions instead of electrons, and can occur in any material with ions. Orientation (or molecular) polarization exists only in materials where the molecules have a permanent dipole moment. In the absence of an electric field these dipoles are arranged randomly, but the dipoles can move and align themselves with the electric field when it is applied. Thermal energy from the environment can increase the disorder in the dipoles, so at sufficiently high temperatures the dipoles will no longer align with the electric field (assuming that the field strength is not increased). The dipoles are also more free to move in liquids and gases, while in solids they are restricted by bonds. Due to the large number of possible permanent molecular dipoles, the orientation polarization mechanism can be observed over a wide time scale ($10^{-9} - 10^{-3}$ s) [106]. Finally, several applications make use of heterogeneous materials consisting of several dielectrics. The accumulation of charges at the interfaces between these components results in interfacial polarization, which has a longer relaxation time ($> 10^{-3}$ s) than orientation polarization [107].

Due to the speed of the relaxations of electronic and ionic polarization mechanisms, they are often considered to be *momentary*. On the other hand, orientation and interfacial polarization mechanisms are slower processes, and the charges and dipoles take time to realign with an alternating electric field. At low frequencies, the switching electric field is slow enough for the dipoles to sufficiently follow the field. At higher frequencies, the slower polarization mechanisms can no longer keep up with the field, resulting in a reduction in the polarization and a subsequent decrease in the relative permittivity with increasing frequency. The permittivity and susceptibility of the dielectric are then expressed in terms of their real and imaginary components. The complex relative permittivity (ϵ_r*) as a function of angular frequency (ω) is represented by Equation (2.2) [106]. The dielectric properties can also be represented by the complex susceptibility (χ_r*) instead of the permittivity, given in Equation (2.3) [108].

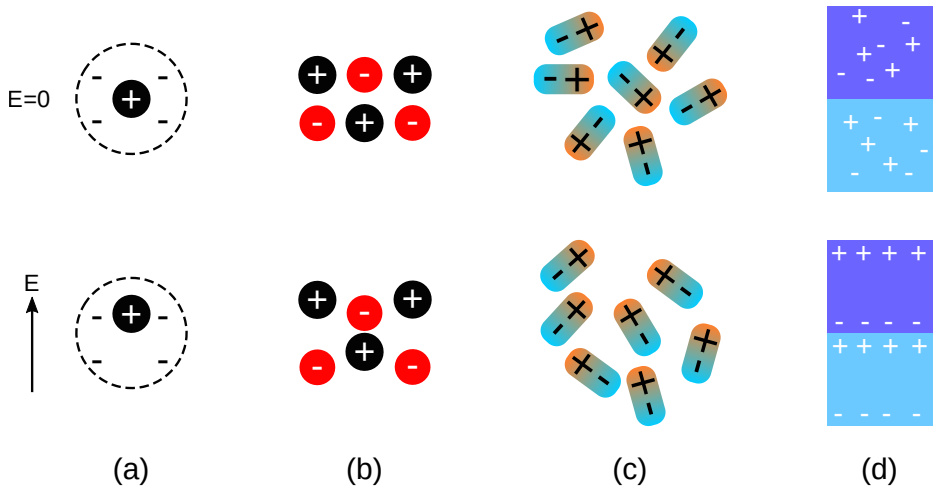

Figure 2.13. Polarization mechanisms in dielectrics, showing the charges and dipoles in the absence and presence of an electric field: **(a)** Electronic, **(b)** ionic, **(c)** orientation (molecular), and **(d)** interfacial (surface) polarization.

$$\epsilon_r{}^*(\omega) = \epsilon_r'(\omega) - i\epsilon_r''(\omega) \tag{2.2}$$
$$\chi_r{}^*(\omega) = \chi'(\omega) - i\chi''(\omega) \tag{2.3}$$

Here ϵ_r' is the real relative permittivity, $\epsilon_r{}''$ is the imaginary relative permittivity, χ' is the real susceptibility, and χ'' is the imaginary susceptibility.

2.4.1 The Debye model

The Debye model of dielectric relaxation assumes that the dipoles in the material are ideal and non-interacting with a single relaxation time [108]. ϵ' and ϵ'' can then be expressed in terms of the relaxation time (τ), angular frequency (ω), the static permittivity (ϵ_s), and the permittivity at a practical upper frequency limit (ϵ_∞), as given in Equations (2.4) and (2.5) [109]:

$$\epsilon'(\omega) = \epsilon_\infty + \frac{\epsilon_s - \epsilon_\infty}{1 + \omega^2\tau^2} \tag{2.4}$$
$$\epsilon''(\omega) = \frac{\omega\tau(\epsilon_s - \epsilon_\infty)}{1 + \omega^2\tau^2} \tag{2.5}$$

The changes in the real and imaginary permittivities are displayed in Figure 2.14. For a specific dielectric relaxation at low frequencies ($\omega\tau \ll 1$) the dipoles follow the applied field perfectly and there is no phase shift (δ) between the dipole orientation and the field, and so $\epsilon'' \approx 0$. Upon increasing the frequency, the dipoles follow the field partly, resulting in a phase shift that causes $\epsilon''> 0$. This phase shift leads to dielectric losses and a corresponding reduction in ϵ'. At higher frequencies ($\omega\tau \gg 1$), the dipoles can no longer follow the field, and ϵ'' ≈ 0 again, and ϵ' becomes constant. If there are several relaxation mechanisms present in a material, Equations (2.4) and (2.5) are adjusted to fit each mechanism, as shown in Figure 2.14.

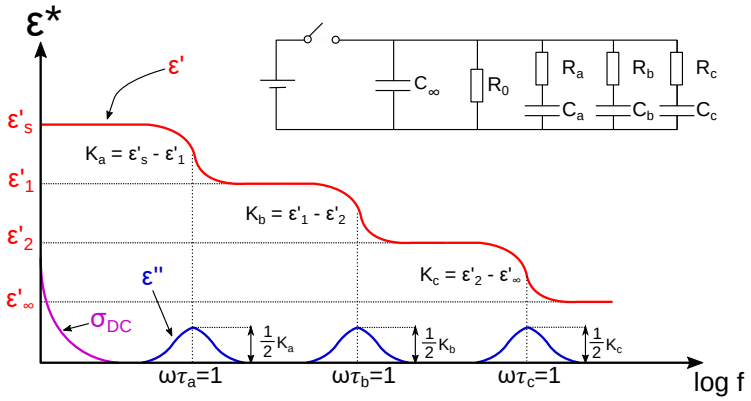

Figure 2.14. Frequency dependence of the real (ϵ') and imaginary (ϵ'') permittivities showing three relaxation mechanisms (represented by K_a, K_b, and K_c), including the losses due to conductivity (σ_{DC}). The equivalent circuit for this system is included.

The dielectric losses (when $\epsilon'' \neq 0$) may be caused by the transfer of energy from the electric field to the material [110], resulting in the the rotation of molecules with permanent dipoles, or by absorption of charges at any interfaces or inhomogeneities, or by oscillation of charges. The loss angle δ, which represents the phase-shift between the dipoles and the field, quantifies the material's inherent dissipation of electromagnetic energy. $\tan\delta$ is the dielectric loss factor, and is commonly used to characterize the losses in the material. $\tan\delta$ consists of a reactive power loss component (dielectric loss, represented by the first term in Equation (2.6)) as well as an active power loss component (loss due to conductivity σ, represented by the second term in Equation (2.6)) [110]. When applying DC voltage ($\omega \rightarrow 0$), the first term becomes negligible and the losses are primarily caused by the conductivity.

$$\tan\delta = \frac{\epsilon_r''}{\epsilon_r'} + \frac{\sigma}{\omega\epsilon_r'\epsilon_0} \tag{2.6}$$

The Debye response can also be represented by an equivalent electric circuit, included in Figure 2.14. The response is obtained with a series combination of a frequency-independent capacitance C and a resistance R, which give a peak frequency $\omega_p = (RC)^{-1}$, which is the reciprocal of the relaxation time τ. When several relaxation mechanisms are active, additional RC-units can be added to the equivalent circuit. The conductivity (σ) and ϵ_∞ are represented by the resistor R_0 and the capacitance C_∞, respectively. The capacitances C_x and resistances R_x for each relaxation ($x = a, b, c$) are functions of the change in ϵ' (K_x), which are shown in Figure 2.14.

2.4.2 Deviations from the Debye model

In reality, few materials or systems exhibit the Debye response, and deviations are common [108]. The Debye response is rare because most complex systems inevitably contain more than one type of dipole with variations in the relaxation time or the interactions between the dipoles. The shape of the ϵ" peaks are then broader or asymmetric, indicating that there may be a distribution of relaxation times [109]. Several different models have been proposed for obtaining this distribution. One common approach is to fit the experimental data with a number of empirical expressions obtained in the frequency domain that are based on "non-Debye" processes with more than one relaxation time. The general biparametric Havriliak-Negami function, given in Equation (2.7) [111], uses the characteristic parameters α and β to define the form of the distribution and divergence from the Debye model.

$$\epsilon^* = -i\left(\frac{\sigma_0}{\epsilon_0\omega}\right)^N + \epsilon_\infty + \sum_{i=1}^{\infty}\left[\frac{\Delta\epsilon_i}{\left(1+(i\omega\tau)^\alpha\right)^\beta}\right] \tag{2.7}$$

α is the width (or broadening) parameter, and specifies the slope of the low frequency side of the relaxation in ϵ''. β is the asymmetry (or skewness) parameter, and -$\alpha\beta$ gives the slope of the high frequency side of ϵ''. ϵ_∞ is the permittivity at the high frequency limit and σ_0 is the DC conductivity. If $\alpha = \beta = 1$, then the relaxation exhibits the ideal Debye response. If $\beta = 1$ and $0 < \alpha < 1$, the relaxation exhibits a Cole-Cole response, typically seen in amorphous solids and

some polymers. If $\alpha = 1$ and $0 < \beta < 1$, the relaxation exhibits a Davidson-Cole response, which is present in liquids and polymer solutions. The Havriliak-Negami function is generally suitable for describing the dielectric response in polymers, but does not necessarily provide a physical interpretation [110].

A different interpretation of dielectric phenomena emerged from the works of Jonscher, and Dissado and Hill [110]. Jonscher proposed a universal mechanism in all dielectric materials due to the common power law behaviour [112], where the dielectric susceptibility (χ) shows a frequency dependence with fractional power laws [113], as shown below:

$$\chi''(\omega) \propto \begin{cases} \omega^m, & \omega \ll \omega_p \\ \omega^{n-1}, & \omega \gg \omega_p \end{cases} \tag{2.8}$$

Here m and n are between 0 and 1, and ω_p is the characteristic frequency of the loss peak. Dissado and Hill developed a quantum mechanical approach to make predictions of real dielectric behaviour. In the Dissado-Hill theory, materials are assumed to be composed of clusters that show cooperative behaviour during the relaxation process [114]. A cluster can be considered to be a spatially limited region with a partially regular structural order of dynamically connected individual units [115]. The relaxations are therefore also "clustered", and not treated independently. Different motions may arise between the relaxation entities (i.e. dipoles or mobile charges) due to electrostatic interactions, electromechanical forces from changes in cluster shape or size, or changes in the potential surface [115]. The exponents n and m refer to the degree of cooperation within a cluster and between separate clusters, respectively, and are related to the structural regularities of the dielectric material [115].

In addition to the high and low frequency branches of the dielectric loss peak specified in Equation (2.8), which arise due to the cooperative interaction of the charge and dipole clusters, the region near the peak frequency (ω_p) may be dominated by a Debye-like response [116]. The universal law proposed by Jonscher also includes a "carrier" response due to the charge carrier polarization of quasi-mobile and weakly-bound electronic or ionic charges. In this dielectric response, no loss peak is observed and the response becomes strongly frequency dependent in the low-frequency region. This *low frequency dispersion* (LFD) is caused by the low mobility charge carriers dominating the polarization at low frequencies [113]. As a result, LFD is observed most commonly in carrier-dominated systems (such as fast ionic conductors), but may also be found in humid insulators or polymers at elevated temperatures (i.e. above the glass transition where

ionic mobility is sufficiently high) [110]. The LFD phenomenon is also referred to by Dissado and Hill as a 'quasi-DC' (QDC) behaviour, and is described as the movement, or hopping, of charges within restricted channels. The separation of charges from their weakly-bound counter charges becomes larger than the cluster size at low frequencies, resulting in the increase in susceptibility (and subsequently, the permittivity) [115]. The distinctive characteristics of both the dipolar and carrier responses in the universal law are shown in Figure 2.15. For the carrier response, at low frequencies where LFD emerges the exponent n_2 is close to zero, while at higher frequencies the exponent n_1 is close to unity, implying a low-loss system [113].

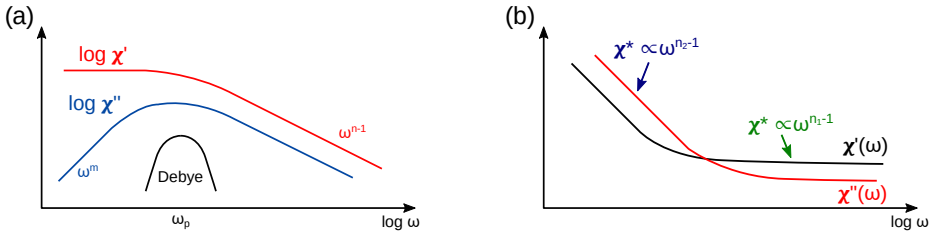

Figure 2.15. **(a)** The general shape of the non-Debye dielectric response according to the universal law. The Debye response is included as a comparison. The slopes of log χ' and log χ'' are parallel at high frequencies. **(b)** The dielectric response of a system dominated by low mobility charge carriers, with two fractional power laws for low and high losses with n_1 close to unity and n_2 close to zero, respectively. The LFD is observed in the low-frequency part. The images are adapted from [112].

2.4.3 The dielectric breakdown strength

When a sufficiently large voltage is applied across an electrical insulating material for an extended period of time, the material will experience a dielectric breakdown where it becomes a conductor and an electric current can flow [117]. An example of dielectric breakdown is the effect of lightning during a storm, where a high potential difference arises between the clouds and the ground. The air acts as the insulator between them, and breaks down when a critical potential difference is reached. The dielectric breakdown strength (DBS) is the electric field strength at the point of breakdown, and is an intrinsic property of the insulating material. The voltage required for a breakdown will depend on not only the breakdown strength of the material but also the size and shape of the object. Dielectric breakdowns are stochastic processes, meaning that statistical methods must be used to predict or describe breakdown values. The Weibull distribution [118] is employed in electrical insulation system design for

characterizing the dielectric breakdown strength [119]. The Weibull distribution is used as a two-parameter (α and β) function, where α is the scale parameter representing the voltage or electric field that would result in a 63 % probability of breakdown, and β is the shape parameter representing the distribution of breakdowns.

There are two fundamental mechanisms of breakdown [120]. The first is electronic breakdown, where electrons obtain sufficient energy to be excited over the band gap between the valence and conduction bands. The second mechanism is avalanche breakdown, where conduction band electrons have enough energy to liberate more electrons from atoms by collisions. In reality however, most materials will experience a dielectric breakdown before the intrinsic breakdown strength is reached due to extrinsic effects such as mechanical or thermal failures and ageing effects. For example, temperature rises due to Joule heating or heating by dielectric dissipation loss may melt the material, leading to dielectric failure; some soft insulating materials also can be reduced in thickness by Maxwell stresses when subjected to voltage, resulting in enhancement of the electric field and a subsequent positive feedback loop [121].

2.4.4 Partial discharges and electrical treeing

Partial discharge (PD) in solid insulation can be a potential source of failure in the materials. A PD is a discharge that does not completely bridge the distance between the high voltage conductor and the ground electrode, resulting in local degradation of the insulation via ionization and a reduced lifetime [122]. Insulation systems consisting of solid polymer materials are particularly susceptible as they have no resistance to PDs and degrade permanently [122]. The main sources of PD may be weak regions in the material (due to ageing effects through a combination of various electrical, mechanical, thermal or chemical stresses) with a lower dielectric strength, or local defects (such as voids) where the electric field is enhanced [123]. Extended PD activity can lead to electrical treeing, a pre-breakdown phenomenon in solid insulation where the PDs form dendritic paths that progressively grow and branch into hollow channels in the shape of trees. Figure 2.16 shows the different profiles of electrical trees, which may be either tree-like or bush-like, depending on the number of branches and how early the branching begins. Electrical treeing is problematic in polymers, rubbers, and epoxy resins, and will eventually lead to breakdown once it is initiated and allowed to continue. Treeing takes place over four stages: an incubation period, followed by initiation of the tree, then the propagation (tree growth), and finally a total breakdown. Apart from PD, other processes may occur that can lead to initiation of treeing, such as mechanical fatigue or charge injection

and extraction [121]. Repeated injection and extraction of high energy electrons from the electrode can lead to charge build-up and material degradation (via polymer chain scission and oxidation), resulting in a decrease in the breakdown strength. The built-up charge will also generate a higher electric field during the opposite cycle of AC voltage. If the energy of the electrons are sufficient, a partial breakdown occurs, leading to tree initiation.

Figure 2.16. **(a)** The profile of electrical trees in poly(methyl methacrylate), and the formation of **(b)** linear (tree-like) trees with few branches, and **(c)** bush-like trees with multiple branches close to the initiation point, in polyethylene. Both images are reprinted with permission from Springer Nature Customer Service Centre GmbH: Springer Nature, Polymer Nanocomposites Electrical and Thermal Properties by Xingyi Huang and Chunyi Zhi, 2016.

The transition from inception to propagation is marked by current pulses from discharges in a gas-filled channel [124]. These discharges can inject charges into the polymer around the discharge head, thereby acting similar to the electrode during initiation. Repeated discharges would then result in the extension of the tree. In cases where the channel walls are conductive, the growth may be propagated even in the absence of any partial discharges [124]. Different types of PD are observed to exhibit distinguishable phase-resolved partial discharge (PRPD) patterns, such as those shown in Figure 2.17.

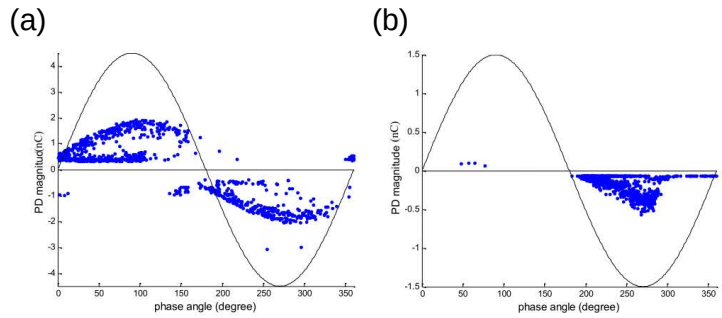

Figure 2.17. Phase-resolved partial discharge (PRPD) patterns of **(a)** void and **(b)** surface discharges on XLPE material. Reprinted with permission from [125], 2012 IEEE.

During electrical treeing, void and surface discharges are the most common types of PD. The discharge patterns for PDs within voids or cavities manifest on both cycles of the voltage [122], as seen in Figure 2.17a. The inception voltage is typically higher than the extinction voltage due to presence of free charge carriers that remain after PD is initiated. The PD pattern may change with time however, as the surface of the void or the pressure inside may change with the discharges [122]. Surface discharges occur in regions where the electrical stress is at a tangent to the material surface [122]. These discharges may bridge large distances, and show higher PD on the negative cycle of the voltage. Similar to void discharges, inception and extinction voltages are different as the charge carriers on the surface change the electric field locally [122].

Large bursts in PD activity are typically associated with long discharge paths that result in branched-tree growth (tree-like trees) [124]. Bush-like trees were observed to form when there was an increase in the amount of injected charge around the tree tips or at branching points, associated with small local discharges in the tree close to the zero voltage points on the applied waveform [124]. A similar observation was made by Lv et al. [126], where the PD patterns showed two types of void discharges - 'wing-like' or 'turtle-like' in long, narrow channels and short-wide channels, respectively. Figure 2.18 displays examples of wing-like and turtle-like PD patterns. PDs with lower magnitudes may also be present that do not contribute to the growth of the tree, as they do not possess enough energy, but may contribute to the widening of the tree channels and carbonisation of the channel walls.

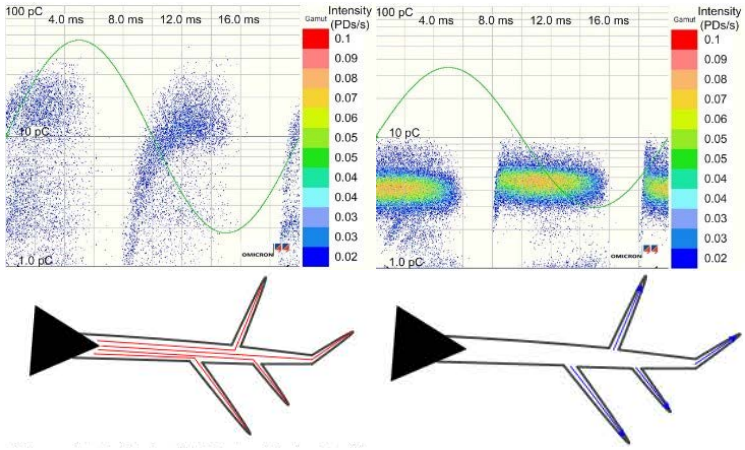

Figure 2.18. Examples of PRPD patterns representing **(a)** wing-like, and **(b)** turtle-like PD, along with a sketch of the discharge route for the corresponding PD. Reprinted with permission from [126], 2017 IEEE.

Eventually the tree will extend to the ground electrode, and after a certain gaseous discharge process the material experiences the final breakdown [121]. In some cases 'reverse trees' have also been observed in the final stage prior to breakdown, where a tree also starts growing from the ground electrode towards the high voltage needle electrode instead [126–128]. However, the cause of the formation of such reverse trees is not well understood, although it appears that the formation of a primary, filamentary tree is required [128].

2.5 Epoxy nanocomposites as high voltage insulation materials

Epoxy is used commonly as electrical insulation in power equipment and other electrical components, such as in dry (cast-resin) transformers, rotating machines and motor windings, printed circuit boards, gas insulation switchgear spacers, bushings, and generator groundwall insulation systems [4, 129, 130]. The good adhesive properties and excellent chemical resistance of epoxy alongside the necessary electrical properties make epoxy attractive for such applications. However, some mechanical reinforcement of the epoxy may be necessary, depending on the requirements of the application or equipment, due to its high

brittleness and low fracture toughness (0.5-0.7 MPa $m^{1/2}$) [131]. Inorganic fillers, such as metal oxides (e.g. SiO_2, TiO_2, Al_2O_3, MgO), nitrides (e.g. Si_3N_4, BN), or carbon nanotubes, have been used as additives to improve the mechanical properties [132–134], decrease water absorption [135], and improve the thermal conductivity [136,137]. There is, however, a trade-off, as the use of micron-sized filler particles often results in a degradation of the electric strength [5].

2.5.1 Dielectric properties

The use of nano-sized fillers in epoxy for dielectrics and electrical insulation have attracted attention since the early 2000s [52]. Nelson and Fothergill were two of the first researchers to report the disparity in dielectric properties between composites with nanoparticle and micron-sized particle fillers [5]. They reported a reduction in the real relative permittivity of epoxy-TiO_2 nanocomposites from that of pure epoxy, compared to the increase observed in conventional microcomposites (shown in Figure 2.19). Most importantly, the DC breakdown strength of the composites decreased from ~3000 kV mm^{-1} to ~1500 kV mm^{-1} for both the micro- and nanocomposites with increasing filler content. However, the decrease was steeper initially for the microcomposites, and the breakdown strength of the nanocomposites did not decrease significantly until the filler content exceeded 10 wt%. The nanocomposites also exhibited LFD with parallel slopes of -1 for the real and imaginary permittivities, as well as a flattening of the loss tangent (tan δ) at low frequencies (below 10^{-1} Hz), indicating the presence of low mobility charge carriers. Pulsed electro-acoustic (PEA) measurements also showed a reduction in the space charges present in nanocomposites, compared to microcomposites, as well as a more homogeneous charge distribution.

Singha and Thomas [4,138] investigated epoxy micro- and nanocomposites with TiO_2, Al_2O_3, and ZnO fillers, and found similar effects on the dielectric properties. For low filler contents (below 1 wt%), the nanocomposites exhibited smaller real relative permittivities and tan δ than that of pure epoxy. At higher filler contents of nanoparticles (above 5 wt%) or with the use of micron-sized particles, the permittivity and tan δ increased significantly. However, the AC breakdown strength was lower for all the composites compared to pure epoxy (Weibull scale parameter of 52.30 kV mm^{-1}). The opposite behaviour was observed between the TiO_2 and Al_2O_3, as the decrease in the dielectric strength was greater for the microcomposites for a given filler content of Al_2O_3, whereas the decrease was greater for the nanocomposites with TiO_2. On the other hand, Nascimento et al. [139] reported improvements in the breakdown strength of nanocomposites containing Al_2O_3 and ZnO, although the benefits were largest at lower filler contents (below 3 wt%). Decrease of the breakdown strength at higher

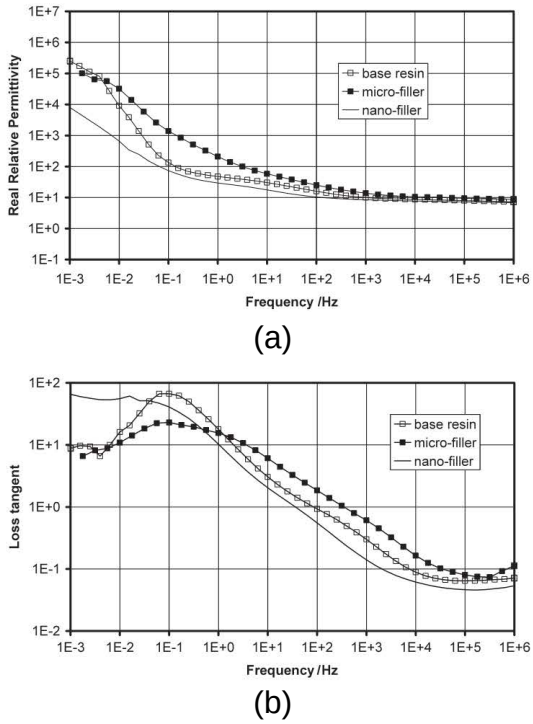

Figure 2.19. **(a)** Real relative permittivity, and **(b)** loss tangent of epoxy resin, micro- and nanocomposites with TiO_2 as filler, at 393 K. Reproduced with permission from [5], IOP Publishing, all rights reserved.

filler loadings was attributed to a percolated interface, creating a conductive pathway.

Kochetov et al. [140] measured the complex permittivity of several different nanocomposites, including Al_2O_3, AlN, MgO, SiO_2, and BN as fillers. The particles (except SiO_2) were surface modified using GPTMS to aid their dispersion. All of the nanocomposites (except those containing SiO_2) exhibited a decrease in the real permittivity at filler contents below 5 wt%. The permittivity was observed to be lowest at a filler content of 2 wt% for almost all the different filler materials. They also reported that the type of inorganic filler used appeared to have no effect on the permittivity, but rather the size of the particles was important, showing a larger increase in the permittivity with increasing size of

the nanoparticles. The different behaviour observed in the SiO_2 nanocomposites was attributed to the unknown surface modification of the particles (which was present as received from the suppliers). Figure 2.20 shows the effect of the filler types and the filler size on the real permittivity of the nanocomposites [140].

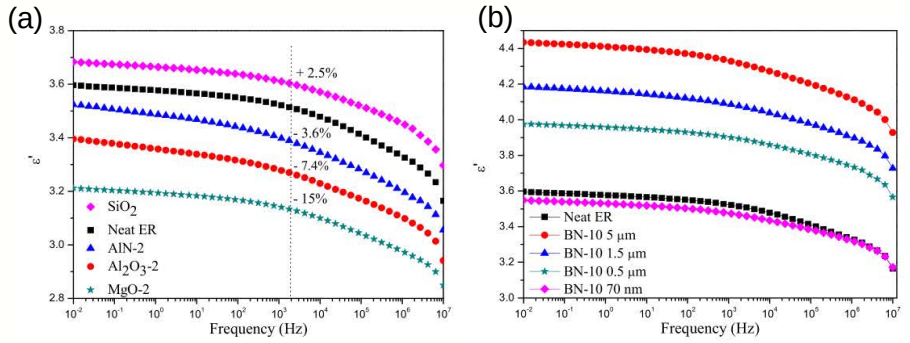

Figure 2.20. Variations in the real permittivity (ϵ') of nanocomposites with **(a)** 2 wt% of different filler particles, and **(b)** 10 wt% of BN with different particle sizes. Reprinted with permission from [140], 2012 IEEE.

The importance of surface modification of the nanoparticles was also reported by others. Virtanen et al. [141] tested the AC dielectric breakdown strength of epoxy-SiO_2 nanocomposites with the SiO_2 surface modified by different bimodal-polymer-brushes. The brushes consisted of short molecules (oligo-thiophene or ferrocene) and long chains of poly(glycidyl methacrylate) (PGMA). For 2 wt% filler content, the breakdown strength increased in all samples, but most significantly in the one containing SiO_2 with PGMA and thiophene (increase in Weibull scale parameter from 187 to 277 kV mm^{-1}). More recently Bell et al. [70] performed similar experiments using bimodal brushes with different short molecules (terthiophene, anthracene and thiophene) and correlated the improvements in the breakdown strength with reductions in the free space length (L_f) between the nanoparticles, reporting up to a 34 % increase in the breakdown strength. L_f is defined as the length of the sides of the largest randomly selected square where the most probable number of particles present is zero. L_f is therefore an estimate for the size of the largest polymer regions with no filler particles, and was observed to be inversely related to the grafting density of the ligands. Siddabatuni et al. [69] reported a decrease in the breakdown strength when unmodified TiO_2 nanoparticles were added to epoxy, but the use of organophosphate ligands to modify the particle surface resulted in an increase in the breakdown strength. The real relative permittivity however was increased in all the nanocomposites compared to pure epoxy. Yeung and

Vaughan [142] also reported similar findings as Siddabatuni et al., where the breakdown strength decreased when unmodified SiO_2 nanoparticles were used, but increased noticeably (from 182 to 268 kV mm^{-1}) when varying amounts of GPTMS was used as surface functionalization.

Imai et al. [129] prepared composites containing a mixture of nano- and micron-sized filler particles consisting of a modified layered silicate and silica, respectively. This type of composite, hereby referred to as a nano-microcomposite, was found to exhibit higher breakdown strengths than a conventionally filled epoxy (both with the same filler content of micron-sized particles). The authors attributed this to obstruction of electrical treeing by the nano layered silicates due to the more densely packed structure and smaller distances between nearest neighbours. Iyer et al. [130] studied similar nano-microcomposites with spherical silica particles and a higher filler content than in the work by Imai et al. but with contrary results. Both the conventional microcomposites and nano-microcomposites exhibited lower breakdown strengths, although the decrease was smaller for the latter. On the other hand, nanocomposites with 2 and 5 wt% filler content possessed a higher breakdown strength than pure epoxy. Liang and Wong [143] also investigated microcomposites, nanocomposites, and nano-microcomposites containing either SiO_2 or Al_2O_3. They reported an increased breakdown strength in all the different types of composites, although the nano-microcomposites exhibited the highest strength. Conversely, the nano- and microcomposites exhibited lower partial discharges on the surface compared to the nano-microcomposites.

Table 2.2 summarizes the changes in dielectric properties, highlighting selected results from literature. There are several inconsistencies in the reported results. In many cases there were improvements observed in both the dielectric breakdown strength and the real relative permittivity, while in others only one of the properties benefited from the use of nanoparticles. In some materials, both properties diminished but the nanocomposites still performed better than microcomposites. Generally the type of nanoparticle used as the filler does not appear to affect the dielectric properties significantly, but the amount of filler used or the surface modification of the particles are critical. This indicates the significance of the dispersion of the nanoparticles, as both the filler content and surface properties will affect how well the particles are dispersed in the epoxy and the degree of agglomeration. As noted earlier, the procedures used in the preparation of the nanocomposites vary as well, which also contribute to the state of dispersion.

Table 2.2. Comparison of the dielectric properties (DBS and ϵ_r') of epoxy nanocomposites from selected literature.[1]

Filler	Content [wt%]	Morphology and state of dispersion	Preparation and surface modification	Change in dielectric properties	Ref.
SiO_2	2	20 nm particles in 0.9-3 μm agglomerates	Stirring and ultrasonication, with GPTMS	Increase in AC DBS by 30-47%, and in ϵ_r' up to 12%, depending on amount of GPTMS.	[142]
Al_2O_3	0-5	45 nm particles, but dispersion was not reported	High shear mechanical mixing	Decrease in AC DBS by 23-28%.	[4]
TiO_2	0-10	50 nm particles, but dispersion was not reported	High shear mechanical mixing	Decrease in AC DBS by 34-46%. Slight decrease in ϵ_r' for filler content < 1 wt%.	[4]
Al_2O_3	2	10-200 nm particles dispersed randomly	High shear mechanical mixing, with GPTMS	Increase in DC DBS by 38%. Decrease in $\epsilon_r'$by 4%.	[144]
MgO	2	22 nm particles, but dispersion was not reported	High shear mechanical mixing, with GPTMS	Increase in DC DBS by 3%. Decrease in ϵ_r' by 16%.	[144]
SiO_2	2	Randomly dispersed particles with size < 50 nm	High shear mechanical mixing, with bimodal polymer ligands [2]	Increase in AC DBS by 22-48%, depending on type of ligand used.	[141]
TiO_2	5 (vol%)	32 nm anatase particles, but dispersion was not reported	Ball milling, with organophosphate ligands [3]	Increase in DC DBS by 6-30%, depending on type of ligand used. Increase in ϵ_r' (at 10 kHz) by 33-60%.	[69]

Continued on next page

Table 2.2. continued

Filler	Content [wt%]	Morphology and state of dispersion	Preparation and surface modification	Change in dielectric properties	Ref.
Al_2O_3	5	7 nm particles dispersed randomly in 50-200 nm clusters	Roll milling	Increase in AC DBS by 4% and higher PD resistance.	[145]
Al_2O_3	0.4	10 nm particles in 50-200 nm clusters	Extrusion mixing	Increase in AC DBS by 49% and in ϵ_r' by 8%.	[139]
ZnO	0.2	100 nm particles in 100-300 nm clusters	Extrusion mixing	Increase in AC DBS by 26% and in ϵ_r' by 25%.	[139]
SiO_2	0.5	50 nm particles, but dispersion was not reported	High speed stirring, with GPTMS	Decrease in ϵ_r' by 30%.	[146]
SiO_2	5	5-15 nm particles in 100-500 nm agglomerates	High shear mechanical mixing, with hexamethyl disilazane	Increase in DC DBS by 27%, and decrease in ϵ_r' (at 50 Hz) by 5%.	[147]
SiO_2	3	30 nm particles in 100 nm agglomerates	Stirring, with APTES	Increase in DC DBS by 27%, and decrease in ϵ_r' by 5%.	[148]

[1] DBS measured using either average values or the Weibull scale parameter α, and ϵ_r' measured at 25 °C and 1 kHz unless specified otherwise.
[2] Ligands consisted of oligothiophene or ferrocene on long poly(glycidyl methacrylate) (PGMA) chains.
[3] Ligands consisted of self-assembled monolayers of organophosphate ligands, such as (amino/nitro/chloro)-phenyl phosphate.

2.5.2 Electrical treeing and partial discharges

Increased resistances to partial discharges and electrical treeing have been observed in nanocomposites, compared to pure epoxy. A summary of the different treeing behaviours and PD properties is presented in Table 2.3. Alapati and Thomas [149] demonstrated an increase in the propagation time for trees in epoxy-Al_2O_3 nanocomposites. Nyamupangedengu and Cornish [150] reported a reduction in the magnitude of PD observed in nanocomposites filled with either SiO_2, Al_2O_3 or MgO, compared to pure epoxy. However, the reduction in PD did not necessarily correspond to an increase in time to failure, which was found to increase with the filler content [150]. Imai et al. [151] observed an increased breakdown time, which was amplified significantly at higher temperatures, and the electrical tree propagation speed was ~50 % for layered-silicate nanocomposites compared to pure epoxy. Imai et al. also reported a significant increase in tree branching in nanocomposites, while electrical trees in pure epoxy were more linear, as seen in Figure 2.21. Chen et al. [152] and Raetzke et al. [153] both demonstrated increases in the tree initiation time in layered-silicate nanocomposites, respectively. Nakamura et al. [154] reported both a decrease in the tree growth speed as well as a transition from branched to bushy trees with increasing SiO_2 nanoparticle content at several temperatures (as shown in Figure 2.22), while exhibiting both wing-like and turtle-like PRPD patterns. Chen et al. [155] highlighted the importance of the quality of particle dispersion for the treeing resistance, showing significant increases in the time from initiation to breakdown in surface-treated SiO_2 nanoparticles compared to unmodified nanoparticles which were more poorly dispersed.

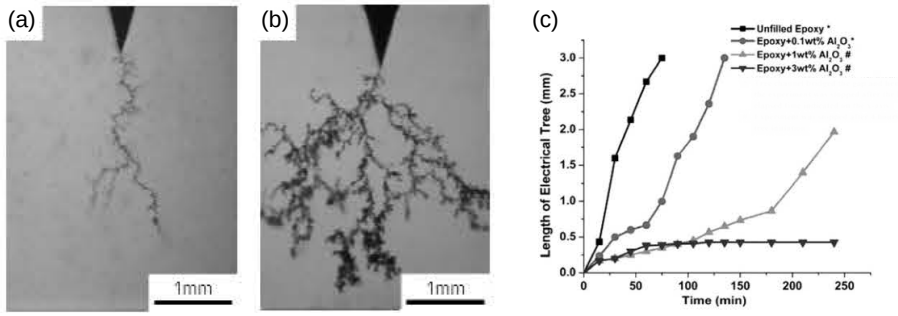

Figure 2.21. Electrical tree patterns in **(a)** pure epoxy, and **(b)** epoxy-layered silicate nanocomposite at 10 kV. **(c)** A comparison of propagation times for electrical trees in pure epoxy and epoxy-Al_2O_3 nanocomposites. **(a)** and **(b)** were reprinted with permission from [151], 2007 IEEE. **(c)** was reprinted from [149].

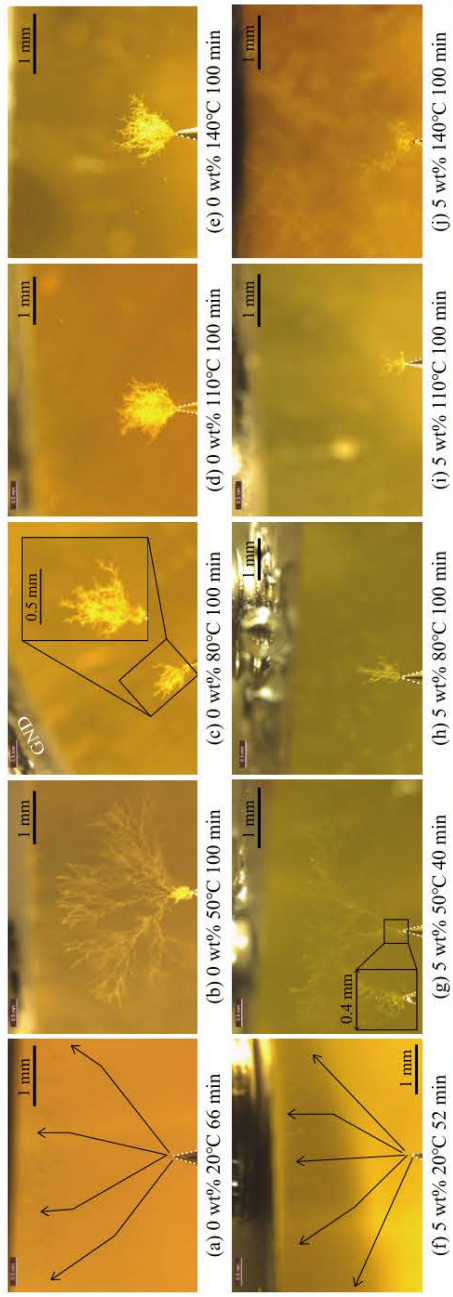

Figure 2.22. Electrical tree patterns for pure epoxy and 5 wt% epoxy-SiO_2 nanocomposites at different temperatures. Reprinted with permission from [154], 2020 IEEE.

Table 2.3. Summary of electrical treeing and partial discharge properties in selected epoxy-based nanocomposites

Filler	Content [wt%]	Tree initiation conditions	Tree morphology, growth, and PD behaviour	Ref.
Al_2O_3	5, 10	Nanocomposites suppressed tree initiation at 10 kV.	Trees were more bushy at 10 kV in nanocomposites than in pure epoxy; the opposite was observed at 20 kV, and the trees grew faster.	[156]
Al_2O_3	0.1, 1, 3	Increased tree initiation times (at 15 kV) with increasing filler content	Trees increasingly bushy and slower growth rate with increasing filler content.	[149]
MgO, SiO_2, Al_2O_3	0.5, 2, 5	Trees initiated at 20 kV. Time to initiation was not specified.	Reduced PD activity and magnitude in all nanocomposites. Nanocomposites (0.5 wt% filler) exhibited shorter times to failure.	[150]
SiO_2	1, 3, 5	Increase in both initiation time and time to failure with increasing filler content.	Bursts of PD for functionalized nanoparticles; continuous PD for bare nanoparticles.	[155]
SiO_2	5, 10	Trees initiated at 18 kV but the time to initiation was not specified.	Reduction in tree growth speed with increasing filler content. Trees also became more bushy at higher filler content. Initially high PD activity measured, but PD was extinguished later during tree growth.	[154]
Layered silicate	5	Increase in tree initiation time at both 10 and 14 kV.	Reduction in tree length and surface erosion depth in nanocomposites at all voltages.	[153]
Layered silicate	Unspecified	Increase in tree initiation time at 6, 10 and 14 kV for nanocomposites.	Decrease in surface erosion depth in nanocomposites.	[152]

2.5.3 High temperature effects on the complex permittivity

Dielectric spectroscopy experiments at higher temperatures (up to 200 °C) have revealed interesting relaxation behaviours in the complex permittivity for epoxy and its nanocomposites. At room temperature, epoxy exhibits a single relaxation, typically between 10^2 and 10^6 Hz, that corresponds to secondary relaxation processes. This is known as the β-relaxation, and is caused by the movement of local polar groups attached to the main epoxy chain - in this case, primarily the -OH groups [157]. At temperatures close to and above the glass transition, another relaxation process emerges, known as the α-relaxation, which is caused by the molecular chain movement or motion of segmental chains that becomes possible above the glass transition [158]. However, at even higher temperatures (above 100 °C) and low frequencies (below 1 Hz), an additional phenomenon is observed for both pure epoxy and its nanocomposites, where both the real and imaginary permittivities exhibit a sharp increase with decreasing frequency, as seen in Figure 2.23.

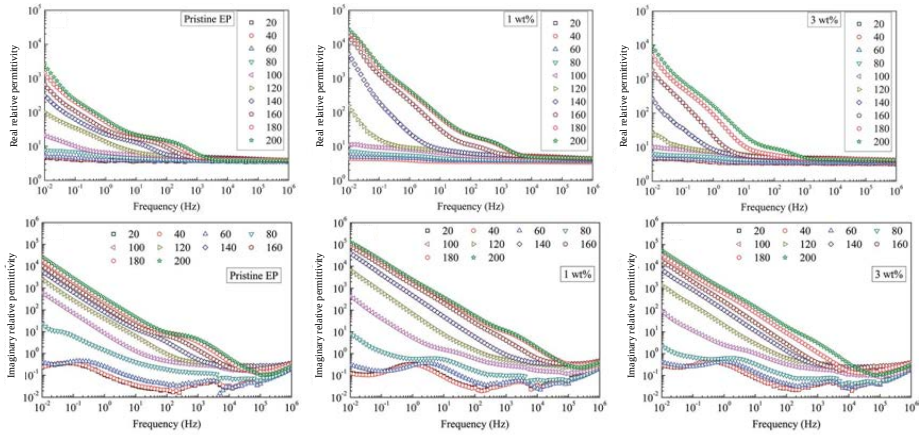

Figure 2.23. The real (top row) and imaginary (bottom row) relative permittivities of pure epoxy (pristine EP) and epoxy-SiO_2 nanocomposites (1 and 3 wt%) with hyperbranched-polyester-treated SiO_2 between 20 and 200 °C. Adapted from [148] with permission from the Royal Society of Chemistry.

This behaviour is commonly attributed to electrode polarization (EP), caused by accumulation of space charges at the interface between the epoxy and the electrode [159]. The delay in charge transfer at the interfaces results in an additional interfacial polarization on a macroscopic level [160]. Others, however, have attributed the rapid increase in the permittivities to the LFD (or QDC)

effect [115,148,161,162]. Figure 2.24 displays an example of the complex permittivity behaviours for the different relaxation phenomena. Since lower relative permittivities and dielectric losses are preferred for high voltage insulation materials, it becomes evident that the glass transition temperature is another important property since this sudden increase in permittivity becomes significant only above the glass transition.

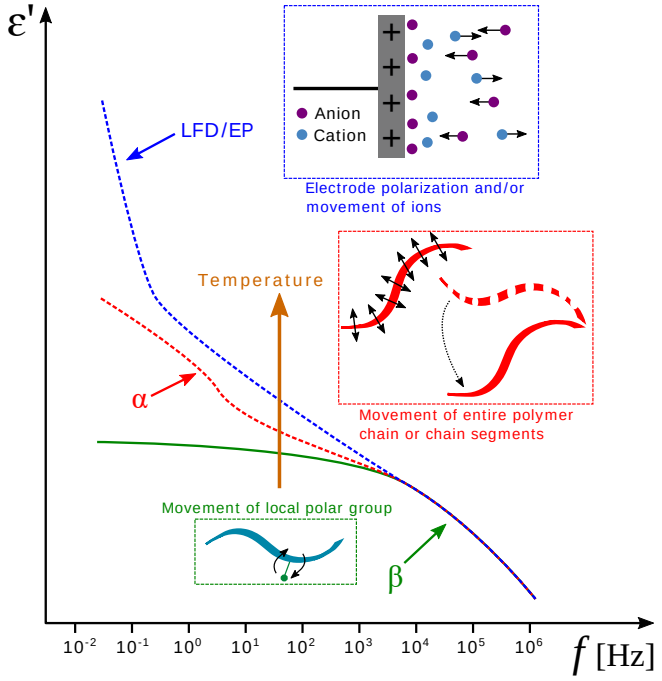

Figure 2.24. Schematic showing the representative behaviour of the real permittivity (ϵ') with different relaxation phenomena in epoxy with increasing temperature, as well as the mechanisms involved for each relaxation.

2.5.4 The thermomechanical properties

The demands on the dielectric properties of epoxy are not the only ones to be considered when it comes to application as high voltage insulation, as the thermal properties are also key to its performance. Additionally, insulation materials are constantly subjected to abrasion and high shear stresses, which might result in cracks or delamination leading to electrical discharge and failure [1]. As a thermosetting polymer, both the mechanical and dielectric properties of epoxy

are related to its glass transition, which is affected by a multitude of factors. The incorporation of inorganic oxide nanoparticles has therefore resulted in a wide spread of effects, with little consistency between different studies [6]. Some studies have demonstrated a decrease in the glass transition temperature (T_g) at low filler loads, but an increased T_g at higher filler loads [4, 133, 163]. Others have demonstrated that the changes in T_g are dependant on the surface modification used [69, 88, 89, 164, 165] or the size of the particles [164]. In some cases at high filler contents, the increase in T_g was observed to be smaller, or T_g was even observed to decrease [88, 133]. Several studies have also demonstrated a decrease in T_g upon inclusion of the nanoparticles, even when surface modified nanoparticles were used [142, 166]. A unique case was reported by Zhang et al. [134] where a second glass transition was observed, which behaved differently from the first glass transition. The second T_g increased with increasing nano-SiO_2 load, whereas the first T_g decreased with increasing load. The emergence of a second, distinct glass transition is predicted by the model proposed by Tsagaopoulos and Eisenberg [57], but no other reports of such behaviour have been found in literature for epoxy nanocomposites. Table 2.4 displays the differences observed in the changes in T_g in various epoxy nanocomposites. Generally, the interactions between the filler and the polymer matrix are held responsible for the changes in T_g. These interactions, which are more likely when the particles are well-dispersed (which maximises the interfacial area) or are chemically bonded to the epoxy chains via coupling agents, can immobilize the polymer chains. This would mean that more energy is required to overcome these interactions and mobilize the chains during the glass transition, leading to an increase in T_g [133]. According to this "chain immobilization theory", invariance or decreases in T_g are attributed to a lack of local interfacial interactions which can affect the dynamics of the polymer chains.

The thermal stability of epoxy is another important property as a higher thermal stability will reduce the risk of degradation of the insulation material from high temperatures generated during operations (e.g. heat dissipation from dielectric losses or flashovers). Generally the initial thermal stability is increased upon the inclusion of inorganic oxide nanoparticles [20, 85, 102, 165, 167–169], although some exceptions are observed [137,170] when the particles are large or poorly-dispersed. The initial degradation temperature (which is the temperature required for 5 % mass loss in the material) for epoxy and its nanocomposites is typically between 250 and 350 °C.

Traditionally inorganic particles are used to reinforce the mechanical properties of polymers; nanoparticles can potentially give larger improvements in these properties compared to the micrometer-sized particles [171]. The increased

number of interfacial interactions can enhance the flexural and tensile strengths as well as the fracture toughness in epoxy, as they allow uniform stress transfer from the polymer matrix to the nanoparticles [132, 133, 163]. The elastic moduli (E) is also expected to increase due to the significantly larger elastic moduli of the inorganic oxides, based on the Halpin-Tsai or Lewis-Nielsen models [133, 163, 166, 171, 172]. At low filler loads the predicted increase in E is observed experimentally, although deviations are seen at high filler loads which are often attributed to agglomeration effects. Figure 2.25 shows an example of the relative improvements in the various mechanical properties of nanocomposites. Epoxy-SiO_2 nanocomposites (Figure 2.25a) exhibited increased toughness, microhardness, and flexural modulus with increasing SiO_2 content. The epoxy-TiO_2 nanocomposites (Figure 2.25b) exhibited increased ultimate tensile strength, Young's modulus, strain-to-break, and tensile toughness with increasing TiO_2 content, but only up to ~7 wt% TiO_2.

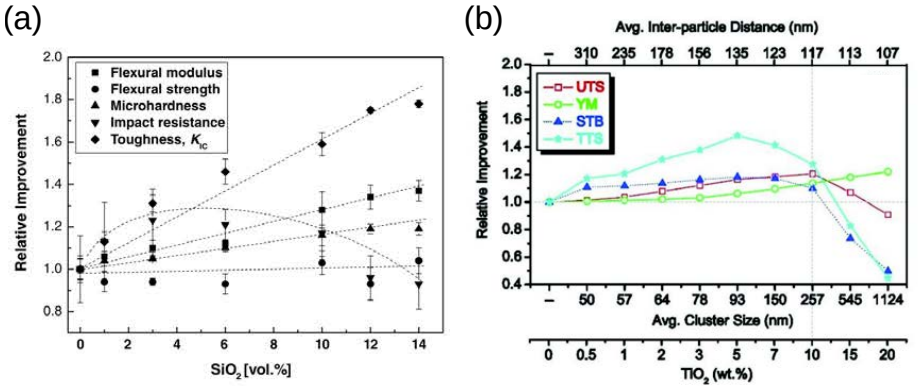

Figure 2.25. Relative improvements in flexural and tensile properties for **(a)** SiO_2 and **(b)** TiO_2 nanocomposites, respectively, with changes in nanoparticle content. In **(b)** the abbreviations in the legend stand for (from top to bottom) ultimate tensile strength, Young's modulus, strain-to-break, and tensile toughness. **(a)** was reprinted from [134], with permission from Elsevier. **(b)** was reprinted from [133], with permission from Elsevier.

The intrinsic brittleness of epoxy is also influenced by the inorganic filler. However this is not well understood, with conflicting results being reported in literature regarding the effect of different fillers on the ductility of epoxy nanocomposites [6]. Some studies indicate that the surface modification (and subsequently the state of dispersion) will affect the properties of the composite. Particle-particle interactions in agglomerates may also lead to uneven distribution of stress, which can lead to failure in the material.

Table 2.4. Changes in the glass transition temperature (T_g) of epoxy nanocomposites from selected literature. The temperature in brackets denotes the reported glass transition for pure epoxy.

Filler	Load [wt%]	T_g [°C]	Notes	Ref.
SiO_2	2.5-30	79-82 (80)	T_g increased with increasing filler content	[163]
TiO_2	0-10	62-80 (65)	T_g decreased for high filler loads	[133]
SiO_2	0-9	87-96 (91)	T_g dependant on particle size and surface modification	[164]
Al_2O_3	0-10	101-112 (112)	T_g decreased when particles were modified with APTES	[166]
SiO_2	2	74-81 (80)	T_g decreased with increasing amount of GPTMS	[142]
TiO_2	16	85-100 (99)	T_g varied with ligands used	[69]
TiO_2	0-10	61-69 (70)	T_g decreased initially, but increased with increasing filler load	[4]
Al_2O_3	0-5	61-68 (70)		
SiO_2	0-24	77-88 (82)	Irregular changes in T_g with smaller particles	[171]
SiO_2	0-7	102-115 (104)	T_g decreased initially, and then increased, with increasing filler content. The increase was smaller for high filler contents	[148]
SiO_2	0-5	115-119 (116)	T_g increased initially, and then decreased, with increasing filler content	[161]
BN	0-5	94-96 (93)	T_g increased with increasing filler content	[160]
SiO_2	0-25	42-53 (44)	T_g increased initially, and then decreased, with increasing filler content	[88]
SiO_2	10	125 (90)	-	[20]
TiO_2	10	128 (90)	-	
SiO_2	0-15	42-50 (45)	T_g increased when particles were modified with GPTMS	[89]
SiO_2	0-22	95-112 (95)	T_g increased with increasing filler content	[167]

2.6 Molecular dynamics simulations of epoxy nanocomposites

Molecular dynamics (MD) simulations are used to study the properties of condensed matter by analysing the motion of atoms in a molecular system by modelling the system with approximate interaction potentials [173]. MD simulations are founded upon the basic principles of statistical mechanics, and are therefore commonly used to describe the microscopic dynamical behaviour of individual atoms in a system [174]. However, to achieve this properly a description of the inter-particle interactions is necessary, and a common way to approach this is to use a *force field*. A force field is a set of interatomic and intra-atomic parameters that describes the energy dependence of a system on its particle coordinates [175]. The different terms in a force field expression may describe intramolecular or local contributions to the total energy (e.g. from bond stretching, angle bending, dihedral, and improper torsions), van der Waals interactions, and Coulombic interactions [175]. Commonly used force fields for simulations of polymers include OPLS, COMPASS, and AMBER, which were initially derived for biological systems [173, 175]. The parameters used in the different force fields are obtained from *ab initio* or semi-empirical quantum mechanical calculations, or from experimental parameters [175].

The use of force fields allow large-scale calculations to be performed with relatively low computational resources. However, one limitation of empirical force field based simulations is that they can be applied only to systems that contain functional groups that were included in the development of the force field. Another challenge is that most force fields limit simulations by restricting the system to a single molecular connectivity - in other words, they cannot describe chemical reactions (e.g. bond breaking and forming) [174]. Certain force fields have been derived (e.g. ReaxFF, AIREBO, REBO [176]) that can break bonds, but with a high computational cost. This presents one of the challenges in simulating epoxy resins and other thermoset polymers due to the presence of cross-links between the different polymer chains. Cross-links in epoxy must therefore be introduced manually into the system.

Different methods have been used for building structures of cross-linked epoxy. One approach is to build the cross-linked network structure first using a coarse-grained model and then convert it to an atomistic description [177]. Alternatively, one may start with a physical mixture of the monomers and the cross-linking molecules, and then perform "reactions" (polymerization) in conjunction with the MD simulation [177]. The latter approach has been employed in several works investigating the thermoelastic behaviours of epoxy and its nanocompo-

sites [177–181]. The cross-linking reactions may be performed in a single step where all of the potential chemical bonds between the monomers are formed. This results in a large strain in the system, as many atoms will now be bonded at distances larger than the bond length [177]. Alternatively, a multi-step process may be used, where in every step the reacting atom pairs within a specified cut-off distance are bonded, and the system is relaxed using MD simulation [177]. When there are no atom pairs available within the cut-off distance for reactions, the system is mixed before the next step.

Simulations of epoxy nanocomposites have been performed using a variety of force fields, cross-linking agents and algorithms, and filler types (either as particles e.g. SiO_2 or Al_2O_3, or as nanosheets (BN) and nanotubes (carbon)). Table 2.5 shows results from selected works in literature investigating simulated properties of epoxy nanocomposites. The quality of the parametrization of force fields will also affect the accuracy of the measurements, and systems that are simulated under conditions that differ greatly from those used in the parametrization will require careful handling. Therefore, comparisons between simulations performed with different force fields are challenging. Since force fields are based on numerous approximations, simulations using them should be validated with comparisons to corresponding experimental results [175]. Additional considerations for the models used for the nanoparticles, and the inclusion of surface functionalization or interfacial bonding, should also be made when performing MD simulations. One common feature in the simulations listed in Table 2.5 is that the positions of the nanoparticles are fixed at the centre of a periodic unit cell. While the epoxy chains can be mobile around the particle, the particle itself is generally fixed and does not move much, resulting in what is effectively a uniform dispersion of particles. It would therefore be interesting to simulate the properties of nanocomposites with varying states of dispersion of the nanoparticles, or even situations without spherical particles.

Table 2.5. Selected works from literature investigating the thermal and mechanical properties of epoxy-based nanocomposites containing inorganic nanoparticles.

Filler	Force field	Variable	Observations	Ref.
POSS [a]	AMBER	Filler content	No significant change in glass transition. Lower CTE at 5 wt%. [b]	[177]
SiO_2	Unspecified	Particle size	Increase in T_g and Young's modulus in all nanocomposites, but greatest for smallest particle size.	[182]
Al_2O_3	COMPASS	Particle size	Increase in both Young's and Shear modulus in all nanocomposites, but greatest for smallest particle size.	[183]
SiO_2	COMPASS	Interfacial bonding	Increased T_g and lower mobility of atoms at interface when interfacial bonding is present, compared to no bonding between epoxy and nanoparticle.	[184]
Boehmite	Dreiding	Interfacial bonding	Increase in stiffness at interface for strong chemical bonding between boehmite and epoxy.	[185]
SiO_2	COMPASS	SCA amount	Increased T_g, thermal conductivity, and elastic and shear moduli, but decreased CTE with increased grafting ratio of SCA.	[186]
SiC	COMPASS	Particle size	Increased T_g and elastic modulus in all nanocomposites, but greatest for smallest particle size. CTE below T_g increased with increasing particle size.	[178]

[a] Polyhedral oligomeric silsesquioxane.
[b] Coefficient of thermal expansion (CTE).

3 Methods and experimental details

3.1 Synthesis of nanocomposites

3.1.1 Materials used

Table 3.1 lists the chemicals used for the preparation of pure epoxy resins and *in-situ* synthesized nanocomposites.

Table 3.1. Chemicals used in the synthesis of epoxy nanocomposites

Chemical	**Abbreviation**	**Purity [%]**	**Producer**
Diglycidyl ether of bisphenol-A	DGEBA	-	Merck
Poly(propylene glycol) bis(2-aminopropyl ether)	POPDA	-	Merck
Tetraethyl orthosilicate	TEOS	98	Merck
Titanium (IV) isopropoxide	TIP	97	Merck
Aluminium isopropoxide	AIP	98	Merck
3-(aminopropyl) triethoxysilane	APTES	98	Merck
3-(glycidyloxypropyl) trimethoxysilane	GPTMS	98	Merck
Hydrochloric acid (36 %)	HCl	-	Merck
Ammonia solution (35 %)	NH_3 (aq)	-	Merck
Acetic acid	CH_3COOH	-	Merck
Silicon dioxide, 10-20 nm	SiO_2	-	Merck
Anhydrous 2-propanol	C_3H_7OH	99.5	Merck
Loctite Frekote 55-NC	-	-	Henkel

Diglycidyl ether of bisphenol-A (DGEBA), with a molecular weight (M_w) of 340.41 g mol^{-1}, was used as the epoxy monomer. Poly(propylene glycol) bis(2-aminopropyl ether) (M_w of 230 g mol^{-1}), also known as poly(oxypropylene diamine) (POPDA) or the trade name Jeffamine D230, was used as the curing agent for the epoxy. 3-(aminopropyl) triethoxysilane (APTES) and 3-(glycidyl oxypropyl) trimethoxysilane (GPTMS) were used as the silane coupling agents for surface functionalization of both the *in-situ* prepared and pre-synthesized inorganic oxide nanoparticles. The inorganic alkoxides tetraethyl orthosilicate (TEOS), titanium (IV) isopropoxide (TIP), and aluminium isopropoxide (AIP) were used as precursors for the syntheses of SiO_2, TiO_2, and Al_2O_3, respectively. Loctite Frekote 55-NC was used as a release agent for the molds.

3.1.2 Preparation of pure epoxy samples

Samples of pure epoxy, to be used as a reference, were prepared by mixing DGEBA with the curing agent POPDA in a 2:1 molar ratio of DGEBA:POPDA (1:1 ratio of epoxide groups to amine groups). In preliminary samples, the mixing was performed with a magnetic stirrer at ambient conditions for 15 min, followed by degassing in vacuum for 15-20 min to remove air bubbles introduced during the stirring. The resin was then poured into cylindrical Teflon molds (for samples with 30 mm diameter and 5-15 mm thickness) and cured at 100 °C for 5 h. The walls of the Teflon molds were lightly waxed with high-vacuum silicone grease to enable easier ejection from the molds.

Based on the quality of data obtained from these preliminary samples, the casting procedure was altered for subsequent samples. The DGEBA and POPDA were instead mixed inside a vacuum chamber with a mechanical stirrer for 30 min. Afterwards, the resin was injected into a stainless-steel mold (for discs with 40 mm diameter and 1 mm thickness) while under vacuum. The mold was then placed in a pressure chamber at 100 °C for 5 h with 10-12 bars of N_2 gas. Loctite Frekote 55-NC was used as a release agent for the mold prior to casting.

3.1.3 Preparation of epoxy nanocomposites with *in-situ* synthesis of SiO_2, TiO_2, and Al_2O_3

Table 3.2 provides an overview of the different epoxy nanocomposites prepared using the *in-situ* approach and the variations in the synthesis parameters. Figure 3.1 shows a general schematic outline of the *in-situ* synthesis procedures of SiO_2, TiO_2, and Al_2O_3 nanoparticles in epoxy. The preparation of the nanocomposites was performed entirely inside a fume cupboard to limit exposure to any toxic fumes that may emerge from the heated epoxy.

3.1.3.1 Synthesis of SiO_2

The chronological two-step procedure used by Afzal and Siddiqi [88] was adapted for the preparation of SiO_2 *in situ* in epoxy. DGEBA was heated to 80 °C under reflux in a round-bottom flask on a heating mantle. The SCA was added to the DGEBA and mixed with a magnetic stirrer for 1 h. Afterwards the temperature was reduced to 60 °C and the required amount of TEOS (for a specific SiO_2 content) was added, and stirred for another hour. Distilled water, brought to the desired pH using either HCl or NH_3 solution, was then added (in the molar ratio 2:1 for H_2O:TEOS and 1.5:1 for H_2O:SCA) to initiate the hydrolysis and condensation of TEOS and the SCA. The mixture was stirred at 60 °C

Table 3.2. Overview of the synthesis parameters of various *in-situ* epoxy nanocomposites.

Filler	Content [wt%]	SCA	SCA:DGEBA mass ratio	pH	Notes
SiO_2	5	-	-	2	[a]
	2, 3, 4, 5	GPTMS	1:10	2	
	1, 2, 3, 4, 5	APTES	1:10	2	
	1, 2, 3, 5	APTES	1:10	7	[b]
	1, 2, 5	APTES	1:10	11	
	5	APTES	1:30	7	
	5	APTES	1:30	11	
TiO_2	1, 3, 5	APTES	1:30	7	
Al_2O_3	1, 3, 5	APTES	1:30	7	

[a] Preliminary cylindrical samples prepared without mixing of resin and curing agent in vacuum, and without N_2 pressurization during curing. Samples were cast in Teflon molds.

[b] Disc-shaped samples prepared by mixing resin and curing agent in vacuum, and with N_2 pressurization during curing. Samples were cast in stainless-steel molds, with injection under vacuum.

for 4 h, and then at 80 °C for 1 h. It was then removed from the round-bottom flask and poured into a polyethylene terephthalate (PET) beaker and stirred at 80 °C overnight (approximately 15 h) to remove alcohol by-products or unreacted water. The resin was then mixed with the curing agent under vacuum, cast into the molds, and then cured under N_2 pressurization for 5 h at 100 °C.

3.1.3.2 Synthesis of TiO_2

DGEBA and APTES was mixed in a PET beaker at 80 °C with a magnetic stirrer for 1 h. Simultaneously, the required amount of TIP was transferred to a glass container and mixed with anhydrous 2-propanol using ultrasonication for 30 min. Prior to the transfer of TIP, the syringe was flushed with Ar gas, and the transfer was conducted by maintaining a flow of Ar gas at the tip of the syringe needle, to prevent the hydrolysis of TIP from moisture in the air. After the ultrasonication, the TIP/2-propanol mixture was added dropwise to the silanized epoxy mixture while stirring at 50 °C. Afterwards, the required amount of distilled water for hydrolysis and condensation was mixed with anhydrous 2-propanol

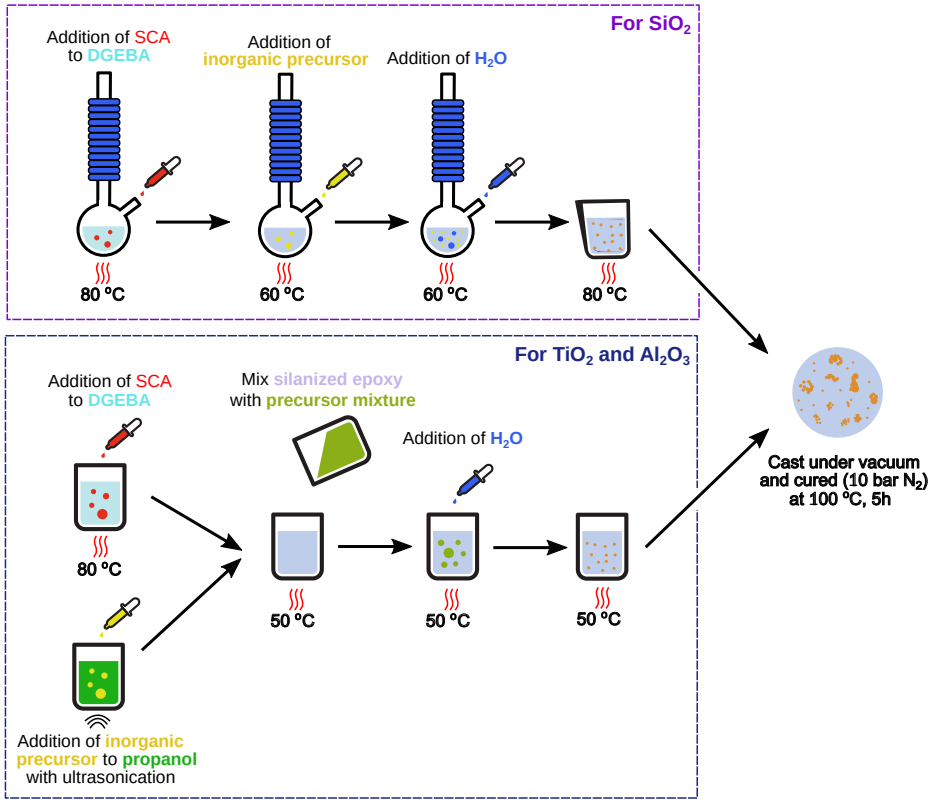

Figure 3.1. Schematic outlining the synthesis procedure for preparing epoxy-SiO_2 (top) and epoxy-TiO_2 or epoxy-Al_2O_3 (bottom) nanocomposites.

using ultrasonication, and then added dropwise to the reaction mixture. The reaction mixture was left stirring at 50 °C until all the excess 2-propanol was removed. The nanocomposite resin was further mixed with the curing agent and cast using the aforementioned procedures.

3.1.3.3 Synthesis of Al_2O_3

DGEBA and APTES were mixed in a PET beaker at 80 °C with a magnetic stirrer for 1 h. The required mass of AIP was dissolved in anhydrous 2-propanol at 70 °C before being added dropwise to the epoxy mixture, followed by dropwise addition of distilled water. The mixture was stirred overnight and the excess 2-propanol was removed, before being mixed with the curing agent and cast.

3.1.4 Synthesis of *ex situ* epoxy-SiO_2 nanocomposites

Purchased SiO_2 nanoparticles (10-20 nm) were functionalized with APTES. APTES was first added to 96 % ethanol with the pH reduced to 5 using acetic acid. After hyrolysis of the APTES, the SiO_2 nanoparticles were added and the mixture was stirred overnight (15-18 h). This was followed by centrifugation and washing with ethanol 3 times to retrieve the functionalized nanoparticles from the mixture, which were then dried in a heating cabinet. For each gram of SiO_2, 1 mL of APTES was used. The functionalized nanoparticles were then mixed with the required volume of POPDA. Small amounts of SiO_2 (~0.1-0.2 g) were added in steps, alternating between mechanical mixing with a machine dispersing tool (produced by IKA) and an ultrasound probe for each step. After all the SiO_2 was added and dispersed in the POPDA, the mixture was added to DGEBA, cast and cured as previously described.

3.2 Characterization

3.2.1 Morphology and dispersion of the nanoparticles

TEM and STEM images were recorded with a JEOL JEM 2100F, equipped with an Oxford X-MAX 80 SDD detector for energy-dispersive X-ray spectroscopy (EDS) analysis. An accelerating voltage of 200 kV was used. The samples were prepared as 50-100 nm thick slices using an ultramicrotome and a diamond knife. EDS element analysis was performed using the software Aztec.

The state of dispersion of the epoxy-SiO_2 nanocomposites was characterized using the free space length (L_f) of unfilled epoxy. TEM images were processed on the software ImageJ 1.52a with a fast-Fourier transform (FFT) bandpass filter. This processing reduced the noise in the TEM and STEM background images, increasing the accuracy of the binary images prepared by thresholding. Between 2 and 4 images from different grid locations on the TEM samples were used for each specimen in order to ensure reproducibility. The computation of L_f was performed on MATLAB using the algorithm and code provided by Khare and Burris [187], and the computation was performed three times for each TEM image. A starting estimate of 150 nm or 300 nm was used for L_f, depending on the size of the particle clusters in the sample.

3.2.2 Structural characterization

SAXS measurements were performed at the Department of Chemistry, University of Oslo, with a Bruker NanoSTAR instrument operating with a Cu micro-

source at 50 kV and 600 µA, and a Våntec-2000 detector. Samples with 1 mm thickness were used, and the measurements were performed over a scattering vector (q) range of 0.009 - 0.3 Å^{-1}. A glassy carbon standard was used for the calibration of absolute intensity. Measurements were performed with an acquisition time of 20 min. Background scattering from air was removed by subtracting the scattering intensity of the empty sample cell. The SAXS data was analyzed using the unified exponential/power-law model developed by Beaucage [188]. The fits to the model were performed using SasView 5.0.1. The unified model describes hierarchical systems with two or more structural levels in scattering that are represented by [189]:

$$I(q) = \sum_{i=1}^{n} \left(G_i \exp\left(\frac{-q^2 R_{g,i}^2}{3} \right) + B_i \exp\left(\frac{-q^2 R_{g,i+1}^2}{3} \right) q*_i^{Pi} \right) \tag{3.1}$$

$$q* = \frac{q}{\operatorname{erf}\left(\frac{k q R_{g,i}}{\sqrt{6}} \right)^3} \tag{3.2}$$

Here, G and B are pre-factors to the Guinier (first exponential) and Porod (second exponential) terms in Equation (3.1) respectively, n is the number of structural levels, R_g is the radius of gyration, and P is the Porod exponent in the power-law scattering regimes. The constant k in Equation (3.2) is not included in SasView. G is defined as [190]:

$$G = N_p(\rho_e V_p)^2 \tag{3.3}$$

where N_p is the number of particles or polymer coils in the scattering volume, ρ_e is the electron-density difference between the particle and the matrix, and V_p is the particle volume. B is a pre-factor specific to the type of power-law scattering, and is thus defined according to the regime in which P falls [190]. P reflects the fractal dimension (D_f) of the structure, which may be a mass fractal structure ($P < 3$), a surface fractal structure ($3 < P < 4$), or a structure with a smooth, sharp surface ($P = 4$) [191].

The approximate size of inorganic structures or domains (d), assuming they are spherical, can be calculated using [192]:

$$d = 2\left(\sqrt{\frac{5}{3} R_g^2} \right) \tag{3.4}$$

The correlation length (ξ) between the domains or clusters is related to the maximum of the peak (q_{max}) according to [15]:

$$\xi = \frac{2\pi}{q_{max}} \tag{3.5}$$

Fourier transform infrared (FTIR) spectroscopy was performed using a Bruker Vertex 80v spectrophotometer equipped with a Bruker Platinum attenuated total reflectance (ATR) diamond. Thirty two scans were recorded at a resolution of 1 cm^{-1}. For the cured resins, samples of 0.5-1 mm thickness were pressed down onto the ATR diamond. For the *in situ* measurements, a drop of the liquid reactant mixture (after different time periods during the reaction) was placed on the diamond.

Raman spectroscopy was performed using a WITec Alpha 300R instrument with a monochromatic diode laser (λ = 532 nm) at 10 mW power. Three accumulations were measured for each sample, with each accumulation collected over an integration time of 60 s. Measurements were performed on the same transparent discs that were used for the FTIR spectroscopy.

NMR spectra were measured at the Department of Materials and Environmental Chemistry, Stockholm University, on a Bruker Avance-III spectrometer. $^{1}H \rightarrow {}^{29}Si$ cross-polarization magic-angle spinning (CPMAS) spectra were collected with a magnetic field strength of 14.1 T (Larmor frequencies of 600.1 and 119.2 MHz for ^{1}H and ^{29}Si, respectively) using 7.0 mm zirconia rotors at a MAS rate of 5.0 kHz. Acquisitions involved proton 90° excitation pulse of 4 µs and matched spin-lock fields of v_H = 60 kHz and v_C = 40 kHz. Contact time of 5 ms was used and SPINAL-64 proton decoupling at 60 kHz. Signal transients from 16384 to 28672 with 4 s relaxation delays were collected. The samples were ground down using a metal file to form a fine powder for the experiment. The NMR peaks were deconvoluted using Origin 2018b, and the degrees of condensation for Q and T species, $[\alpha_S i]_Q$ and $[\alpha_S i]_T$ respectively, were calculated using [21]:

$$[\alpha_{Si}]_Q = \frac{\sum iQ_i}{4} \tag{3.6}$$

$$[\alpha_{Si}]_T = \frac{\sum iT_i}{3} \tag{3.7}$$

Here, Q_i and T_i are the fractions of Q_i and T_i structure units with i siloxane bonds (Si-O-Si) attached to the central silicon.

3.2.3 Mechanical properties

Dynamic mechanical analysis (DMA) was performed on a TA DMA850 instrument using a 3-point bending setup and 12 mm x 3 mm x 60 mm rectangular samples. The samples were scanned from 30 to 200 °C at a ramp rate of 3 °C min^{-1} and in oscillation mode with a frequency of 1 Hz and an amplitude of 30 µm.

The tensile mechanical properties were investigated using a Zwick Roell zwickiLine Type Z2.5 TN instrument with a laserXtens Compact extensometer. The tensile tests were performed on dogbone shaped samples according to specifications from the ASTM D638-14 standard. The samples were first cast in a solid block using stainless steel molds, and then cut into the dogbone shape using a water jet. The measurements were performed at room temperature with a strain rate of 0.01 mm/min and a pre-load of 2 kN, on 4-8 samples of each composition tested.

3.2.4 Thermal analysis

Differential scanning calorimetry (DSC) was performed using a Netzsch DSC 214 Polyma instrument. The nanocomposite samples (5-10 mg) were heated and cooled between 0 and 200 °C for four cycles in a nitrogen atmosphere (N_2 gas flow at 40 mL min^{-1}). Heating and cooling rates of 10 °C min^{-1} were used, and the cooling was achieved with liquid nitrogen. A sapphire crystal was used, with the same temperature program, as a standard for calculating the heat capacity of the samples using the Polyma analysis software. The T_g was measured from the temperature at the end of the increase in heat capacity.

Thermogravimetric analysis (TGA) of the nanocomposites was performed with a Netzsch STA 449C. The samples were placed in an alumina crucible with a synthetic air flow of 30 mL min^{-1}. The samples were first heated to 120 °C and held for 30 min, then heated further to 900 °C at 10 °C min^{-1}. The same temperature program was used for measuring the mass loss in functionalized SiO_2 particles.

3.2.5 Surface area of functionalized nanoparticles

Specific surface areas of functionalized and bare SiO_2 nanoparticles were measured using the Brunauer-Emmett-Teller (BET) method [193] by nitrogen adsorption on a Micrometrics Tristar 3000 at 77 K. The particles were degassed for 12 h at 120 °C in vacuum prior to the measurements. Assuming non-porous and spherical particles, the particle diameter (d_{BET}) was calculated from the specific surface area (S_{BET}) and the particle density (ρ_p) using [15]:

$$d_{BET} = \frac{6000}{S_{BET}\rho_p} \tag{3.8}$$

3.2.6 Dielectric properties

Dielectric properties were measured from room temperature to 200 °C with a Novocontrol Spectrometer in a BDS1200 sample cell. An Alpha Beta dielectric analyzer was used. Measurements were performed between 10^{-2} and 10^{6} Hz on at least 3 samples for each composition. The preliminary cylindrical (30 mm diameter and 3-15 mm thick) epoxy-SiO_2 samples were first ground with SiC paper (#800, #1200, and #2000 grade) to flatten the top and bottom surfaces, before they were sputtered with gold electodes. These measurements were conducted using an electric field of 0.1 V mm^{-1}. Disc-shaped nanocomposite samples (40 mm diameter, 1 mm thickness) that were subsequently prepared were sputtered directly with gold electrodes, and only the edge of the disc was ground with #1200 grade SiC paper to prevent direct electrical contact between the top and bottom electrode. These samples were measured using an electric field of 1 V mm^{-1}.

3.2.7 Resistance to electrical treeing

Electrical treeing measurements were performed using the electrical circuit shown in Figure 3.2a and c. A 50 Hz AC variable voltage supply was connected with a high voltage transformer to reach voltages up to 25 kV. Samples with a needle-plane configuration (Figure 3.2b) were prepared by casting in stainless steel molds with a brass bar at the bottom for connection to the ground electrode plate. The gap between the needle (connected to the high voltage electrode) and the ground electrode was 2 mm (± 0.3 mm). For each of the different types of nanocomposites, 10-12 samples were tested. Figure 3.2c shows the setup on the high voltage side inside a Faraday cage. Figure 3.2d shows the connection of the sample to the high voltage and ground electrodes in the sample cell. The samples were immersed in transformer oil (Midel 7131) to prevent surface flashovers.

Partial discharges (PD) during the tree growth were detected using a capacitive sensor consisting of a coupling capacitor and an Omicron system. The threshold for PD detection was set at 350 fC. The tests were performed by increasing the voltage in steps of 2.5 kV, starting from 5 kV and up to 25 kV, with a step duration of 10 min, to initiate the electrical tree. If the tree was not initiated within 25 kV, the voltage was kept at 25 kV for up to two hours. Once the tree was initiated the voltage was reduced to 10 kV immediately and the PD measurements were started. Images of the tree to follow the growth were taken using the CCD camera at intervals of 1 min throughout the duration of the growth. The experiment was stopped when the tree was close to or reached the ground electrode.

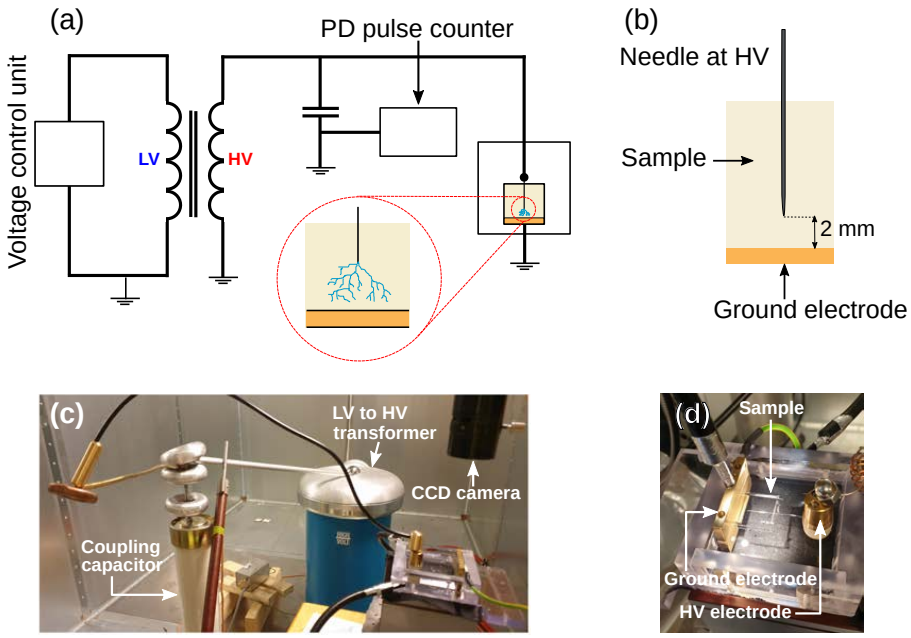

Figure 3.2. **(a)** Circuit diagram of the electrical treeing setup, showing the components on the low voltage (LV) and high voltage (HV) sides. **(b)** Illustration of a typical sample used for treeing measurements. **(c)** Image of the setup showing the different components on the HV side inside a Faraday cage. **(d)** A closer image of the sample inside a sample cell, submerged in oil and connected to the HV and ground electrodes.

Electrical treeing experiments were performed on selected samples with different compositions of 5 wt% inorganic oxide filler, prepared using different synthesis conditions. Optical images of the trees after they were grown were recorded with a Keyence digital microscope. The box-counting method using the FracLac v2.5 plug-in on ImageJ 1.52a was used to estimate the fractal dimension of the trees from the CCD images.

3.2.8 Dielectric breakdown

The AC dielectric breakdown strength of pure epoxy was measured using different modifications of the experimental setup, due to challenges in obtaining accurate measurements. Table 3.3 summarizes the differences in each setup for measurements of the breakdown strength in pure epoxy. The samples were tested in the different setups, with 3-5 samples in each setup. The general setup

for the measurements is shown in Figure 3.3a, where the test cell is submerged in transformer oil (Midel 7131). In Setup No. 1, the samples (10 cm diameter and 0.5 mm thick discs) were placed between two cylindrical brass electrodes which were encased in epoxy (Figure 3.3b). The epoxy encasement was used to prevent other materials (e.g. impurities, transformer oil) from coming close to the region with high electrical field. The diameters of the flat exposed surfaces of the electrodes were 2 cm, and the edges of the electrodes were curved according to the Rogowski profile [194] to obtain a uniform electrical field through the test area. A 25 kg weight was placed on top of the high voltage electrode to ensure good contact between the electrodes and the sample. The voltage was increased using the step-up procedure specified by the the ASTM D149-97a standard. Steps of 5 kV with a step duration of 2 min were used, starting from 10 kV.

Table 3.3. Variations in the experimental setup for the dielectric breakdown strength measurements.

Setup No.	**Thickness [mm]**	**Pressurized oil**	**N_2 in curing**	**Electrodes**
1	0.5	No	No	Epoxy encasing.
2	0.5	No	No	No epoxy encasing. Larger ground electrode.
3	0.5	Yes	No	No epoxy encasing. Larger ground electrode.
4	~0.25-0.3	Yes	Yes	No epoxy encasing. Same shape/size for HV and ground electrodes.

The next set of measurements (Setup No. 2) was performed with the same setup, but removing the epoxy casings on the brass electrodes. A schematic of the bare high voltage electrode is shown in Figure 3.3c. In addition, the diameter of the flat surface of the ground electrode was increased to 6.65 cm to provide sufficient support for the sample placed on top of it.

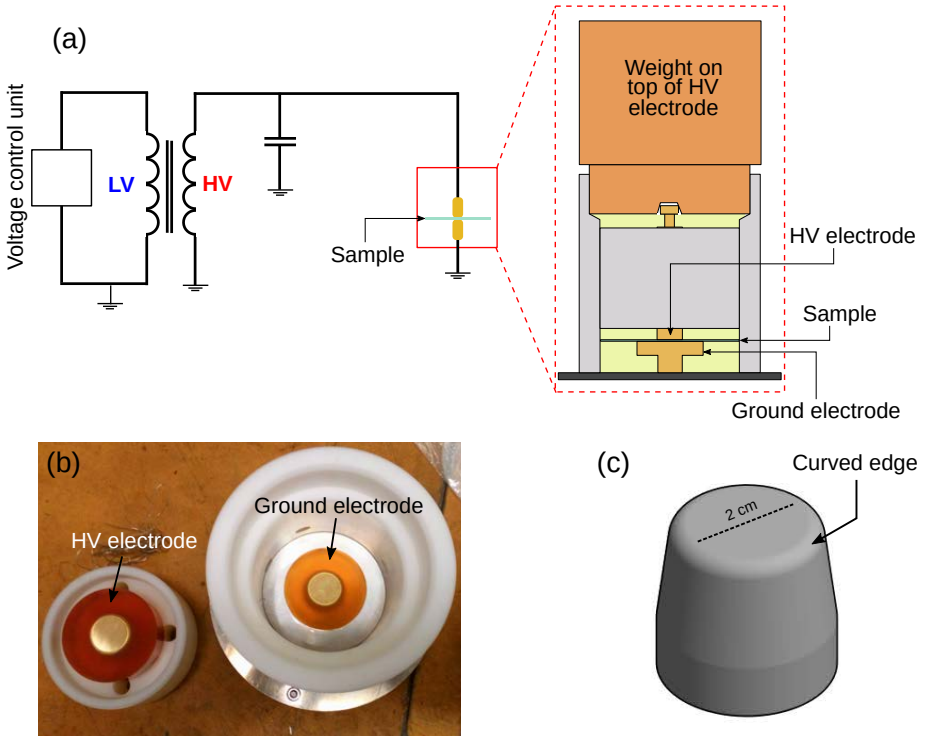

Figure 3.3. **(a)** Circuit diagram and experimental setup for the dielectric breakdown strength measurements. **(b)** The brass electrodes encased in epoxy used in Setup No. 1. **(c)** The profile of the electrode (without the epoxy casing).

Afterwards, in Setup No. 3 the measurements were performed using pressurized oil. The test cell was moved into a pressure vessel filled with transformer oil, and the oil was pressurized to a minimum of 20 bar and stabilized overnight. The final set of measurements (Setup No. 4) were performed using the pressurized oil, and with both the ground and high voltage electrodes having the same profile. The sample thickness was decreased to ~0.25-0.3 mm, and the samples were cured under N_2 pressurization.

3.3 Molecular dynamics simulations

3.3.1 Building the model for epoxy and the curing agent

The structural models for the DGEBA and POPDA molecules, shown in Figure 3.4a and b, were built using the OPLS-AA force field [195] using geometries obtained from LigParGen [196–198]. The data files obtained from LigParGen include information on the atom properties (number and types of atoms, atom positions, charges, and velocities), molecular topology (number and types of bonds, angles, dihedrals, and improper dihedrals), and force field parameters (coefficients for the each type of atom, bond, angle, dihedral, and improper dihedral). Angles refer to the angle between two bonds forming between three molecules, and dihedrals refer to the angle between two planes forming between four molecules. Improper dihedrals are those that form when a central atom is bonded to three atoms (e.g. sp^2 carbon). LigParGen assigns charges by fitting parameters to each atom independently, resulting in the same atoms at different ends of the molecules having different charges. The charges were therefore adjusted slightly (by 5 % at most) to keep them equal in the same atoms in symmetric molecules. In addition, since several molecules would be reacted to form cross-links in the system, the total charge of each molecule must be neutral.

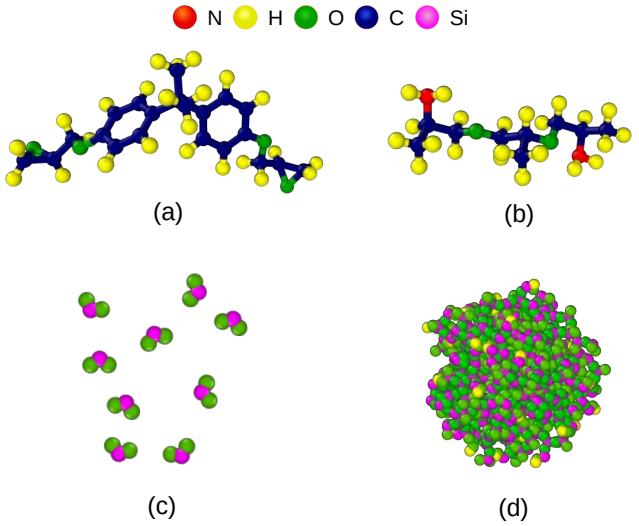

Figure 3.4. Constructed models of the different molecules used in the MD simulations: **(a)** DGEBA; **(b)** POPDA with x = 2; **(c)** SiO_2 nanoparticle; **(d)** SiO_2 molecular units.

POPDA molecules ($H_2N-[CH(CH_3)H_2O]_x-C_2H_5NH_2$) were prepared with two different chain lengths (x = 2 and x = 3) that were used in a 1:1 ratio to obtain a mixture that most closely resembled the POPDA used in the experiments (with M_w = ~230 g mol^{-1}). The Lennard-Jones potential cut-off was set at 10 Å, and long range electrostatics was handled using particle-particle and particle-mesh (pppm) with an accuracy of 10^{-5} [199]. The simulations were carried out on the software LAMMPS [199], with a timestep of 1 fs unless specified otherwise.

3.3.2 Equilibration and cross-linking of the epoxy

A stoichiometric mixture of the DGEBA an POPDA molecules were mixed and relaxed in the simulation initially, using the canonical ensemble (NVT) with a Nose-Hoover thermostat set at 300 K for 0.3 ns. After relaxation, the box was compressed using the isothermal-isobaric ensemble (NPT) with 10 atm pressure over 1 ns. After compression, the structures were relaxed again using the NVT ensemble until the average pressure fluctuated around 1 atm and the density of the system stabilized above 1 g cm^{-3}. The box contained ~1300 molecules (~59600 atoms), with a box size of ~85 Å.

The cross-linking between the DGEBA and the POPDA was then performed using a Python script. Figures 3.5 and 3.6 show how the two cross-linking reactions are performed, and the algorithm used for performing the reactions. The parts of the DGEBA and POPDA molecules that are involved in the reaction are shown, and each atom, bond, angle, dihedral, and improper dihedral in these parts were assigned unique identifiers. A cut-off distance of 5 Å was set for the cross-linking reaction. Terminal carbon atoms in epoxide groups in DGEBA and nitrogen atoms in amine groups in POPDA were given specific atom types (1 and 2 in Figure 3.5, respectively). If the distance between a carbon atom of type 1 and a nitrogen atom of type 2 was within the cut-off distance, then the first reaction took place. The atom types of the reacting carbon and nitrogen atoms were changed (to 4 and 3, respectively, in Figure 3.5), and specific bonds were removed and new bonds were introduced to form the cross-linked molecules. This also means that certain angles and dihedrals were no longer present, but an additional number of new angles and dihedrals formed. In addition, the hydrogen atom on the amine group was now bonded with the oxygen in the epoxide group, thus the atom type for both hydrogen and oxygen atoms changed (from 6 to 7 and 8 to 9, respectively, in Figure 3.5). The charges of the atoms involved in the reaction were also adjusted so that the total charge of the new reacted molecule was neutral.

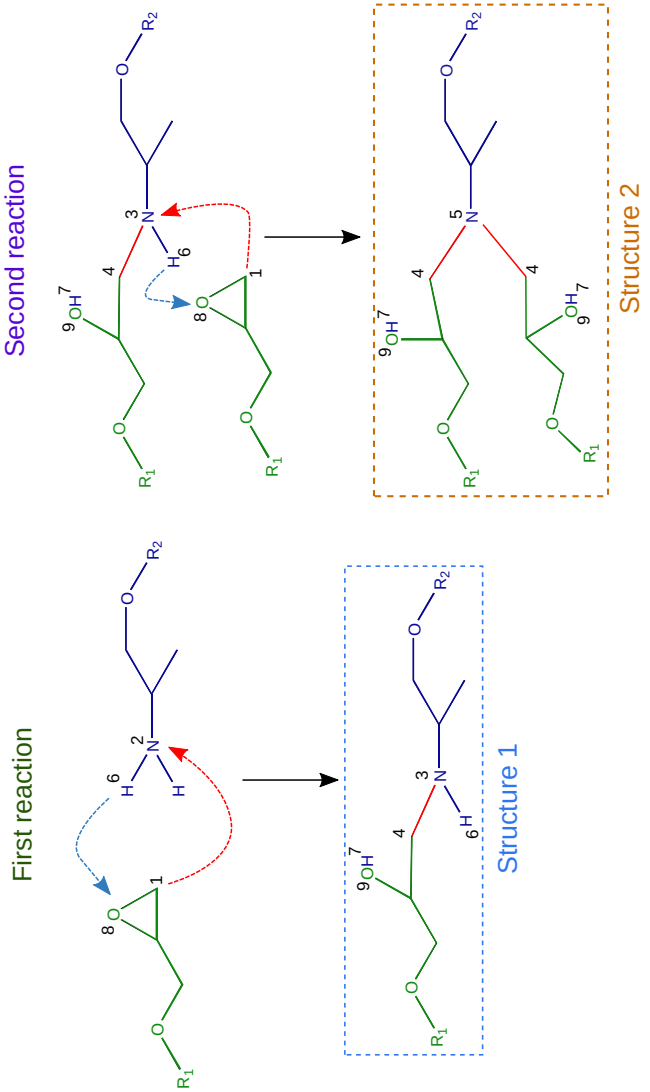

Figure 3.5. Illustration of how the cross-linking reactions are performed using the Python script in the MD simulations. The black numbers next to the C, H, N, and O atoms show the assigned atom types.

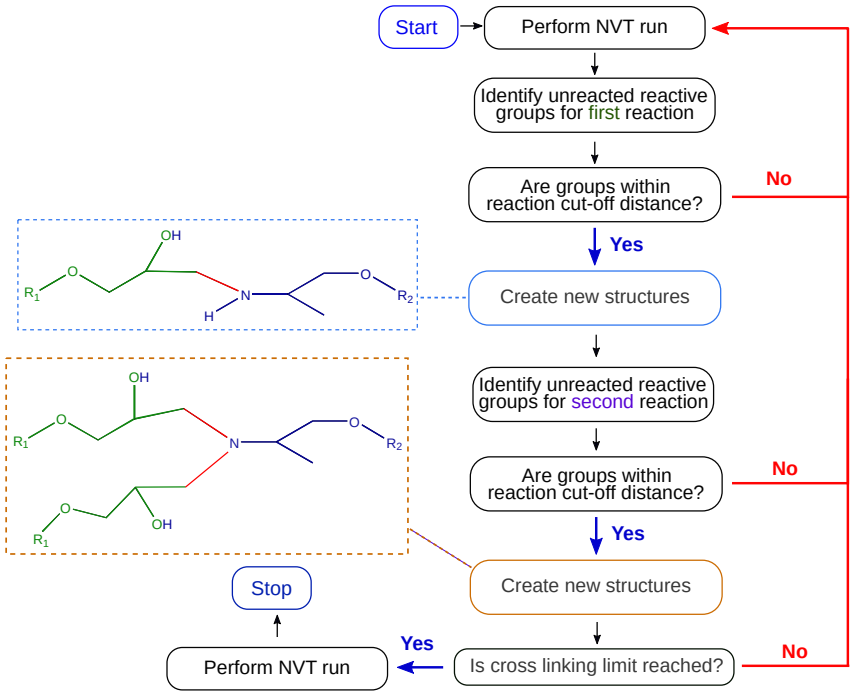

Figure 3.6. Schematic showing the algorithm used by the Python script for the cross-linking reactions during the curing of the epoxy system in the MD simulations.

If no more atoms were present within the cut-off distance that could participate in the first reaction, then the Python script identified unreacted terminal carbons (atom type 1) that were close to nitrogen atoms that have already reacted once (atom type 3). If the distance between them was within the cut-off limit, then the second reaction was performed similarly to the first, resulting in a fully reacted nitrogen atom (atom type 5 in Figure 3.5).

Once all the reactive groups available that were within the cut-off distance for the reaction were identified and the cross-links were formed, a short NVT run was performed to move and mix the molecules further, and the entire cross-linking procedure was performed again. This was repeated until the targeted cross-linking degree was reached. Two pure epoxy systems with ~60 % and ~90 % cross-linking were investigated.

3.3.3 Incorporation of SiO_2 into the epoxy

Two approaches were used to introduce SiO_2 into the simulations. In both models, 12-6 Lennard-Jones (LJ) potentials, Coulomb potentials, and harmonic bonds and angles were used [200]. In the first model (Model I), ~640000 simple SiO_2 molecular units, as shown in Figure 3.4c, were compressed at 10 atm and 300 K in the NPT ensemble over 1 ns. The box was annealed at 500 K in the NVT ensemble over 1 ns, and then relaxed to ambient temperature. A custom program was then used to cut out a "nanoparticle" with defined size (Figure 3.4d), and hydroxyl groups (-OH) were added to the surface. The program was further used to form reactions between neighbouring SiO_2 units to form 3 and 4 coordinated Si centers. After the reaction, the nanoparticle was relaxed under 300 K in the NVT ensemble over 0.3 ns. A simulation box containing ~1300 molecules of stoichiometrically mixed DGEBA and POPDA was merged with the nanoparticle, which was placed centrally. The overlapping DGEBA an POPDA molecules were deleted, and the box was compressed and cross-linked as described earlier. The nanoparticles with sizes of 1, 2 and 3 nm correspond to the equivalent of 1, 5 and 15 wt% filler content.

In the second model (Model II), the simple SiO_2 units were used without any bonds forming between them, or any "particle" shape. The molecules were introduced into the simulation box in amounts corresponding to 1, 3, and 5 wt% alongside the DGEBA and POPDA molecules (~1300 in total). The box was mixed at 300 K in the NVT ensemble over 0.3 ns. The compression and cross-linking were performed afterwards, as described above. A cross-linking degree of ~80 % was reached in the nanocomposites.

3.3.4 Simulation of properties

3.3.4.1 The glass transition temperature

The glass transitions of the simulated epoxy and nanocomposites were measured from the change in density with temperature. An NVT ensemble was run over 0.3 ns at selected temperatures between 250 and 500 K. The initial 100 000 steps in each run were used to stabilize the temperature. The glass transition temperature was estimated from the plot of density as a function of temperature. The intersection of the slopes of the density far below and above the glass transition region was used as a measure of the glass transition temperature.

3.3.4.2 Elastic modulus

Tensile stretching simulations were performed by deforming the unit cell along the x-axis in an NPT ensemble at 300 K. A rate of 10^{-5} ps^{-1} was used for the deformation over 0.1 ns, and the pressure along the y and z-axes was set to 0. The simulations were repeated 15 times using different starting geometries for the unit cell, which were prepared with unique velocity seeds in a high temperature NVT run over 0.1 ns. The Mooney-Rivlin derived stress-strain relation [201], Equation (3.9), was used to generate a stress-strain curve for the measured data points. In Equation (3.9), σ is the stress, ϵ is the strain, and a_1-a_5 are fitting parameters. The elastic moduli were measured from this stress-strain curve using the elastic region up to 1 % strain.

$$\sigma = \left(a_1 + \frac{a_2}{a_3(1+\epsilon) + \frac{a_4}{\sqrt{1+\epsilon}} + a_5} \right) \left(1 + \epsilon - \frac{1}{(1+\epsilon)^2} \right) \tag{3.9}$$

3.3.4.3 Thermal conductivity

Thermal conductivities were calculated at 300 K and 1 atm with the On-the-fly Calculation of Transport Properties (OCTP) plug-in for LAMMPS [202]. The mean square displacements of the total energy current (heat flux) were plotted against simulation time. The thermal conductivities were calculated using the Einstein relation in:

$$\lambda_T = \lim_{t \to \infty} \frac{1}{2t} \frac{V}{k_B T^2} \langle \left(\int_0^t J_\alpha(t') dt' \right)^2 \rangle \tag{3.10}$$

Here, k_B is the Boltzmann constant, T is the temperature, and J_α is the heat flux.

3.3.4.4 Radial distribution functions

Radial distribution functions (RDFs) were calculated for selected atom types using the OCTP plug-in for LAMMPS. This method was selected due to allowing for computation of RDFs beyond the LJ cut-off value (10 Å), as well as a built-in correction for finite size-effects in the plug-in [202]. The asymptotic behaviour of the RDF in a finite-sized system goes to a limit which is not one, which can be corrected empirically by accounting for the correct bulk density of atoms [203]. The calculations were performed in a microcanonical ensemble (NVE) for 1 ns at 300 K and 1 atm. The corrected RDFs was calculated using:

$$g_{ij}^{corrected}(r) = g_{ij}(r) \frac{N_j \left(1 - \frac{4\pi r^3}{3V} \right)}{N_j \left(1 - \frac{4\pi r^3}{3V} \right) - \Delta N_{ij}(r) - \delta_{ij}} \tag{3.11}$$

Here, N_j is the number of particles of type j in the system, V is the system volume, $\Delta N_{ij}(r)$ is the excess number of particles of type j within a sphere of radius r around particle type i, and δ_{ij} is the Kronecker delta [203]. Coordination numbers ($n(r')$) at distance r' were calculated using:

$$n(r') = 4\pi\rho \int_0^{r'} g(r) r^2 dr \tag{3.12}$$

Here ρ is the average density of the system.

Results and Discussion

4 Epoxy-SiO_2 nanocomposites

In this chapter, the varying morphologies and structures of the SiO_2 synthesized *in situ* under different conditions are presented. The resulting dielectric, thermal, and mechanical properties of the nanocomposites are then reported, and the changes in the properties with various factors are discussed. A brief comparison with *ex-situ* nanocomposites is shown, followed by the results of the molecular dynamics simulations of epoxy-SiO_2 nanocomposites.

4.1 Structure and morphology of the *in-situ* synthesized SiO_2

4.1.1 The state of dispersion of the nanoparticles

The effects of the synthesis conditions, including the choice and amount of coupling agent, on the state of dispersion of the nanoparticles can be observed in the TEM images of the nanocomposites shown in Figure 4.1. The SiO_2 functionalized with APTES formed a significantly more homogeneous dispersion of nanoparticles. The particles are, however, not discrete in shape, but arranged in irregularly shaped clusters. Figure 4.1a and b show how the dispersion of the SiO_2 changes when the SiO_2 content is reduced (at pH 2, and with an APTES:DGEBA mass ratio of 1:10). At 2 wt% SiO_2, the clusters become difficult to discern in the TEM, but are more easily identified in the STEM images (shown in inset).

Increasing the pH to 7 during the synthesis in nanocomposites prepared with APTES did not lead to a significant change in the state of dispersion of the SiO_2 (Figure 4.1c). Increasing the pH further to 11, however, did result in the presence of a few larger clusters or agglomerates, such as those shown in Figure 4.1d. The most significant change to the state of dispersion resulted from a decrease in the amount of APTES, both at pH 7 and pH 11. Figure 4.1e exhibits epoxy with 5 wt% SiO_2 prepared at pH 11 with an APTES:DGEBA mass ratio of 1:30. The clusters are less frequent and spaced further apart, but are also significantly larger compared to those prepared with an APTES:DGEBA mass ratio of 1:10. Figure 4.1f shows the significant change in the particle morphology when GPTMS is used instead of APTES under the same conditions (5 wt% SiO_2, pH 2, GPTMS:DGEBA mass ratio of 1:10). Large agglomerates exceeding 1 μm were formed, and these were not homogeneously dispersed.

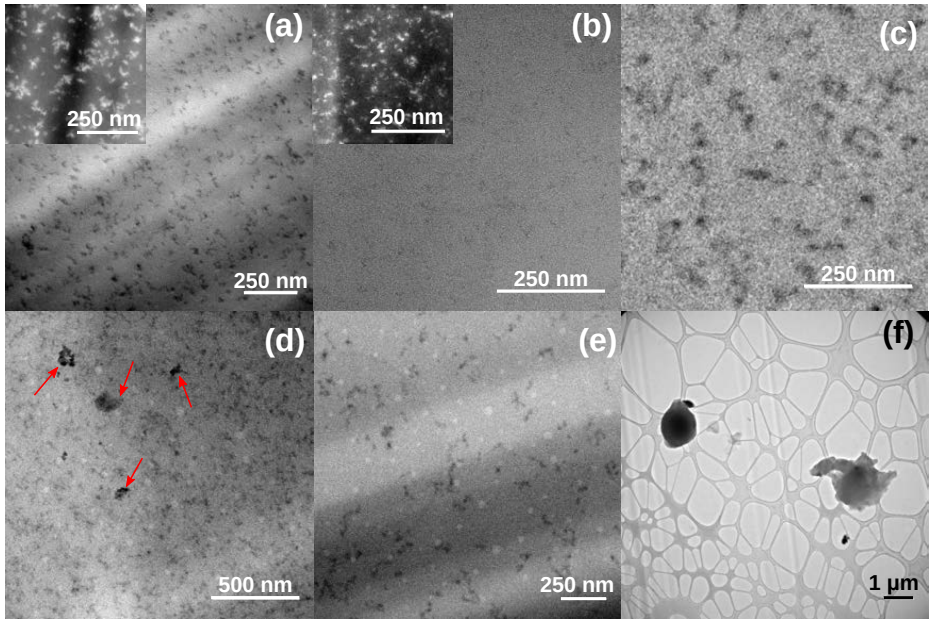

Figure 4.1. Bright field TEM images of SiO_2 nanoparticles synthesized *in situ* in epoxy: **(a)** 5 wt% and **(b)** 2 wt%, at pH 2 and APTES:DGEBA mass ratio of 1:10; 5 wt% with APTES:DGEBA mass ratio of 1:10 at **(c)** pH 7, and **(d)** pH 11; **(e)** 5 wt% in pH 11 with APTES:DGEBA mass ratio of 1:30; **(f)** 5 wt% at pH 2 and GPTMS:DGEBA mass ratio of 1:10. The insets in **(a)** and **(b)** show dark field STEM images from the same samples where the nanoparticle clusters are more easily visible. The red arrows in **(d)** point to the larger agglomerates that have formed.

A significant difference is observed in the nanocomposites prepared without any surface functionalization. Figure 4.2 shows TEM images of the various particle morphologies of the SiO_2 formed without any SCA (APTES or GPTMS). Most of the SiO_2 formed micron-sized agglomerates consisting of large (> 250 nm) non-spherical particles. However, some regions were found with clusters of closely spaced, monodisperse (70-80 nm) completely spherical nanoparticles, while in other regions elongated flakes were present.

4.1.1.1 Quantifying the state of dispersion

A quantitative characterization of the state of dispersion of the nanoparticles, and not a simple qualitative evaluation of the TEM images, is useful for comparing the effects of various parameters (e.g. cluster sizes, filler content, size of

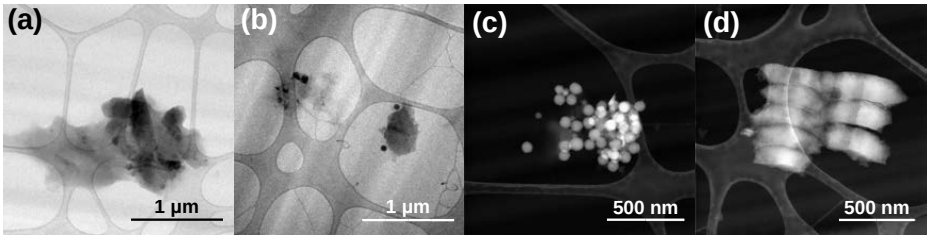

Figure 4.2. Bright field TEM **(a,b)** and dark field STEM **(c,d)** images of various SiO_2 morphologies formed in the nanocomposites without SCA (5 wt% SiO_2 content), exhibiting both spherical sub-100 nm particles, as well as large micron-sized agglomerates and elongated flakes.

unreinforced polymer, etc.) on the properties of the nanocomposites. In this work, the free space length of unfilled polymer regions (L_f) and the average size of the clusters were used to evaluate the state of dispersion in the epoxy-SiO_2 nanocomposites prepared with APTES. Figure 4.3 shows the changes in these parameters with pH in nanocomposites with 2 and 5 wt% SiO_2.

L_f increased with increases in both pH and the filler content, indicating larger regions of unfilled polymer. The dispersion of SiO_2 was significantly more homogeneous at lower filler content (2 wt%), as shown by the miniscule variation in the calculated values of L_f in Figure 4.3a. L_f increased significantly in nanocomposites when the amount of the coupling agent (APTES) was reduced (over 200 nm at pH 11 and over 120 nm at pH 7, instead of between 80 and 120 nm). The increased spacing between the particle clusters seen in Figure 4.1e was reflected in the substantial increase in L_f.

Changes in the average cluster size were similar to those observed for L_f. At a higher filler content (5 wt%) the particle clusters were generally between 20 and 60 nm at all pH, whereas at lower filler content (2 wt%) they were between 10 and 20 nm at pH 2, and between 20 and 60 nm at pH 11. At pH 2 and pH 7, the largest clusters did not exceed 80-100 nm. However, at pH 11 and a filler content of 5 wt%, agglomerates above 100 nm were more frequent, typically between 120 and 150 nm (shown in Figure 4.3b), in addition to the smaller clusters. Upon reduction of the amount of APTES at pH 11, only large agglomerates, usually between 100 and 120 nm, were observed. Such agglomerates were not present however at pH 7, even with a reduction in the amount of APTES.

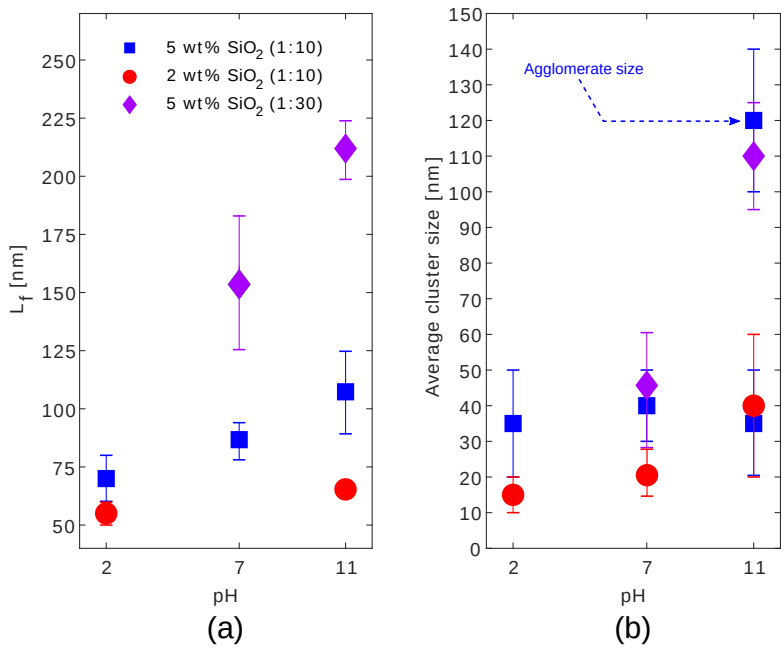

Figure 4.3. Evaluation of the state of dispersion with variations in pH, filler content and amount of SCA (shown in parentheses as mass ratio of APTES:DGEBA). Changes in **(a)** L_f, and **(b)** average cluster size are shown for nanocomposites with 2 and 5 wt% SiO_2. L_f for 2 wt% SiO_2 at pH 7 could not be calculated due to poor TEM image quality.

4.1.2 The organization of the SiO_2 clusters

The SAXS scattering profiles of pure epoxy and the nanocomposites prepared under different pH conditions are shown in Figure 4.4a-c. The scattering of pure epoxy did not show any significant features apart from a peak emerging at a scattering vector (q) above the measured range. In all the nanocomposites the scattering is increased significantly, although the scattering intensity does not necessarily correlate with the SiO_2 content. Broad features referred to as Guinier knees, marked by blue arrows in Figure 4.4, are present in the nanocomposites initially between 0.02 and 0.1 $Å^{-1}$ at low SiO_2 content. At higher SiO_2 content, two such features are observed instead, one generally between 0.01 and 0.03 $Å^{-1}$ with a higher intensity, and another between 0.07 and 0.24 $Å^{-1}$ with a lower intensity. The two "knees-like" features are separated by a linear region of scattering known as a Porod slope, marked by red arrows in Figure 4.4. The emergence of these features is quite consistent across samples prepared under

different pH conditions, although at pH 11 the feature at high q is only present in composites with 5 wt% SiO_2. Additionally, for the nanocomposite with 5 wt% SiO_2 prepared at pH 11 with a reduced amount of APTES, the Guinier knee at high q is absent. Each Guinier knee and the slope of the Porod scattering is a combined scattering feature resulting from the size and organization of the SiO_2 clusters. The Porod slope is equivalent to the fractal dimension (D), which describes the power-law dependence of the scattering intensity and indicates whether the scattering is caused by a structure with mass or surface fractals.

The position of the knee can provide an estimate for the size of the inorganic domains responsible for the scattering. The presence of multiple features at different q indicates that the SiO_2 nanoparticles are forming a hierarchical structure, where the domains or clusters at each structural level consists of the domains formed in the previous structural level. The unified exponential/power-law model [188,189] was therefore used to describe the structural organization. The scattering data was fitted to the model, which describes each structural level in terms of Guinier's law and a structurally limited power law for the knee-like and the linear Porod regions, respectively (Equation (3.1)). The fits were performed with two structural levels where applicable (nanocomposites with larger amounts of SiO_2 exhibiting two knee-like features). In the case of nanocomposites with only one large feature instead of two (usually at lower filler contents), the unified model was found to be unsuitable, and individual Guinier and power-law models were used over smaller q intervals. The fits are shown in Figure 4.4d-f, and the structural parameters obtained from the fits are shown in Table 4.1.

Table 4.1 shows that the SiO_2 structures formed in the nanocomposites tend to initially form mass fractal structures (with $1.4 < D < 2.2$) with sizes between 7 and 15 nm. Upon increasing the SiO_2 content, these structures can cluster together to form larger structures (between 20 and 45 nm) that make up the secondary structural level. These structures, however, exhibit a higher fractal dimension (with $2.1 < D < 3.8$), indicating the formation of structures with surface fractals in addition (for those with $3 < D < 4$). For the secondary structural level, D increases with the filler content in all the nanocomposites, and at 5 wt% SiO_2 D is above 3, regardless of the synthesis conditions. The pre-factors G and B showed similar trends in the nanocomposites prepared at different pH. Generally, G showed little change for the first structural level, and increased significantly from 2 or 3 to 5 wt% in the second structural level. B was relatively unchanged with filler content at the first structural level, but decreased with filler content in the second structural level.

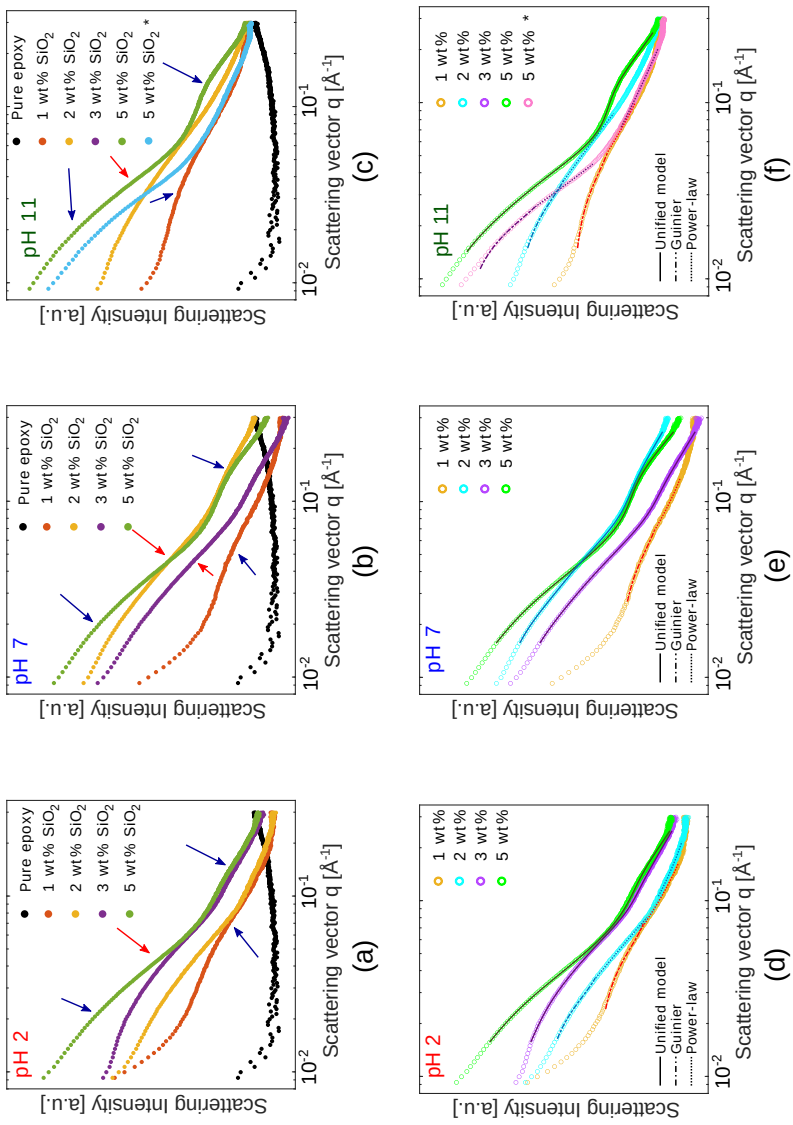

Figure 4.4. SAXS profiles (top) and the corresponding fits to the different models (bottom), for epoxy-SiO_2 nanocomposites with APTES synthesized at **(a,d)** pH 2, **(b,e)** 7, and **(c,f)** 11. The (*) in **(c)** and **(f)** indicates the nanocomposite prepared with a reduced amount of APTES (APTES:DGEBA mass ratio of 1:30).

Table 4.1. Structural parameters, including the fractal dimensions (D), the radii of gyration (R_g), the Guinier pre-factor (G), and the power-law pre-factor B, of the inorganic structures in the epoxy-SiO_2 nanocomposites at each structural level, obtained from fitting of the SAXS scattering data to either the unified exponential/power law model, or to individual Guinier and power-law models. D corresponds to P in Equation (3.1). The sizes of the inorganic domains (d) was calculated using Equation (3.4).

pH	Filler content [wt%]	Level	D [a]	R_g [a] [nm]	d [nm]	G [cm^{-1}]	B [cm^{-1}]
2	1 [b]	1	1.98	4.2	10.9	-	-
	2 [b]	1	1.75	-	-	-	-
		2	2.16	8.5	22.0	-	-
	3	1	1.46	3.8	9.7	0.25	1×10^{-3}
		2	2.5	13.1	33.7	2	5×10^{-5}
	5	1	1.98	2.9	7.4	0.25	1×10^{-3}
		2	3.2	16.4	42.4	45	3×10^{-5}
7	1 [b]	1	1.88	4.1	10.5	-	-
	2	1	1.42	3.4	8.6	0.27	5×10^{-4}
		2	1.91	11.0	28.5	7.1	1×10^{-3}
	3	1	1.57	3.7	9.6	0.25	1×10^{-3}
		2	2.59	12.9	33.3	5	6×10^{-5}
	5	1	2.17	2.8	7.2	0.24	1×10^{-3}
		2	3.17	16.3	42.0	45	3×10^{-5}
11	1 [b]	1	1.80	5.3	13.7	-	-
	2 [b]	1	1.86	8.3	21.4	-	-
	5	1	2.13	3.1	8.1	0.25	1×10^{-3}
		2	3.24	13.9	35.8	45	3×10^{-5}
	5 [bc]	1	1.37	-	-	-	-
		2	3.71	12.5	32.2	-	-

[a] The error in the calculated values from the fits is ± 0.05 for both D and R_g.

[b] These were fit to individual Guinier and Power-law models instead of the unified exponential/power law model.

[c] Sample prepared with an APTES:DGEBA mass ratio of 1:30 (instead of 1:10, which is the case for the other samples in this table).

4.1.3 Bonding in the *in-situ* nanocomposites

The progress of the silanization of the epoxy by the SCA and the sol-gel reactions of TEOS was followed by FTIR spectroscopy. Figure 4.5 shows the FTIR spectra of the reaction mixture recorded after the addition of APTES and TEOS, as well as 5 and 18 h after the addition of H_2O to the reaction mixture.

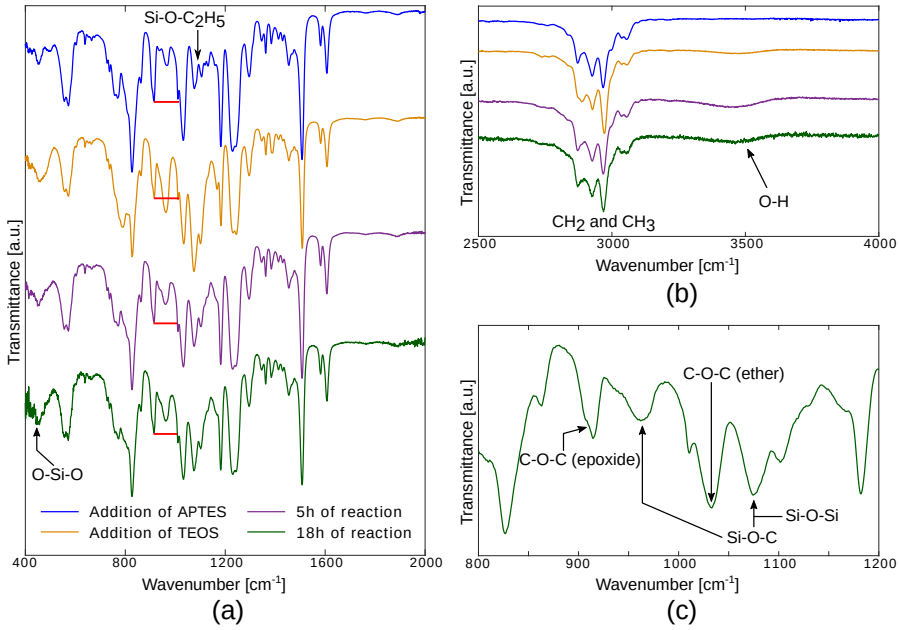

Figure 4.5. FTIR spectra during the *in-situ* sol-gel reaction. **(a)** and **(b)** show the spectra from the mixture at various times of the reaction. **(c)** shows a magnified part of the spectra after the hydrolysis and condensation reactions are complete, highlighting the important IR bands from the different groups present. The spectra were taken *in situ* during the preparation of an epoxy-SiO_2 nanocomposite with 5 wt% SiO_2 at pH 2 and APTES:DGEBA mass ratio of 1:10, and normalized to the band at 1509 cm^{-1}.

The silanization of the DGEBA chains by the opening of the epoxide rings by the amine groups (-NH_2) in APTES (in a reaction similar to that shown in Figure 2.2) is observed from the decrease in the band at 915 cm^{-1}. This band is assigned to the C-O-C group in the epoxide ring [204]. The red lines in Figure 4.5a indicate this decrease relative to the signal at 1036 cm^{-1}, which is assigned to the C-O-C aromatic ether group in the DGEBA chains [204] that remains unchanged through the sol-gel reactions. The addition of APTES resulted in the bands

between 940 and 970 cm^{-1}, and the double bands between 1050 and 1150 cm^{-1} from the Si-O-C bonds in the alkoxide. As the reaction between APTES and DGEBA proceeded, the double bands became weaker due to hydrolysis of the alkoxide groups. Upon addition of TEOS, the bands assigned to the alkoxide increased in intensity again, due to the larger volume of TEOS being used compared to APTES. As the hydrolysis of TEOS proceeded, both an increase in the O-H band (at 3200-3400 cm^{-1} as seen in Figure 4.5b) and a decrease in the double bands at 1050-1150 cm^{-1} were observed (Figure 4.5a, after 5 h of reaction). However, after the reaction had proceeded overnight, the band between 1050 and 1150 cm^{-1} showed an increase again, due to the formation of Si-O-Si groups from the condensation reactions once hydrolysis was completed. The Si-O-Si groups give several strong overlapping bands in the region 1000-1300 cm^{-1} (highlighted in Figure 4.5c), depending on how long or branched the siloxane chains are [205,206]. Additionally, the O-Si-O rocking band is observed to emerge at 450 cm^{-1}.

Figure 4.6a shows the FTIR spectra of cured pure epoxy and nanocomposite samples, normalized for the band at 1509 cm^{-1} (not shown in the figure). Both the pure epoxy and the nanocomposites exhibit a double band between 1050 and 1150 cm^{-1}. The bands in the spectrum of the epoxy-SiO_2 nanocomposite are at 1076 and 1098 cm^{-1} and are broader, whereas the bands in pure epoxy are at 1083 and 1101 and are sharper. The bands in pure epoxy can be attributed to stretching vibrations in the C-O bond present in the curing agent [207]. There is, therefore, a considerable overlap between these bands and the Si-O-Si or Si-O-C bands in the cured nanocomposites. Additionally, the presence of the O-Si-O rocking band at 450 cm^{-1} is more evident, compared to that in Figure 4.5. The sharp band from the epoxide ring (915 cm^{-1}) shows a significantly decreased intensity, which, in addition to the broad O-H band at 3300-3600 cm^{-1}, indicates that most of the epoxy chains have been cross-linked in the curing process.

In the Raman spectra shown in Figure 4.6b, differences are observed for pure epoxy and the nanocomposites (prepared at pH 2) between 450 and 520 cm^{-1}. The nanocomposites presented either a sharp band at 483 cm^{-1} or a broad band between 470 and 510 cm^{-1}. The former is referred to as the D_1^* band, whereas the broad band observed for the nanocomposites with a higher SiO_2 content appears to consist of an overlap of the D_1^* band and another band (referred to as D_1) at 493 cm^{-1}. Both the D_1^* and D_1 bands are due to the formation of four-membered ring or cage structures consisting of Si-O links [208,209]. For smaller amounts of SiO_2 or nanocomposites prepared under different pH conditions, these bands were absent. No other differences between the pure epoxy and the nanocomposites were observed in the rest of the measured spectra.

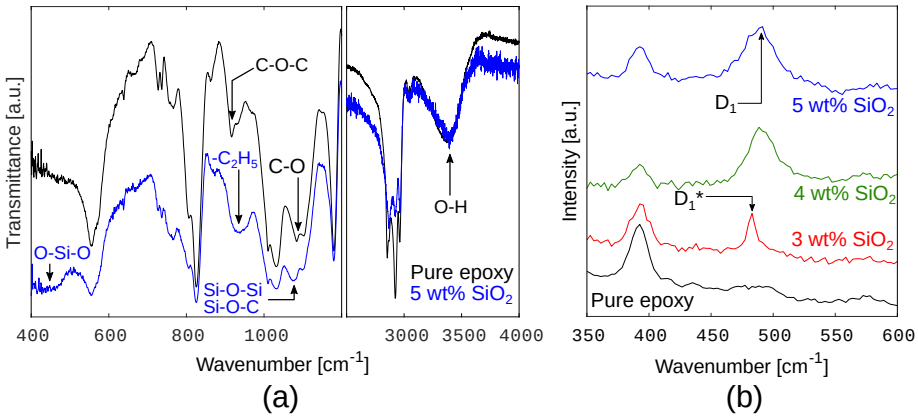

Figure 4.6. **(a)** FTIR spectra of cured pure epoxy and epoxy-SiO_2 nanocomposite (5 wt% SiO_2, pH 7, APTES:DGEBA mass ratio of 1:10), showing IR bands in the ranges 400-1200 cm^{-1} and 2500-4000 cm^{-1}. **(b)** Raman spectra of cured pure epoxy and epoxy-SiO_2 nanocomposites (pH 2, APTES:DGEBA mass ratio of 1:10), showing the Raman shifts for four-membered SiO rings (D_1 and D_1^*).

^{29}Si NMR was used to determine the degree of condensation within the Si-O-Si network. The NMR spectra of the nanocomposites prepared under different conditions are shown in Figure 4.7. For the epoxy-SiO_2 nanocomposites prepared with APTES (Figure 4.7a), the spectra were similar regardless of the pH used. The chemical shifts between -40 and -80 ppm correspond to T^x signals ($0 \leq x \leq 3$), where x represents the number of $-C_2H_5$ or -OH groups on hydrolysed APTES that have been replaced by an -O-Si bond via condensation. The shifts between -80 and -120 ppm correspond to Q^y signals ($0 \leq y \leq 4$), where y represents the number of $-C_2H_5$ or -OH groups on hydrolysed TEOS that have undergone condensation [210]. The NMR spectra of the nanocomposites prepared with GPTMS (Figure 4.7b), however, are slightly different.

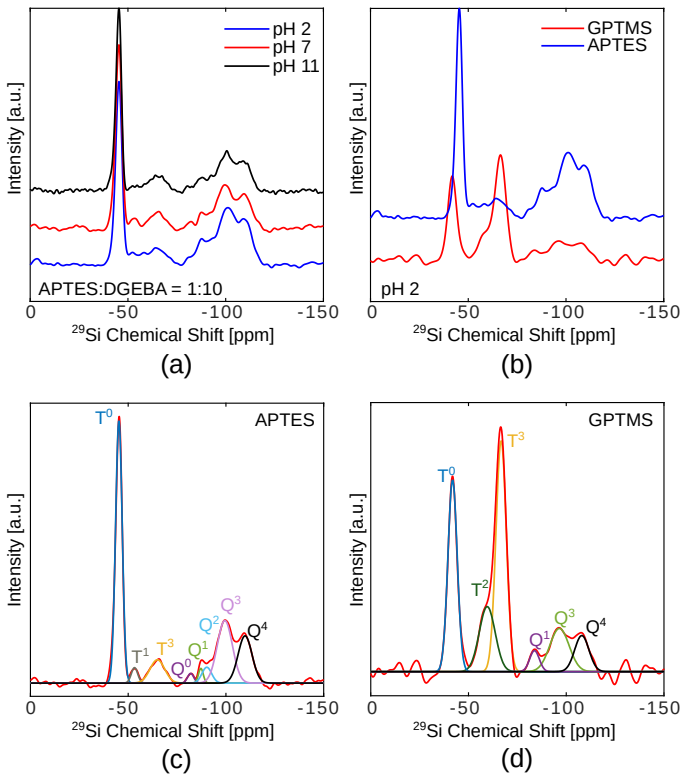

Figure 4.7. ^{29}Si NMR (CP-MAS) spectra of epoxy-SiO_2 nanocomposites with 5 wt% SiO_2 prepared with **(a)** APTES at pH 2, 7, and 11, and **(b)** with APTES and GPTMS at pH 2. **(c)** and **(d)** show the deconvoluted shifts from the spectra for the nanocomposites prepared with APTES and GPTMS, respectively, at pH 2. The chemical shifts are with respect to TMS.

Figure 4.7c and d show the deconvolution of the various chemical shifts into the individual T^x and Q^y signals in nanocomposites prepared with APTES and GPTMS, respectively. The T^0 peak was most prominent in all the spectra of the samples prepared with APTES, alongside much weaker T^1 and T^3 features. However, in the samples prepared with GPTMS, the T^3 peak was higher than T^0, which had a lower intensity than for the nanocomposites with APTES. Additionally, a T^2 peak was observed as a shoulder to the T^3. Another difference between the nanocomposites with APTES and with GPTMS was the strength (or intensity) of the Q^y peaks. These were more prominent in the nanocomposites

with APTES than in those with GPTMS. However, the nanocomposites with APTES exhibited all five types of Q^y peaks, whereas the nanocomposites with GPTMS did not present the Q^0 or Q^2 peaks. The degrees of condensation $[\alpha_{Si}]_Q$ and $[\alpha_{Si}]_T$ were calculated to be 0.77 and 0.17, respectively, for the nanocomposites prepared with APTES, and 0.77 and 0.59, respectively, for those prepared with GPTMS. Changes in the pH were not observed to affect the degree of condensation in the samples prepared with APTES.

4.1.4 Discussion

4.1.4.1 Effect of the SCA on the synthesis pathway and morphology of the SiO_2

As seen in Figure 4.2, the use of a coupling agent is necessary for ensuring sufficient dispersion of the *in-situ* synthesized SiO_2 with a consistent particle morphology. The use of APTES resulted in a homogeneous dispersion of the SiO_2 prepared *in situ* in the epoxy, as seen in Figure 4.1a-e. However, despite several previous works in literature employing GPTMS to successfully functionalize and disperse pre-synthesized nanoparticles using an *ex-situ* approach, the use of GPTMS in the *in-situ* synthesis was not as equally successful, as evidenced in Figure 4.1f. This difference in the state of dispersion may be due to differences in how the APTES and GPTMS interact with the epoxy and the TEOS during the synthesis, shown schematically in Figure 4.8. APTES contains an amine ($-NH_2$) group at one end of the molecule which can directly form a cross-link with the epoxide (C-O-C) groups of two DGEBA molecules, similarly to the curing agent. GPTMS, however, has another epoxide group instead, and therefore cannot form a bond with other DGEBA molecules until the curing agent is added.

Hoebbel et al. [211] previously reported that the chemical shift for the T^0 signal in ^{29}Si NMR is more negative for fewer -OH (and more $-OC_2H_5$) groups attached to Si. Figure 4.7 shows that the T^0 signal in APTES is observed at a chemical shift of -45 ppm instead of the expected -40 to -43 ppm [167, 211], therefore indicating that some of the APTES is not completely hydrolysed. The FTIR spectrum (Figure 4.6a) confirms the presence of $-OC_2H_5$ groups attached to Si in the APTES, verifying the lack of complete hydrolysis. Additionally, the lower degree of condensation of the T shifts in APTES (0.17) compared to the GPTMS (0.59) indicates that self-condensation might occur within GPTMS. This self-condensation would prevent the GPTMS from successfully functionalizing the synthesized SiO_2.

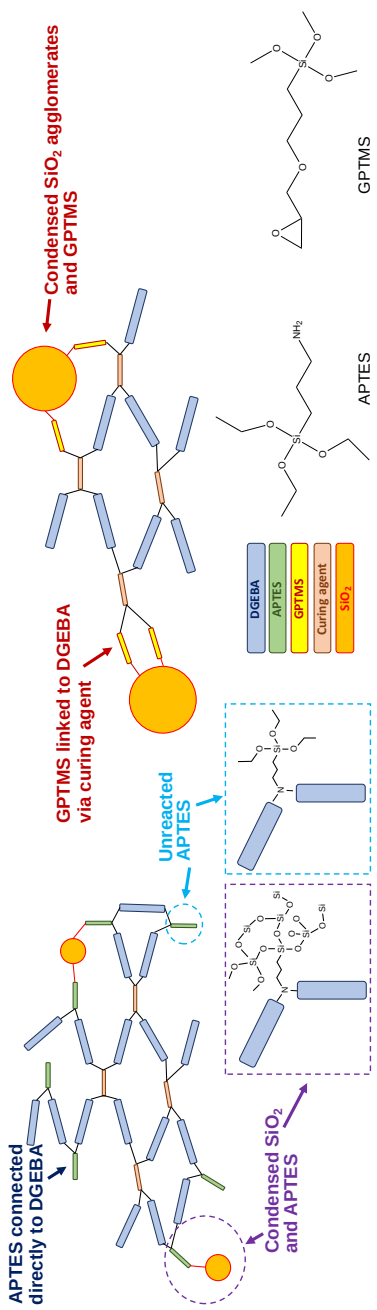

Figure 4.8. Schematic illustrating how the two SCAs, APTES and GPTMS, form chemical links between the organic and inorganic components in the nanocomposites. Reproduced with permission from [212].

Since the Si in GPTMS is bonded to 3 -OCH_3 groups (instead of the -OC_2H_5 groups in APTES or TEOS), the GPTMS can also be hydrolysed faster than TEOS [14], and can begin condensing earlier. The GPTMS is added quite early in the synthesis but is not anchored to the DGEBA until the final stages of the nanocomposite synthesis when the curing agent is added. Hence, the self-condensation results in the large agglomerates observed that are not too dissimilar from when no SCA is used.

On the other hand, all of the nanocomposites prepared with APTES result in SiO_2 exhibiting similar morphologies and structures visually (as seen in Figure 4.1). This may be explained by the ability of APTES to immediately react with the DGEBA chains, providing multiple possible condensation sites for the hydrolysed TEOS, which the GPTMS is unable to do. Therefore, TEOS can begin condensing at different points, resulting in a more homogeneous morphology with smaller SiO_2 structures or clusters. The quantitative analysis (Figure 4.3) reveals how reduced amounts of APTES noticeably affects the state of dispersion of the SiO_2, with increases in both the size of the clusters, the frequency and size of larger agglomerates, and the free space length. Figure 4.9 highlights the difference in L_f in the nanocomposites when the amount of APTES is reduced at both pH 7 and 11. With fewer APTES molecules, there are fewer anchor sites for the condensation of TEOS with a direct chemical link to the DGEBA chains, resulting in larger SiO_2 structures that are positioned further from one another.

4.1.4.2 Structure and dispersion of the SiO_2

Several studies have reported the formation of fractal structures of SiO_2 in *in-situ* epoxy nanocomposites, with SAXS profiles similar to those observed in this work. Donato et al. [91] reported both mass and surface fractals in SiO_2 depending on the selection of ionic liquid for surface modifications. Perchacz et al. [18] showed SAXS profiles similar to those observed for the low SiO_2 content nanocomposites prepared in this work, featuring a Guinier knee between 0.01 and 0.1 $Å^{-1}$ with D~2, when an amine-based catalyst was used. Ponyrko et al. [21] also reported similar SAXS profiles with a single knee-like feature, but with more compact structures instead and a higher mass fractal dimension, depending on whether an aqueous or non-aqueous synthesis was used. However, none of these materials exhibited the formation of multiple structural levels (within the measured q range) as shown in this work.

The SAXS profiles shown in Figure 4.4 highlight the formation of the two structural levels in a hierarchical organization in the SiO_2 clusters. Figure 4.10 shows an example of such an organization, as well as representations of the different

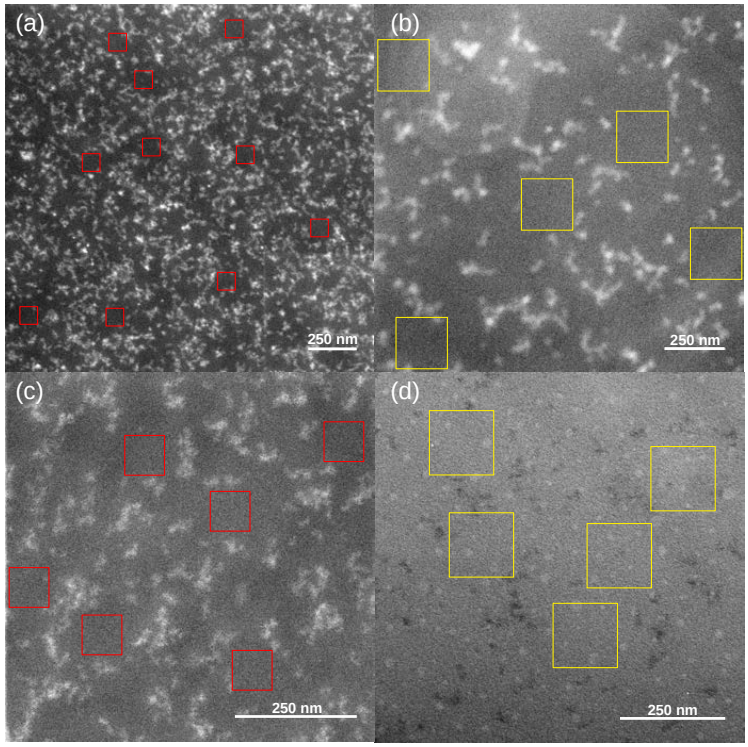

Figure 4.9. State of dispersion and cluster sizes for *in-situ* synthesized SiO_2 at **(a,b)** pH 11 and **(c,d)** pH 7 with APTES:DGEBA mass ratios of **(a,c)** 1:10 and **(b,d)** 1:30. The SiO_2 content in all four cases was 5 wt%. The red and yellow boxes visualize the sizes of L_f in the different compositions (~105, 205, 86, and 156 nm in **(a)**-**(d)**, respectively).

regions that give specific values of D. At the first level, the SiO_2 forms mass fractal structures consisting of polymer-like chains of Si-O-Si links. At higher filler contents, a secondary structural level forms which consist of multiple units of the first structural level. Hence, the base unit of a secondary structure may be a cluster or network composed of the mass fractal chains that form the preceding structural level.

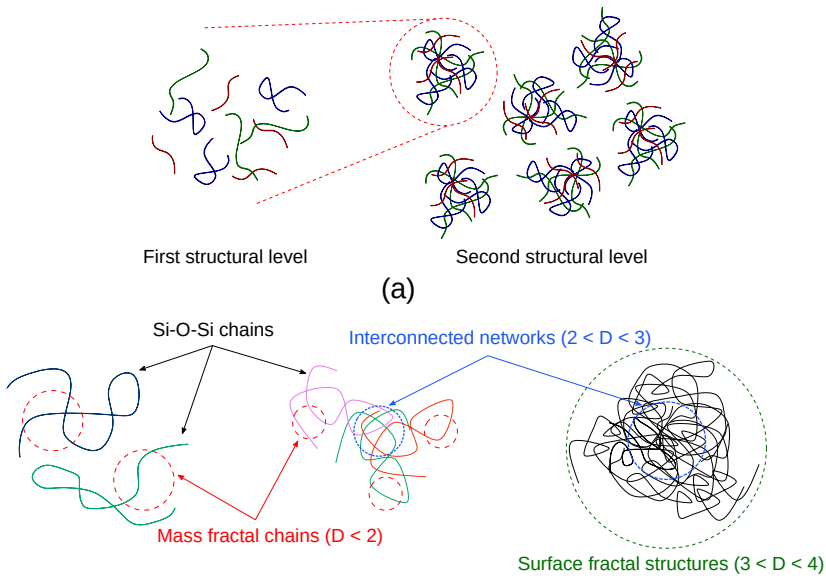

Figure 4.10. Illustration exemplifying **(a)** two structural levels where a surface fractal cluster is composed of mass fractal chains, and **(b)** the different regions of the SiO_2 structures that result in the fractal dimensions obtained from the fits to the SAXS profiles.

Figure 4.11 shows a representation of the proposed changes in the SiO_2 structures with the filler content in the nanocomposites prepared at pH 7, although a similar trend is observed at pH 2 and 11 as well. Table 4.1 shows that in the cases where the unified model could be used, the fractal dimension at both structural levels generally increased with increasing filler content. This indicates an increased degree of networking and cross-linking between the polymeric mass fractal chains of SiO_2, both within the first structural level and also in the fractal aggregates comprising the secondary structural level. However, in the cases where only one broad feature was observed in the scattering at low SiO_2 content, the unified model was not used. The obtained D from the fit to the power-law model was higher than those obtained for the first structural level at higher SiO_2 contents. This would imply that at lower amounts of SiO_2, there is some degree of networking or coiling between the mass fractal chains, but upon increasing the SiO_2 content, e.g. from 1 to 2 wt% at pH 7, the degree of coiling is decreased in the chains comprising the first structural level. The decreased

coiling may be attributed to the possibility that as the second structural level begins to form, there is not enough SiO_2 to enable the chains in the primary level to extend and coil to the same degree, resulting in shorter chains with a lower D in the first structural level. Upon further increases in the SiO_2 content, D increased again for the first structural level, indicating that the mass fractal chains had again began to coil and cross-link between each other to a greater degree.

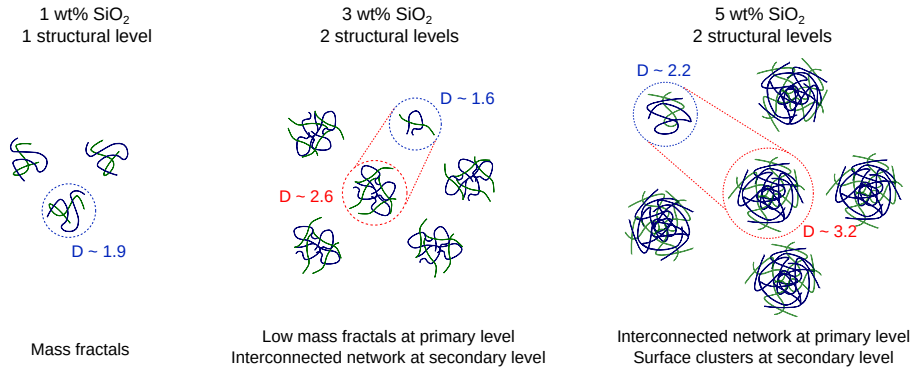

Figure 4.11. Representation of the proposed changes in the structure of the *in-situ* synthesized SiO_2 in the nanocomposites prepared at pH 7. The structures within the blue dotted circles represent the first (or only) structural level that make up the second structural level shown in the red dotted circle.

The average sizes of the clusters in the second structural level (d in Table 4.1) were quite close to the sizes shown in Figure 4.3 and exhibit similar trends with increasing filler content. However, the presence of larger agglomerates (such as those seen at pH 11, e.g. in Figure 4.1d) was not evident in the SAXS profiles due to the limitation of the measured q range. This may explain why in the case of the nanocomposite prepared at pH 11 with a reduced amount of APTES (1:30 APTES:DGEBA mass ratio), the cluster size obtained from the SAXS measurements was ~32 nm, whereas from the TEM images they were observed to be closer to ~110 nm. However, the SAXS profile for this sample shows only one knee-like feature at low q, and is missing the feature at higher q that is observed in the corresponding nanocomposite with 1:10 APTES:DGEBA mass ratio. It could be possible that this Guinier-knee at low q corresponds with the primary structural level in these nanocomposites where the dispersion is poorer, and that an additional knee may be present at even lower q (beyond the range of the measurement) that corresponds to the agglomerates observed in Figure 4.9b. Based on the consistency of the dispersion observed in several

TEM images, the agglomeration is significantly less at lower SiO_2 contents, and becomes more prevalent at 5 wt% of SiO_2. When the amount of APTES was reduced at pH 7, the only significant change in the dispersion was in L_f, which increased as it did at pH 11. No significant change was observed in the cluster sizes, however, whereas at pH 11 larger clusters and agglomerates formed due to the reduction of the APTES.

The changes in the pre-factors in Equation (3.1), *G* and *B*, can also shed some light on the structure of the SiO_2. For the first structural level, *G* exhibited little change with filler content, which implies a lack of change in both the cluster numbers comprising the first structural level, and in the cluster volume. For the second structural level, however, *G* generally increased significantly, corresponding to an increase in both the number of particles and the cluster volume. This increase is expected, since larger and more numerous clusters form with increased SiO_2 content, resulting in a larger volume. *B* is generally proportional to the cluster or particle surface area, and therefore inversely proportional to the cluster or particle size. Therefore, the changes in *B* observed in Table 4.1 are also usually consistent with the increasing size of the clusters in the second structural level with increasing SiO_2 content.

4.1.4.3 Growth mechanism of the SiO_2 during synthesis

The changes in the SiO_2 structure with filler content suggest an evolution in the growth mechanism as more of the SiO_2 precursor (TEOS) is added, changing from an initial "cluster-cluster" growth model to a "monomer-cluster" growth model. The proposed changes in the growth mechanism are illustrated in Figure 4.12. The NMR spectra in Figure 4.7c show that there are few Q^0 groups present in the nanocomposites, meaning that most of the TEOS monomers have reacted completely. However, there is a larger number of Q^3 and Q^4 groups than Q^1 and Q^2. This distribution of the different Q groups suggests that the primary growth mechanism in the initial stages is "cluster-cluster", with a strong hydrolysis and slow condensation in the limited number of TEOS monomers [14]. In this mechanism, a "sea" of monomers forms a collection of clusters, via "random walk" movements, which condense with each other. This results in the formation of more open mass-fractal structures due to the slow hydrolysis resulting in longer, polymer-like chains of Si-O-Si links, as reflected in the *D* in Table 4.1 for low SiO_2 contents. The cluster-cluster growth occurs when there is a limited source of monomers, and most condensation occurs preferentially between Q^0 and Q^1 species until the monomers are depleted [14]. As a result, a large number of Q^2 and Q^3 species form.

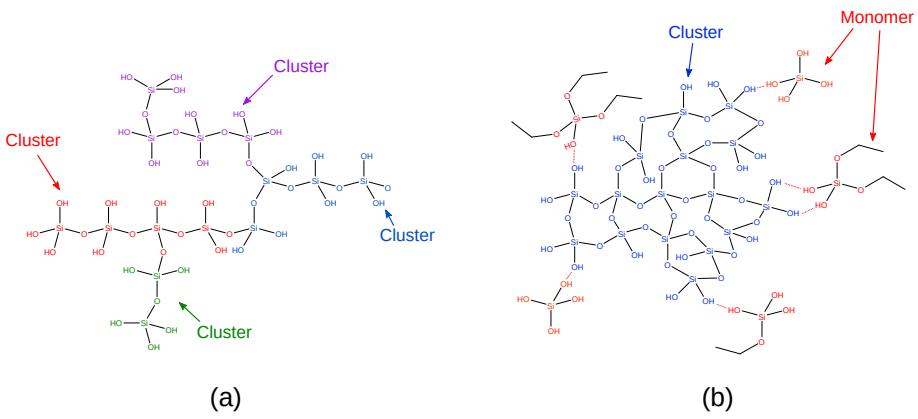

Figure 4.12. Schematic showing the proposed **(a)** cluster-cluster and **(b)** monomer-cluster growth mechanisms.

As the SiO_2 content is increased using a larger amount of TEOS, a "monomer-cluster" mechanism overtakes the "cluster-cluster" growth process [14], since the monomers are not longer depleted after the initial cluster-cluster growth. This growth mechanism results in more closed and compact SiO_2 structures with surface fractals. In the monomer-cluster growth, a continual source of monomers is required which condense preferentially with already formed clusters, resulting in an increase in the number of Q^4 species and decrease in Q^1 and Q^2 species.

The growth mechanism should be affected by the pH of the system during synthesis. The cluster-cluster growth is promoted at lower pH due to the increase in the hydrolysis rate, and the monomer-cluster growth is promoted at higher pH due to the increase in the condensation rate [14]. The change in the hydrolysis and condensation rates does not affect the total degree of condensation ($[\alpha_{Si}]$), which remains relatively constant at all pH values. However, the similarity in the changes in D and the observed morphologies from TEM indicate that the hydrolysis and condensation rates are not affected as strongly by the pH as expected. This may be due to the fact that the reactions are not proceeding in a completely aqueous environment, since all the precursors are mixed in the epoxy resin. Due to the higher viscosity of the resin compared to aqueous solutions, the mixing and subsequent reactions of the precursors might be diffusion-limited. Diffusion-limited growth results in structures with D~2.5 and D~1.8 for monomer-cluster and cluster-cluster growth, respectively [14]. This appears to be the case when small amounts of TEOS are used (low SiO_2 content), as seen in Table 4.1. Upon increasing the amount of TEOS (higher SiO_2

contents), it is likely that the growth mechanisms become reaction-limited, as a larger number of TEOS monomers are available and do not need to diffuse as far, resulting in higher values of D (~3 and ~2.1 for monomer-cluster and cluster-cluster growth, respectively [14]).

To summarize, there is an evolution in the growth mechanism, independent of pH, from cluster-cluster growth at low amounts of TEOS to monomer-cluster growth at high amounts of TEOS. This change leads to a similar evolution in the fractal morphologies of the synthesized SiO_2, forming open mass fractals at low SiO_2 contents to closed surface fractals (but not smooth particles) at higher SiO_2 contents. It is also likely that the processes change from being diffusion limited to reaction limited as the amount of TEOS monomers is increased. However, it is possible that at pH 11 the monomer-cluster growth occurs at an earlier point than in the nanocomposites prepared at pH 2 or 7, due to the formation of larger agglomerates. This is also observed when the amount of APTES is reduced (Figure 4.9) at both pH 7 and 11, and the SiO_2 at pH 11 forms larger clusters than those at pH 7.

4.1.4.4 Challenges in the analysis of the TEM and SAXS data

Although L_f is a useful tool for quantifying the state of dispersion, there are certain limitations in its implementation. Firstly, L_f is measured using two-dimensional images, and it is unknown how representative this is for a three-dimensional volume of material. The correlation lengths (ξ) between the SiO_2 clusters were determined from the q range of the features in Figure 4.4 and Equation (3.5). ξ was estimated to be ~4.2-6.3 nm and ~25-42 nm for the primary and secondary structural levels, respectively. The estimated values of ξ were significantly smaller than the L_f calculated for the different nanocomposites (53-200 nm, depending on composition or synthesis conditions). Therefore, it is possible that L_f is overestimated. Another potential source of error is in the conversion of the TEM images to the binary images upon which the calculation is performed, since the image thresholds are adjusted manually. The estimation of L_f can therefore be made more accurate and statistically significant by using more images (e.g. 10-15 instead of 3-5).

The fits of the SAXS data to both the unified model and the Guinier and power-law models can be improved with a wider q range in the measurements, which could reveal the presence of any additional structural levels at both lower and higher q. Lysenkov et al. [213] reported a similar hierarchical structure of SiO_2 nanoparticles when synthesized *in situ* using a non-aqueous route, but with three structural levels instead of two. The third level possessed a mass fractal organization of the SiO_2 clusters. In addition, the clusters and agglomerates

formed were larger than those observed in Figure 4.1, but exhibited similar trends in D and R_g as seen in Table 4.1. Therefore, the performance of SAXS measurements over a wider q range is recommended for a more detailed analysis of the structural organization of the *in-situ* synthesized SiO_2. An additional step would be to include a structure factor when performing the fits to the unified model, since then the interactions between the particle clusters will be taken into account.

Despite these limitations, the techniques used in this work are, however, still useful for identifying trends in the dispersion quality. It is therefore important to corroborate results independently from multiple methods. Both the calculated values from SAXS (correlation lengths and cluster sizes) and from the TEM images (L_f and cluster sizes) show consistent trends, showing that that the distance between the SiO_2 clusters, the sizes of the clusters themselves, and the frequency of agglomeration increased with increasing SiO_2 content. The changes in L_f also highlight the importance of the amount of SCA that is used in the synthesis.

4.2 Dielectric properties of the epoxy-SiO_2 nanocomposites

In this chapter, the dielectric properties of the epoxy nanocomposites prepared with APTES are presented. Due to the agglomeration and poor dispersion of the SiO_2 in nanocomposites prepared without APTES and with GPTMS, the dielectric properties of those materials were not investigated further.

4.2.1 The complex permittivity at room temperature

Figure 4.13 presents the real relative permittivities (ϵ_r') and dielectric loss tangents (tan δ) for epoxy-SiO_2 nanocomposites prepared at both pH 7 and 11. The nanocomposites were prepared using an APTES:DGEBA mass ratio of 1:10, but those with 5 wt% were also prepared using a reduced amount of APTES (mass ratio of 1:30). For nanocomposites prepared at pH 7 (Figure 4.13a), the real permittivity (ϵ_r') increased with increasing SiO_2 content up to 3 wt% SiO_2. Nanocomposites with 5 wt% SiO_2 exhibited a lower permittivity than pure epoxy. Changing the APTES:DGEBA mass ratio from 1:10 to 1:30 for 5 wt% SiO_2 did not lead to any significant change in ϵ_r'.

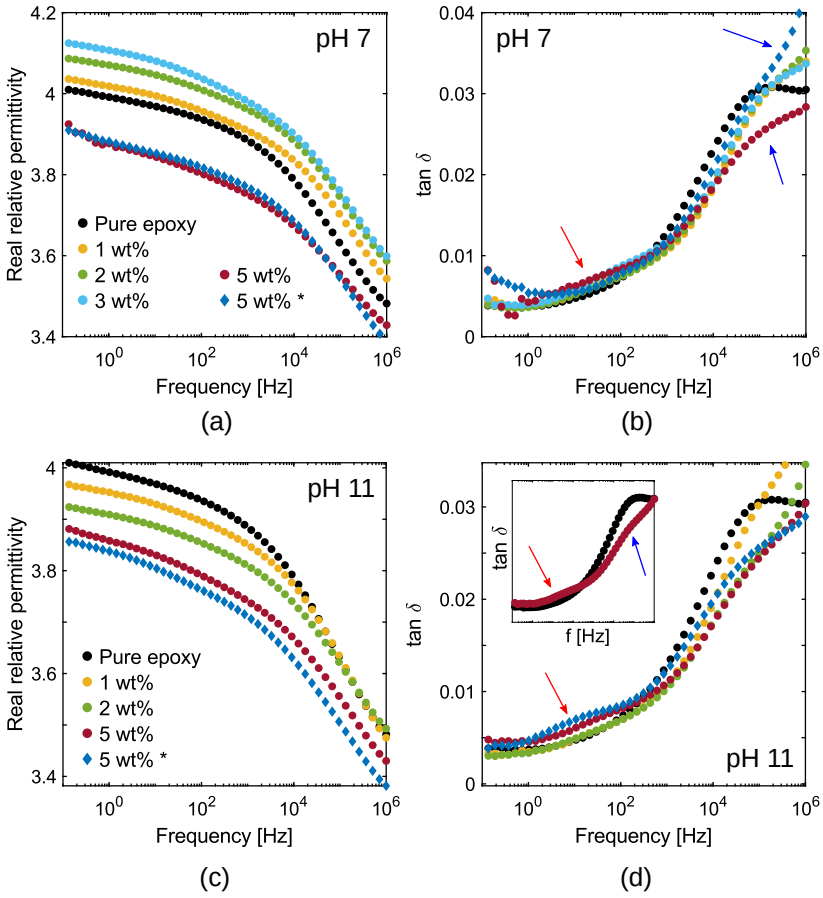

Figure 4.13. The **(a,c)** real relative permittivities and **(b,d)** dielectric loss tangents (tan δ) of pure epoxy and epoxy-SiO_2 nanocomposites prepared under conditions of **(a,b)** pH 7 and **(c,d)** pH 11. The * indicates composites prepared with a APTES:DGEBA mass ratio of 1:30 instead of 1:10. The inset in **(d)** highlights the differences in the relaxations between nanocomposites and pure epoxy. The blue and red arrows point to the changes in the β-relaxation and the presence of a new relaxation, respectively.

The tan δ in pure epoxy exhibited a single asymmetric peak at around 10^5 Hz for the β-relaxation. In all the nanocomposites, the β-relaxation appeared as a shoulder on a second peak that was outside the measured range (indicated by the blue arrows in Figure 4.13b and d). At pH 7, the tan δ between 10^3 and 10^5

Hz was slightly lower for all the nanocomposites than the pure epoxy. However, above 10^5 Hz tan δ was larger in the nanocomposites with 1-3 wt% SiO_2. At 5 wt%, tan δ decreased significantly in the same frequency range if sufficient APTES was used. Reducing the APTES:DGEBA mass ratio to 1:30 resulted in a subsequent increase in tan δ again, similar to that which was observed at lower SiO_2 contents. An additional feature present in the tan δ for all the nanocomposites was a new relaxation peak between 1 and 100 Hz (indicated by the red arrows in Figure 4.13b and d). Therefore, the nanocomposites exhibited a slightly higher tan δ in this region than the pure epoxy.

At pH 11, ϵ_r' decreased with increasing SiO_2 content, unlike at pH 7. Moreover, the nanocomposite prepared with a lower APTES:DGEBA mass ratio (and 5 wt% SiO_2) exhibited the lowest permittivity overall (Figure 4.13c). Changes in the tan δ were more similar to those observed for nanocomposites prepared at pH 7. The shape of the β-relaxation is altered similarly, but the tan δ in the nanocomposites is lower than that in pure epoxy over a wider frequency region. In addition, reducing the amount of APTES did not result in an increase in tan δ again, as was observed at pH 7. The new relaxation also appears to be more prominent, as shown in Figure 4.13d. The inset in the same figure highlights the major differences in the tan δ between pure epoxy and the nanocomposites, showing both the change to the β-relaxation and the new relaxation at lower frequencies. The latter can be hard to determine due to the overlap of multiple data points in the plots.

The dielectric spectroscopy performed on the nanocomposites prepared at pH 2 with APTES resulted in a lower quality of data, and is shown in Figure B.2 in the Appendix. The lower quality was attributed to the fact that these preliminary samples were thicker (5-15 mm instead of 1 mm), thereby possessing a lower capacitance which increased the error in the measurements. This led to the modification of the casting procedure which resulted in the nanocomposites that were presented in Figure 4.13.

4.2.2 Fits of the room temperature complex permittivity to the Havriliak-Negami and Dissado-Hill functions

From the tan δ in Figure 4.13, it is evident that the dielectric relaxations in the pure epoxy and the nanocomposites cannot be described as a Debye response. The real and imaginary permittivities were therefore fitted to both the Havriliak-Negami (HN) and Dissado-Hill (DH) models to quantify the deviation from the ideal Debye response. Figure 4.14 shows fits of both models to the complex permittivity of pure epoxy. The fit became poor at lower frequencies (below 1 Hz for the DH fit and 100 Hz for the HN fit) when only a single relaxation

term was used. In addition, the real permittivity was observed to continue to increase instead of flattening out (Figure 4.14a and c). The inclusion of a second relaxation term, shown in Figure 4.14b and d, optimized the fit in both models. The fits were performed in the frequency region between 10^{-1} and 10^{5} Hz.

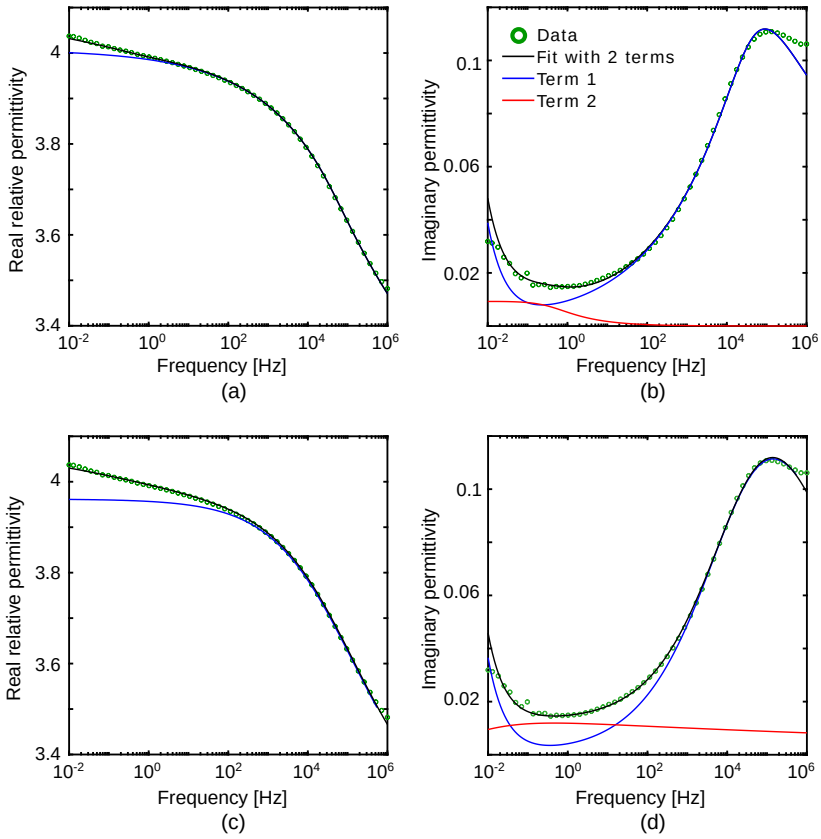

Figure 4.14. Fits of the real and imaginary permittivities of pure epoxy to the **(a,b)** Dissado-Hill and **(c,d)** Havriliak-Negami models, showing a total fit consisting of two relaxation terms, as well as the terms for each individual relaxation.

Fits of the HN and DH functions to the imaginary permittivities of selected nanocomposites are shown in Figures 4.15 and 4.16. Two relaxation terms were used for the fits, one for the β-relaxation, and one for the new relaxation between 1 and 10^3 Hz (highlighted in the inset in Figure 4.13d). The additional

term that was used in the fit for pure epoxy (shown in Figure 4.14) was not included here, since it overlaps with the new relaxation in the same frequency region. In certain samples the conductivity was higher, causing an increase in the imaginary permittivity at low frequencies (shown in Figures 4.15 and 4.16 as σ). The parameters obtained from the fits are presented in Tables 4.2 and 4.3.

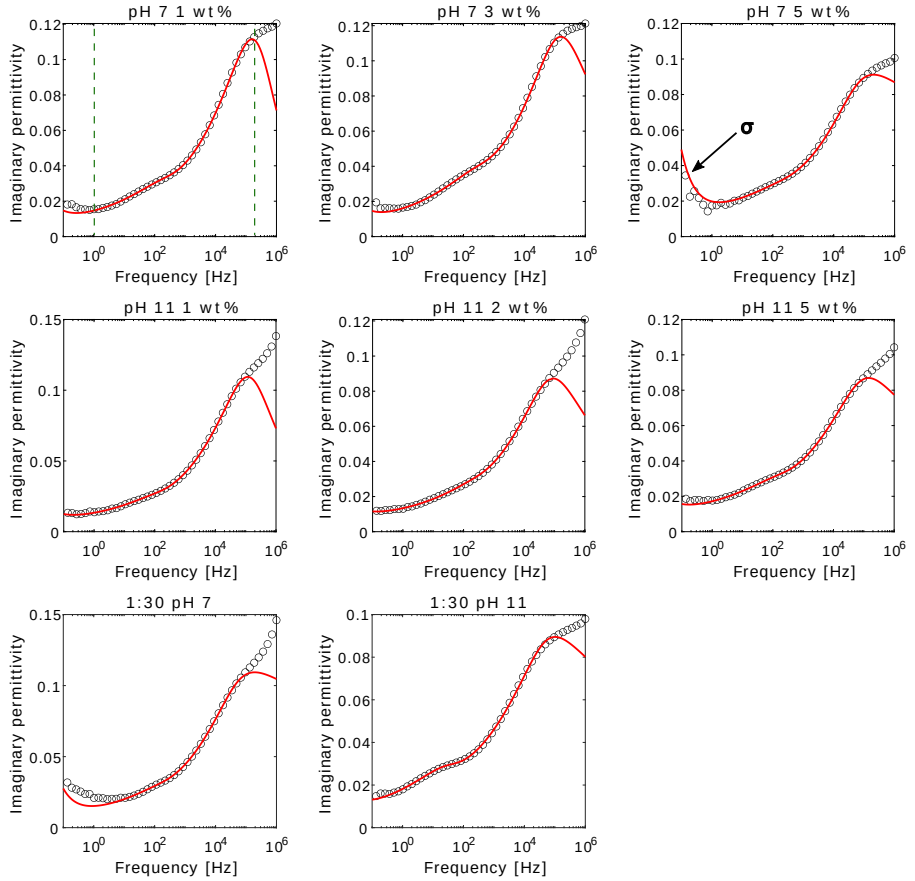

Figure 4.15. Fits of the imaginary permittivities of selected epoxy-SiO_2 nanocomposites to the Dissado-Hill function. The plots in the bottom row labelled 1:30 refer to nanocomposites prepared with an APTES:DGEBA mass ratio of 1:30 at pH 7 and 11 and with 5 wt% SiO_2. The green dashed lines in the first plot show the frequency range over which the data was fit to the function.

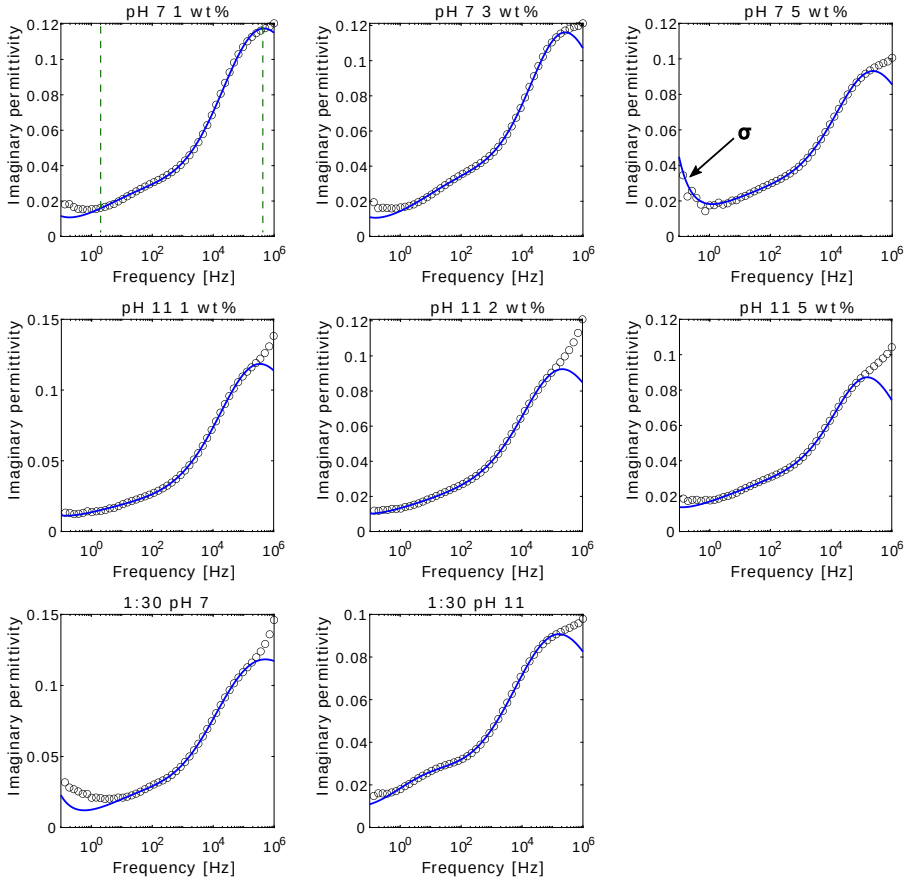

Figure 4.16. Fits of the imaginary permittivities of selected epoxy-SiO_2 nanocomposites to the Havriliak-Negami function. The plots in the bottom row labelled 1:30 refer to nanocomposites prepared with an APTES:DGEBA mass ratio of 1:30 at pH 7 and 11 and with 5 wt% SiO_2. The green dashed lines in the first plot show the frequency range over which the data was fit to the function.

Table 4.2. Parameters obtained from the fits of the imaginary permittivity of pure epoxy and epoxy-SiO_2 nanocomposites prepared in different conditions to the Dissado-Hill function.

Sample	β-relaxation				Second relaxation term			
	$\Delta\epsilon$	τ [s]	n	m	$\Delta\epsilon$	τ [s]	n	m
Pure epoxy	1.07	3.3×10^{-6}	0.89	0.25	0.62	0.36	0.49	0.01
1:10, pH 7 [a]								
1 wt%	0.55	5.6×10^{-7}	0.48	0.25	0.092	5.8×10^{-4}	0.014	0.080
3 wt%	0.76	1.1×10^{-6}	0.78	0.25	0.099	5.1×10^{-4}	0.30	0.11
5 wt%	1.34	2.3×10^{-6}	0.94	0.24	0.44	9.9×10^{-4}	0.48	0.014
1:10, pH 11 [b]								
1 wt%	0.60	1.1×10^{-6}	0.66	0.26	0.15	1.1×10^{-3}	0.01	0.032
2 wt%	0.63	2.1×10^{-6}	0.81	0.24	0.36	5.3×10^{-4}	0.01	0.014
5 wt%	0.89	1.9×10^{-6}	0.89	0.21	0.22	7.5×10^{-4}	0.05	0.025
1:30, 5 wt% SiO_2 [c]								
pH 7	1.77	3.0×10^{-6}	0.95	0.25	0.11	8.5×10^{-4}	0.01	0.044
pH 11	1.11	3.3×10^{-6}	0.2	0.20	0.05	4.1×10^{-3}	0.01	0.16

[a] Nanocomposites prepared at pH 7 with APTES:DGEBA mass ratio of 1:10.
[b] Nanocomposites prepared at pH 11 with APTES:DGEBA mass ratio of 1:10.
[c] Nanocomposites prepared with APTES:DGEBA mass ratio of 1:30 and 5 wt% SiO_2.

According to the fits to the DH model (Table 4.2), the relaxation time (τ) for the β-relaxation is generally lower in the nanocomposites compared to the pure epoxy. Reduction in the amount of APTES, however, results in a higher τ compared to nanocomposites prepared with more APTES. The relaxation strength ($\Delta\epsilon$) initially decreased for low filler contents, but increased with subsequent increases in the filler content at both pH 7 and 11. However, reducing the APTES:DGEBA mass ratio resulted in a decrease in $\Delta\epsilon$. The indexes n and m are the shape parameters for the relaxation loss peak in the DH function. m for the β-relaxation shows relatively little variation, with only a small decrease with increasing filler content. n, however, exhibits a relatively large decrease initially at low SiO_2 content, but increases with increasing amount of SiO_2. An exception is observed when the amount of APTES is reduced at pH 11, which resulted in the largest decrease in n.

The second relaxation term used for the fits are not the same for the pure epoxy and the nanocomposites, as these are most probably two different relaxations

in the same frequency region. However, the changes in the parameters for the different nanocomposites can be compared with each other to evaluate how the dipoles in this new relaxation are behaving. The second relaxation in the nanocomposites exhibited a decrease in τ when the filler content was increased to 2 or 3 wt%, but then τ increased at 5 wt% SiO_2. The opposite behaviour is observed for $\Delta\epsilon$. n usually increased with increasing amount of SiO_2, although this was significantly less at pH 11. Reducing the amount of APTES resulted in very low values of n. No consistent trends could be identified for m.

Table 4.3. Parameters obtained from the fits of the imaginary permittivity of pure epoxy and epoxy-SiO_2 nanocomposites prepared in different conditions to the Havriliak-Negami function.

Sample	**β-relaxation**				**Second relaxation term**			
	$\Delta\epsilon$	τ **[s]**	α	β	$\Delta\epsilon$	τ **[s]**	α	β
Pure epoxy	0.71	3.3×10^{-6}	0.43	0.62	0.32	62.1	0.55	0.055
1:10, pH 7 [a]								
1 wt%	0.81	1.2×10^{-6}	0.44	0.54	0.13	3.6×10^{-3}	0.37	1
3 wt%	0.67	1.3×10^{-6}	0.48	0.65	0.17	1.6×10^{-3}	0.36	1
5 wt%	0.54	1.3×10^{-6}	0.46	0.66	0.17	2.0×10^{-3}	0.30	1
1:10, pH 11 [b]								
1 wt%	0.75	1.3×10^{-6}	0.45	0.59	0.15	1.4×10^{-2}	0.30	0.67
2 wt%	0.55	1.9×10^{-6}	0.46	0.58	0.19	3.2×10^{-3}	0.26	0.76
5 wt%	0.42	1.8×10^{-6}	0.51	0.65	0.25	8.3×10^{-4}	0.25	1
1:30, 5 wt% SiO_2 [c]								
pH 7	1.11	3.9×10^{-6}	0.44	0.31	0.09	4.5×10^{-3}	0.43	1
pH 11	0.67	2.7×10^{-6}	0.39	0.65	0.11	2.1×10^{-2}	0.42	1

[a] Nanocomposites prepared at pH 7 with APTES:DGEBA mass ratio of 1:10.
[b] Nanocomposites prepared at pH 11 with APTES:DGEBA mass ratio of 1:10.
[c] Nanocomposites prepared with APTES:DGEBA mass ratio of 1:30 and 5 wt% SiO_2.

According to the fits to the HN model (Table 4.3), the same changes were observed as in the DH model for τ of the β-relaxation. The opposite behaviour was observed in the relaxation strength, as there was an increase in $\Delta\epsilon$ followed by a subsequent decrease with increasing SiO_2 content. In this model, α and β are used as the width and asymmetry parameters, respectively. α was generally slightly larger for the nanocomposites compared to pure epoxy (one exception

being the nanocomposite prepared with less APTES at pH 11). β usually exhibited a decrease initially at low SiO_2 content, but then increased again with increasing SiO_2 content.

The parameters for the new relaxation in the nanocomposites obtained from the HN model also showed different trends to those obtained from the DH model. τ generally decreased with increasing SiO_2 content, whereas $\Delta\epsilon$ increased with increasing SiO_2 content. α decreased with increasing SiO_2 content, and the decrease was more significant at pH 11. However, reduction in the amount of APTES led to a smaller decrease in α at both pH 7 and 11. At pH 7 (or with a lower amount of APTES), β was unchanged at a value of 1; at pH 11 however, β was initially lower at low SiO_2 content, but increased to 1 with increasing amount of SiO_2.

4.2.3 Complex permittivity above room temperature

At temperatures approaching the glass transition and above, the complex permittivity of epoxy and its nanocomposites exhibited significant increases in both the real relative permittivity and the imaginary permittivity. Figures 4.17 and 4.18 show the the real relative permittivities (ϵ'_r) for selected nanocomposites prepared at pH 7 and 11, respectively, at different temperatures. The permittivity for pure epoxy at higher temperatures is included in Figure 4.17.

In pure epoxy, an α-relaxation emerged above 80 °C, which shifted to higher frequencies with increasing temperature. Additionally, ϵ'_r increased significantly at low frequencies (below 10 Hz) and above 120 °C. The nanocomposites exhibited similar changes in the permittivity, but with a few differences. At lower filler contents (e.g. 1 wt%), the α-relaxation was observed at a lower temperature, and the subsequent increase in the permittivity was also observed at a lower temperature. This was more significant at 1 wt% than at 2 wt% SiO_2, as seen in Figure 4.17 - ϵ'_r reached ~1000 for 1 wt% SiO_2, but only ~70 in 2 wt% SiO_2 at 90 °C and 10^{-2} Hz, compared to 7 for pure epoxy at the same frequency and temperature.

For higher filler contents (5 wt%), the α-relaxation was observed at the same temperature as for pure epoxy. Subsequently, the increase in ϵ'_r at 5 wt% SiO_2 was substantially less than at 1 and 2 wt% SiO_2. In all the nanocomposites however, the real permittivity above 120 °C exceeded that of pure epoxy by at least an order of magnitude. For example, in pure epoxy ϵ'_r reached ~5000 at 200 °C whereas for 5 wt% SiO_2 at pH 7, a value of ~10^5 was observed (Figure 4.17).

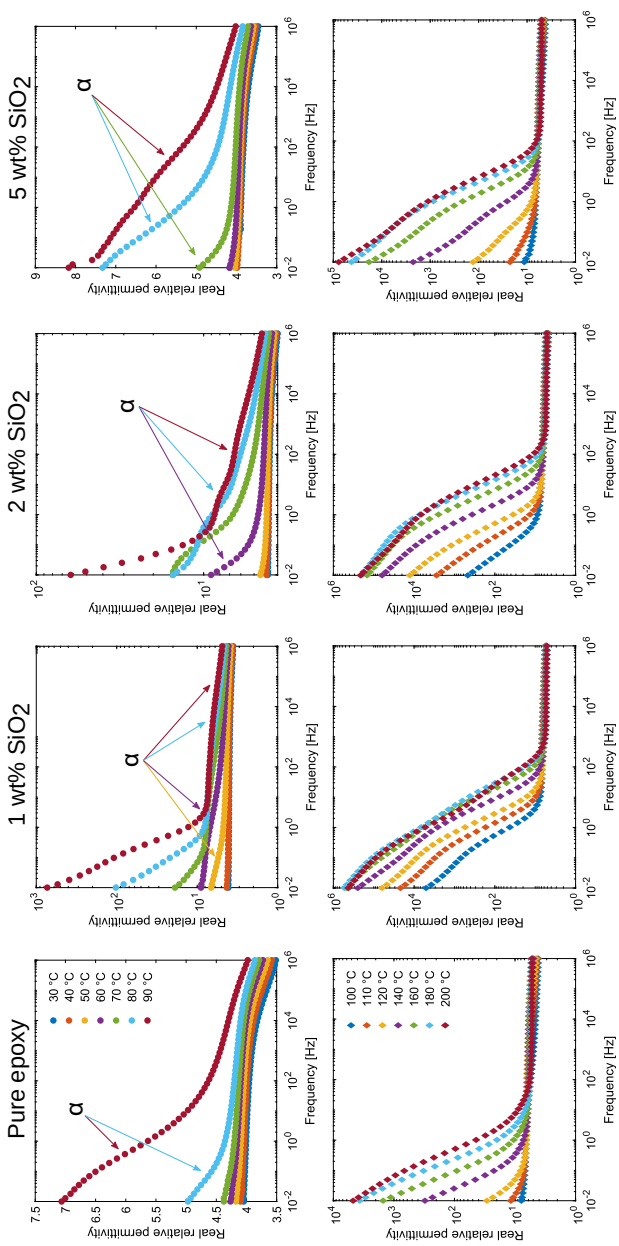

Figure 4.17. The real relative permittivities in the ranges 30-90 °C (top row) and 100-200 °C (bottom row) for pure epoxy and selected epoxy-SiO_2 nanocomposites prepared at pH 7 with an APTES:DGEBA mass ratio of 1:10. The arrows point to the α-relaxation at different temperatures.

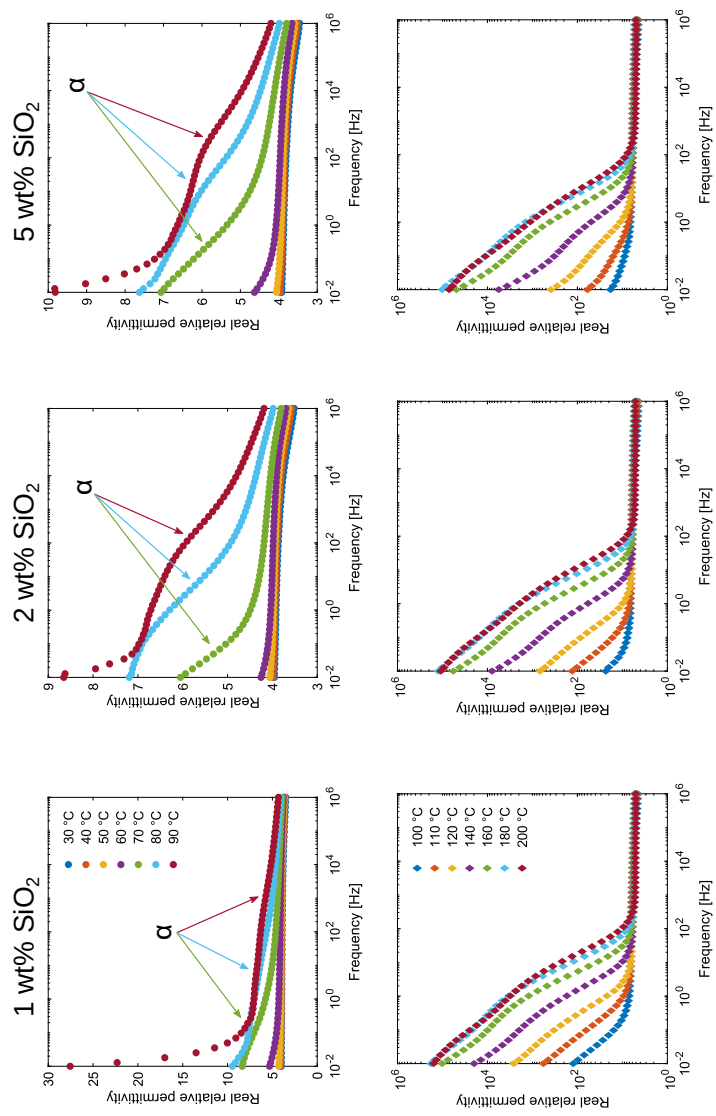

Figure 4.18. The real relative permittivities in the ranges 30-90 °C (top row) and 100-200 °C (bottom row) for pure epoxy and selected epoxy-SiO_2 nanocomposites prepared at pH 11 with an APTES:DGEBA mass ratio of 1:10. The arrows point to the α-relaxation at different temperatures.

Similar changes were observed for the nanocomposites prepared at pH 11, as seen in Figure 4.18. While the α-relaxation emerged at slightly lower temperatures (60-70 °C), the increase in ϵ_r' at temperatures below 100 °C was not as high as it was in nanocomposites prepared at pH 7. Above 100-120 °C, ϵ_r' exhibited a significant increase at low frequencies, and exceeded the values displayed by pure epoxy at the same temperatures.

Figure 4.19 shows the imaginary permittivity (ϵ_r'') as a function of temperature for pure epoxy and nanocomposites with 5 wt% SiO_2. The black arrows point to the tan δ "peak" for the α-relaxation. As seen from the bottom row in Figure 4.19, at temperatures above 100 °C ϵ_r'' increased significantly at low frequencies, although the point of increase and the peak for the α-relaxation shifted to higher frequencies with increasing temperatures. Due to the substantial increase in ϵ_r'', the α-relaxation became obscured and "flatter" in the plots. The red arrows point to the regions where the slope of the imaginary permittivity approached -1. The increase in imaginary permittivity was significantly higher in the nanocomposites than in pure epoxy.

Figure 4.20 shows the imaginary permittivities of nanocomposites prepared with an APTES:DGEBA mass ratio of 1:30 at pH 7 and 11 (both with 5 wt% SiO_2). The same trends in the imaginary permittivity emerged with increasing temperature in these nanocomposites. However, the increase in ϵ_r'' was not as high at pH 11 when compared to the corresponding nanocomposite prepared with more APTES (APTES:DGEBA mass ratio of 1:10, shown in Figure 4.19). However, the increase in ϵ_r'' was higher for the nanocomposite prepared at pH 7 with a reduced amount of APTES. Similar observations as those made above are found on comparing the real permittivities at higher temperatures as well. ϵ_r' in the nanocomposites was higher at pH 7 and lower at pH 11 when the amount of APTES was reduced.

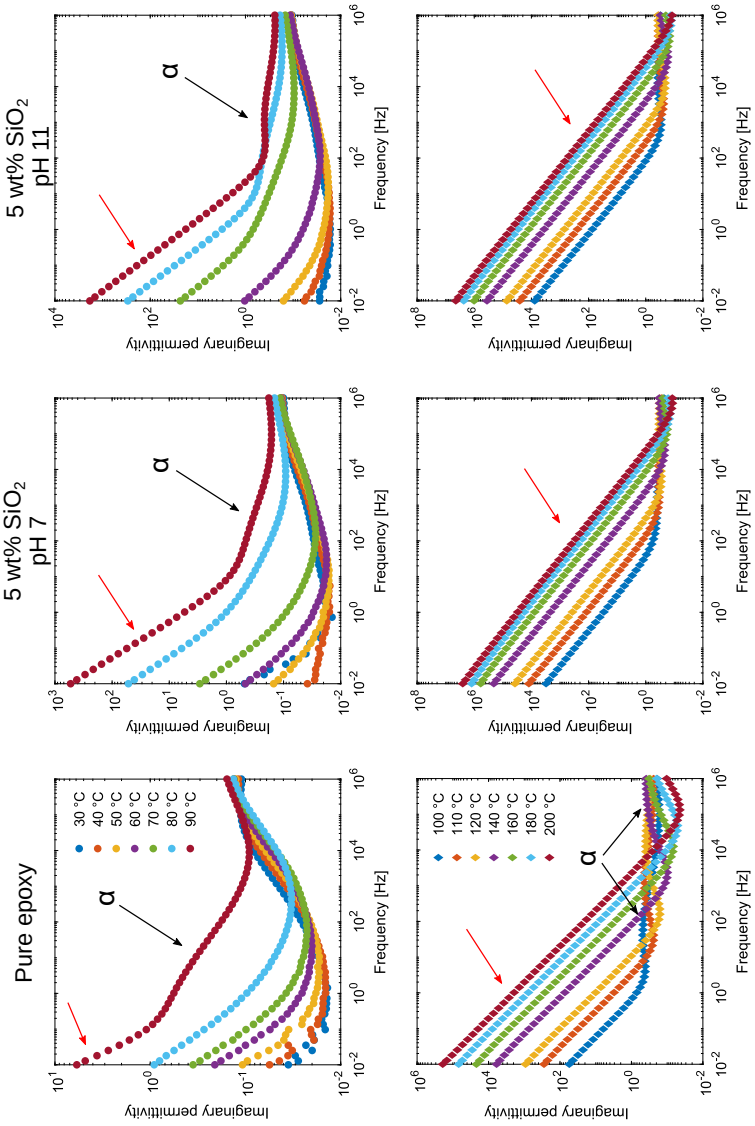

Figure 4.19. The imaginary permittivities in the ranges 30-90 °C (top row) and 100-200 °C (bottom row) for pure epoxy and epoxy-SiO_2 nanocomposites (5 wt%) prepared at both pH 7 and 11 with an APTES:DGEBA mass ratio of 1:10. The black arrows show the α-relaxation, and the red arrows point to where the slope of ϵ_r'' is ~-1.

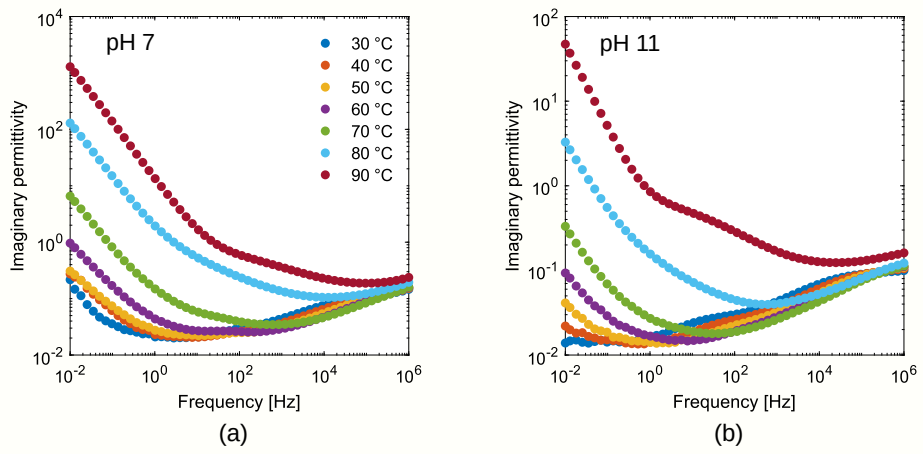

Figure 4.20. Comparison of the imaginary permittivities from 30-90 °C for epoxy-SiO_2 nanocomposites (5 wt%) prepared with an APTES:DGEBA ratio of 1:30 at **(a)** pH 7 and **(b)** pH 11.

4.2.4 Discussion

4.2.4.1 Complex permittivity at room temperature

The most noticeable effects of the inclusion of the nanoparticles are manifested in the changes in the β-relaxation, as well as the introduction of the new dielectric relaxation at low frequency. Several authors have reported the emergence of a similar relaxation on the inclusion of nanoparticles in epoxy, albeit sometimes in different frequency ranges. Yeung and Vaughan [142] reported a relaxation peak emerging at 0.1 Hz in ϵ_r'' when unmodified SiO_2 nanoparticles were added to epoxy, and attributed this relaxation to adsorbed water at the nanoparticle surface. Alhabil et al. [214] reported a relaxation in epoxy-Si_3N_4 nanocomposites between 0.1 and 10 Hz, although this was present only for 2 wt% of Si_3N_4 and not for 5 wt%. Singha and Thomas [4] reported a significant increase in tan δ for nanocomposites with 10 wt% of TiO_2 nanoparticles which also showed a peak around 10^3 Hz. Therefore, it appears that any relaxations associated with the nanoparticles tend to emerge between 0.1 and 10^3 Hz, indicating that the dipoles involved in these relaxations are "stiffer" than the O-H associated with the β-relaxation. The new relaxation may therefore correspond to dipoles on the SiO_2 clusters that are more restricted in their movements, and cannot keep up with the electric field switching at higher frequencies.

The β-relaxation is strongly affected in all the nanocomposites, indicating that there are some interactions between the SiO_2 and the O-H on the epoxy chains. For example, the formation of hydrogen bonds between the O-H on the DGEBA and the silanol (Si-OH) groups on the particle surface, or even weak van der Waal's interactions, could be present at the interfaces. The strength of the β-relaxation is also influenced by the cross-linking density of the epoxy network [214], which could be affected by the presence of the SiO_2. It is possible that the incorporation of the nanoparticles has resulted in an additional relaxation at frequencies above 10^6 Hz, and the β-relaxation now appears as a shoulder on this new relaxation. Possible sources for this relaxation include the N-H dipoles in unreacted APTES molecules or partially cross-linked APTES with DGEBA, or uncondensed Si-OH and Si-O-C in alkoxides. Another alternative is that the relaxation above 10^6 Hz was already present, and that adding the nanoparticles has resulted in the relaxation shifting to a lower frequency. This option is highly unlikely, however, as the only other relaxation reported for epoxy at higher frequencies are associated with localized intramolecular motions of the epoxide groups [109], which should be absent in cured epoxy resins.

Generally a reduction in the permittivity at all frequencies (as seen in Figure 4.13c) implies that there are fewer dipoles in general that can respond to the electric field, whereas an increase (as seen in Figure 4.13a) implies the opposite and that the material has become more polarizable. Hence, the nanoparticles appear to have different effects on the permittivity depending on the filler content and the pH conditions during synthesis. At pH 7, the SiO_2 structures initially appear to make the epoxy more polarizable, but beyond a certain SiO_2 content (> 3 wt%) the nanocomposite becomes much less polarizable than pure epoxy. Meanwhile at pH 11, the nanocomposite becomes less polarizable consistently with increasing SiO_2 content.

4.2.4.2 Application of the Havriliak-Negami and Dissado-Hill functions

Fits of the imaginary permittivity (ϵ_r'') to the Havriliak-Negami (HN) and Dissado-Hill (DH) functions were performed to allow quantitative comparisons between the different nanocomposites. The inclusion of the additional relaxation term in pure epoxy below the β-relaxation results in a better fit to both models (as seen in Figure 4.14). However, the origin for this relaxation in the pure epoxy is unknown, and its shape appears to be quite different in the DH and HN models. This second relaxation term in the fits for the pure epoxy coincides with the new relaxation that emerges in the nanocomposites, which does in fact present a subtle peak in tan δ and in ϵ_r''. Additionally, a conductivity term must be included to model the increase in ϵ_r'' at low frequencies. Another challenge in fitting the data to both the models is the presence of dipole relaxations beyond

the measurement range, necessitating boundaries to the frequency range of that data that is fitted (shown by the green dashed lines in Figures 4.15 and 4.16). However, one risks eliminating the influence of these dipole responses on the parameters obtained from the fits. This is most relevant for the β-relaxation, as this relaxation appears as a shoulder on another relaxation that could not be included in the fit.

Bearing all this in mind, it is still possible to extract useful information from the trends observed in the various parameters for the nanocomposites. A common feature in both models is the shift of the β-relaxation to higher frequencies (lower τ), meaning that the O-H dipoles in the cross-linked DGEBA chains are less stiff in the nanocomposites than in the pure epoxy. This effect is diminished when the amount of APTES is reduced in the nanocomposites, which suggests that the influence of either the particle dispersion, or the effect of the APTES itself, on the O-H dipoles is reduced. The changes in the n parameter in the DH model indicate an eventual increase in the ordering within the dipole clusters for the β-relaxation with sufficiently high SiO_2 content. These effects are illustrated in Figure 4.21, where the presence of homogeneously dispersed SiO_2 structures increases the degree of ordering within the dipole clusters, which consist of DGEBA chains that exhibit cooperative behaviours during relaxation. The increased ordering in these clusters is consistent with the observed changes in the β and α parameters in the HN model, which show that the distribution of relaxation times for the O-H dipoles become slightly narrower and more symmetric with increasing SiO_2 content. At low SiO_2 contents, or when the dispersion is poor, the O-H dipole clusters were more disordered than in pure epoxy.

For the new relaxation at a lower frequency, increasing the amount of SiO_2 resulted in a broader relaxation peak according to the HN model. The wider distribution of relaxation times may be expected when more varied and different SiO_2 morphologies form with both mass and surface fractal structures. Reducing the amount of APTES has the opposite effect, which may be attributed to more similar dipoles being present in larger SiO_2 agglomerates. The parameters obtained from the DH model suggest that the dipole clusters for the new relaxation are usually disordered. Increasing the SiO_2 content can lead to an increase in the ordering of these dipoles, in a trend similar to the effect seen in the β-relaxation.

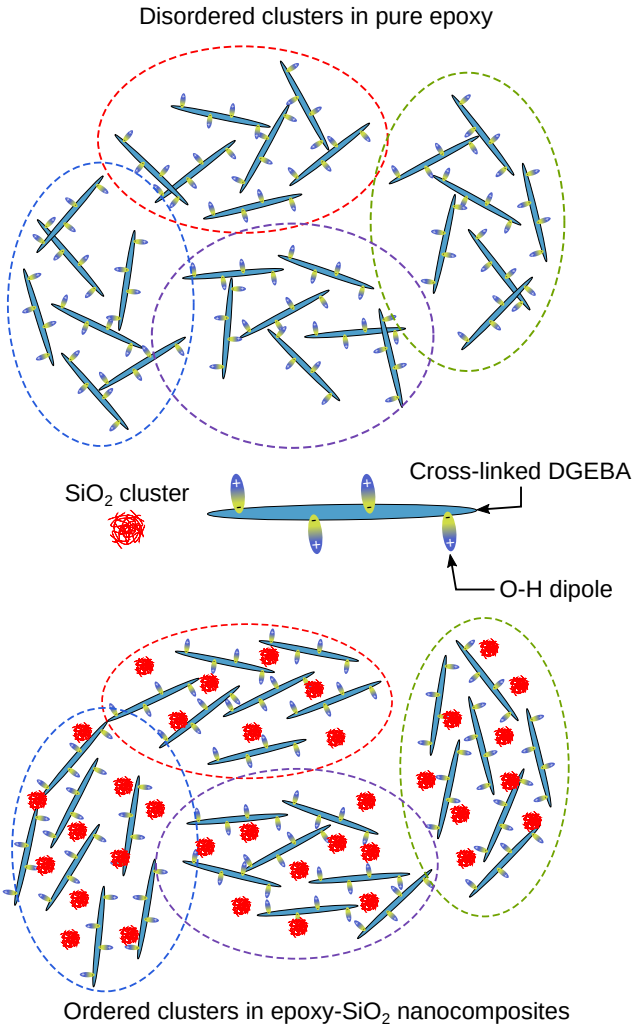

Figure 4.21. Illustration of the dipole clusters in (top) pure epoxy and (bottom) epoxy-SiO_2 nanocomposite, showing the O-H dipoles on cross-linked DGBEA chains. The organization of the dipoles in the clusters (which are shown by the dotted lines), are affected by the presence of homogeneously dispersed SiO_2 clusters.

The fits to the two models presents a contradiction when considering the effect of the SiO_2 on the strength ($\Delta\epsilon$) of the β-relaxation. A visual evaluation of

the tan δ in Figure 4.13b and d indicates that the β-relaxation is weaker in the nanocomposites, especially at 5 wt% where the tan δ peak is smaller than that of pure epoxy. This observation is consistent with the obtained values of $\Delta\epsilon$ from the HN model, where $\Delta\epsilon$ decreased with increasing SiO_2 content. Fits to the DH model, however, gave values of $\Delta\epsilon$ which showed the opposite trend with increasing SiO_2 content. However, the height and symmetry of a peak in ϵ_r'' is also determined by the α/β or n/m parameters in the HN and DH models, respectively. It is difficult to determine what $\Delta\epsilon$ should be from the ϵ_r' since no measurements were taken above 10^6 Hz, which will therefore introduce some uncertainty into the parameters obtained from the fits.

4.2.4.3 Complex permittivity at higher temperatures

Usually above 50 °C more pronounced changes were observed in the complex permittivity for the different nanocomposites. A common feature is the shift of the observed relaxations to higher frequencies with increasing temperature. This increase is expected due to the increased mobility of the epoxy chains as the glass transition is approached. The movements along the chain are no longer restricted and the various dipoles can respond more easily to the switching of the electric field at higher frequencies. At the glass transition, the epoxy becomes more rubbery and the movement of entire molecular segments, instead of just smaller groups along the chain, will become the primary dielectric relaxation. Therefore, the α-relaxation observed in Figures 4.17 and 4.18 corresponds to the glass transition, and the emergence of the α-relaxation shows at which temperature the glass transition begins. The beginning of the transition is more dependent on the SiO_2 content at pH 7 than at pH 11, and is generally earlier in nanocomposites with a low amount of SiO_2.

As the temperature is increased further beyond the glass transition, the α-relaxation also shifts to higher frequencies and the β-relaxation disappears, as the O-H dipoles are no longer the prominent dipole due to the increased flexibility of entire segments of the epoxy chains. The real permittivity does not flatten out at lower frequencies after the α-relaxation, but instead continues to increase rapidly. The α-relaxation then appears as a shoulder on what appears to be an additional, massive dielectric relaxation. This is not, however, an actual relaxation since ϵ_r' just continues to increase indefinitely to extremely high values and there is no corresponding loss peak.

As seen in Figure 4.19, ϵ_r' and ϵ_r'' both increased substantially at low frequencies above the glass transition. The slope of the increase in ϵ_r'' (~-1) indicates that this behaviour is indicative of charge transport [215], but is not a case of DC conductivity since ϵ_r' is not independent of frequency [110]. This simulta-

neous increase in both the real and imaginary permittivities resemble the low frequency dispersion (LFD) effect, as no loss peak is observed and the dielectric response is strongly frequency dependent in the low-frequency region. Dissado and Hill also refer to this as 'quasi-DC' (QDC) due to it resembling the DC conductivity [108,216]. This quasi-DC behaviour can be observed in both the epoxy and the nanocomposites, as shown in Figure 4.22, although the effect is stronger in the nanocomposites. The conductivity is seen to decrease with decreasing frequency, and deviates from the red dashed line which it would have followed if it was independent of frequency.

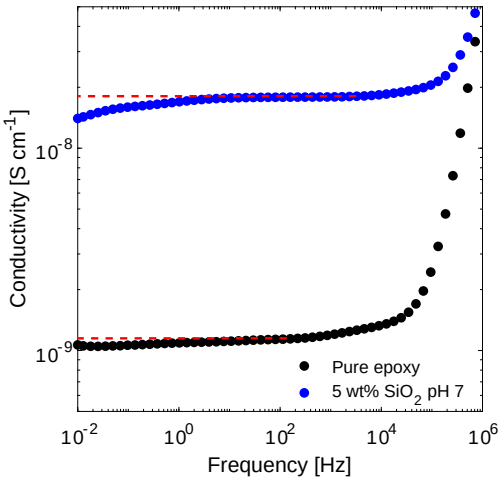

Figure 4.22. Comparison of the conductivities of pure epoxy and nanocomposite with 5 wt% SiO_2 (prepared at pH 7) at 200 °C. The straight, red-dashed lines are used to check if the conductivity is frequency independent or not.

The LFD effect in pure epoxy is most likely caused by the presence of Na^+ and Cl^- that are remnant from the synthesis of the DGEBA monomers. The concentration of these ions is low, but enough to cause charge transport at sufficiently high temperatures (above the glass transition) when the epoxy becomes more rubbery and ion mobility is increased. Several other works have also reported this phenomenon in pure epoxy and in epoxy nanocomposites [139, 142, 148, 160, 214,215]. Jonscher [108] stated that the LFD effect would also be responsible for an increase in the real susceptibility (χ') at low frequencies, which corresponds with the increase observed in ϵ_r'. However, Fuqiang et al. [215] and Huang et al. [158] have attributed the increase in ϵ_r' to an electrode polarization (EP) effect, where ion blockage occurs at the electrode-sample interface. The blockage would be caused by the same ions responsible for the LFD effect, so it is possible

that both effects (charge transport by ions resulting in LFD and eventual ion accumulation at the electrodes causing EP) are responsible for the increased ϵ_r' and ϵ_r''.

Due to the combined LFD/EP effect, the α-relaxation becomes obscured in the imaginary permittivity due to the rapid increase in ϵ_r''. Figure 4.23 shows the complex imaginary modulus (M") of pure epoxy and nanocomposites with 5 wt% SiO_2. In M", the LFD/EP effect manifests as an additional peak instead of an exponential increase in ϵ_r', and the corresponding peak for the α-relaxation is less obscured. The relaxations occur at a higher frequency in the modulus spectra, compared to the permittivity spectra [217]. The small peak for the new relaxation introduced for the nanocomposites is also evident in the modulus spectrum, but shifted to between 10 and 10^3 Hz. Both the shift in the peaks for the LFD/EP effect in M" to higher frequencies and the larger increase in both ϵ_r' and ϵ_r'' in the nanocomposites suggest that the number of charge carriers is much higher in the nanocomposites than the pure epoxy. This is most likely due to ions from the precursors for the synthesis of the SiO_2, or any remnant by-products that were not removed completely (e.g. ethanol from the sol-gel reactions).

Yang et al. [148] demonstrated a similar LFD/EP effect in nanocomposites using pre-synthesized SiO_2, but with an inhibition of the LFD/EP effect in the nanocomposites. This highlights one challenge of the *in-situ* synthesis procedure, as such an approach is likely to introduce additional charge carriers that may degrade the performance of the nanocomposites at higher temperatures. Reducing the amount of APTES at 5 wt% SiO_2 appears to result in opposite effects at pH 7 and pH 11, as seen from comparing Figures 4.19 and 4.20. For a given SiO_2 content, at pH 7 the increase in ϵ_r'' is larger in the nanocomposites prepared with less APTES, whereas at pH 11 the increase in ϵ_r' is larger in nanocomposites prepared with more APTES. Yeung and Vaughan [142] also reported an LFD/EP effect in nanocomposites with pre-synthesized SiO_2. However, they attributed this to adsorbed water on the SiO_2 surface, and that increasing the amount of SCA for surface modification resulted in fewer adsorbed water molecules, leading to a diminished LFD/EP effect. This explanation is unlikely to be valid for the *in-situ* synthesized nanoparticles, since the particles are made directly in the epoxy and not exposed to moisture. However, it is possible that any unreacted water from the synthesis of SiO_2 may also contribute to the LFD/EP effect.

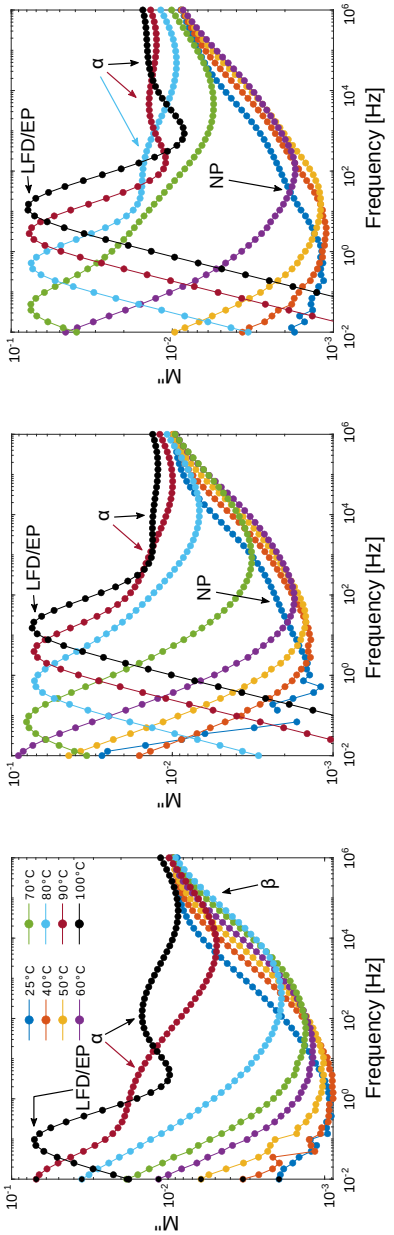

Figure 4.23. Imaginary moduli of **(a)** pure epoxy, and nanocomposites with 5 wt% SiO_2 prepared at **(b)** pH 7 and **(c)** pH 11 with APTES:DGEBA mass ratio of 1:10. The arrows indicate the peaks for the α and β-relaxations and the LFD/EP effect, as well as the new relaxation introduced with the nanoparticles (NP).

4.3 Electrical treeing resistance

4.3.1 Tree morphology and growth behaviour

Figures 4.24 to 4.27 show optical images of the electrical trees grown in pure epoxy and the epoxy-SiO_2 nanocomposites. Since the channels could be difficult to discern, they were illustrated using manually drawn lines. The electrical trees grown in pure epoxy (Figure 4.24) consisted of fine branches, most of which moved towards the ground electrode. However, a few channels grew more horizontally from the needle. All of the trees were initiated at 25 kV, although different durations at the initiation voltage were required for each specific sample. Table 4.4 summarizes selected properties related to the electrical treeing behaviour observed in pure epoxy and in different epoxy-SiO_2 nanocomposites. For simplicity, the different types of nanocomposites are referred to by the series names used in Table 4.4. Trees were initiated in only 4 samples for each composition, and were grown at 10 kV in all the samples.

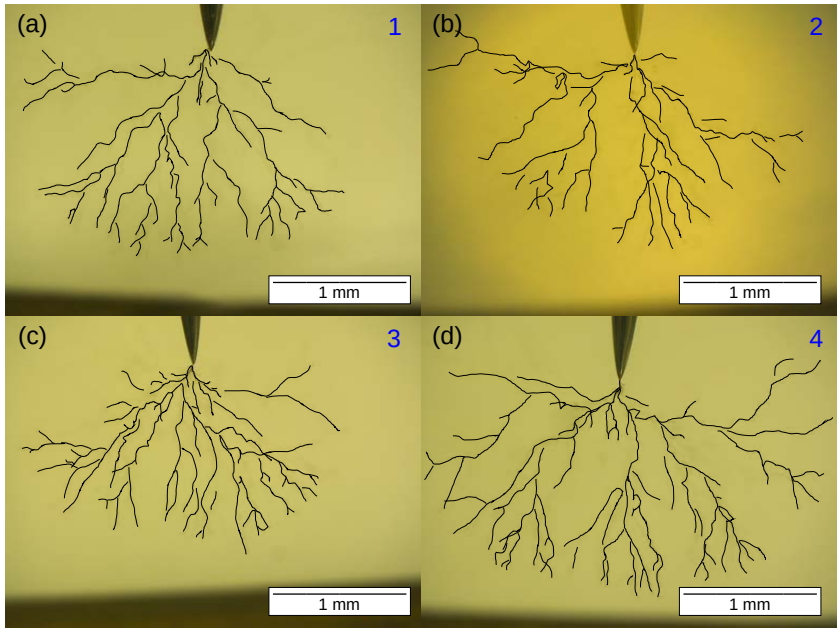

Figure 4.24. Optical images of electrical trees in pure epoxy. The numbers refer to the sample number in the Pure epoxy series in Table 4.4. The unedited images are shown in Figure B.3

Table 4.4. Electrical treeing properties of pure epoxy and selected epoxy-SiO_2 nanocomposites with 5 wt% SiO_2, grown at 10 kV.

Series	Synthesis conditions [a]	No.	Initiation voltage [kV]	Time [s]	Growth rate [mm min^{-1}]	Horizontal spread [mm]	Average channel width [μm]	D_f [b]
Pure epoxy	-	1	25	60	0.030	2.5	4.2	1.57
		2	25	- [c]	0.035	2.9	4.6	1.52
		3	25	1573	0.030	2.3	2.4	1.58
		4	25	800	0.031	3.1	4.0	1.51
S1	1:10, pH 7	1	20	721	0.015	1.9	4.8	1.42
		2	20	501	0.023	2.3	4.3	1.45
		3	10	110	0.022	2.1	3.9	1.49
		4	20	104	0.028	2.7	3.7	1.45
S2	1:30, pH 7	1	25	117	0.041	2.6	2.1	-
		2	20	37	0.036	2.0	2.2	1.60
		3	25	374	0.039	2.7	1.7	1.56
		4	20	84	0.030	1.9	2.2	1.51
S3	1:30, pH 11	1	10	190	0.051	1.0	3.6	-
		2	10	0	0.069	1.5	2.9	-
		3	15	104	0.05	1.6	1.9	-
		4	20	370	0.045	1.7	2.1	-

[a] APTES:DGEBA mass ratio and pH used in the synthesis of SiO_2.
[b] Estimated fractal dimension of the trees.
[c] Data was lost due to a power outage during the measurement.

Figure 4.25 shows the trees grown in epoxy nanocomposites with 5 wt% SiO_2 prepared at pH 7 with an APTES:DGEBA mass ratio of 1:10 (S1 series in Table 4.4). The trees look similar to those in pure epoxy, but it can be seen that the number of branches forming in the nanocomposites were fewer. The spread of the branches (measured horizontally from the images) was lower on average, and the tree channels were generally narrower. In sample 1 (Figure 4.25a) there were two groups of branches that formed with a slightly bushier tree base (shown in the inset). The branches tended to stick closer to one another within each group of branches, and the tree growth in this sample was noticeably slower.

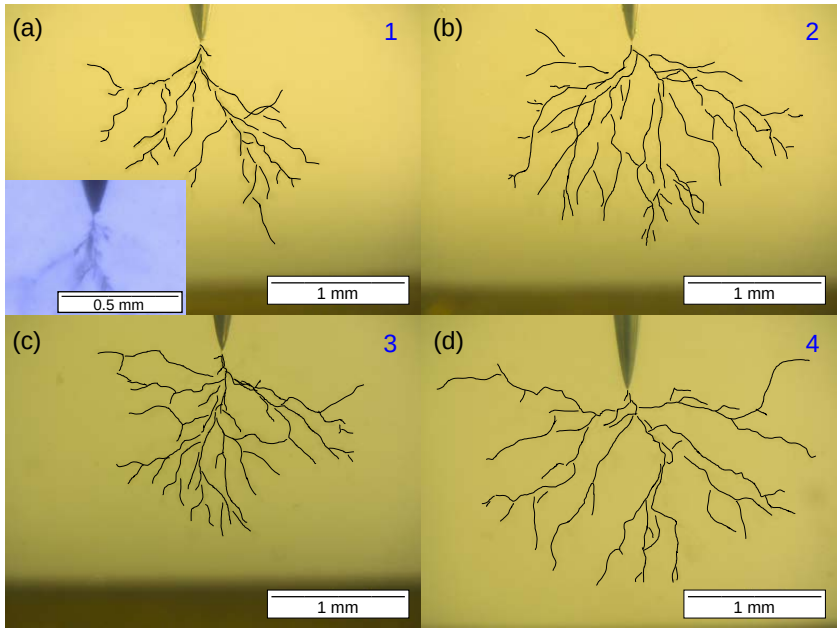

Figure 4.25. Optical images of electrical trees in epoxy-SiO_2 nanocomposites prepared at pH 7 and 1:10 APTES:DGEBA mass ratio. The numbers refer to the sample number for the S1 series in Table 4.4. The unedited images are shown in Figure B.4

The average growth speed of the trees that formed in the S1 nanocomposites was slower compared to pure epoxy. Despite the slower growth, a lower voltage and a shorter time at that voltage was usually required to initiate the trees in these nanocomposites. Additionally, in pure epoxy the trees did not begin to grow at 10 kV for ~30 min after initiation, whereas in all the nanocomposites the tree growth began immediately when the voltage was set to 10 kV.

Figures 4.26 and 4.27 show the different trees grown in the nanocomposites prepared with less APTES at pH 7 and pH 11, respectively (S2 and S3 series in Table 4.4). Reducing the amount of APTES reduced the resistance towards electrical treeing in the nanocomposites. As seen in Table 4.4, the average tree growth speed was higher in the nanocomposites prepared with less APTES, most noticeably in those prepared at pH 11 (S3 series). While the initiation voltage was slightly decreased in some of the S2 nanocomposites, the trees in the S3 nanocomposites were initiated at significantly lower voltages than pure epoxy. The tree channels were also narrower than those in pure epoxy or the S1 nanocomposites.

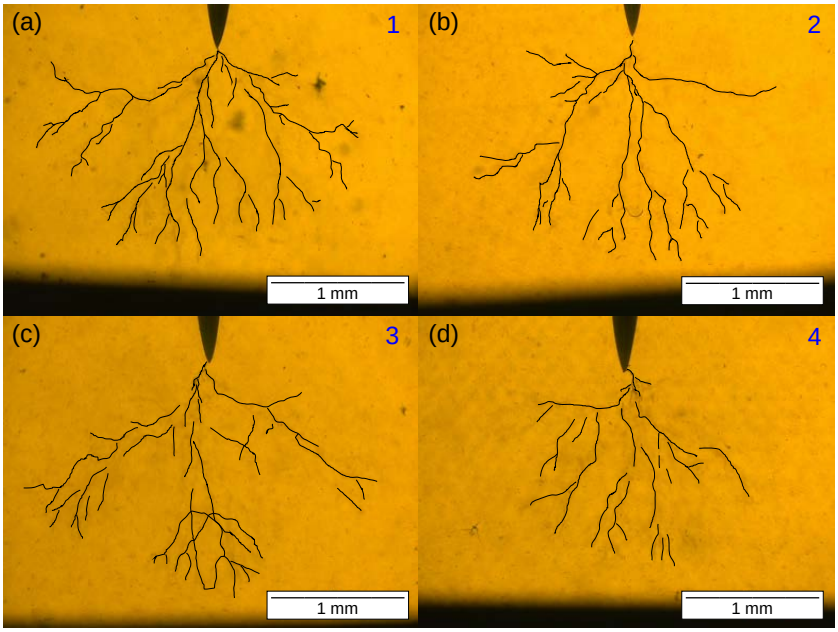

Figure 4.26. Optical images of electrical trees in nanocomposites prepared at pH 7 and 1:30 APTES:DGEBA mass ratio. The numbers refer to the sample number for the S2 series in Table 4.4. The unedited images are shown in Figure B.5

The trees were more linear and grew directly towards the ground electrode in the S3 nanocomposites, while the trees in the S2 nanocomposites spread a horizontal distance similar to those in the S1 nanocomposites. The poorer dispersion of the SiO_2 in the S3 nanocomposites (seen in Figure 4.1e) and the increased number of agglomerates affected the opacity of the samples, which, in addition to the thinner tree channels, made it more difficult to observe the trees.

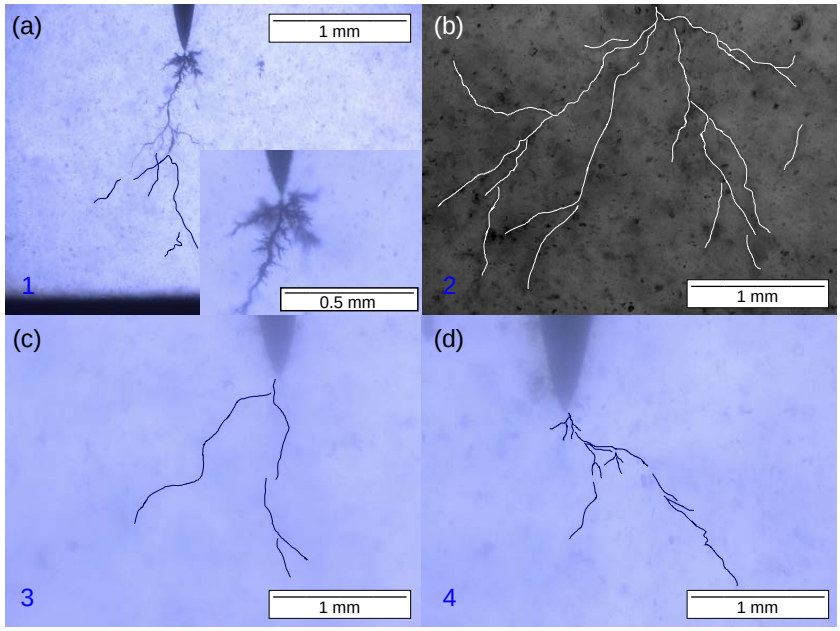

Figure 4.27. Optical images of electrical trees in nanocomposites prepared at pH 11 and 1:30 APTES:DGEBA mass ratio. The numbers refer to the sample number for the S3 series in Table 4.4. The unedited images are shown in Figure B.6

Figure 4.28 shows the growth progress over time throughout the entire duration of treeing. The S3 nanocomposites had a faster tree growth overall, whereas the S2 nanocomposites had similar (or in one case, slower) growth rates compared to pure epoxy in the initial stages. However, the growth in the S2 nanocomposites sped up after some time (around approximately 20 min). The S1 nanocomposites exhibited either similar or slower initial growth compared to pure epoxy, and the growth became slower as time progressed. Sample 1, shown in Figure 4.25a, stood out by exhibiting remarkably slow tree growth progress, as indicated by the blue "-o-" line.

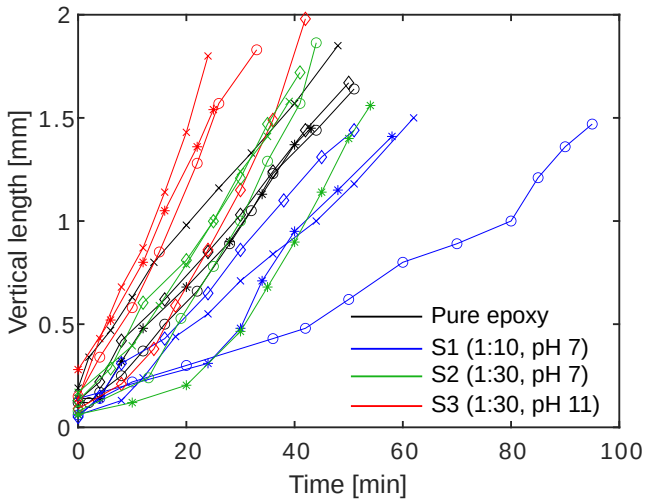

Figure 4.28. Electrical tree growth displayed as the increase in the vertical tree length, directly from the needle to the ground electrode, over time at 10 kV. The time was measured from when the tree growth started. The APTES:DGEBA mass ratio and pH used for the synthesis of the different series are shown in the legend.

Table 4.4 also includes the estimated values of D_f for the different trees, and Figure 4.29 shows selected examples of the CCD images as well as the corresponding binary representations of the trees used for the estimation of D_f. D_f could not be estimated in the S3 nanocomposites due to the poor image contrast. The trees generally had a D_f below 2, and the average D_f for the S1 nanocomposites was lower than that of pure epoxy. The S2 nanocomposites, however, exhibited a similar average D_f to that of pure epoxy. In the images shown in Figure 4.29, the groupings of the different branches are shown with the coloured lines, which were determined from the optical microscope images. The tree branches or sections that were growing close to one another in a specific direction were grouped together. Different groups of branches in the trees grown in pure epoxy tend to spread out uniformly in multiple directions, forming a shape similar to a broccoli-head. The trees in the S1 nanocomposites grew similarly to those in pure epoxy, but the spread of the tree branches was more limited and some of the branches were packed slightly closer together in their group. In the S2 and S3 nanocomposites, the groups of branches were packed closer and the branches did not spread out horizontally to the same degree as in pure epoxy or the S1 nanocomposites, preferring to grow directly towards the ground electrode (as also seen earlier in Figures 4.26 and 4.27).

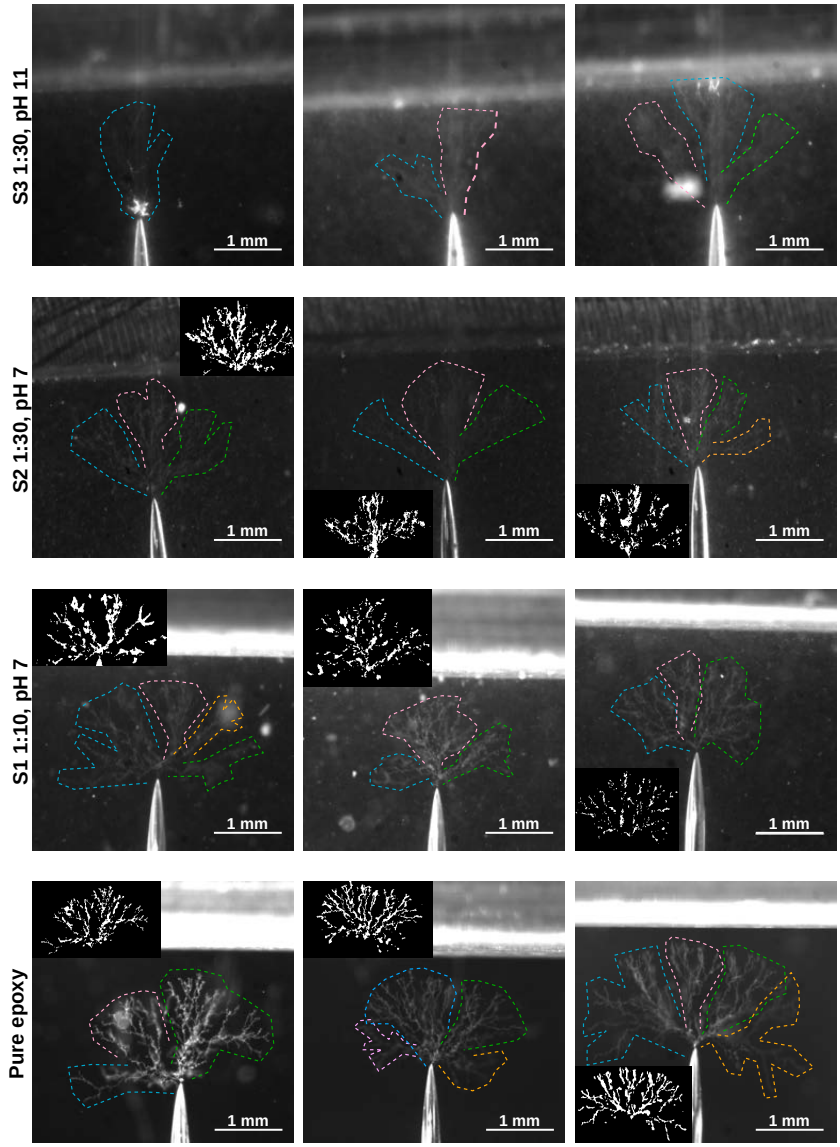

Figure 4.29. CCD camera images of the electrical trees grown in pure epoxy and epoxy-SiO_2 nanocomposites, showing the different groups of branches (indicated by the coloured dashed lines) in the trees. The insets show the corresponding binary representations of the trees obtained from the respective CCD images.

4.3.2 Partial discharge properties during treeing

Figure 4.30 shows an example of the different types of phase-resolved partial discharge (PRPD) patterns obtained at different stages of tree growth in pure epoxy after initiation. Figure 4.30a shows the faint scatters of PD forming that resemble a wing-like PD region in the first ~30 min period after tree initiation in pure epoxy (where no tree growth was observed). Once the tree growth started, the PD activity increased significantly, exhibiting primarily a wing-like pattern but also a small region of turtle-like PD (Figure 4.30b). This initial burst of PD lasted for approximately 5-10 min in most of the samples. Afterwards, the wing-like PD was extinguished and only a very low, flat region of turtle-like PD was observed during the remainder of the tree growth (Figure 4.30c). The following sequence of PD evolution was observed consistently in all of the pure epoxy samples where trees were grown (Pure epoxy series in Table 4.4). Initially there was only wing-like PD (~0-5 min), followed by a period exhibiting both wing and turtle-like PD (~5-10 min). Finally, the PD activity was very low for the remainder of the treeing duration, with low PD magnitude. The intensity of the PD, however, did vary between samples. Figure 4.31 compares different pure epoxy samples, where trees were initiated and grown at 10 kV. In the initial 5 min in all three samples, wing-like PD was most prevalent. In the next 5 min however, only turtle-like PD was observed in sample 2, whereas sample 3 exhibited a mix of wing- and turtle-like PD. Sample 4 showed only wing-like PD in the same time period. After these 10 min, all the samples showed very low magnitude turtle-like PD, similar to that shown in Figure 4.30c.

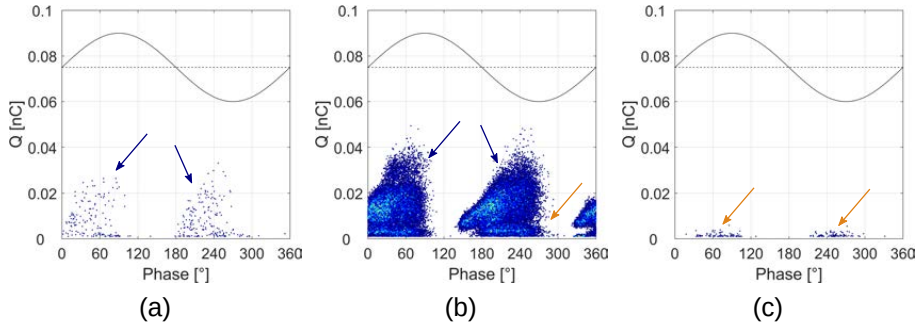

Figure 4.30. Examples of different PRPD patterns in pure epoxy (sample 1 in Table 4.4) **(a)** after tree initiation but before tree growth commenced, **(b)** during the first 5-10 minutes after tree growth began, and **(c)** 10-15 minutes after tree growth began. The blue and orange arrows indicate wing and turtle-like PD regions, respectively.

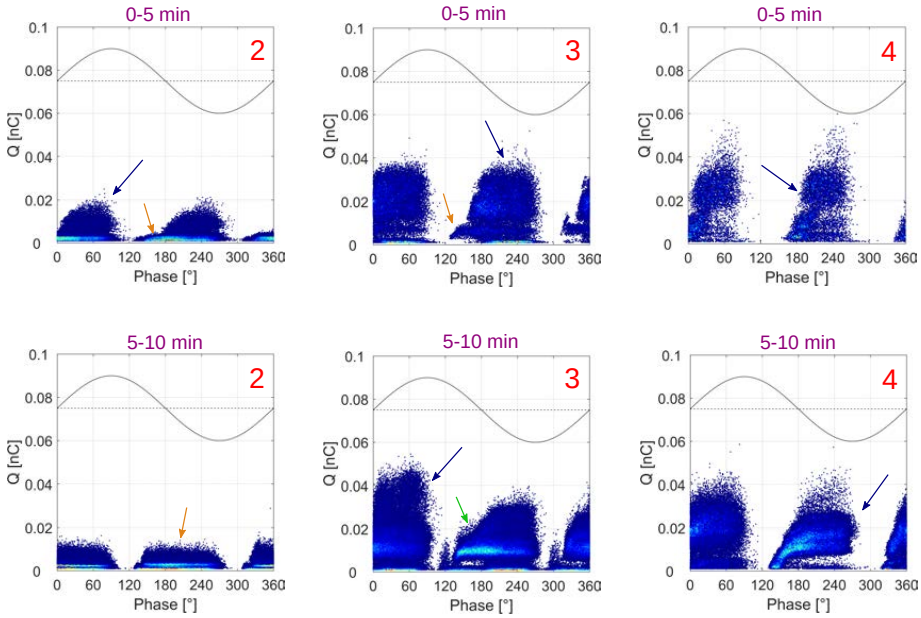

Figure 4.31. Comparison of the different types of wing- and turtle-like PD regions formed in the initial period of tree growth in different pure epoxy samples. The numbers indicate which samples from the pure epoxy series in Table 4.4 the PRPD plots correspond to. The blue, orange and green arrows indicate wing-like, turtle-like, and mixed PD regions, respectively.

Figure 4.32 shows the PRPD patterns at different times in the S1 nanocomposites. These nanocomposites presented a similar evolution in the PD behaviour to that of pure epoxy, but in some cases with a longer period of extensive wing-like PD activity than in pure epoxy. The wing-like PD persisted between 10 and 35 min in samples 1 and 3, and up to 10 min in samples 2 and 4, while the trees remained close to the needle tip. Afterwards, when the trees grew further away, only the low magnitude turtle-like PD was recorded (similar to that seen in Figure 4.30c). Sample 1, shown in Figure 4.25a, exhibited several regions of wing and turtle-like PD that overlapped and occupied different magnitudes of PD, showing the occurrence of several separate groups of discharges during the tree growth. Towards the later stages of tree growth that still exhibited wing-like PD (~20-35 min), the discharge magnitude was much higher than recorded in other samples, up to 0.1 nC. The other samples in the S1 nanocomposites exhibited PD magnitudes that were lower and closer to that seen in pure epoxy. However,

during different periods in the tree growth, certain regions of PD were loosely connected, or even disconnected, from the other PD regions. This is seen most clearly in Sample 3 at 5-10 min in Figure 4.32.

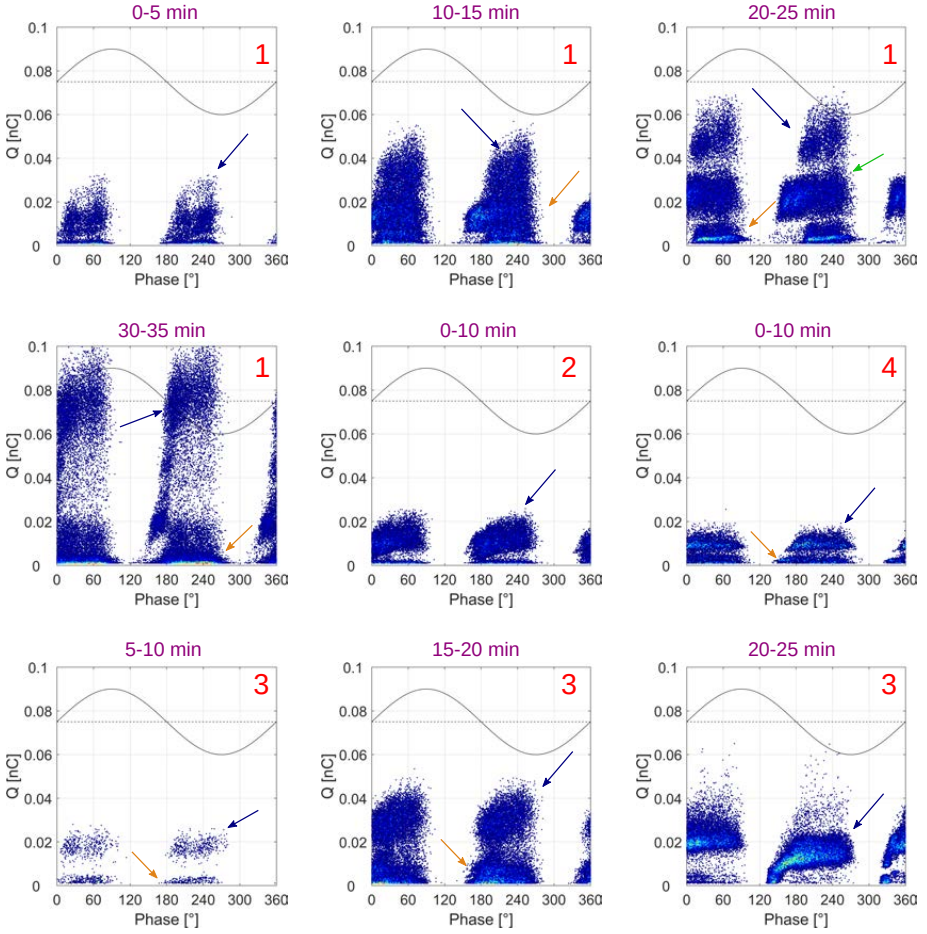

Figure 4.32. Phase-resolved partial discharge patterns for nanocomposites, prepared at pH 7 with APTES:DGEBA mass ratio of 1:10, at different time periods during the tree growth. The numbers indicate which samples in the S1 series in Table 4.4 the PRPD plots correspond to. The blue, orange and green arrows indicate wing-like, turtle-like, and mixed PD regions, respectively.

Figure 4.33 shows the PRPD patterns recorded in S2 nanocomposites. These were similar to the S1 nanocomposites, and in some cases also exhibited disconnected certain regions of PD (e.g. in Sample 4 in Figure 4.33 at 10-15 min). For Sample 2 in Table 4.4, no wing-like PD regions were recorded during the growth at 10 kV, and only the flat band of PD observed in the later stages of treeing was present.

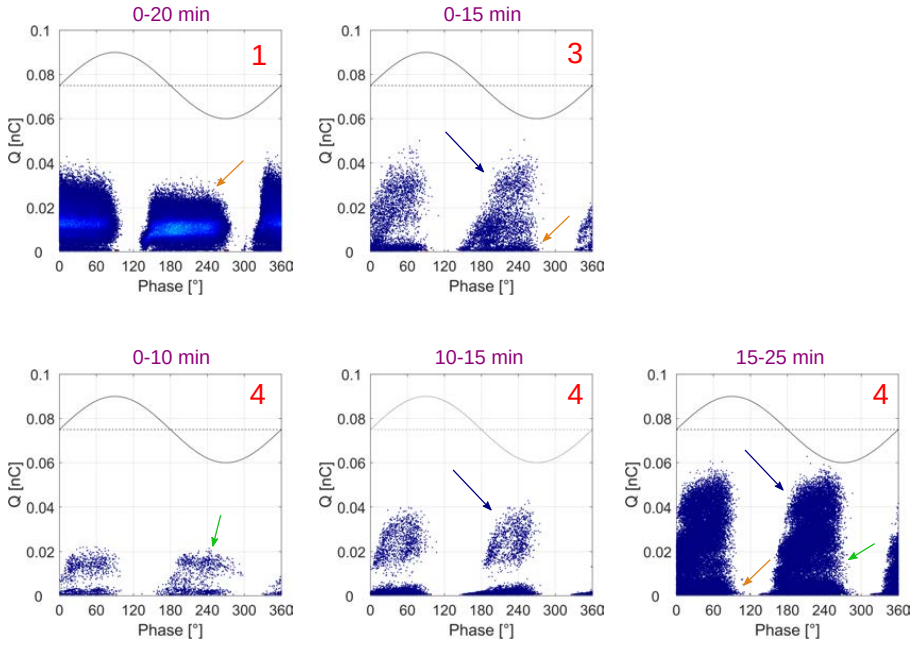

Figure 4.33. Phase-resolved partial discharge patterns for nanocomposites, prepared at pH 7 with an APTES:DGEBA mass ratio of 1:30, taken over different time periods during the tree growth. The numbers indicate which samples in the S2 series in Table 4.4 the PRPD plots correspond to. The blue, orange and green arrows indicate wing-like, turtle-like, and mixed PD regions, respectively.

In the S3 nanocomposites the PD activity was comparatively lower in three of the tested samples (No. 2, 3, and 4), and the wing-like regions had low magnitude and were extinguished within 10 min, similar to the pure epoxy. Sample 1, however, was an exception. Figure 4.34 shows the PRPD patterns recorded in this sample over the entire duration of the tree growth (~35 min). A high PD activity and discharge magnitude persisted throughout the entire treeing period, in contrast to all the other samples where eventually the wing-like PD

was extinguished. In addition, the discharge magnitude was significantly higher compared to the other nanocomposites and the pure epoxy, and was as high as 0.08 nC even in the first 5 min of tree growth. There was a significant overlap of several regions of wing and turtle-like PD at all stages of tree growth. The PD magnitude was significantly higher in the positive half-cycle of the voltage phase after 15 min, resulting in asymmetric PD patterns.

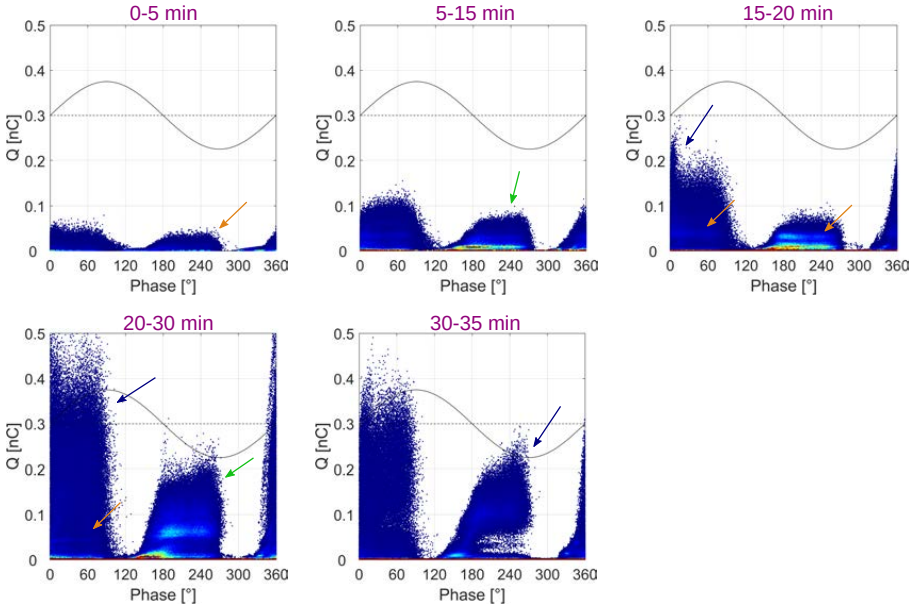

Figure 4.34. Phase-resolved partial discharge patterns for Sample 1 in the S3 series in Table 4.4, prepared at pH 11 with APTES:DGEBA mass ratio of 1:30, over the entire period of tree growth. The blue, orange and green arrows indicate wing-like, turtle-like, and mixed PD regions, respectively.

4.3.3 Discussion

4.3.3.1 The tree growth and morphology

Tree initiation is a stochastic process that depends not only on the strength of the electrical field, but also the presence of defects or sources of electrons near the needle tip for sufficiently high discharges that can erode through the material. The tree initiation rate was consistently low (initiated in ~30-40 % of the samples tested), even at 25 kV for up to 1 h. The low initiation rate indicates that both

the pure epoxy and the nanocomposites exhibit inherent resistance towards initiation of electrical trees. One possible reason for the low initiation rate may be the use of N_2 pressurization during the curing process. Most reported works stress the need for vacuum before casting, as air bubbles can be a severe weakness for the dielectric properties. However, none have reported the use of a pressurized environment during curing, which minimizes the size of any air bubbles that are remaining in the resin even after vacuum degassing.

The initiation voltage of the trees for pure epoxy was always higher than for the nanocomposites, indicating that there are more defects or electron sources in the nanocomposites. Comparisons of the tree initiations to other works are difficult, however, since the testing procedures used were different. Tree initiations reported in literature typically involve the use of a fixed voltage (usually between 10 and 15 kV) and measuring the time to initiation [127, 152, 153,155,218]. As seen in Table 4.4, there is a large variance in the time to initiation at the voltage even in the case of pure epoxy, where all the samples initiated at the same voltage. Comparisons between the different types of nanocomposites are more difficult, since different samples in a series initiate at different voltages. Generally, however, the average time to initiation is lower in the nanocomposites than in the pure epoxy. This is opposite to what is expected, as reports on *ex-situ* composites reported increases in the initiation time at a fixed voltage in nanocomposites compared to pure epoxy [152, 153, 218].

As an electrical tree grows, it will seek the path of least resistance through the material in the direction of the electrical field. Therefore, there must be regions in the S2 and S3 nanocomposites that are more susceptible to erosion by discharges than in the pure epoxy or S1 nanocomposites, allowing the trees to grow faster and more directly towards the ground electrode. The reduced degree of branching also demonstrates that the tree did not need to frequently find alternate routes with lower resistance. On the other hand, the trees in the S1 nanocomposites show multiple short thorns on the main tree channels, shown in Figure 4.35, giving the appearance of pine leaves. These thorns did not fully develop into individual tree branches, and the frequency of these thorns is higher in the S1 nanocomposites compared to pure epoxy. This "pine leaf" structure indicates that the electrical tree experiences a greater difficulty in growing through the S1 nanocomposites compared to the pure epoxy or the S2 or S3 nanocomposites. The multiple thorns form due to the resistance in the current path of tree channel, but the discharges are not high enough to contribute to the growth of these thorns into fully developed branches.

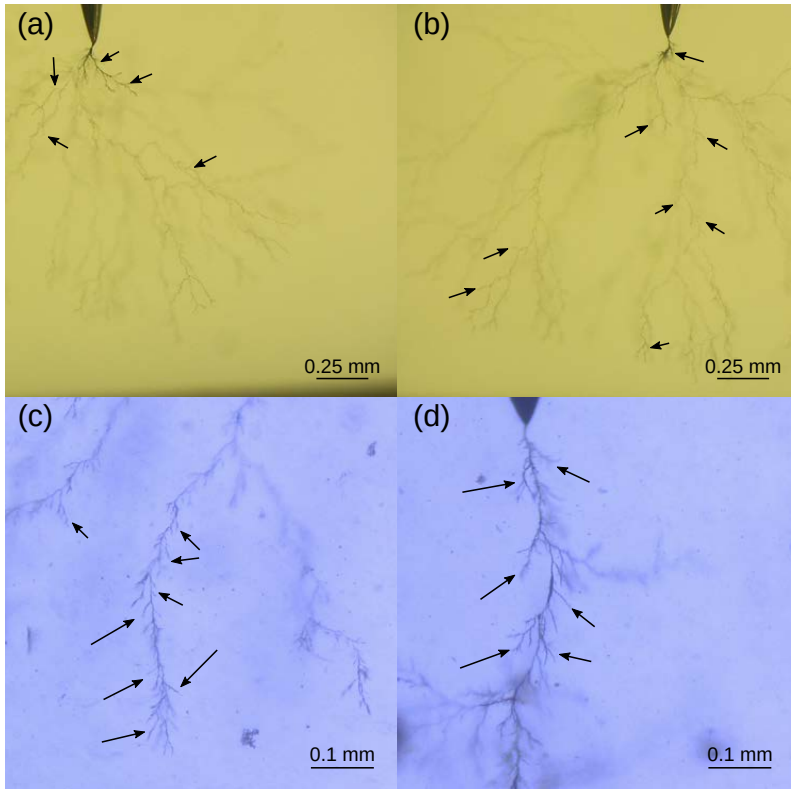

Figure 4.35. Comparison of the "pine leaf" like structures on the branches of **(a,b)** pure epoxy and **(c,d)** SiO_2 nanocomposites prepared at pH 7 with 1:10 APTES:DGEBA mass ratio. The arrows point to regions where the "thorns" have formed on a primary tree channel.

The growth rates of the trees subsequently affect the tree morphology, with the faster growing trees generally exhibiting a narrower horizontal spread, less branching, and larger D_f. D_f acts as an indicator for the branch density [219], with larger values indicating a greater density (or closer packing) of the branches. All the nanocomposites exhibit branched trees ($1 < D_f < 2$ for branched trees and $2 < D_f < 3$ for bushy trees [220]), but D_f was higher for the S2 nanocomposites, showing a higher branch packing density. Although D_f could not be measured for the S3 nanocomposites, comparatively higher values of D_f are expected as the the tree channels are bundled closer together, despite the trees being more linear and with fewer branches. While D_f can be a useful indicator of the density

of the branches and the degree to which an electrical tree is bushy or branched, care should be taken when interpreting the results of the fractal dimensions estimated from two-dimensional projected images. When the tree branches grow too far in or out of the focal plane of the images, information is lost in the projected images, giving the appearance of bushier trees than they actually are.

4.3.3.2 Partial discharge behaviour

Representative plots for the PD activity over time are shown in Figure 4.36, measured from right after tree initiation. For pure epoxy (Figure 4.36a), scattered bursts of wing-like PD were recorded during the initial delay period where no tree growth was observed. From the moment the tree started growing, a continuous band of wing-like PD was observed for a brief time (~3 min in the sample represented in Figure 4.36a). In the nanocomposites, the tree growth was immediate, and the bursts of PD were generally more frequent (shorter intervals between them) and lasting a longer time (~8 min in the sample shown in Figure 4.36b). In both cases after the wing-like PD ceased, only turtle-like PD with lower discharge magnitude was observed for the remainder of the tree growth. Champion and Dodd [221] reported a similar PD activity over time in branched trees. The PD behaviour is therefore consistent with the morphology of the trees observed earlier in Figures 4.24 to 4.27, and that characterized by the D_f. However, it is unexplained why the wing-like PD patterns disappear as the tree grows beyond a certain distance from the needle tip. Wing and turtle-like PD patterns have been reported previously in several works, although different authors suggest different sources for the PD. Wu et al. [222] and Lv et al. [126] show similar PD patterns for trees grown in polyethylene and epoxy, respectively, and attribute the wing-like PD to discharges along longer tree channels (or the entire tree length), and turtle-like PD to discharges along shorter channels or distances (e.g. at the tip of the trees). One would expect, based on these findings that with longer branches, wing-like patterns should persist with greater magnitude as the tree became longer.

This discrepancy may be explained by consideration of whether the tree channels are conducting or non-conducting. Dodd et al. [223] reported wing and turtle-like PD in non-conducting and conducting trees, respectively. Therefore, a proposed explanation for the PD behaviour in these materials is that the tree channels transition from an non-conducting to conducting. Figure 4.37 presents an illustration for the mechanism for this transition as the tree grows.

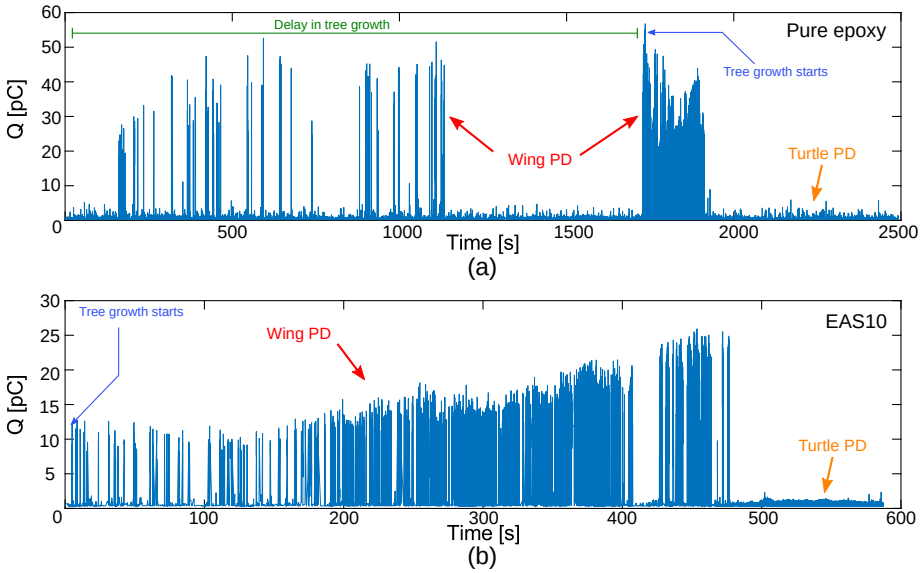

Figure 4.36. The PD activity over time for **(a)** pure epoxy and **(b)** S1 nanocomposite. The measurement of the PD activity was started right after tree initiation when the voltage was set to 10 kV.

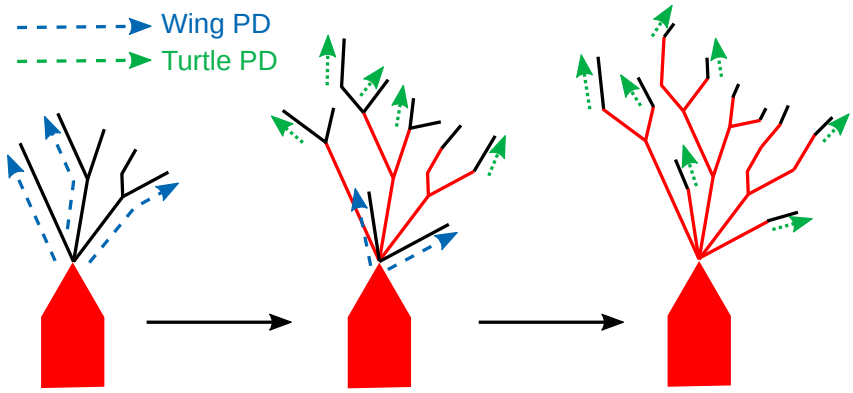

Figure 4.37. Schematic illustrating the development of the electrical tree from the needle tip (in red) along with the different types of partial discharges, and the transition from non-conducting (black lines) to conducting (red lines) tree channels.

The tree formed at initiation is non-conducting, and the electric field maximum lies at the tip of the high voltage needle electrode. The build-up of potential from the needle tip to the ends of the tree causes large partial discharges in the gas-filled tree channels, which are the wing-like PD that are observed. These discharges cause breakdown of the surrounding resin, resulting in carbonization of the channel walls, turning them conductive. As this happens, new tree channels may be initiated from the needle tip where the same discharge behaviour occurs. As the channels become more conductive, the front of the electric field effectively moves away from the needle tip and closer to the ends of the tree. This shift in the electric field means that the highest electric field strength is no longer at the needle tip but closer to the tree tips, where the field strength is amplified due to the tree channels being narrower than the needle tip. The amplification occurring at the tree tips explains why tree growth can proceed at a lower voltage than the voltage required for tree initiation. Hence, the electric potential difference at the tree tips becomes weaker, resulting in smaller discharges over shorter distances, giving turtle-like PD. Eventually all of the tree except the tips of most branches will be conducting, and the wing-like PD is extinguished and only turtle-like PD is observed.

The PD behaviour can also be used to explain some of the different observations made during the tree growth. The S3 nanocomposites exhibited the fastest tree growth, and short-lived wing-like PD. In addition, the magnitude of the PD was low in general, which could be attributed to the narrower average channel diameters (Table 4.4). The only exception to this was observed in Sample 1 (Figure 4.27a) where the initial base of the tree (close to the needle) consisted of very thick (~15-20 μm) tree channels. This resulted in the large PD observed in Figure 4.34, with overlapping wing and turtle-like PD. The PD magnitude also increased with time, indicating that the tree channels remained conductive throughout the growth period. A possible explanation for this deviation is that the conductive material from breakdown products could not be deposited due to the constant erosion of the channel walls at the tree base, resulting in the thicker channels. It is unknown why this is observed in only one S3 nanocomposite, but could be due to a poorer sample quality. The PD behaviour observed for the S1 nanocomposite with the slowest tree growth (Sample 1 in Table 4.4 and Figures 4.25 and 4.32) also stands out, with the wing-like PD persisting for a longer duration than most nanocomposites. This behaviour can be due to the fact that the growth of the tree in the initial stage is significantly slower (the blue "-o-" line in Figure 4.28). The slower growth rate, combined with the tree channels not becoming significantly thicker, means that fewer breakdown products are formed from the discharges, resulting in a longer time taken for the channels to become conductive.

In some of the nanocomposites, certain regions of PD appear to be disconnected from the others at times, such as those seen in Sample 4 in Figure 4.33. This indicates a floating potential in parts of the tree channels, resulting in charging and discharging of a region with well-defined capacitance. This could be caused by irregular intervals at which the channels become conductive, resulting in neighbouring conductive and non-conductive regions where one of the regions act as a "floating potential capacitance". The separation in the PD signal shows that the positions of these regions are somewhat fixed during the measurement period.

4.4 Thermal and mechanical properties of the nanocomposites

4.4.1 Glass transition and thermal stability

The glass transition of the epoxy-SiO_2 nanocomposites showed significant variations with the synthesis conditions. Figure 4.38a shows the changes in T_g with filler content for the different types of nanocomposites prepared with either APTES or GPTMS, at different pH with APTES, and with different amounts of APTES.

In the nanocomposites prepared with APTES, T_g initially decreased before subsequently increasing when the amount of SiO_2 was increased. The nanocomposites prepared with GPTMS, however, showed a noticeable increase in T_g even at lower filler contents, up to 95 °C at 5 wt% SiO_2. In contrast, for 5 wt% SiO_2 prepared with APTES the highest T_g observed was 87 °C, an increase of just 4 °C over pure epoxy. Additionally, while the nanocomposites prepared at pH 2 and 7 exhibited similarities in the changes in T_g with filler content, those prepared at pH 11 showed only small changes in T_g compared to pure epoxy.

Figure 4.38b shows the thermal decomposition of pure epoxy and epoxy-SiO_2 nanocomposites prepared at pH 7. The thermal stability of the nanocomposites was increased compared to pure epoxy, and was found to be independent of the synthesis conditions or the filler content. Up to ~320 °C, there was no difference in the thermal stability of pure epoxy and the nanocomposites. Between 320 and 340 °C, the pure epoxy decomposed significantly, resulting in a mass loss of approximately 28 %, whereas the nanocomposites underwent a mass loss of only ~2 %. The thermal decomposition of the pure epoxy plateaued slightly between 400 and 450 °C, whereas for the nanocomposites this plateau was between 450 and 530 °C. The thermal decomposition was complete for the pure epoxy at around 580 °C, whereas it was complete for the nanocomposites at around 630-

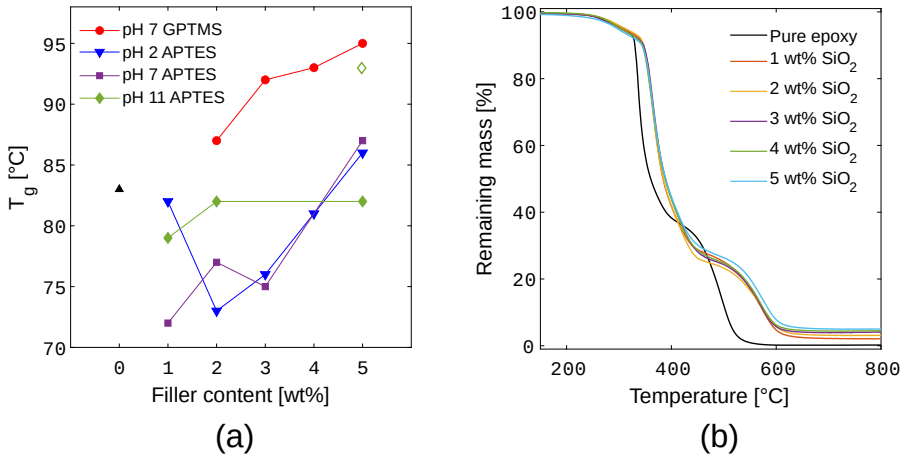

Figure 4.38. **(a)** The glass transition temperatures (T_g) of epoxy-SiO_2 nanocomposites prepared using different synthesis conditions, as a function of SiO_2 filler content. The T_g of pure epoxy is shown as the black triangle at 0 wt% SiO_2. The closed markers are for nanocomposites prepared with an SCA:DGEBA mass ratio of 1:10, and the open marker is for a mass ratio of 1:30. The error in each measurement is ± 2 °C. **(b)** The thermogravimetric analysis of epoxy-SiO_2 nanocomposites prepared at pH 7 with an APTES:DGEBA mass ratio of 1:10, with different SiO_2 contents.

650 °C. FTIR spectroscopy was used to verify that the remaining mass after the thermal decomposition was SiO_2.

4.4.2 Tensile and elastic properties

The tensile elastic properties of epoxy-SiO_2 nanocomposites prepared with APTES (1:10 mass ratio of APTES:DGEBA) at pH 7 are shown in Figure 4.39, which also illustrates the general trends in the average properties over all the samples measured for each filler load. The average elastic moduli exhibited a similar trend as the T_g. The addition of a low amount of SiO_2 decreased the elastic moduli, but further increases in the SiO_2 content resulted in an increase. The ultimate tensile strength (UTS), however, showed a consistent decrease with increasing SiO_2 content in the nanocomposites. The strain at failure did not show any significant differences up to 3 wt% of SiO_2, but upon increasing the filler content to 5 wt%, the strain at failure increased significantly. It should be noted that the nanocomposites generally demonstrated a much larger variation in the measured elastic moduli and strain at failure between samples with the same filler content than the variation observed in pure epoxy samples.

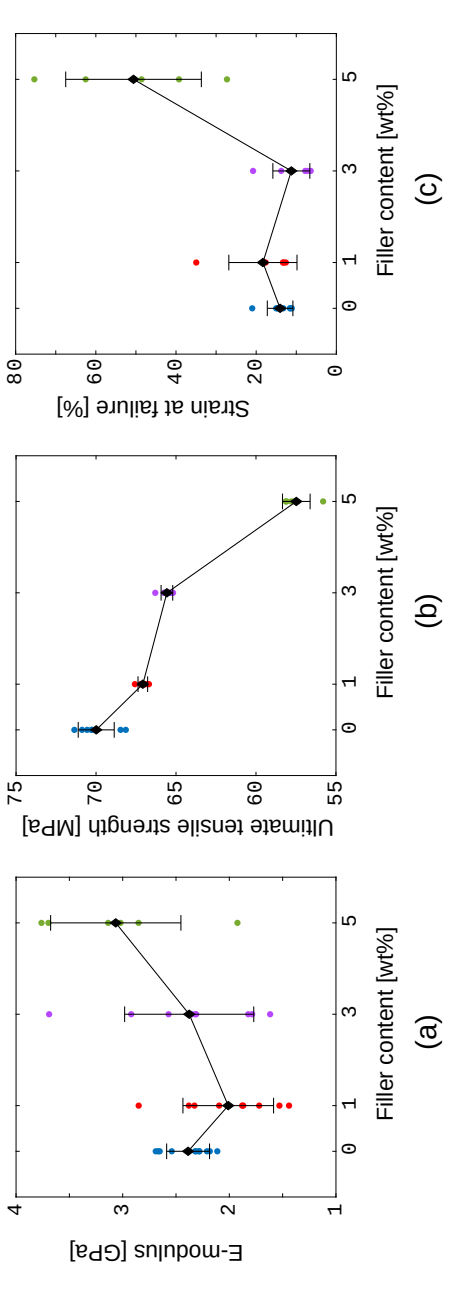

Figure 4.39. The measured tensile properties of epoxy-SiO_2 nanocomposites prepared with APTES at pH 7 (APTES:DGEBA mass ratio of 1:10). **(a)** The tensile elastic moduli. **(b)** The ultimate tensile strength. **(c)** The strain at failure.

Figures 4.40 to 4.43 show the fracture surfaces of pure epoxy samples and epoxy-SiO_2 nanocomposites with 1, 3, and 5 wt% of SiO_2, respectively (prepared at pH 7 with APTES:DGEBA mass ratio of 1:10). Defects and other features on the fracture surfaces are marked by blue arrows. In the pure epoxy samples, the fracture surface was relatively smooth and flat. In most of the samples, the fracture origin was at the surface of the material, as the cracks were seen to initiate along the edges as seen in Figure 4.40a and b. The fracture origins are marked by red arrows. Some regions were also observed where there was a bowed conical surface, as seen in Figure 4.40c and d, that is slightly elevated or depressed.

Fracture surfaces in nanocomposites with 1 wt% SiO_2 were similar to those in pure epoxy, but with increased surface roughness. Figure 4.41a and b highlight the different features in these fracture surfaces, which are more frequent than in pure epoxy. Figure 4.41c and d also show that the cracks can be initiated within the material, and not only at the material surface as in pure epoxy. In addition, microcracks were observed close to other cracks or defects, such as that shown in Figure 4.41c. The nanocomposites with 3 wt% SiO_2 exhibited a significantly rougher fracture surface, as observed in Figure 4.42a. Microcracks, shown in Figure 4.42b, were more frequent than in the nanocomposites with 1 wt% SiO_2. However, the fracture origin was primarily at the material surface, and so most cracks still initiated at the edges of the fracture surfaces. These were identified by following the river markings, shown in Figure 4.42c and d. Nanocomposites with 5 wt% SiO_2 also exhibited fracture origins at the material surface. However, unlike the pure epoxy or nanocomposites with less SiO_2, crack initiation was not observed at multiple sites in the samples. In addition, the fracture surfaces at 5 wt% SiO_2 showed a development of the surface roughness with increasing distance from the fracture origin. The regions in the immediate vicinity of the origin was a smooth, and mirror-like with few features. Beyond this "mirror"-region, the surface become rougher and a "mist" region forms, where the crack accelerates in an unstable manner. Further away, the surface becomes increasingly rougher and forms a "hackle" region. The mirror, mist, and hackle regions are most evident in Figure 4.43a, with the fracture origin at the top-right corner (marked by the arrow). In all of the nanocomposites with 5 wt% SiO_2, the fracture origins were observed in the corners of the square cross-section of the fracture surfaces. The microcracks shown in Figure 4.43b were prevalent all over the mist and hackle regions, compared to nanocomposites with 1 or 3 wt% SiO_2 where these were observed only close to the cracks or other defects.

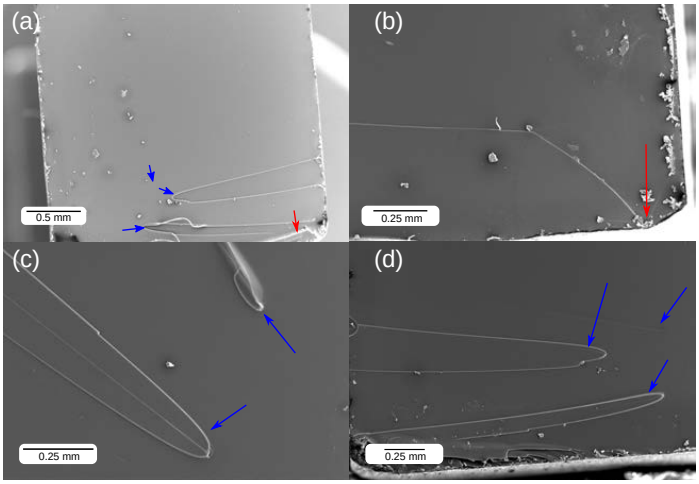

Figure 4.40. Fracture surfaces of pure epoxy samples after mechanical failure during tensile measurements. The blue arrows point to defects or other features on the fracture surfaces, the red arrows point to the fracture origin.

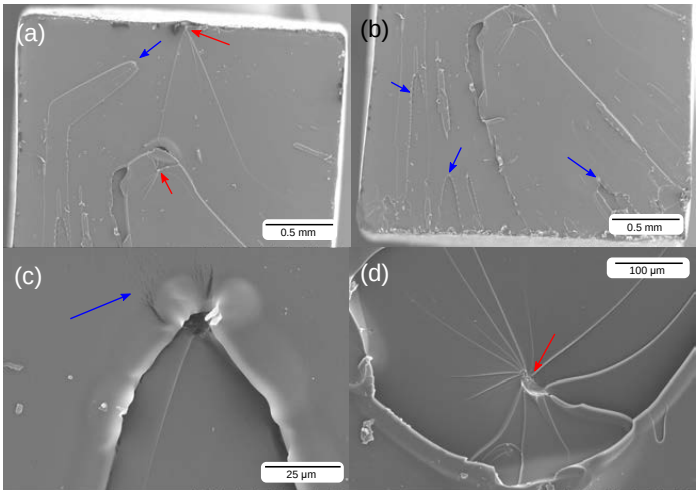

Figure 4.41. Fracture surfaces of epoxy-SiO_2 nanocomposite samples with 1 wt% SiO_2. The red arrows point to possible sites of the fracture origin, and the blue arrows point to cracks or other features on the fracture surfaces

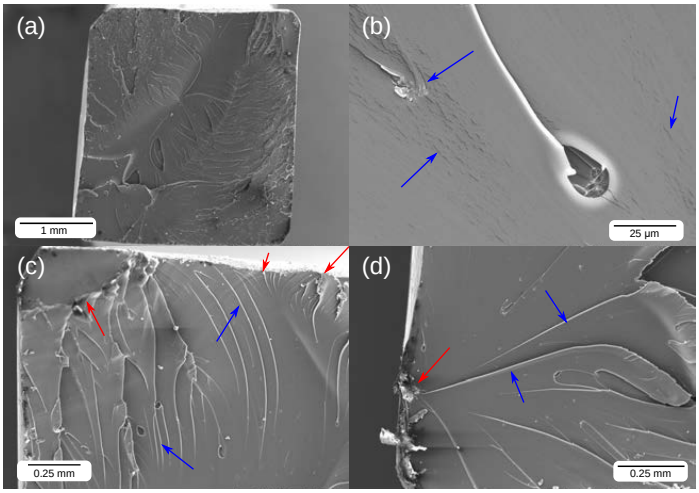

Figure 4.42. Fracture surfaces of epoxy-SiO_2 nanocomposite samples with 3 wt% SiO_2. The red arrows point to possible sites of fracture origin, and the blue arrows point to river markings, microcracks, or other features on the fracture surfaces.

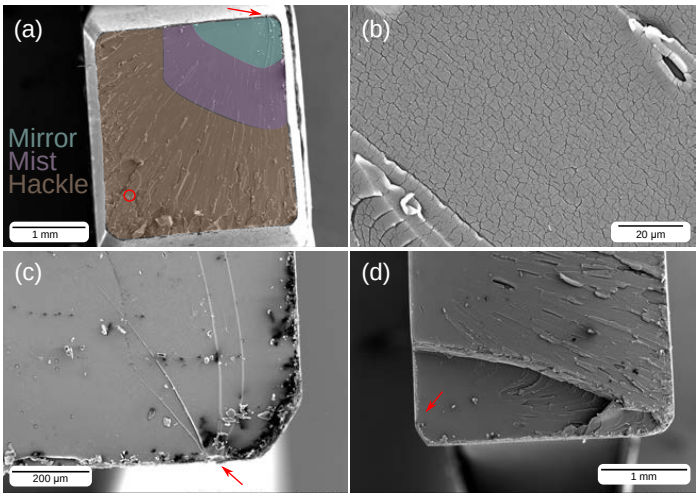

Figure 4.43. Fracture surfaces of epoxy-SiO_2 nanocomposite samples with 5 wt% SiO_2. The region highlighted by the red circle in **(a)** is shown in **(b)** The red arrows point to the fracture origins.

Figure 4.44 shows the complex elastic moduli (storage modulus G' and tan δ) of the same nanocomposites shown in Figure 4.39. At room temperature, the storage modulus increased with increasing SiO_2 content. However, above the glass transition only the 5 wt% specimen exhibited a higher storage modulus than pure epoxy. The T_g was also measured from the position of the tan δ peak. The changes in T_g with SiO_2 content show the same behaviour when measured by DMA and DSC. Initially, there was a decrease in T_g with a small amount of SiO_2, followed by an increase when the SiO_2 content was increased beyond a threshold. Unlike the DSC measurements, the T_g for the nanocomposite with 5 wt% SiO_2 was not higher than that of pure epoxy. Hence, the nanocomposites exhibited a lower T_g than pure epoxy according to DMA. The tan δ data in Figure 4.44b presented on a logarithmic scale shows that the peak observed for pure epoxy possesses a shoulder at a temperature above the peak temperature, which is also present in the nanocomposites. However, the nanocomposites possess an additional feature, also appearing as a shoulder, in between this shoulder and the maximum (highlighted by the arrows). The change in the height of the tan δ peak with SiO_2 content also presented a trend similar to that observed for the T_g. The peak intensity initially increased at low SiO_2 content (1 and 3 wt%), and then decreased at higher content (5 wt%). Additionally, the area under the peaks are larger in the nanocomposites than in the pure epoxy.

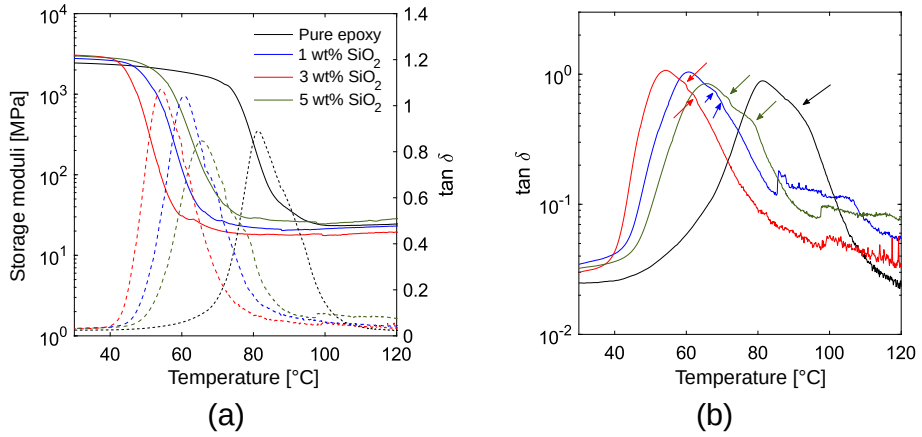

Figure 4.44. The dynamic mechanical behaviour of epoxy-SiO_2 nanocomposites prepared with APTES:DGEBA mass ratio of 1:10. **(a)** The elastic storage modulus (solid lines) and loss tangent (tan δ, dashed lines). **(b)** The tan δ on a logarithmic scale, highlighting the features in tan δ as marked by the arrows.

4.4.3 Discussion

4.4.3.1 Thermal properties of the nanocomposites

The glass transition temperatures for pure epoxy and the nanocomposites, prepared at pH 7 with 1:10 APTES:DGEBA mass ratio, measured using DSC (Figure 4.38a) and using DMA (Figure 4.44) are compared in Table 4.5. The temperature at which the α-relaxation was first observed from the dielectric spectroscopy measurements is also included. The same trends are observed using these three different characterization methods. T_g was initially lower in nanocomposites with a low SiO_2 content compared to pure epoxy, but subsequently increased when the SiO_2 content was increased.

Table 4.5. Comparison of the glass transition temperatures (T_g) obtained from different measurement techniques for pure epoxy and epoxy-SiO_2 nanocomposites prepared at pH 7, with an APTES:DGEBA mass ratio of 1:10.

Sample	**DSC** [°C]	**DMA** [°C]	**Dielectric spectroscopy** [°C]
Pure epoxy	83	81	> 70
1 wt% SiO_2	72	61	> 50
2 wt% SiO_2	77	- [a]	> 60
3 wt% SiO_2	75	56	> 60
5 wt% SiO_2	87	66	> 70

[a] No measurements were made for this sample using DMA

There are some discrepancies in the values for T_g obtained from the different measurements. In the case of the dielectric spectroscopy, the measurements were taken at 10 °C intervals, but parts of the α-relaxation could sometimes be seen at lower temperatures in the low frequency region. The DMA measurements were also performed on a larger volume of sample (several grams) compared to the DSC measurements (in the range of milligrams). This, combined with the different heating rates used in the DSC (10 °C/min) and in the DMA (2 °C/min) means that the thermal histories of the same material used in the two techniques will be quite different, resulting in different values for T_g in the same nanocomposites.

There are additional features above the peak temperature in tan δ in the nanocomposites, compared to the pure epoxy, as observed in Figure 4.44b. Multiple peaks in tan δ could indicate a second glass transition, as predicted by Tsagaropoulos and Eisenberg [57]. Alternatively, if the peaks are sufficiently close to one another or are shoulders on another peak, there could be multiple regions in the cured resin that approach the glass transition separately from

one another. This may occur if there are inhomogeneities in the cross-linking density or if the curing reaction was incomplete. The latter can be discarded as no exothermic shifts were observed for both the pure epoxy and the nanocomposites during the DSC measurements, shown in Figure 4.45. The presence of the additional shoulders in the tan δ for the nanocomposites is then most likely due the degree of cross-linking in the epoxy being affected in the vicinity of the nanoparticles, possibly at or close to the interfaces.

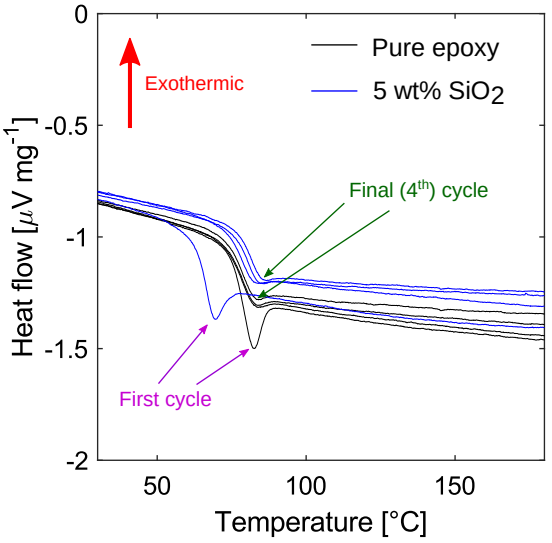

Figure 4.45. The heat flow during DSC measurements of pure epoxy and nanocomposite with 5 wt% SiO_2 (prepared at pH 7 with 1:10 APTES:DGEBA mass ratio). The heat flows are shown for all four cycles of the measurement.

The glass transition can be seen during all four cycles of the DSC measurement as the endothermic shift in the heat flow between 60 and 90 °C in Figure 4.45. The first cycle always exhibited an earlier glass transition with an endothermic peak compared to the next three cycles, which were reproducible. This feature is due to the material experiencing molecular relaxations, and the release of stresses built into the material during processing. This could also be a possible reason for the lower T_g observed in DMA measurements, since there the samples are not pre-heated to above the glass transition prior to measurement.

The thermal stability of the nanocomposites, compared to the glass transition temperature, did not vary significantly with the synthesis conditions, and was higher than the thermal stability of the pure epoxy (Figure 4.38b). Bauer et

al. [85] attributed the plateau in the thermal degradation to char formation and the carbonization of the epoxy. In the nanocomposites, the plateau is wider, and occurs at a higher temperature and when a lower % of the original mass is remaining, showing that the inclusion of the SiO_2 nanoparticles both delays the onset and increases the duration of this process. The differences in the thermal stabilities of nanocomposites with different SiO_2 contents are subtle, and it appears that including small amounts of SiO_2 is sufficient to slow down the thermal degradation of epoxy.

4.4.3.2 Mechanical properties

Table 4.6 shows a comparison of both the elastic and storage moduli measured using tensile tests and DMA, respectively, at room temperature, as well as the storage modulus (measured using DMA) at 120 °C. The DMA measurements were performed using 3-point bending instead of a tensile deformation, but despite this the obtained values for the storage modulus are not too dissimilar from those obtained for the elastic modulus. The increase in elastic modulus at higher SiO_2 contents is expected, as similar developments were reviewed in literature [6]. The increase in the elasticity of the nanocomposites is also reflected in the storage modulus, but the storage modulus did not decrease initially at 1 wt% SiO_2 as it did in the elastic modulus.

Table 4.6. Comparison of the elastic moduli and storage moduli obtained from tensile testing and from DMA measurements, respectively, for pure epoxy and epoxy-SiO_2 nanocomposites prepared at pH 7, with an APTES:DGEBA mass ratio of 1:10. All the units are given in GPa.

Sample	**Tensile**	**DMA (3-point bending)**	
	Elastic modulus (25 °C)	**Storage modulus (25 °C)**	**Storage modulus (120 °C)**
Pure epoxy	2.39	2.43	0.025
1 wt% SiO_2	2.01	2.73	0.023
3 wt% SiO_2	2.38	2.87	0.019
5 wt% SiO_2	3.07	3.00	0.029

There is a consistent decrease in the UTS of the nanocomposites with increasing SiO_2 content. The decrease in strength from that of pure epoxy is initially low for 1 and 3 wt% SiO_2, but is quite significant for 5 wt% SiO_2. However, the ductility of the material increased with increasing SiO_2 content, as the strain at which failure occurs increased, especially at 5 wt% SiO_2. It is unclear why, despite

the increased plastic deformation prior to failure, the UTS of the nanocomposites decreased with increasing filler content. The fracture surfaces shown in Figures 4.40 to 4.43 highlight the increasing roughness of the surface at higher filler contents. The rougher surface is often due to crack deflection or bifurcation [166, 224], but this was more prominent only at 3 and 5 wt% SiO_2, since the surfaces at 1 wt% were still relatively smooth. Other common features observed in nanocomposites such as particle pullout (debonding) or plastic void growth [133, 166, 225] were not observed in the fracture surfaces. The microcracks that formed on the rougher sections of the fracture surfaces appeared similar to those observed in ceramic gels after shrinkage, particularly at higher SiO_2 contents as seen in Figure 4.43b. At lower SiO_2 content these microcracks appear close to the points where larger cracks are pinned or deflected (e.g. Figure 4.41b and Figure 4.42b). At 5 wt% microcracks were visible on most of the fracture surface, although these appear to be different from those observed at 1 and 3 wt% SiO_2.

The area underneath the tan δ peaks in the DMA data (Figure 4.44b) is larger in the nanocomposites than in pure epoxy due to the increased broadness of the tan δ. The larger area corresponds to an improvement in the damping ability of the nanocomposites, meaning that they are able to dissipate energy more effectively than pure epoxy. This is consistent with the increased roughness and ductility of the nanocomposites (especially at 5 wt%) observed from the tensile tests, which makes the decrease in the UTS unexpected.

4.5 *Ex-situ* epoxy-SiO_2 nanocomposites

Ex-situ epoxy-SiO_2 nanocomposites were prepared using pre-synthesized nanoparticles, both with and without surface functionalization with APTES. Figure 4.46 shows the morphology and dispersion of the unfunctionalized SiO_2 particles in the epoxy. The particles (10-20 nm) generally formed agglomerates between 200 nm and 2 μm. The agglomerates were also densely packed, forming closed structures. The nanocomposites containing SiO_2 functionalized with APTES showed slight improvements in the state of dispersion, shown in Figure 4.47. The agglomerates formed were usually smaller (200-500 nm), as seen in Figure 4.47a and b. Larger agglomerates were fewer in number, and the SiO_2 particles were less densely packed within the agglomerates, resulting in more porous or open structures, as highlighted in Figure 4.47c and d.

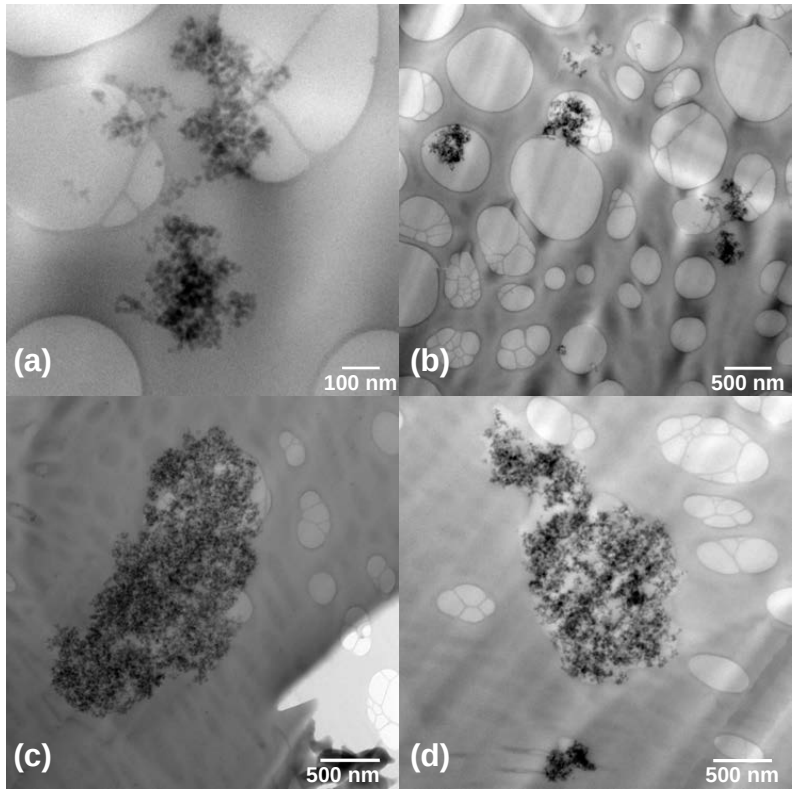

Figure 4.46. TEM images of epoxy-SiO_2 nanocomposites prepared *ex situ*, containing 0.5 wt% of pre-synthesized SiO_2 without surface functionalization.

The pre-synthesized SiO_2 particles were characterized after functionalization with APTES, prior to mixing with the epoxy. TGA measurements of the particles confirm the presence of moisture on the nanoparticle surface, and also reveal that the APTES constitutes ~19 % of the mass of the SiO_2. BET measurements show the particles have a specific surface area of ~58 $m^2\,g^{-1}$, which corresponds to a particle coverage of ~33 APTES molecules nm^{-2}, assuming that the particles do not agglomerate. Despite the improvement in the state of dispersion of the SiO_2 when APTES was used, it was still worse when compared to the nanocomposites where the SiO_2 was prepared *in situ*. This difference in the state of dispersion is more significant when considering that the *ex-situ* nanocomposites contain only 0.5 wt% SiO_2, in contrast to the 5 wt% SiO_2 shown in Figure 4.1a.

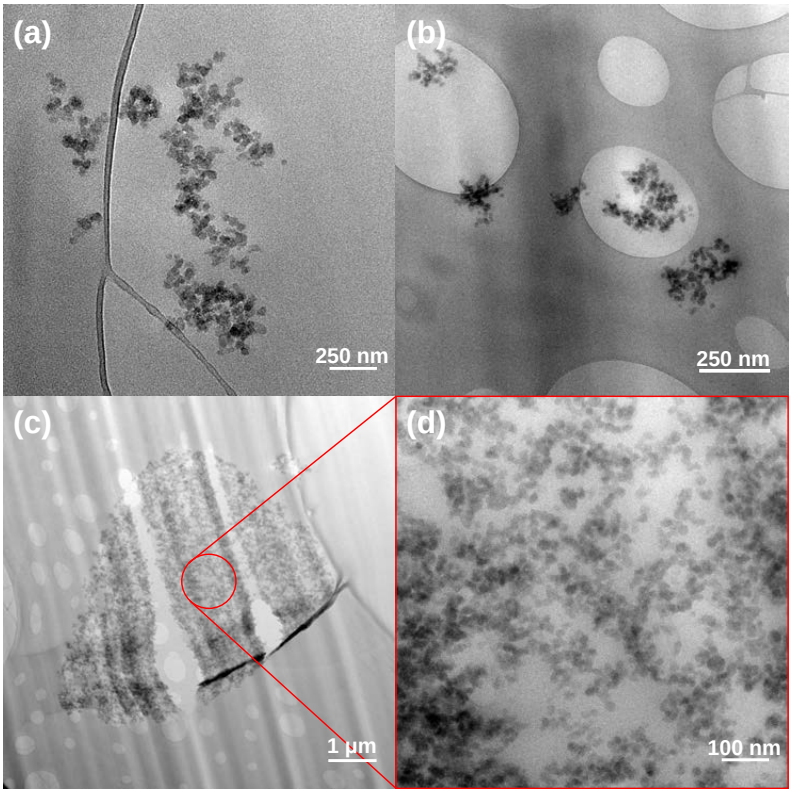

Figure 4.47. TEM images of epoxy-SiO_2 nanocomposites prepared *ex situ*, containing 0.5 wt% of pre-synthesized SiO_2 with surface functionalization using APTES. **(a)** and **(b)** show the smaller agglomerates with open structures. **(d)** shows a magnified region within the agglomerate shown in **(c)**.

Figure 4.48 shows the real relative permittivity and tan δ of the *ex-situ* nanocomposite (with 0.5 wt% SiO_2) compared to pure epoxy. Despite the presence of agglomerates, both ϵ'_r and tan δ of the *ex-situ* nanocomposites were lower than that for pure epoxy in different frequency regions. At frequencies below ~5000 Hz, ϵ'_r of the *ex-situ* nanocomposite was lower. Meanwhile, tan δ was lower for the *ex-situ* nanocomposite above ~1 Hz. The β-relaxation showed changes similar to those observed in Figure 4.13b and d. The tan δ peak for the β-relaxation appeared as a shoulder on another peak, as shown by the right arrow in Figure 4.48b. In addition, the shape of ϵ'_r is flatter in the *ex-situ* nanocomposite, and the β-relaxation appears to be taking place over a wider frequency range, as

shown by the increase in ϵ'_r over 10^4 Hz. The same effect is not observed in the shapes of ϵ'_r in the *in-situ* nanocomposites (Figure 4.13a and c). The new relaxation observed at low frequencies for the *in-situ* nanocomposites is also observed in the *ex-situ* nanocomposites, highlighted by the left arrow in Figure 4.48b. This relaxation is present at a lower frequency in the *ex situ* nanocomposites than in the *in situ* nanocomposites.

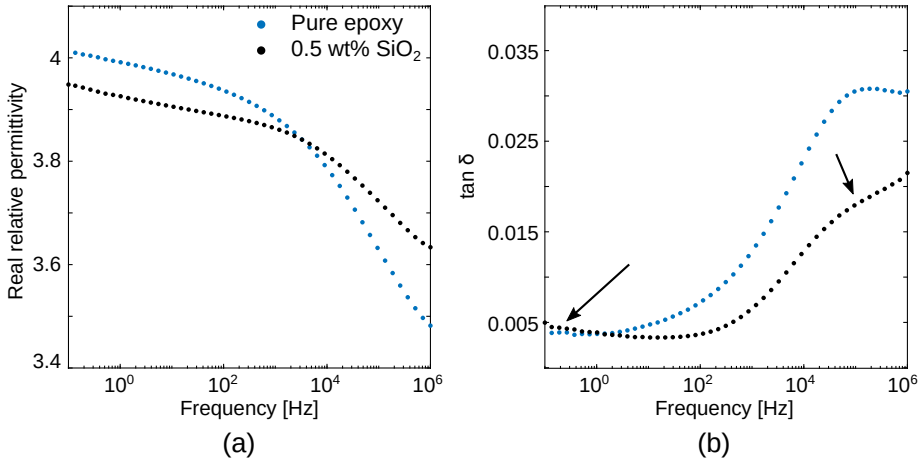

Figure 4.48. The **(a)** real relative permittivity and **(b)** dielectric loss tangent of pure epoxy and the *ex situ* epoxy-SiO_2 nanocomposite prepared using APTES, with 0.5 wt% of pre-synthesized SiO_2.

The complex permittivity of the *ex-situ* nanocomposites at higher temperatures is displayed in Figure 4.49. The permittivity behaves similarly to the nanocomposites prepared *in situ*. The T_g for the *ex-situ* nanocomposite was also decreased with the low filler content, as the α-relaxation emerged between 60 and 70 °C. The LFD/EP effect is present, as evidenced by the increase in ϵ''_r above the glass transition at low frequencies. However, the increase in ϵ'_r and ϵ''_r above the glass transition is not as large as was observed for the *in-situ* nanocomposites with low SiO_2 content (1 wt%).

Figure 4.50 shows the fits of ϵ''_r of the *ex-situ* nanocomposite to both the HN and DH functions, and the obtained parameters. Table 4.7 compares these parameters for pure epoxy, the *ex-situ* nanocomposite, and the *in-situ* nanocomposite with 1 wt% SiO_2 (pH 7, 1:10 APTES:DGEBA mass ratio) from Tables 4.2 and 4.3. The β-relaxation is observed at a lower frequency in the *ex-situ* nanocomposites, and the relaxation is also narrower due to increased ordering in the dipole clus-

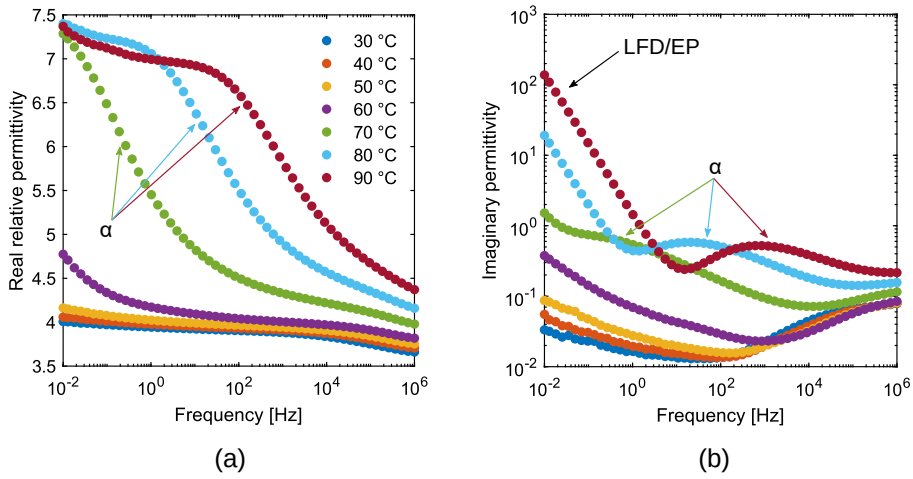

Figure 4.49. The **(a)** real relative permittivity and **(b)** imaginary permittivity of the *ex situ* epoxy-SiO_2 nanocomposite prepared using APTES, with 0.5 wt% of pre-synthesized SiO_2, between 30 and 90 °C.

ters. However, the β-relaxation is also more asymmetric. Therefore, the presence of the SiO_2 particles in the *ex-situ* nanocomposites, compared to the *in-situ* nanocomposites, appears to lead to the O-H dipoles becoming less responsive to the electric field, but with increased ordering in the clusters. Likewise, the new relaxation is also observed at a lower frequency, and the dipole clusters are more organized in the *ex-situ* nanocomposites than in the *in-situ* nanocomposites.

The dielectric spectroscopy showed that permittivities and losses in the *ex-situ* nanocomposites are comparable to the *in-situ* nanocomposites for small amounts of SiO_2, even if the state of dispersion is significantly poorer in the *ex-situ* nanocomposites. In addition, the difference in the morphology of the SiO_2 particles in the *ex-situ* nanocomposite results in a change in the shape of the permittivity plot. The increase in ϵ'_r at high temperatures and low frequencies is more restricted in the *ex-situ* nanocomposite. The agglomeration of the SiO_2 also results in more opaque samples, making it difficult to perform electrical treeing measurements as the needle is no longer visible. In conclusion, the preparation of *ex-situ* nanocomposites with a dispersion quality that is equal to that of the *in-situ* nanocomposites is challenging, especially at higher filler contents.

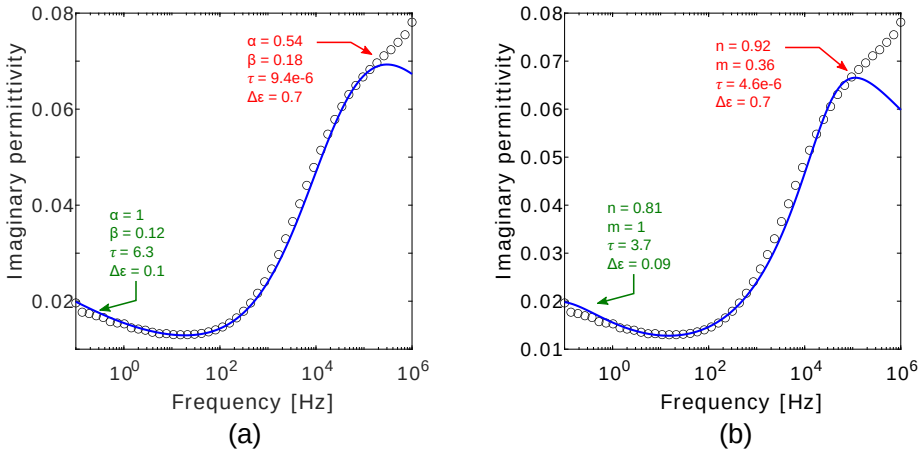

Figure 4.50. Fit of the imaginary permittivity of the *ex-situ* prepared nanocomposite (0.5 wt% SiO_2) to the **(a)** Havriliak-Negami function, and **(b)** Dissado-Hill function. The parameters for the two relaxations used in each function are shown.

Table 4.7. Parameters obtained from the fits of the imaginary permittivity of pure epoxy and epoxy-SiO_2 nanocomposites (*in-situ* with 1 wt% SiO_2 and *ex-situ* with 0.5 wt% SiO_2) to the Havriliak-Negami and Dissado-Hill functions.

Havriliak-Negami function								
Sample	β**-relaxation**				**Second relaxation term**			
	$\Delta\epsilon$	τ **[s]**	α	β	$\Delta\epsilon$	τ **[s]**	α	β
Pure epoxy	0.71	3.3×10^{-6}	0.43	0.62	0.32	62.1	0.55	0.055
Ex-situ SiO_2 [a]	0.70	9.4×10^{-6}	0.54	0.18	0.10	6.3	1	0.12
In-situ SiO_2 [b]	0.81	1.2×10^{-6}	0.44	0.54	0.13	3.6×10^{-3}	0.37	1
Dissado-Hill function								
Sample	β**-relaxation**				**Second relaxation term**			
	$\Delta\epsilon$	τ **[s]**	**n**	**m**	$\Delta\epsilon$	τ **[s]**	**n**	**m**
Pure epoxy	1.07	3.3×10^{-6}	0.89	0.25	0.62	0.36	0.49	0.01
Ex-situ SiO_2 [a]	0.70	4.6×10^{-6}	0.92	0.36	0.09	3.7	0.81	1
In-situ SiO_2 [b]	0.55	5.6×10^{-7}	0.48	0.25	0.092	5.8×10^{-4}	0.014	0.080

[a] 0.5 wt% SiO_2 content.
[a] 1 wt% SiO_2 content, prepared at pH 7 with APTES:DGEBA mass ratio of 1:10.

4.6 Molecular dynamics simulations of epoxy-SiO_2 nanocomposites

In this section, the molecular dynamics calculations of selected thermal and mechanical properties of epoxy-SiO_2 nanocomposites, using two different models for the SiO_2 structures, are presented. The organization of the polymer chains around the SiO_2 structures is investigated, and the potential interactions of the different molecules at the interfaces are discussed. Comparisons are made, where possible, to the measured data to allow verification of the models built for the MD simulations, which may be used to explain experimental results.

4.6.1 Distribution and coordination of the SiO_2 in the models

The two models used to represent SiO_2 in the simulations are illustrated in Figure 4.51. In Model I, the nanoparticle is more crystalline and includes more bonds between SiO_2 units, resulting in the tertiary and quaternary Si atoms, which are shown in Figure 4.52. Tertiary Si have 3 -O-Si bonds, and account for ~60-80 % of the Si in Model I, while the rest of Si are quaternary Si with 4 -O-Si bonds. Since this particle is placed in the middle of a periodic unit cell, it effectively simulates a uniform homogeneous dispersion of SiO_2 particles in the epoxy, since each particle will always have a fixed and equal distance to the particle in the neighbouring cell.

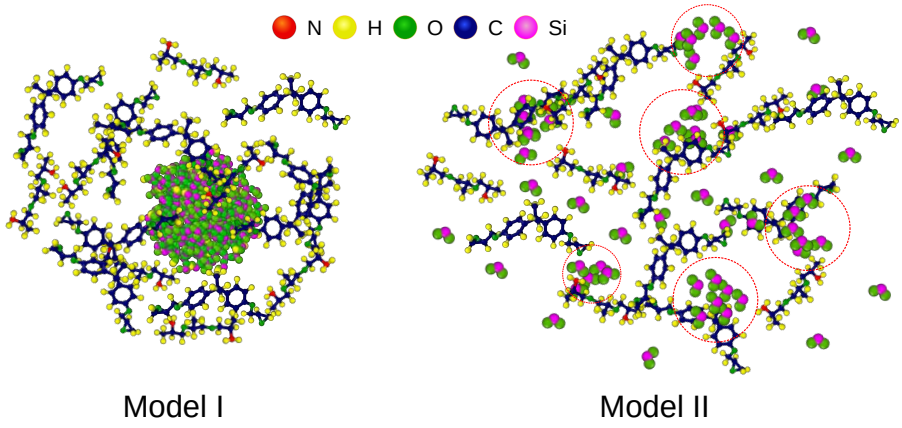

Figure 4.51. Illustration exemplifying the dispersion and structure of SiO_2 in the epoxy-SiO_2 nanocomposites in Models I and II, prior to cross-linking of the epoxy. The red dotted lines show clusters of molecular SiO_2 units in Model II.

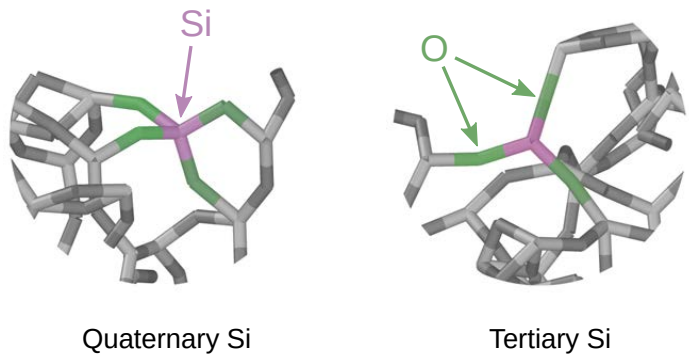

Figure 4.52. Examples of quaternary and tertiary Si atoms, with 4 and 3 -O-Si bonds, respectively, in the nanoparticles built in Model I.

On the other hand, the SiO_2 in Model II consist of simple O-Si-O molecules with no bonds between them, and are spread randomly around amidst the DGEBA and POPDA molecules. Therefore, Model II resembles a random dispersion of SiO_2 instead of a uniform one as in Model I. An additional difference is the lack of surface hydroxy groups in Model II, compared to the ones added to the nanoparticle surface in Model I.

Selected radial distribution functions (RDFs) from Models I and II are shown in Figures 4.53 and 4.54. In Figure 4.53, the RDF plots show the density and distribution of terminal C atoms (in the epoxide groups) and O atoms (in the C-O-C ether groups) in DGEBA, from the quaternary and tertiary Si atoms in the built nanoparticle (shown in Figure 3.4c). Figure 4.53 highlights how the arrangement of the different atoms at the interfaces significantly changes with increasing size of the nanoparticle in Model I. At 1 nm, the RDF plots exhibited sharper and more defined peaks, corresponding to coordination of the specified atoms around the tertiary or quaternary Si atoms at fixed distances. As the nanoparticle size increases, the peaks become broader and more diffuse. In all cases, the coordination generally becomes more uniform with increased distance from the particle surface. This behaviour was consistent for the RDFs of different atoms on the epoxy chains (as shown in Figure 4.53 for both terminal C atoms and O atoms that are more central in the DGEBA molecule). The RDFs obtained from Model II (Figure 4.54) show that the coordination of the different atoms around the Si in the SiO_2 units is different to that in Model I. The changes in the RDF with the varying SiO_2 content are less significant in Model II compared to the changes with particle size observed in Model I.

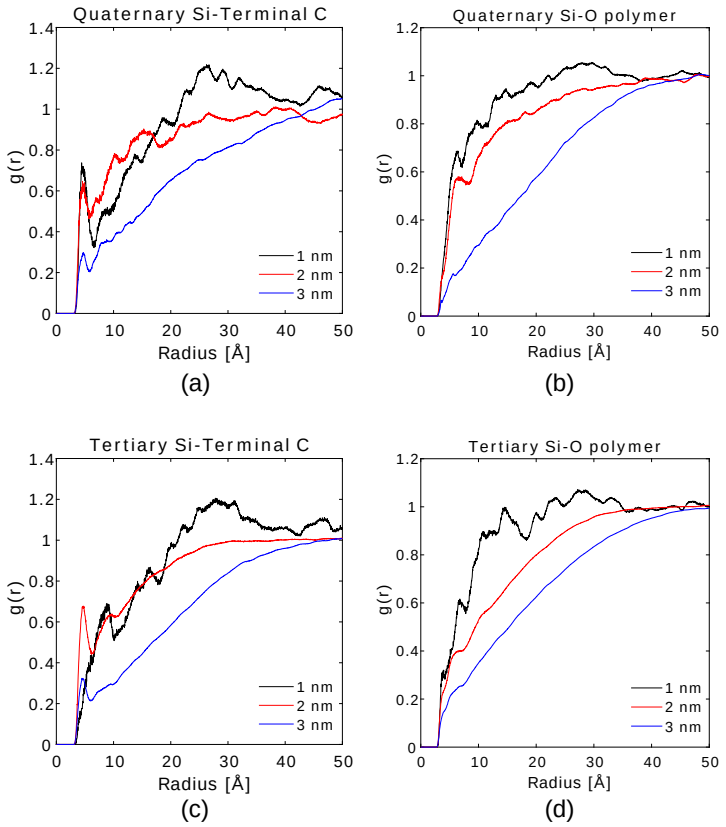

Figure 4.53. Selected RDFs for **(a,c)** terminal C atoms in DGEBA (from the epoxide groups), and **(b,d)** O atoms in the C-O-C ether group of DGEBA (O-polymer) with both quaternary and tertiary Si atoms in Model I as the reference atom. The radius is calculated from the position of the Si atoms.

The distribution and organization of the different atoms from the Si atoms becomes uniform at a shorter distance as well compared to Model I ($g(r)\rightarrow 1$ at ~25 Å instead of >40 Å). The distance at which the RDF approaches 1 can be used as an estimate of the extent of the interfacial region between the SiO_2 and the polymer chains. In Model I with the SiO_2 nanoparticles, the interface extended up to 3-5 nm in larger particles and >5 nm for 1 nm sized particles. In Model II with the SiO_2 molecular units, the interface did not extend beyond 2 nm, and was independent of the SiO_2 content.

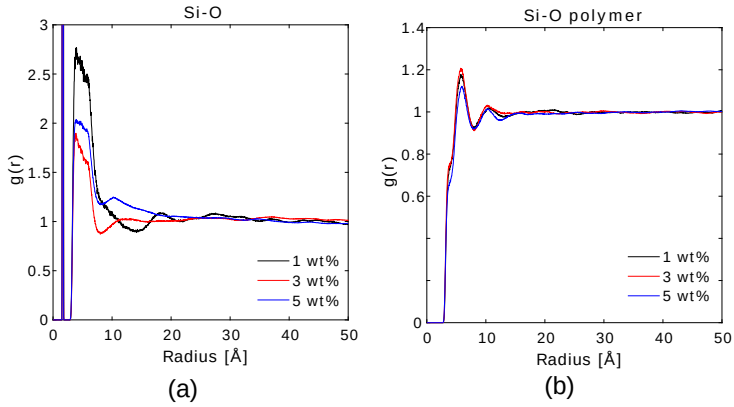

Figure 4.54. Selected RDFs for **(a)** O atoms in the SiO_2 molecular units, and **(b)** O atoms in the C-O-C ether group of DGEBA (O-polymer) with Si atoms from the SiO_2 in Model II as the reference atom. The radius is calculated from the position of the Si atoms.

Table 4.8 shows the coordination numbers of selected atoms with respect to the Si atoms in both Model I and Model II, which were obtained from the RDF plots. In Model I, increasing the nanoparticle size generally led to a decrease in the total coordination numbers of the various atoms around the quaternary and tertiary Si atoms. In Model II, the total coordination of the different atoms around the Si atoms were higher than in Model I. In addition, the coordination numbers of neighbouring Si and O atoms decreased when increasing the SiO_2 content in the system from 1 to 3 wt%, but increased slightly when the SiO_2 content was increased from 3 to 5 wt%.

The coordination numbers for atoms from different parts of the epoxy chains around the Si atoms in both Model I and Model II reveal what the closest and most likely interactions are between the SiO_2 and the polymer. In Model I the most frequent groups surrounding the nanoparticles tend to be the groups at the ends of DGEBA and POPDA chains that are not cross-linked, or the branching N atoms in cross-linked chains. In addition, the RDFs confirmed that there are fewer interactions between the atoms in the nanoparticles with the polymer chains as the particles get larger, which is expected due to the decreasing total interfacial area per unit volume with larger particles.

In Model II, the Si and O atoms from neighbouring SiO_2 units have higher coordination numbers than atoms in the epoxy chains. Therefore there is some degree of clustering of the SiO_2 units after the system is mixed in the NVT ensemble. The clustering of the SiO_2 is also illustrated in Figure 4.51, where

Table 4.8. Coordination numbers of selected atoms with respect to Si atoms in Model I and II.

System	N [a]	H [b]	C [c]	O [d]	NCC [e]	Si [f]	O [g]
Model I Quaternary Si atoms							
1 nm	3.2	0.6	1.6	1.9	1	-	-
2 nm	1.6	0.9	1.2	2.4	0.8	-	-
3 nm	1.4	0.1	0.6	0.3	0.4	-	-
Model I Tertiary Si atoms							
1 nm	1	0.1	2.9	2.1	1.2	-	-
2 nm	2.1	0.5	1.5	1.4	1	-	-
3 nm	1.4	0.2	0.7	0.8	0.3	-	-
Model II							
1 wt%	6.5	2.3	4	4.6	4.7	9.6	9.6
3 wt%	5.3	2.4	4.3	4.7	4.9	6.5	6.4
5 wt%	5.1	2.3	3.9	4.3	4.4	7.7	7.5

[a] Primary amine (N) in unreacted POPDA.
[b] H in aromatic rings in DGEBA.
[c] Terminal C in unreacted epoxide group in DGEBA.
[d] O in C-O-C ether group in DGEBA.
[e] Tertiary amine (N) in POPDA linked to 2 DGEBA molecules.
[f] Si atoms in SiO_2 molecular units.
[g] O in SiO_2 molecular units.

not all the individual SiO_2 units are dispersed far from each other. However, the coordination numbers of both Si and O decreased in the system with 3 wt% SiO_2, showing that the SiO_2 units are less clustered for that filler content. Subsequently, the coordination number of the other atoms (terminal C, aromatic H, O in the C-O-C, and the tertiary amine) to Si increased, showing that the decrease in clustering enabled different parts of the polymer chains to approach the SiO_2 units. Due to the smaller size of the SiO_2 units in Model II, the epoxy chains can surround the SiO_2 to a greater degree, resulting in higher coordination numbers compared to Model I. The change in coordination numbers with SiO_2 content is also less significant in Model II, since the individual SiO_2 units do not change in size.

4.6.2 Thermal and mechanical properties

The calculated values of T_g, the tensile elastic moduli, and the thermal conductivities from the MD simulations are reported in Table 4.9. The measured T_g (from both DSC and DMA) and elastic moduli for epoxy-SiO_2 nanocomposites (prepared at pH 7 with APTES:DGEBA mass ratio of 1:10) are also included for comparison. The T_g presented in Table 4.9 was measured from the intersection between the slopes of the density-temperature plots shown in Figure 4.55, obtained via linear regression at the low and high temperature ends (shown as the dotted lines). Figure 4.56 shows the simulated tensile stress-strain behaviour for the different systems. The fit through the data points was obtained using the Mooney-Rivlin relation (Equation (3.9)). The elastic moduli was calculated from the slope of the fit up to a strain of 1 %.

Increases in the cross-linking degree in pure epoxy resulted in increases in the calculated T_g by 47 % , the elastic modulus by 65 %, and the thermal conductivity by 16 %. The measured values for T_g (from both DSC and DMA) and the elastic modulus for pure epoxy were between those predicted with ~60 and ~90 % cross-linking. In the nanocomposites (both Model I and Model II), a maximum cross-linking of ~80 % was reached. The T_g calculated for Model I was closer to that measured by DMA, whereas the T_g calculated from Model II was closer to that measured by DSC. The nanocomposites in both models exhibited a decrease initially in T_g, followed by an increase with increasing filler content (or particle size). A similar change in the elastic moduli of the nanocomposites using Model II was also observed with increasing filler content or particle size. In all cases, the nanocomposites possessed a lower T_g and elastic moduli than the pure epoxy with 90 % cross-linking. The thermal conductivities of nanocomposites increased with increasing particle size in Model I. The nanocomposites in Model II showed a significantly larger increase in the thermal conductivities for all the systems with different wt% of SiO_2 (above 163 %).

Table 4.9. Calculated and experimentally measured thermal and mechanical properties of pure epoxy and epoxy-SiO_2 nanocomposites from MD simulations. Particles of size 1, 2, and 3 nm in Model I correspond to SiO_2 contents of 1, 5, and 15 wt%, respectively.

SiO_2 content [wt%]	T_g (DSC) [°C]	T_g (DMA) [°C]	T_g (MD) [°C]		E-modulus (experimental) [GPa]	E-modulus (MD) [GPa]		Thermal conductivity (MD) [W m^{-1} K^{-1}]	
			Model I	Model II		Model I	Model II	Model I	Model II
0	83	81	97 [a] 66 [b]		2.49	3.78 [a] 2.29 [b]		0.44 [a] 0.38 [b]	
1	72	61	55	84	2.01	2.35	3.37	0.32	1.16
3	75	56	-	73	2.38	-	2.14	-	1.22
5	87	66	64	96	3.06	2.54	3.33	0.45	1.77
15	-	-	89	-	-	2.75	-	0.62	-

[a] 90 % cross-linking
[b] 60 % cross-linking

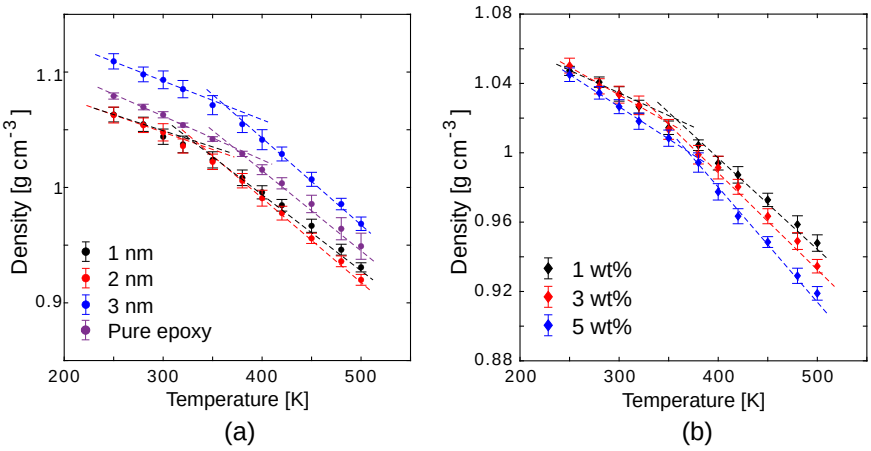

Figure 4.55. The simulated changes in density with temperature for **(a)** pure epoxy (~90 % cross-linking) and epoxy-SiO_2 nanocomposites using Model I, and **(b)** epoxy-SiO_2 nanocomposites using Model II.

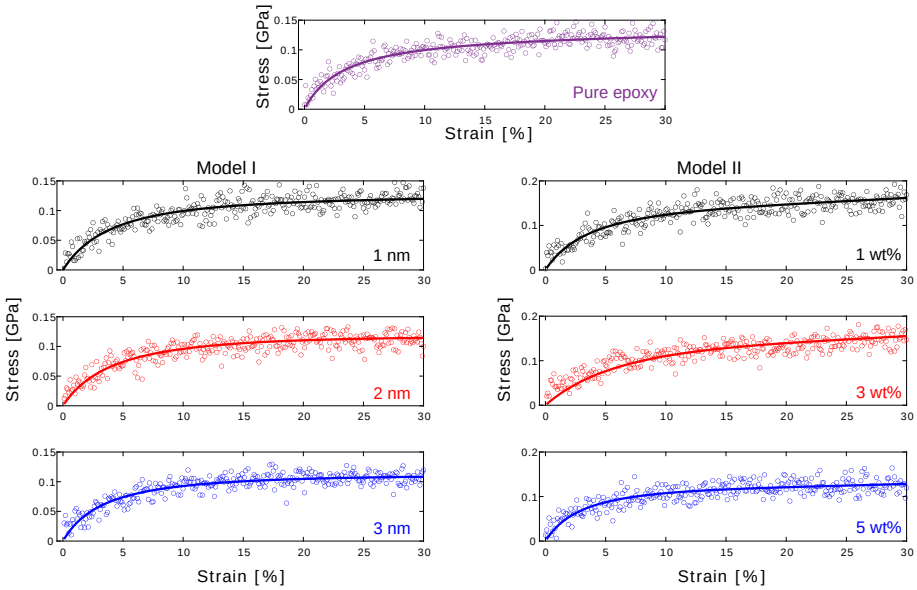

Figure 4.56. The simulated tensile elastic moduli for pure epoxy (~90 % cross-linking) and epoxy-SiO_2 nanocomposites using both Model I and Model II.

4.6.3 Discussion

Both the T_g and the elastic modulus were predicted reasonably well by the MD simulations. A system with a cross-linking degree between ~70 and 80 % would be the most representative model for accurately predicting the T_g of epoxy and its nanocomposites. In reality it is difficult to achieve above ~80-90 % cross-linking, since as the epoxy cures further (as the cross-linking reactions proceed), it becomes more difficult for the DGEBA and POPDA molecules to diffuse around. Hence, there will always be some molecules that have not reacted completely since they are "frozen in", thereby preventing a 100 % cross-linking degree. The DSC measurements shown in Figure 4.45 confirm that all possible cross-linking reactions which can take place in the nanocomposites are completed.

In the nanocomposites, both models exhibited the same trends in the glass transition behaviour compared to the experimental results. The effect of the SiO_2 on the mobility of the epoxy chains was therefore simulated correctly in both cases. Deviations in the predicted properties can be attributed to the differences in how the SiO_2 is incorporated in the two models. In Model I, the inclusion of surface hydroxy groups will affect the interactions between the Si at the surface of the nanoparticles with the epoxy chains. While Model II does not include hydroxy groups, more of the epoxy chains are present closer to the SiO_2 molecules. The closer proximity and interactions might explain why the predicted T_g and elastic modulus are higher in Model II than in Model I, especially for 5 wt% SiO_2. An exception is observed for the nanocomposite with 3 wt% SiO_2, where the SiO_2 units are more dispersed. It is unknown why the clustering is decreased at 3 wt% SiO_2, or why the increased coordination of the atoms from the organic molecules around the SiO_2 resulted in a decrease in both the T_g and the elastic modulus when the opposite is expected.

The calculated thermal conductivities are compared to reported values, as the thermal conductivity was not measured in the present work. Kochetov et al. [226] reported the thermal conductivities of pure epoxy and epoxy-SiO_2 nanocomposites (up to 15 wt% SiO_2), showing an increase from 0.168 to 0.199 $W\,m^{-1}\,K^{-1}$. The thermal conductivity calculated for pure epoxy in this work was more than twice as large even for the system with 60 % cross-linking. However, the increase in thermal conductivity with increasing SiO_2 content was reflected in the calculated values for the nanocomposites using both models. The increase in the thermal conductivity was significantly larger in Model II, and the obtained values were closer to those for thin films of SiO_2 [227, 228]. The mismatch in thermal conductivity might be caused by the assumption that the models do not exhibit significant diffusion. If diffusion of the SiO_2 units is present in Model

II, the potential energy term in the heat flux will be non-zero and its contribution must be added to the total heat flux [229]. Model I, therefore, is the better option for estimating the thermal conductivity of the nanocomposites, since it is not possible for the larger SiO_2 nanoparticle to diffuse through the system compared to the smaller SiO_2 molecules. Thus, the system in Model I should be more representative of the real material.

Although the MD simulations can be quite useful in characterizing epoxy nanocomposites, specific models might be more suitable for predicting different properties under various conditions. Based on the results obtained from the two models employed in this work, it is probable that a hybrid system would provide a better representation of the nanocomposites. In such a hybrid system, the SiO_2 would be in particle form with a defined size, but dispersed randomly in the epoxy rather than in a fixed uniform distribution. The inclusion of bonded interactions at the interfaces, via SCAs for example, can also contribute to improvements in the models and in the predicted thermomechanical properties of the nanocomposites.

5 Epoxy-TiO_2 and epoxy-Al_2O_3 nanocomposites

This chapter discusses the *in-situ* synthesis of TiO_2 and Al_2O_3 in the epoxy and presents the resulting properties, morphologies, and structure of the nanocomposites. It should be noted that while the nanoparticles prepared from the aluminium isopropoxide are referred to as Al_2O_3, it is likely that these inorganic particles are some form of amorphous boehmite (AlO(OH)), which is discussed further in Chapter 5.5.1.

5.1 Structure and morphology of the *in-situ* synthesized TiO_2 and Al_2O_3

The *in-situ* synthesized TiO_2 and Al_2O_3 nanoparticles exhibited different morphologies. Figure 5.1 shows that the TiO_2 formed discrete particles with a well-defined shape, when compared to the SiO_2 clusters described in Chapter 4.1. The particles, pointed out by the arrows in Figure 5.1a, were also more sparse than the SiO_2 but well-dispersed, especially at lower TiO_2 content. Generally, the particles were between 10 and 50 nm (Figure 5.1b,c), but at higher TiO_2 content they were found to also form larger agglomerates (consisting of ~150-200 nm particles), like the one shown in Figure 5.1d.

The Al_2O_3 on the other hand exhibited a variety of morphologies, as shown in Figure 5.2. At lower Al_2O_3 contents, the particles formed diffuse clusters similar to those observed in the epoxy-SiO_2 nanocomposites (as seen in Figure 4.1a and b), only larger in size. Most clusters were around 250 nm (Figure 5.2a), but some large agglomerates of up to 1 μm were also found (Figure 5.2b). At higher filler contents (e.g. 4 wt%), similar clusters (of size ~250 nm) were observed, but these were closer to one another and were far more frequent, as seen in Figure 5.2e-g. However, in certain parts of the samples dispersed particles between 200 nm and 1 μm with a more defined, spherical shape were observed (Figure 5.2h).

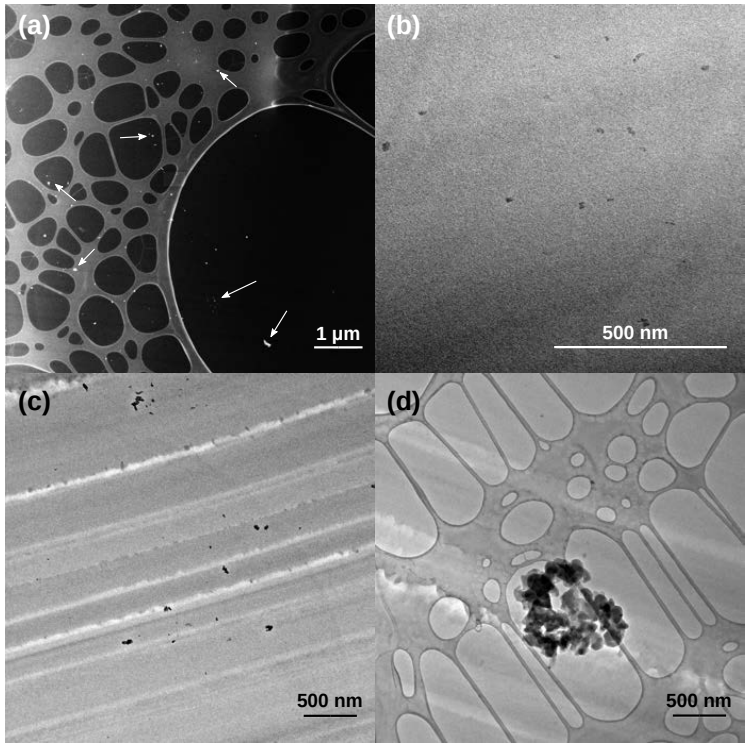

Figure 5.1. (a) Dark field STEM image of epoxy-TiO_2 nanocomposite with 3 wt% TiO_2. **(b, c, d)** TEM images of epoxy-TiO_2 nanocomposites with 5 wt% TiO_2, exhibiting both discrete, irregularly-shaped dispersed particles as well as spherical particles in larger agglomerates. The arrows point to some of the TiO_2 nanoparticles or clusters of particles.

The differences in the morphology between the TiO_2 and Al_2O_3 nanoparticles are reflected by the scattering profiles from SAXS, shown in Figure 5.3. The scattering for the epoxy-TiO_2 nanocomposites exhibited a Guinier plateau between 0.01 and 0.06 $Å^{-1}$, with a Guinier knee at ~0.06-0.1 $Å^{-1}$. Two additional features were observed at low (~0.01 $Å^{-1}$) and high (~0.2 $Å^{-1}$) q. At low q, the scattering intensity increased slightly in all the nanocomposites, whereas at high q it appears that there was an additional but very subtle "bump" in the scattering intensity, as pointed out by the arrow in Figure 5.3a.

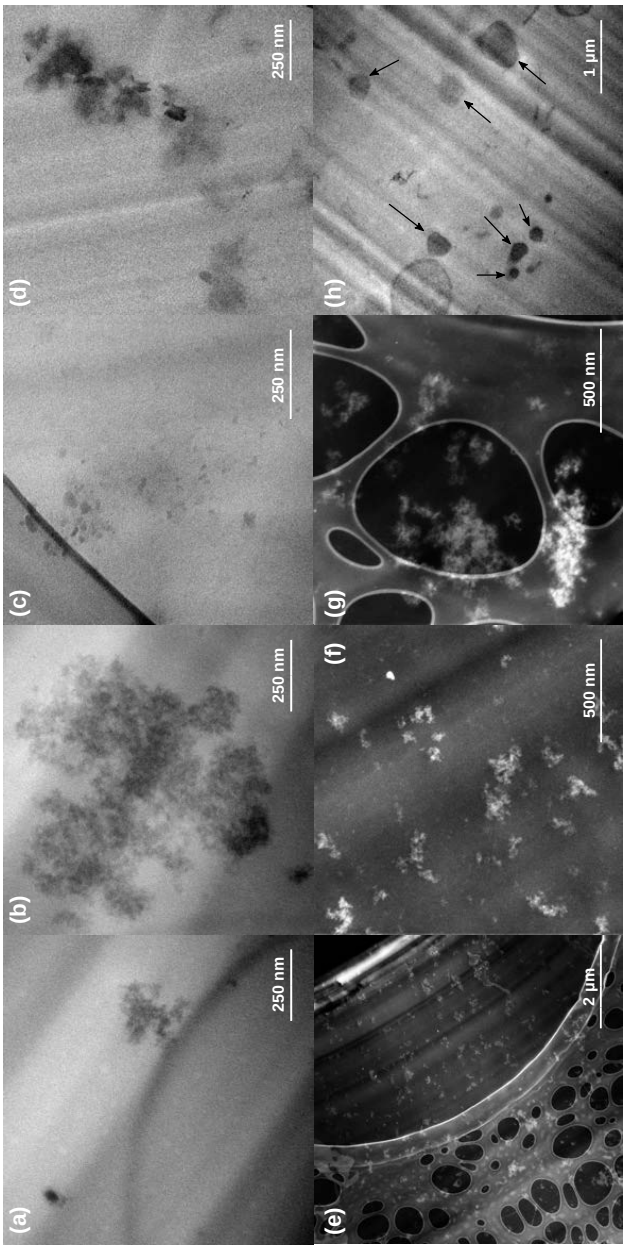

Figure 5.2. TEM and STEM images of the Al_2O_3 nanostructures formed in epoxy containing **(a,b)** 2 wt%, **(c,d)** 3 wt%, and **(e-h)** 4 wt% Al_2O_3. The arrows in **(h)** point to the larger, discrete Al_2O_3 particles.

The epoxy-Al_2O_3 nanocomposites exhibited scattering profiles that were similar to those observed for epoxy-SiO_2 nanocomposites (Figure 4.4a). However, unlike in epoxy-SiO_2 where several Guinier features were evident, for the epoxy-Al_2O_3 nanocomposites the Guinier "knee" is present only at higher Al_2O_3 contents. The "knee" was observed at around 0.1 $Å^{-1}$ in 4 wt% Al_2O_3, and between 0.2 and 0.3 $Å^{-1}$ at 5 wt% Al_2O_3. At lower Al_2O_3 contents, the scattering intensity at high q was higher than that of pure epoxy, but did not exhibit any distinguishable features. At low q, all the nanocomposites exhibited a linear slope in the scattering below 0.03 $Å^{-1}$.

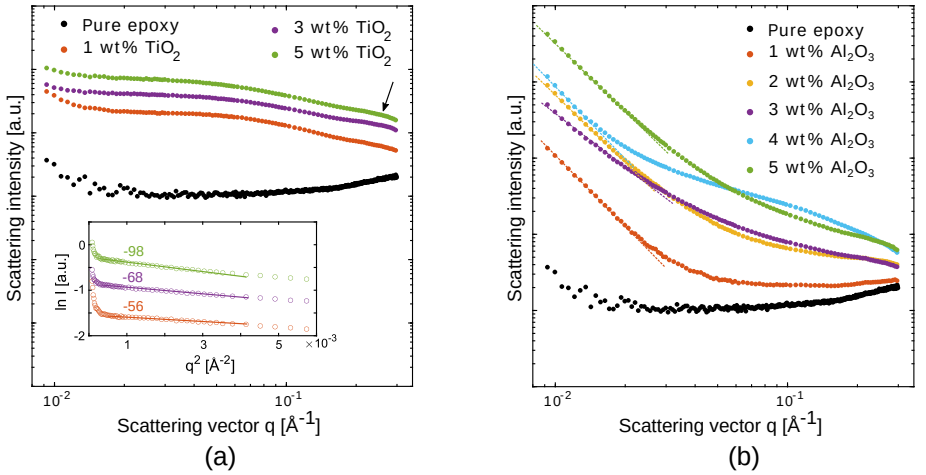

Figure 5.3. SAXS profiles of **(a)** epoxy-TiO_2 and **(b)** epoxy-Al_2O_3 nanocomposites with varying filler contents. The inset in **(a)** shows the Guinier plots, the slopes from which the radii of gyration (R_g) were obtained. The slopes of the plots in **(b)** (shown in dotted lines) give the fractal dimension.

Table 5.1 shows the structural parameters obtained from the analysis of the SAXS data for the nanocomposites. Guinier's law was used to estimate the radii of gyration (from the slope of the Guinier plots shown in the inset in Figure 5.3a) for the TiO_2 structures, from which the structure size (d) was obtained. The TiO_2 particles showed a slight increase in size with increasing filler content, although the sizes estimated were an order of magnitude smaller than those observed in the TEM images. The correlation length (ξ) between the domains appeared to be independent of the TiO_2 content, as the Guinier knees appear in the same q range.

In the epoxy-Al_2O_3 nanocomposites, it was expected that the formation of larger structures seen in the TEM images would result in a feature similar to the Guinier knee at $q < 0.01$ Å^{-1}. The slopes of the linear regions at low q were then used to estimate the fractal dimension (D) of these structures. In the Al_2O_3 nanocomposites D was between 2.3 and 3, although in most cases closer to 3. This indicates the formation of highly networked clusters that are close to forming surface fractals. Additionally, at higher filler contents a Guinier knee emerged at high q, being most noticeable for the nanocomposites with 4 and 5 wt% Al_2O_3. The corresponding correlation lengths were estimated to be 2-6 nm at high filler contents, and below 2 nm for 2 and 3 wt% Al_2O_3.

Table 5.1. Parameters obtained from fits of the Guinier and the power-law models for epoxy-TiO_2 and epoxy-Al_2O_3 nanocomposites.

Filler	R_g [Å]	d [nm]	D	Position of Guinier knee [Å^{-1}]	ξ [nm]
TiO_2 [a]					
1 wt%	12.9	3.3	-	0.05-0.1	6.3-12.6
3 wt%	14.3	3.7	-	0.05-0.1	6.3-12.6
5 wt%	17.1	4.4	-	0.05-0.1	6.3-12.6
Al_2O_3 [b]					
1 wt%	-	-	3	-	-
2 wt%	-	-	2.8	> 0.3	< 2.1
3 wt%	-	-	2.3	> 0.3	< 2.1
4 wt%	-	-	3	0.11-0.2	3.1-5.7
5 wt%	-	-	2.9	0.2-0.3	2.1-3.1

[a] No power-law region was observed at high q.
[b] No Guinier plateau observed, and no suitable fits could be made to the Unified model. The fractal dimension was obtained from the slope of the power-law region at low q.

The progress of the hydrolysis and condensation of the TIP is shown in the IR spectra in Figure 5.4a and b. The bands assigned to Ti-O (485 cm^{-1} [94]) and Ti-O-C (1009 and 1121 cm^{-1}, respectively [94,230,231]) in the alkoxide are present initially, but disappear quickly as the hydrolysis and condensation reactions proceed. The O-H band at around 3500 cm^{-1} is present from the time when the TIP (mixed in anhydrous 2-propanol) is added. The Ti-O-Si band at 949 cm^{-1} [232] is also present. As the reactions proceeded over 3 h, a broader band is observed between 600 and 700 cm^{-1} with sharp features that correspond to Ti-O-Ti bonds [15,94]. In the cured nanocomposites (Figure 5.4c) no significant differences are observed from the pure epoxy, with the exception of the Ti-O-Ti band.

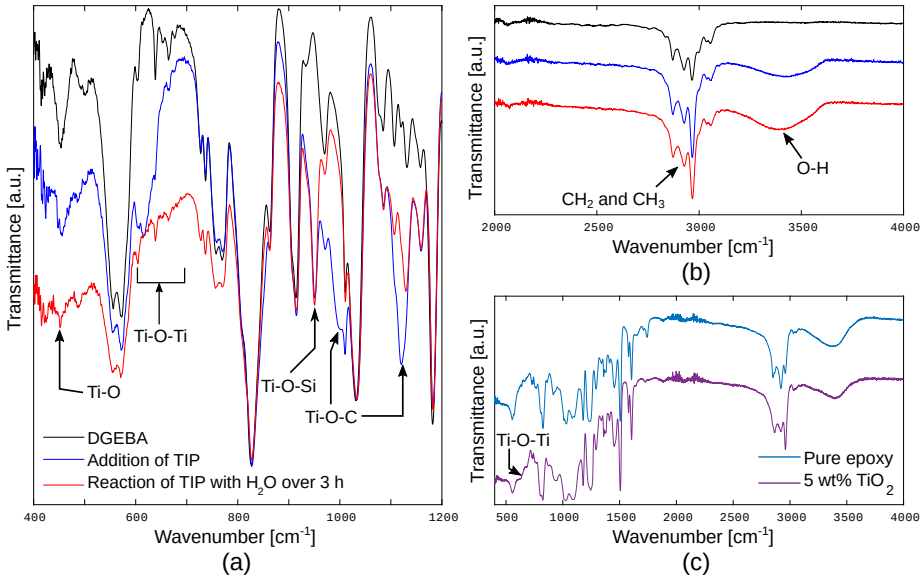

Figure 5.4. (a,b) FTIR spectra of the *in-situ* sol-gel reaction mixture during the synthesis of TiO_2 in epoxy (5 wt%). **(c)** FTIR spectra of the cured epoxy-TiO_2 nanocomposite compared to that of pure epoxy. All the spectra were normalized to the peak at 1509 cm^{-1}.

The subsequent changes in T_g with filler content of the epoxy-TiO_2 and epoxy-Al_2O_3 nanocomposites are shown in Figure 5.5a. T_g was higher for the epoxy-TiO_2 nanocomposites than for pure epoxy, although there was a large decrease in T_g between 3 and 5 wt% of TiO_2. For the epoxy-Al_2O_3 nanocomposites, the T_g varied with filler content. The nanocomposites containing 1 and 4 wt% of Al_2O_3 exhibited a slightly lower T_g, and those containing 2, 3, and 5 wt% exhibited a higher T_g than pure epoxy.

Figure 5.5b shows the thermogravimetric analysis of the epoxy-TiO_2 nanocomposites. Like the epoxy-SiO_2 nanocomposites, the epoxy-TiO_2 nanocomposites started decomposition at ~340 °C, whereas the pure epoxy began its thermal decomposition at 320 °C. The thermal stability of the epoxy-TiO_2 nanocomposites at higher temperatures increased with the filler content, as seen by the position of the plateau in the TGA plots between 400 and 500 °C which shifted to higher amounts of remaining mass with increased TiO_2 content.

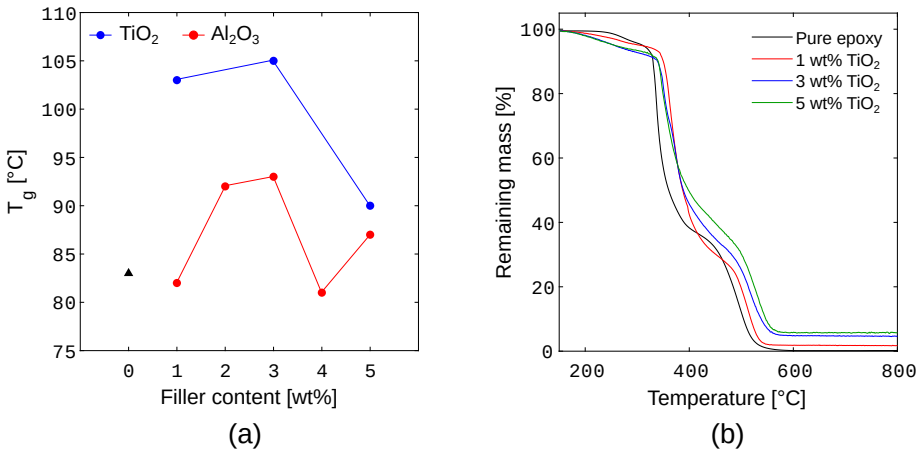

Figure 5.5. **(a)** Glass transition temperature (T_g) of the epoxy-TiO_2 and epoxy-Al_2O_3 nanocomposites as a function of the filler content. The error in the T_g is ± 2 °C. **(b)** The thermogravimetric analysis of epoxy-TiO_2 nanocomposites with different TiO_2 contents.

5.2 Dielectric properties

The real relative permittivities (ϵ'_r) and tan δ for the epoxy-TiO_2 and epoxy-Al_2O_3 nanocomposites at room temperature are presented in Figure 5.6. The TiO_2 nanocomposites exhibited an increase in ϵ'_r at 1 wt% TiO_2, which decreased below that of pure epoxy for 3 wt% TiO_2. At 5 wt% however, ϵ'_r is lower than that of pure epoxy only below ~4.8×10^4 Hz. The permittivity curve is therefore flatter, similar to that observed for the *ex-situ* epoxy-SiO_2 nanocomposite (Figure 4.48a). The changes in the tan δ for the epoxy-TiO_2, shown in Figure 5.6b, are similar to those observed for the *in-situ* epoxy-SiO_2 nanocomposites (Figure 4.13). The β-relaxation is no longer an individual peak but appears as a shoulder on another peak, and the relaxation is smaller (lower tan δ) above 100 Hz for the nanocomposites with 3 and 5 wt% TiO_2. In addition, the new relaxation from the TiO_2 nanoparticles is observed at a lower frequency (between 10^{-1} and 10^2 Hz, as indicated by the arrow in Figure 5.6b), and is stronger than in the epoxy-SiO_2 nanocomposites.

Meanwhile, the Al_2O_3 nanocomposites exhibited a decrease in ϵ'_r, although the decrease was not uniform at all frequencies. The same changes were observed for the β-relaxation in the tan δ as in the epoxy-TiO_2 nanocomposites, although the decrease in tan δ was larger in the epoxy-TiO_2 than in the epoxy-Al_2O_3 nanocomposites. However, the new relaxation observed in the epoxy-SiO_2 and

the epoxy-TiO_2 nanocomposites at low frequencies was evident for only 2 and 5 wt% Al_2O_3, where an increase in tan δ was observed that did not resemble a typical tan δ peak.

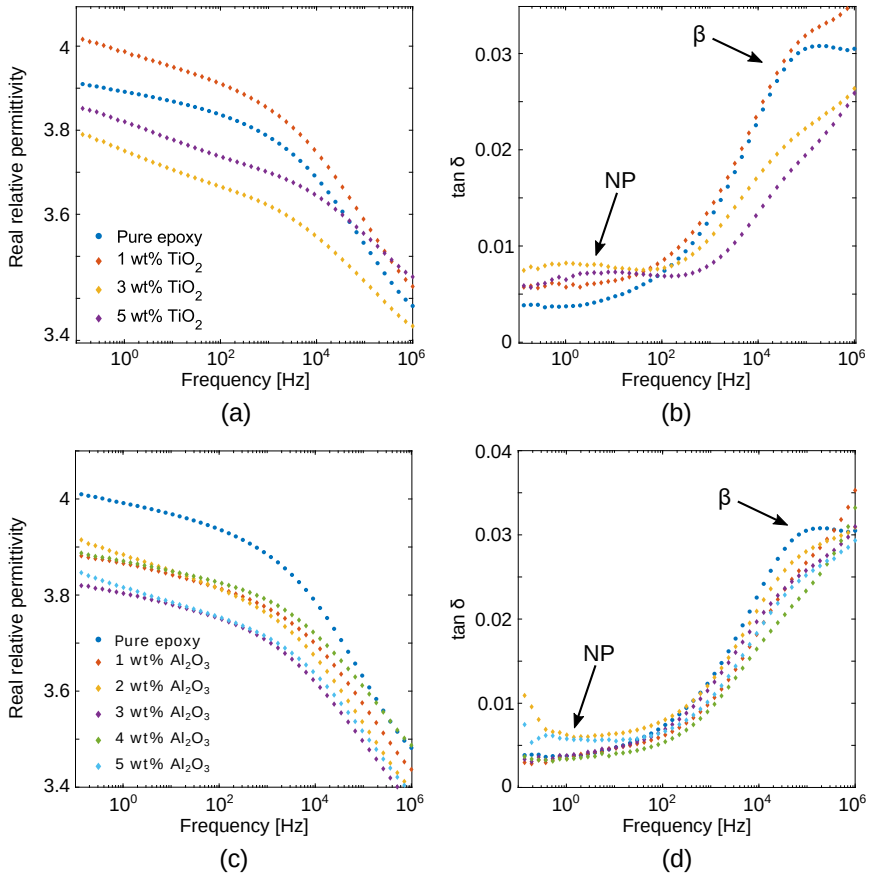

Figure 5.6. **(a,c)** Real relative permittivities and **(b,d)** loss tangents for **(a,b)** epoxy-TiO_2 and **(c,d)** epoxy-Al_2O_3 nanocomposites at room temperature. The arrows in **(b)** and **(d)** show the β-relaxation and the new relaxation from the nanoparticles (NP).

The fits of the imaginary permittivities (ϵ_r'') to the Dissado-Hill (DH) and Havriliak-Negami (HN) functions are shown in Figures 5.7 and 5.8, respectively, and Tables 5.2 and 5.3 show the parameters obtained for the fits.

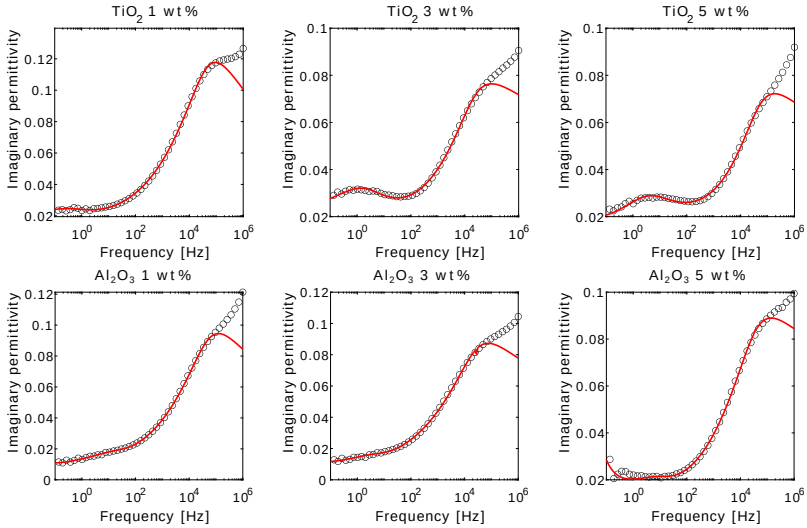

Figure 5.7. Fits of the imaginary permittivities of epoxy-TiO_2 (top row) and epoxy-Al_2O_3 (bottom row) nanocomposites to the Dissado-Hill function.

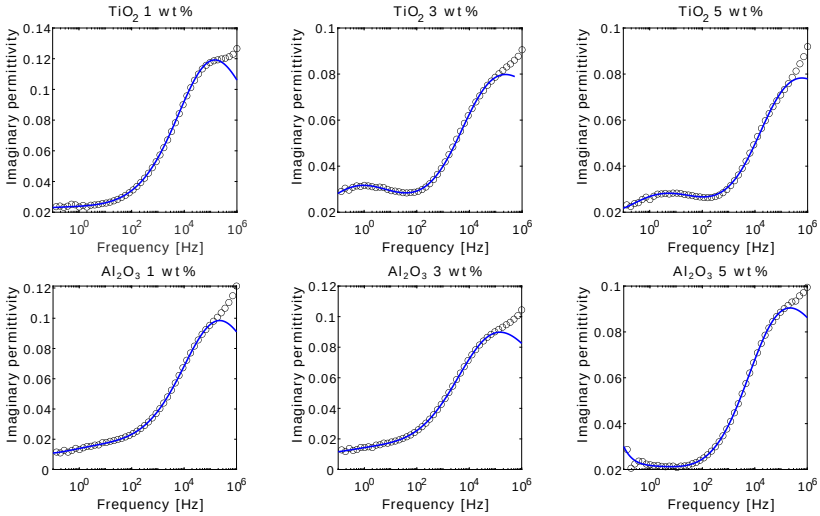

Figure 5.8. Fits of the imaginary permittivities of epoxy-TiO_2 (top row) and epoxy-Al_2O_3 (bottom row) nanocomposites to the Havriliak-Negami function.

Table 5.2. Parameters obtained from the fits of the imaginary permittivity of the epoxy-TiO_2 and epoxy-Al_2O_3 nanocomposites to the Dissado-Hill function.

Sample	β-relaxation				Second relaxation term			
	$\Delta\epsilon$	τ [s]	n	m	$\Delta\epsilon$	τ [s]	n	m
Pure epoxy	1.07	3.3×10^{-6}	0.89	0.25	0.62	0.36	0.49	0.01
Epoxy-TiO_2 nanocomposites								
1 wt%	1.16	3.3×10^{-6}	0.89	0.25	0.43	4.3×10^{-1}	0.74	0.03
3 wt%	1.46	6.4×10^{-6}	0.96	0.26	0.34	7.0×10^{-2}	0.71	0.07
5 wt%	1.06	3.2×10^{-6}	0.95	0.32	0.23	3.7×10^{-2}	0.80	0.14
Epoxy-Al_2O_3 nanocomposites								
1 wt%	1.01	2.9×10^{-6}	0.91	0.26	0.10	7.1×10^{-3}	0.19	0.05
3 wt%	1.16	5.7×10^{-6}	0.93	0.24	0.10	2.7×10^{-2}	0.14	0.05
5 wt%	1.57	4.6×10^{-6}	0.95	0.26	0.85	1.3×10^{-2}	0.40	0.01

Table 5.3. Parameters obtained from the fits of the imaginary permittivity of the epoxy-TiO_2 and epoxy-Al_2O_3 nanocomposites to the Havriliak-Negami function.

Sample	β-relaxation				Second relaxation term			
	$\Delta\epsilon$	τ [s]	α	β	$\Delta\epsilon$	τ [s]	α	β
Pure epoxy	0.71	3.3×10^{-6}	0.43	0.62	0.32	62.1	0.55	0.055
Epoxy-TiO_2 nanocomposites								
1 wt%	0.79	3.8×10^{-6}	0.44	0.54	0.36	1.6	0.16	1
3 wt%	0.89	1.5×10^{-5}	0.48	0.19	0.24	1.0	0.39	0.55
5 wt%	0.85	5.2×10^{-6}	0.50	0.19	0.22	9.3×10^{-2}	0.33	0.82
Epoxy-Al_2O_3 nanocomposites								
1 wt%	0.65	1.7×10^{-6}	0.43	0.66	0.10	4.9×10^{-2}	0.30	0.93
3 wt%	0.75	7.7×10^{-6}	0.42	0.41	0.09	1.4×10^{-1}	0.31	0.99
5 wt%	0.85	9.7×10^{-6}	0.47	0.26	0.17	2.0×10^{-1}	0.29	1

For the β-relaxation, τ exhibited similar changes in both models for the epoxy-TiO_2 samples, initially increasing until 3 wt% of TiO_2 was added, then a slight decrease at 5 wt% TiO_2. In the epoxy-Al_2O_3 samples, τ initially decreased for 1 wt% Al_2O_3, and then increased for higher Al_2O_3 contents. Both types of nanocomposites showed increases in both the α and the n parameters (in the

HN and DH models, respectivley) for the β-relaxation. The m parameter in the DH model showed only a small increase at higher filler contents in the epoxy-TiO_2 nanocomposites. The β parameter for the β-relaxation showed a general decrease with increasing filler content for both types of nanocomposites.

The changes in τ are less consistent between the two different models in the new (second) relaxation for the nanocomposites, but generally τ is smaller at higher TiO_2 contents and larger at higher Al_2O_3 contents. In the DH model, n for the new relaxation exhibited a decrease from 1 to 3 wt%, then an increase from 3 to 5 wt% for both types of nanocomposites. m increased with increasing TiO_2 content and with decreasing Al_2O_3 content. In the HN model, however, the α parameter for the new relaxation increased between 1 and 3 wt% TiO_2, and then decreased between 3 and 5 wt% TiO_2. The β parameter was lower at 3 and 5 wt% TiO_2 than at 1 wt% TiO_2. In the epoxy-Al_2O_3, both the α and β parameters in the HN model showed little change.

Figures 5.9 and 5.10 show the real permittivities of epoxy-TiO_2 and epoxy-Al_2O_3 nanocomposites at higher temperatures. For the epoxy-TiO_2 nanocomposites, the increase in ϵ'_r above the glass transition was larger at higher TiO_2 contents, and the α-relaxation emerged at an earlier temperature as the TiO_2 content was increased. This was most noticeable for 5 wt% TiO_2, as shown in Figure 5.9, where the relaxation was first seen at 50 °C. In the epoxy-Al_2O_3 nanocomposites, the increase in ϵ'_r above the glass transition was stunted in the nanocomposites with a higher Al_2O_3 content (as seen in the bottom right plot of Figure 5.10). Additionally, the α-relaxation was also delayed at 3 wt% Al_2O_3 compared to at 1 wt% and 5 wt%, emerging first at 80 °C instead of 60-70 °C.

Figure 5.11 shows the imaginary moduli for the epoxy-TiO_2 and epoxy-Al_2O_3 nanocomposites between 30 and 90 °C. The same trends observed in the real permittivities with increasing temperature were observed in M" as well. As the TiO_2 content was increased, the peak in M" for the LFD shifted to higher frequencies for a given temperature, and the α-relaxation peak was observed at lower temperatures. In the epoxy-Al_2O_3 nanocomposites, the M" peak for the α-relaxation was observed at 70 and 80 °C for 1 and 5 wt% Al_2O_3, and at 90 °C for 3 wt% Al_2O_3, which is consistent with the observations from Figure 5.10. However, even though the increase in ϵ'_r due to the LFD/EP effect was restricted at 5 wt% Al_2O_3, the corresponding peak in M" was shifted to a higher frequency compared to the nanocomposite with 3 wt% Al_2O_3. In addition, a clear peak in M" was observed for the new relaxation associated with the nanoparticles in the epoxy-TiO_2 nanocomposites (pointed out by the arrows in Figure 5.11), but no such peak was observed for the epoxy-Al_2O_3 nanocomposites.

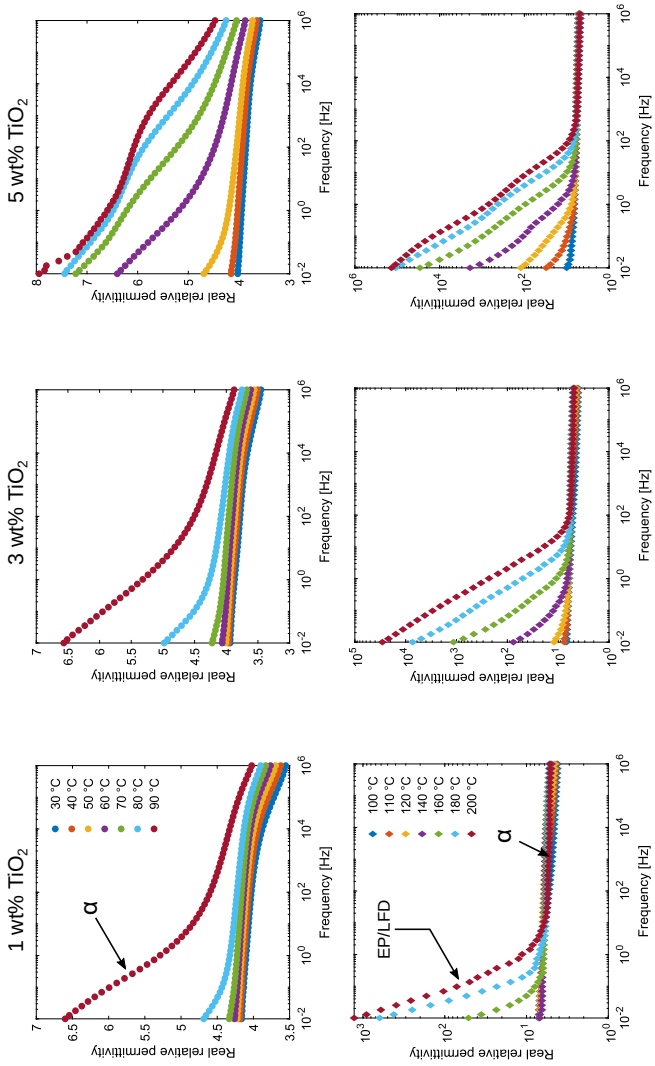

Figure 5.9. The real relative permittivities at 30-90 °C (top row) and at 100-200 °C (bottom row) for representative epoxy-TiO_2 nanocomposites prepared at pH 7 with an APTES:DGEBA mass ratio of 1:30. The arrows point to the α-relaxation and the LFD/EP effect.

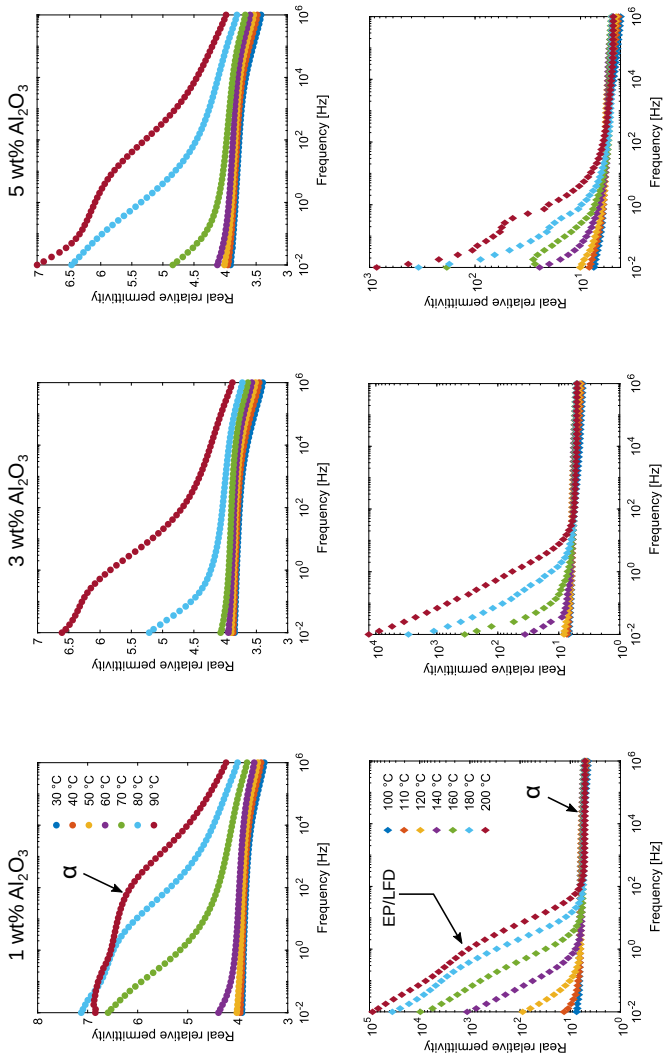

Figure 5.10. The real relative permittivities at 30-90 °C (top row) and at 100-200 °C (bottom row) for representative epoxy-Al_2O_3 nanocomposites prepared at pH 7 with an APTES:DGEBA mass ratio of 1:30. The arrows point to the α-relaxation and the LFD/EP effect.

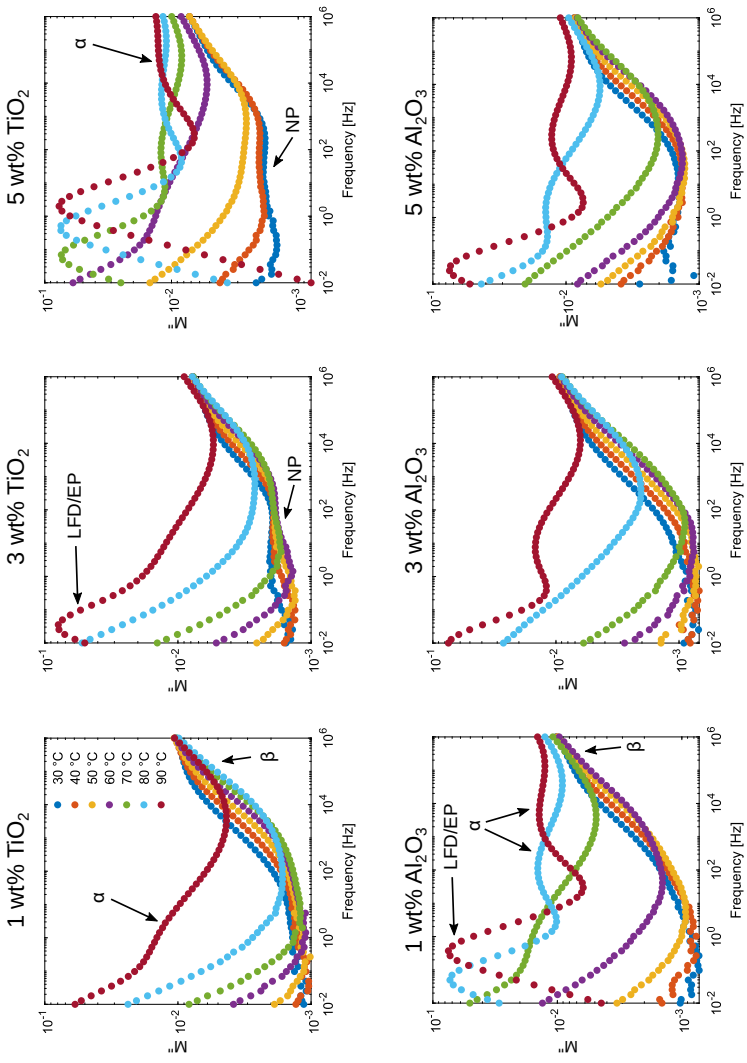

Figure 5.11. The imaginary moduli at 30-90 °C for representative epoxy-TiO_2 (top row) and epoxy-Al_2O_3 (bottom row) nanocomposites prepared at pH 7 with an APTES:DGEBA mass ratio of 1:30. The arrows point to the peaks for the α and β-relaxations, the LFD/EP effect, and the relaxation introduced by the nanoparticles (NP).

5.3 Electrical treeing resistance

Figures 5.12 and 5.13 show the morphology of the trees grown in different TiO_2 and Al_2O_3 nanocomposites, respectively. Table 5.4 summarizes selected properties related to the electrical treeing behaviour. Like the epoxy-SiO_2 nanocomposites, the trees began growing immediately after the voltage was set to 10 kV after tree initiation. Of the 20 samples of both the TiO_2 and Al_2O_3 nanocomposites that were tested, trees were initiated in 6 of each type of nanocomposite.

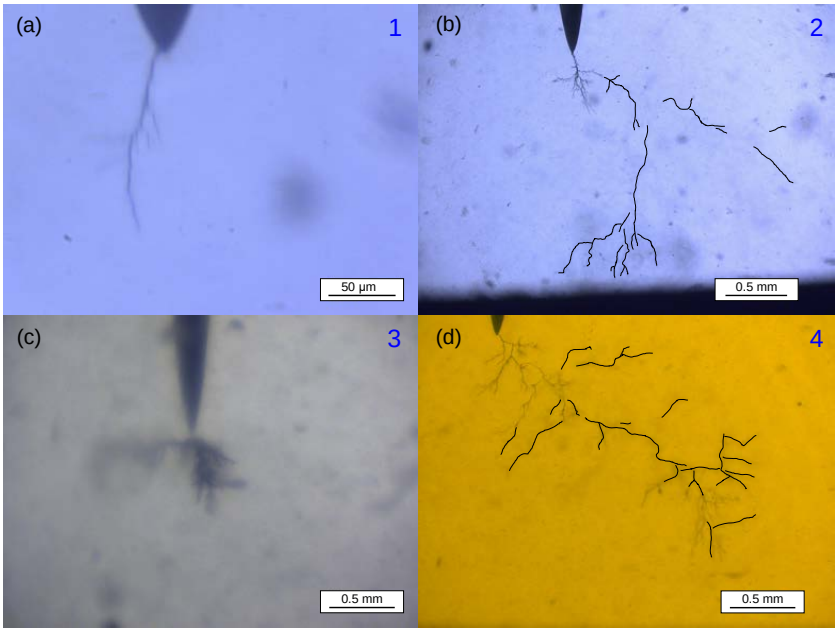

Figure 5.12. Optical images of the trees grown in epoxy-TiO_2 nanocomposites with 5 wt% TiO_2. The numbers refer to the sample number in Table 5.4. The trees were grown at 10 kV, except in **(d)**, which was grown at 15 kV. Unedited images of the trees are shown in Figure B.7

The epoxy-TiO_2 nanocomposites exhibited different growth behaviours and tree morphologies from sample to sample, but all of them demonstrated a larger resistance to tree propagation than pure epoxy. As seen in Table 5.4, the growth rates measured were lower than those observed for pure epoxy (Table 4.4). In sample 1, the tree did not exhibit any growth at 10 kV (Figure 5.12a). In sample 3, a dense and bushy tree formed with much thicker channels, which stopped growing after ~30 min at 10 kV (Figure 5.12c). Other trees were found

to grow quite linearly with a low degree of extended branching. The primary tree channels were quite thick (~5-10 µm) but the branches were narrow (< 2 µm). Sample 4 (Figure 5.12d) did not exhibit any growth at 10 kV, but grew at 15 kV.

The epoxy-Al_2O_3 nanocomposites on the other hand showed extremely slow growth at 10 kV. While sample 7 exhibited no growth after initiation (Figure 5.13a), the others showed limited growth over 1 h, where the trees reached lengths of only 100-200 µm. The tree channels were also thinner than those observed in pure epoxy or the other nanocomposites (with the exception of the S2 and S3 nanocomposites). Another difference between the two types of nanocomposites is in the initiation voltages. For most of the epoxy-TiO_2 nanocomposites, trees initiated at lower voltages than in pure epoxy. Trees in the epoxy-Al_2O_3 nanocomposites all initiated at 25 kV, and often required comparatively longer times before initiation.

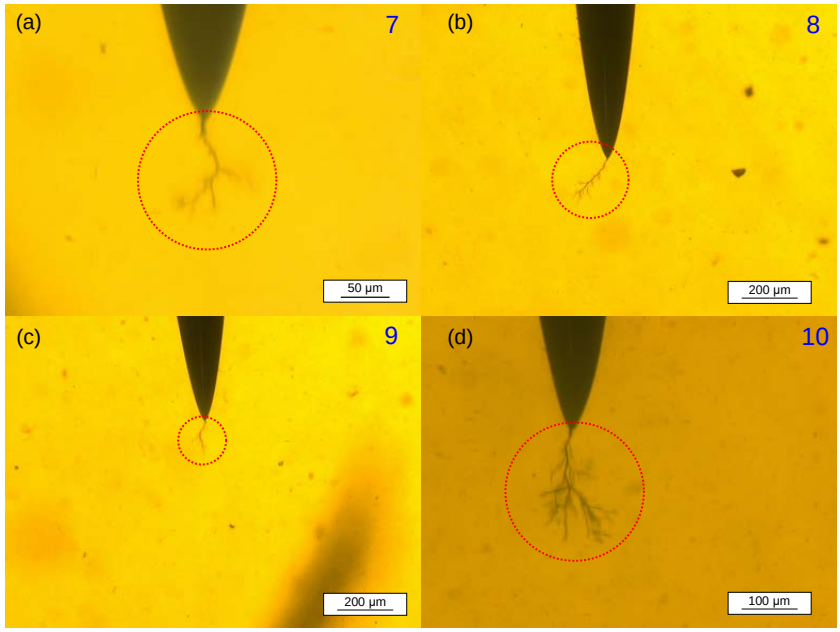

Figure 5.13. Optical images of the trees grown in epoxy-Al_2O_3 nanocomposites with 5 wt% Al_2O_3. The numbers refer to the sample number in Table 5.4. The trees were grown at 10 kV. The red circles show the limited extent of the tree growth after initiation.

Table 5.4. Electrical treeing properties of selected epoxy-TiO_2 and epoxy-Al_2O_3 nanocomposites with 5 wt% filler content.

Sample No.	Initiation voltage [kV]	Time [s]	Growth rate [mm min^{-1}]	Horizontal spread [mm]	Average channel width [μm]	Notes
Epoxy-TiO_2						
1	15	326	-	-	1.7	[1]
2	15	66	0.017	1.8	4.7	[2]
3	10	-	0.017	0.8	24.4	[3,4]
4	15	-	0.022	2.2	4.1	[1,2,5]
5	15	-	0.016	0.8	3.7	-
6	25	-	0.05	1.6	6.8	[6]
Epoxy-Al_2O_3						
7	25	1087	-	-	1.9	[1]
8	25	34	0.002	-	2.0	[7]
9	25	152	0.002	-	2.2	[7]
10	25	1342	0.001	-	2.5	[7]
11	25	664	0.001	-	2.1	[7]
12	25	365	0.002	-	2.8	[7]

[1] No growth at 10 kV.
[2] Part of tree grew more horizontally instead of more vertically towards the ground electrode.
[3] Initiation time is unknown.
[4] Growth stopped completely after 36 min.
[5] Growth rate measured from tree growth at 15 kV.
[6] Significant tree growth at 25 kV before voltage was reduced to 10 kV.
[7] Very short and slow tree growth at 10 kV over 1 h. No horizontal spread due to the short tree length.

One of the epoxy-TiO_2 nanocomposites (sample 4) and three of the epoxy-Al_2O_3 nanocomposites (samples 10-12) where trees were initiated but did not grow at 10 kV, were then exposed to 15 kV voltage. The tree grown in the epoxy-TiO_2 is shown in Figure 5.12d, and the trees grown in epoxy-Al_2O_3 are shown in Figure 5.14. The growth of the tree in epoxy-TiO_2, while faster than at 10 kV, was still slower than in pure epoxy at 10 kV. However, in the epoxy-Al_2O_3 nanocomposites, the trees grew significantly faster at 15 kV. Table 5.5 shows the properties of the trees grown at 15 kV in epoxy-Al_2O_3 nanocomposites. In addition to the faster growth, the trees in epoxy-Al_2O_3 nanocomposites grew much more linearly and straight towards the ground electrode, with very little branching. In comparison, the tree grown in the epoxy-TiO_2 nanocomposite at 15 kV grew more horizontally than vertically, moving towards the ground electrode at an angle instead of straight down.

Table 5.5. Electrical treeing properties in epoxy-Al_2O_3 nanocomposites with trees grown at 15 kV.

Sample No.	Growth rate [mm min^{-1}]	Horizontal spread [mm]	Average channel width [μm]
10	0.136	0.71	1.8
11	0.179	0.69	2.5
12	0.092	0.44	2.7

The partial discharge properties during tree growth in the epoxy-TiO_2 and epoxy-Al_2O_3 nanocomposites generally showed similar developments as in the epoxy-SiO_2 nanocomposites with a few exceptions. Both wing and turtle-like PD patterns were observed, although the PD activity and magnitudes were consistently higher in the epoxy-TiO_2 than the epoxy-Al_2O_3 nanocomposites. Figure 5.15 shows the PRPD patterns for selected epoxy-TiO_2 nanocomposites. Samples 1, 2, 5, and 6 exhibited similar PD patterns over time, and representative PD from sample 2 is shown in the top row of Figure 5.15. The wing-like PD persisted until 25 min, and the PD magnitude increased with time. Sample 3, which formed the bushy tree (Figure 5.12c) showed the highest PD activity and magnitude, shown in the bottom row of Figure 5.15. In addition to the regular wing-like PD, which reached discharge levels up to 0.2 nC, sharp rabbit-ear shaped PD patterns were also observed (shown by the red arrows in Figure 5.12). These PDs were also disconnected from the other regions of wing-like PD.

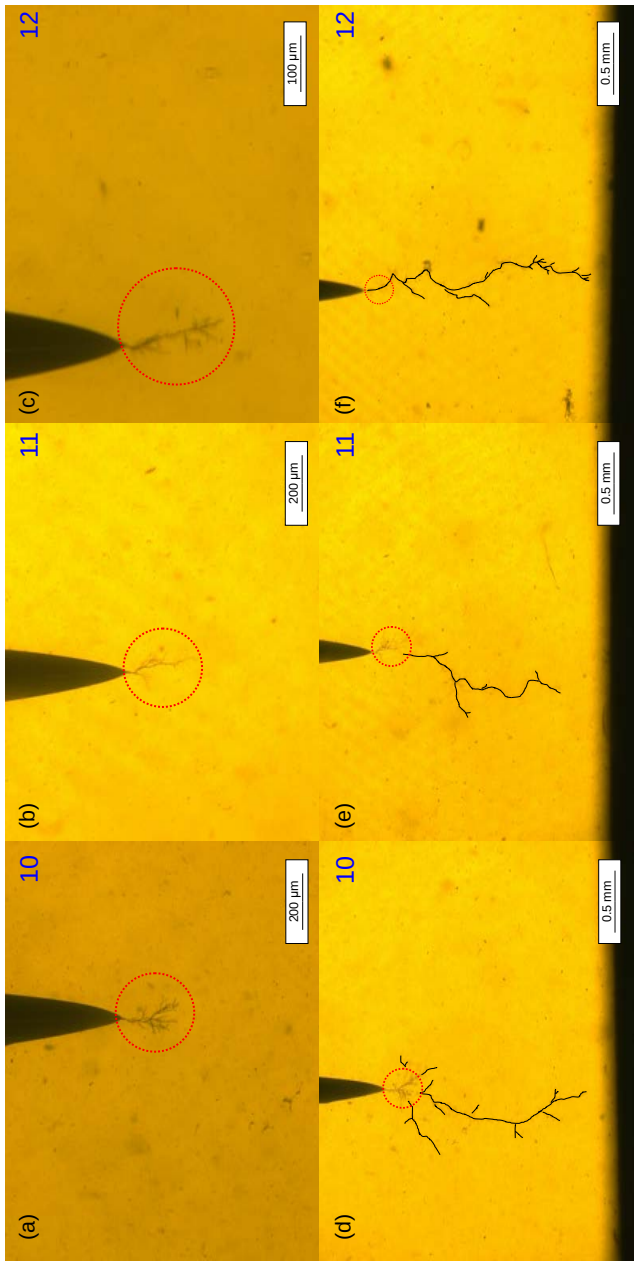

Figure 5.14. Optical images of the trees grown in epoxy-Al_2O_3 nanocomposites with 5 wt% Al_2O_3 at 15 kV. **(a)-(c)** show the trees at the start (when grown at 10 kV), and **(d)-(f)** show the corresponding trees after growth was complete. The numbers refer to the sample number in Table 5.4. The red circles show the extent of the tree growth at 10 kV. Unedited images of the trees are shown in Figure B.9

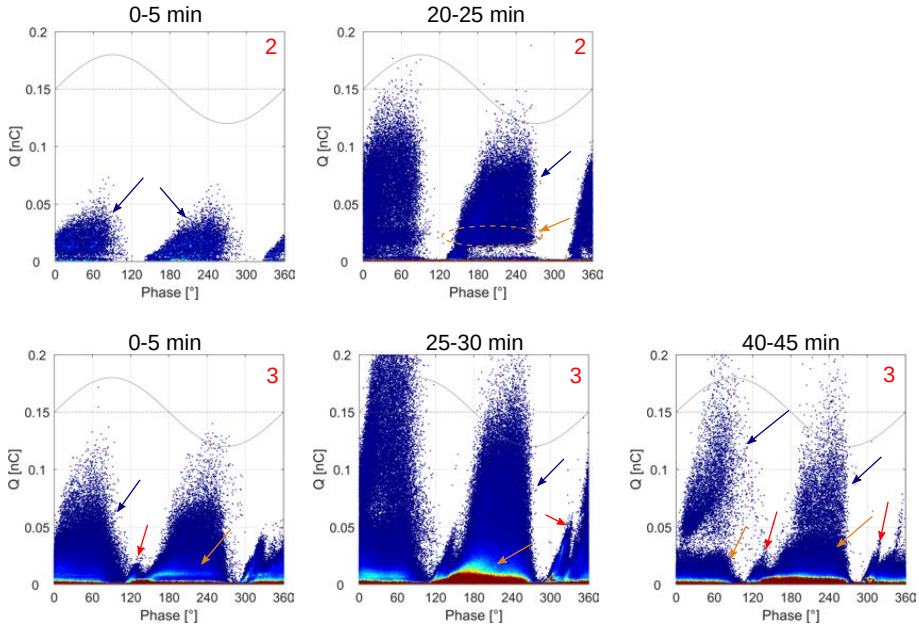

Figure 5.15. Phase-resolved partial discharge patterns for selected samples of epoxy-TiO_2 nanocomposites, showing different time periods during tree growth at 10 kV. The numbers indicate which samples in Table 5.4 the PRPD plots corrspond to. The blue and orange arrows indicate wing-like and turtle-like PD regions, respecitvely, and the red arrows indicate sharper disconnected wing-like PD patterns.

Figure 5.16 shows representative examples of the PRPD patterns in the epoxy-Al_2O_3 nanocomposites when trees were grown at both 10 and 15 kV. Despite the limited tree growth, the wing-like PD were present throughout the entire period (~60-90 min) at 10 kV, and only an increase in the magnitude of the wing-like PD was observed with time. At 15 kV, however, the tree growth was much faster (~9-15 min), and the PD activity was significantly lower. Only a turtle-like PD region formed prominently, as seen furthest right in Figure 5.16, with very few scatterings of wing-PD.

Figure 5.17 shows the PRPD patterns for the single epoxy-TiO_2 nanocomposite (sample 4) where the tree was grown at 15 kV. Both the PD magnitude and activity were higher than in the epoxy-Al_2O_3 nanocomposites where the trees were grown at 15 kV, with discharges reaching up to 0.1 nC. The PD activity increased significantly after 20 min, consisting primarily of wing-like PD. After

30 min, both wing- and turtle-like PD were prominent throughout the remainder of the treeing duration, with PD reaching 0.08 nC.

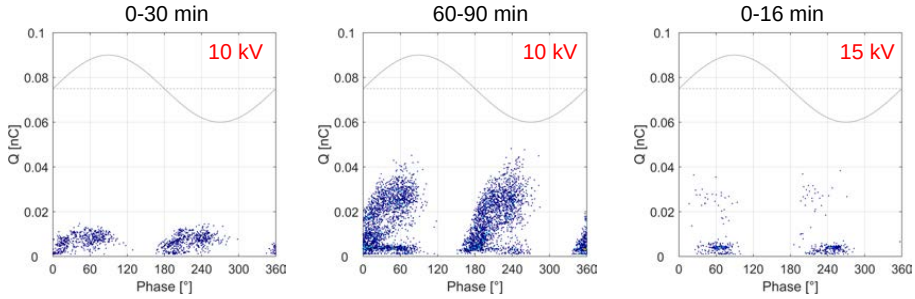

Figure 5.16. Representative phase-resolved partial discharge patterns for epoxy-Al_2O_3 nanocomposites, showing different time periods during tree growth at both 10 and 15 kV.

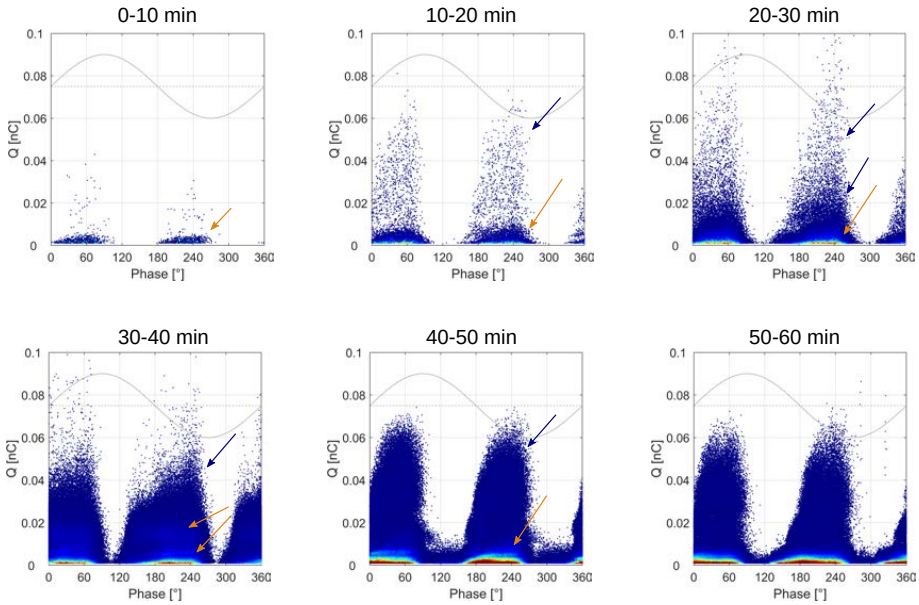

Figure 5.17. Phase-resolved partial discharge patterns for epoxy-TiO_2 nanocomposite with tree grown at 15 kV. The blue and orange arrows indicate wing-like and turtle-like PD regions, respecitvely.

5.4 Mechanical properties of the epoxy-TiO_2 nanocomposites

The measured tensile properties of the epoxy-TiO_2 nanocomposites with different TiO_2 contents are displayed in Figure 5.18. The average elastic modulus increased steadily with increasing TiO_2 content. The UTS also improved with increasing TiO_2 content, with a large increase in the strength between 3 and 5 wt% TiO_2. The strain at failure was significantly lower in the nanocomposites compared to the pure epoxy, and the decrease from pure epoxy was largest upon addition of 1 wt% TiO_2. However, with further increases in the TiO_2 content, there was a slight increase in the strain at failure, albeit still lower than that of pure epoxy.

Figures 5.19 to 5.21 show the fracture surfaces of epoxy-TiO_2 nanocomposites containing 1, 3, and 5 wt% TiO_2, respectively. The origins of the failures were defects in the interior of the specimen (instead of on the edges), which are highlighted by the red arrows in the figures.

For 1 wt% TiO_2 (Figure 5.19a), the fracture surface forms mirror, mist and hackle regions, similar to that observed in the epoxy-SiO_2 nanocomposites with 5 wt% SiO_2. One feature that is different is that all the cracks that radiate outwards from the fracture origin deflect almost perpendicularly at the ends of the mist region, as shown by the black arrows. The hackle region, shown in Figure 5.19b, is rougher than that in the epoxy-SiO_2 nanocomposite. Figure 5.19c shows the fracture origin, which looks quite dissimilar to the fracture origins in pure epoxy and the epoxy-SiO_2 nanocomposites. The surface is rougher, and contains multiple small holes of size 0.1-2 μm which are pointed out by the blue arrows.

Similar features are observed at higher TiO_2 contents. For 3 wt% TiO_2 (Figure 5.20), there is a gap between the mist and hackle regions in which the fracture surface is smooth in certain parts right after the cracks deflect, as shown by the yellow-marked region in Figure 5.20a. The specimen in Figure 5.20a also had two fracture origins, marked by the red arrows, resulting in the failure occurring at different planes in the specimen. Magnified images of both fracture origins are shown in Figure 5.20b and c, where similar features were observed. Figure 5.20d shows the fracture origin in a different specimen with 3 wt% TiO_2, where the voids were less numerous than those shown in Figure 5.20b and c. The holes observed in 3 wt% TiO_2 (Figure 5.20b-d) were more numerous than at 1 wt% TiO_2. In addition, some regions close to the holes had remnant material from the opposite fracture surface. These are marked by the purple arrows, and may correspond to pullouts of the TiO_2 particles.

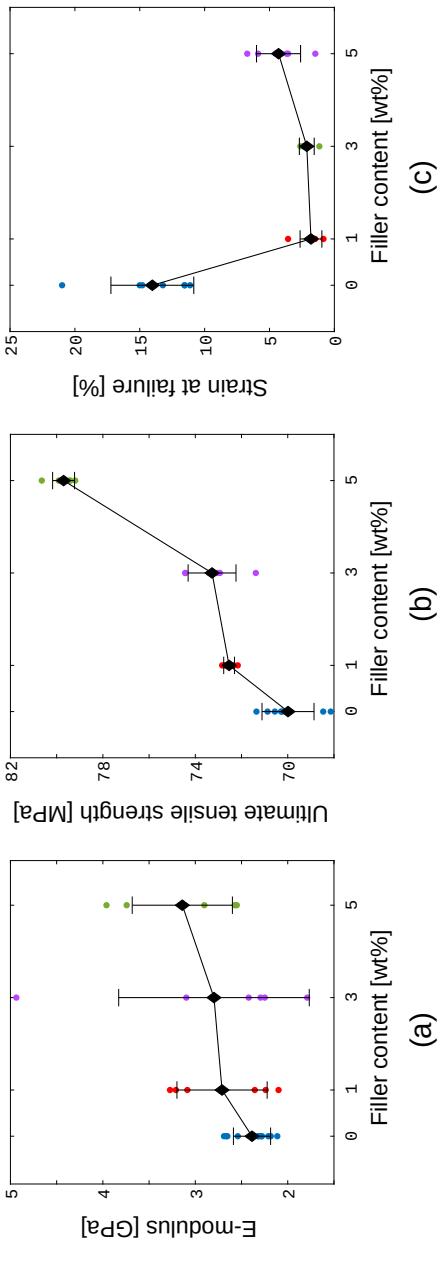

Figure 5.18. The tensile properties of the epoxy-TiO_2 nanocomposites as a function of filler content: **(a)** the elastic modulus, **(b)** the ultimate tensile strength, and **(c)** the strain at failure.

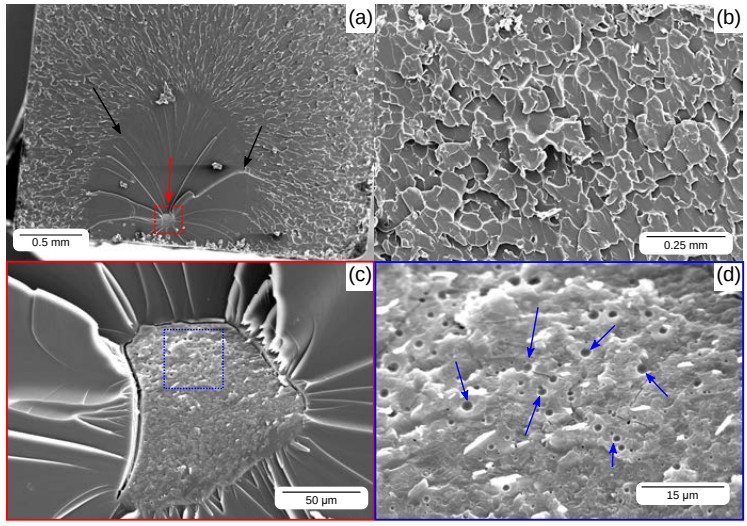

Figure 5.19. The fracture surfaces of epoxy-TiO_2 nanocomposites with 1 wt% TiO_2. In **(a)**, the black arrows point out where the crack front bends away in the mist region and the red arrow show the fracture origin. **(b)** shows a magnified image of the hackle region. **(c)** shows a magnified image of the fracture origin in **(a)**. **(d)** shows a magnification of the central region in **(c)**, with the blue arrows showing the spherical holes in the fracture origin.

Figure 5.21a shows similar developments in nanocomposites with 5 wt% TiO_2. An additional feature was present at the ends of the deflected cracks in the mist region. Some of the cracks, indicated by the green arrows in Figure 5.21b, start forming parabolic lines and markings before the surface roughness increased and the hackle region formed. These were also observed in a different specimen and are shown more clearly in Figure 5.21c. At the fracture origin, shown in Figure 5.21d, regions of suspected particle-pullouts are present, although the voids and holes were less frequent than at lower TiO_2 contents. However, larger voids were more frequent.

5.5 Discussion

5.5.1 Formation of TiO_2 and Al_2O_3 nanoparticles

The nanocomposites with TiO_2 and Al_2O_3 were prepared with a lower mass ratio of APTES:DGEBA (1:30 instead of 1:10). The use of excess APTES runs

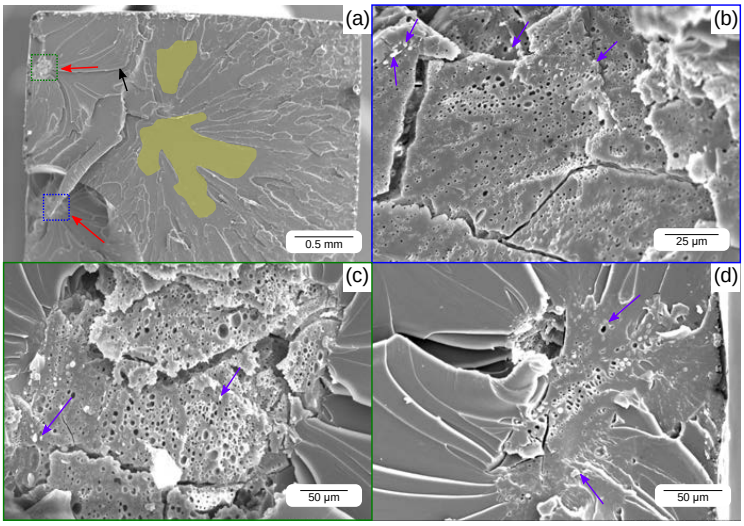

Figure 5.20. The fracture surfaces of epoxy-TiO_2 nanocomposites with 3 wt% TiO_2.The yellow shaded region in **(a)** shows smoother regions between the mist and hackle regions. **(b)** and **(c)** show magnified images of the fracture origins in **(a)**. **(d)** shows the fracture origin in a different sample. The black and red arrows show crack deflections and the fracture origins, respectively. The purple arrows show regions were particle-pullout is suspected.

the risk of preferential condensation of the APTES molecules with each other instead of with the alkoxide precursors. Preferential condensation may lead to a mixture of SiO_2 structures forming instead of the APTES binding the TiO_2 or the Al_2O_3 with the DGEBA molecules.

The differences in the morphologies of the TiO_2 and Al_2O_3 nanoparticles (Figures 5.1 and 5.2) suggest differences in the reactions of the two precursors. In the case of TIP, Ti^{4+} can expand its coordination when unsaturated via different reactions (e.g. olation, oxolation, alkoxy bridging). However, TIP in 2-propanol is monomeric [14, 233], and due to the high oxidation state of the Ti^{4+} it is less stable towards hydrolysis. The fast hydrolysis is evidenced in how quickly the Ti-O-C bands became weaker in the FTIR spectra alongside the emergence of the O-H band (Figure 5.4). The formation of highly condensed TiO_2 particles with a defined shape, as seen in Figure 5.1, is consistent with the morphologies observed in TiO_2 prepared in other works [72, 92, 103] using both aqueous and non-aqueous *in situ* sol-gel syntheses. The SAXS profiles of these nanocomposites (Figure 5.3a) show a single Guinier feature with a plateau at lower q. Such

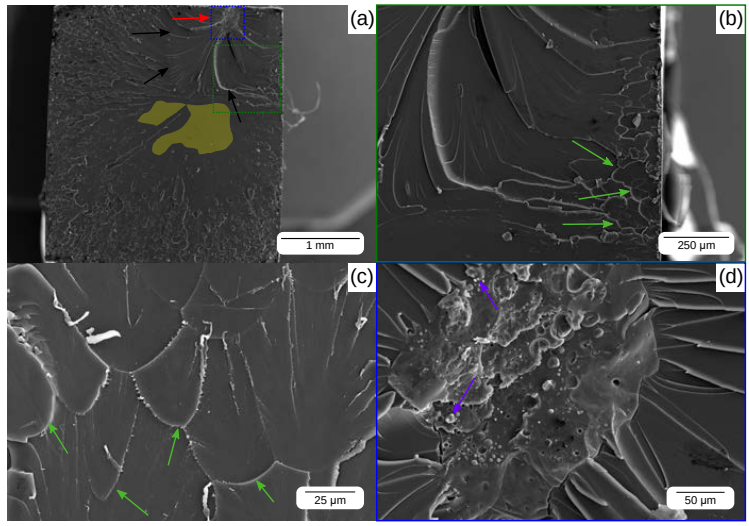

Figure 5.21. The fracture surfaces of epoxy-TiO_2 nanocomposites with 5 wt% TiO_2. The yellow shaded region in **(a)** shows smoother regions between the mist and hackle regions in the fracture surface. **(b)** shows the parabolic features in the magnified region marked by the green dotted square in **(a)**. **(c)** shows parabolic features in a different specimen. The green arrows point out these parabolic features. **(d)** shows the fracture origin marked by the blue dotted square in **(a)**. The black and red arrows show crack deflections and the fracture origins, respectively. The purple arrows show regions were particle-pullout is suspected.

a feature shows that the scattering objects in the material are discrete structures, and are not aggregated or part of a hierarchical structure. This description of the TiO_2 from the SAXS is consistent with the morphologies observed in the TEM. However, the sizes of the particles obtained from Guinier's law are an order of magnitude smaller than those observed in the TEM - 3-5 nm instead of 10-40 nm. Additionally, the position of the Guinier knee is at the same scattering vector irrespective of the TiO_2 content, implying the same correlation length between all the nanoparticles. The correlation lengths are inconsistent with the spacing of the particles observed in TEM, where smaller groups of particles were observed at significantly larger distances, with several µm between the different groups. It is possible that the majority of the TiO_2 particles are much smaller and were not observed by the TEM. The SAXS probes a larger volume of the material, and provides an average structure.

Several authors [234–236] have reported the formation of titanium-oxo-alkoxy (or polyalkoxide) clusters ($TiO_a(OH)_b(OR)_{4-2a-b}$) from hydrolysis of TIP, with sizes in the range of 0.5-2.5 nm [233]. Figure 5.22 shows the structure of the simplest cluster that can form from TIP ($Ti_3O(OR)_{10}$). The clusters are usually obtained from hydrolysis with low molar ratio of H_2O:TIP [237]. A higher ratio results in the eventual precipitation of TiO_2. Simonsen and Søgaard [234] reported the formation of such clusters using a molar ratio of 2.7, forming clusters in size ~3 nm initially. The clusters grew in an induction period, which was dependent on the pH, to ~30 nm through hydrolysis and condensation of surface alkoxy groups in the clusters. For neutral conditions (pH 7), the induction period was ~1 h. Similar polyalkoxide clusters might have formed during the synthesis of the *in-situ* nanocomposites, which were prepared with a H_2O:TIP molar ratio of 2. The clusters may have initially formed due to absorption of small amounts of moisture from air into the anhydrous 2-propanol. At sufficiently low molar ratios of H_2O:TIP (< 1), hydrolysis of TIP forms a stable solution of these clusters [234]. Subsequent addition of water mixed in 2-propanol, resulting in a molar ratio > 1.5, led to the precipitation of larger TiO_2 particles, which are seen in Figure 5.1. The formation of a large number of such polyalkoxide clusters, with a few larger particles, can explain the discrepancy between the TEM images (where the larger precipitated particles are observed) and the SAXS data (where the scattering is primarily caused by the smaller polyalkoxide clusters).

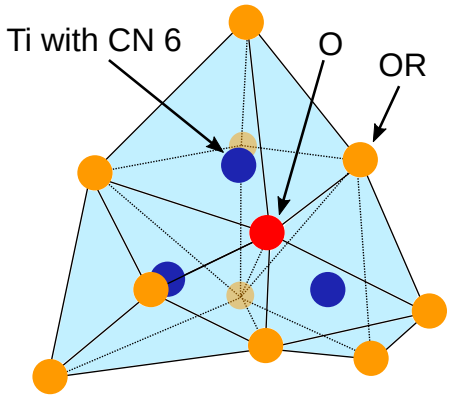

Figure 5.22. Structure of the $Ti_3O(OR)_{10}$ cluster formed from TIP, with 6 coordinated Ti atoms.

The structures formed by the hydrolysis and condensation of aluminium alkoxides depend on the steric hindrance of the alkoxide groups [14]. AIP con-

tains secondary alkoxides, which are sterically more bulky, and unhydrolysed monomers can associate to form oligomers via alcolation. Figure 5.23a shows a possible dimer structure that can be formed from this alcolation, which probably occurs when the AIP is mixed with the anhydrous 2-propanol prior to the mixing with DGEBA and the addition of water. The alcolation therefore results in the formation of less constrained linear species rather than octahedrally coordinated, symmetrical structures [14]. As a result, more open and porous fractal structures of the Al_2O_3 are formed. These structures are evidenced in the SAXS profiles (Figure 5.3b), which resembled those for the epoxy-SiO_2 nanocomposites prepared at pH 11 with a reduced amount of APTES. All the epoxy-Al_2O_3 nanocomposites exhibited fractal dimensions of -2.3 to -3. Additionally, the knee-like feature at high q suggests that the Al_2O_3 also has a hierarchical structure like the SiO_2, but with smaller primary structures and larger secondary structures. However, the unified model could not be applied since the Guinier knee for the secondary structural level lies outside the measured q range. The interconnected networks with surface fractal features are also observed in the TEM images (Figure 5.2a-g). The morphology of the Al_2O_3 is similar to that of the SiO_2 (shown in Figure 4.1a-d), only with much larger clusters (> 200 nm).

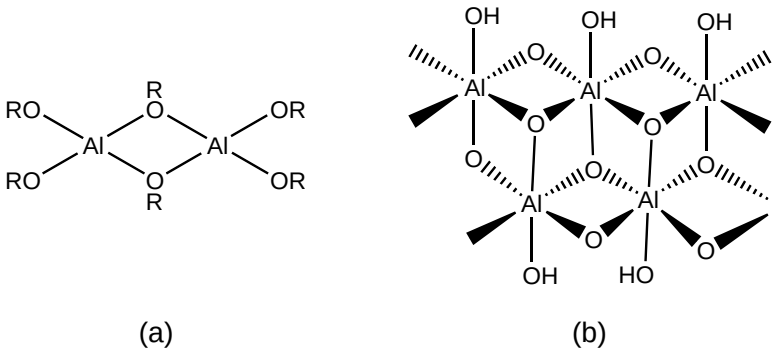

Figure 5.23. **(a)** The dimer formed from alcolation of aluminium isopropoxide in the absence of water. **(b)** The structure of the amorphous boehmite that forms from the hydrolysis and dehydration of the dimer.

Usually, AIP hydrolyses to form aluminium hydroxide, $Al(OH)_3$, which then forms a pseudo-boehmite (AlO(OH)) through dehydration (condensation) [49, 238, 239]. Al_2O_3 does not form from the AlO(OH) unless calcined at higher temperatures (420 °C for γ-Al_2O_3) [49]. It is therefore very likely that the inorganic nanoparticles formed in these nanocomposites are not really Al_2O_3, but a pseudo-Al_2O_3 structure resembling amorphous boehmite (Figure 5.23b). X-ray diffraction (XRD) measurements revealed no trace of crystallinity in the

nanocomposites, and selected area electron diffraction (SAED) in TEM from the particles confirmed the amorphous nature of both the TiO_2 and Al_2O_3 particles.

In some cases (e.g. 4 wt% Al_2O_3), large and spherically-defined particles were observed in some regions (Figure 5.2h). It is possible that some of the clusters may condense to a more compact, closed particle during the curing process, since the temperature is slightly higher than during the *in-situ* reactions, resulting in larger and more defined structures, as seen in Figure 5.2h.

5.5.2 Dielectric properties of the nanocomposites

ϵ'_r decreased in both epoxy-TiO_2 and epoxy-Al_2O_3 nanocomposites, meaning a decrease in the degree of polarization in the material with increasing filler content. Similar effects of the inclusion of TiO_2 or Al_2O_3 in epoxy nanocomposites have been demonstrated in several works. Singha and Thomas [4] demonstrated decreases in both ϵ'_r and tan δ for epoxy-TiO_2 (compared to pure epoxy). Kochetov et al. [140] and Maity et al. [162] both showed decreases in ϵ'_r for epoxy-Al_2O_3 nanocomposites. However, the nanocomposites generally had lower ϵ'_r for filler contents $\leq$ 1 wt%. Kochetov et al. also showed how increasing the filler content above 2 wt% in epoxy-Al_2O_3 nanocomposites led to increases in ϵ'_r [140]. In addition, other works have also demonstrated increases in ϵ'_r and tan δ upon addition of TiO_2 nanoparticles [69, 137].

Even though both the epoxy-SiO_2 and epoxy-Al_2O_3 nanocomposites exhibited decreases in tan δ in the β-relaxation, they did not show the same change in the shape of ϵ'_r as observed in the epoxy-TiO_2 nanocomposites. The fits to the HN function suggest that with increasing filler content, the O-H dipoles in both the epoxy-TiO_2 and the epoxy-Al_2O_3 nanocomposites have a slightly narrower, but increasingly asymmetric distribution of relaxation times. The fits to the DH function indicate that there is increasing order within the O-H dipole clusters in both types of nanocomposites. However, the interactions between the dipole clusters (described by m) are less affected in the epoxy-Al_2O_3 than in the epoxy-TiO_2 nanocomposites. The fragmentation of the dipole clusters increased at higher TiO_2 contents, as evidenced by the higher m [240]. This difference suggests that O-H dipoles are interacting differently with the TiO_2, compared to the SiO_2 and the Al_2O_3. Similar changes, both in ϵ'_r and the m parameter in the DH function, are observed in the *ex-situ* epoxy-SiO_2 nanocomposites (Figure 4.48 and table 4.7).

Other changes to the O-H dipoles (and therefore the β-relaxation) were more similar in both the epoxy-TiO_2 and the epoxy-Al_2O_3 nanocomposites (Tables 5.2 and 5.3). The O-H dipoles became stiffer than in pure epoxy, which may be

caused by restrictions of the dipole movement due to the nanoparticles. The new relaxation at low frequencies associated with the nanoparticles (shown in Figure 5.6b) was more prominent in the epoxy-TiO_2 than the epoxy-Al_2O_3 nanocomposites. The corresponding dipoles for this relaxation were also less mobile in the epoxy-TiO_2 nanocomposites. The relaxation was more symmetric in the epoxy-Al_2O_3, indicating that the response of the dipoles in the Al_2O_3 nanoparticles was more uniform.

At temperatures above T_g, the same LFD/EP effect was also observed in the epoxy-TiO_2 and the epoxy-Al_2O_3 nanocomposites. In both types of nanocomposites, ϵ'_r stayed below ~10 at temperatures below 100 °C (as seen in Figures 5.9 and 5.10), compared to some of the epoxy-SiO_2 nanocomposites (Figure 4.17). However, the epoxy-TiO_2 nanocomposite exhibited lower values of ϵ'_r than pure epoxy above 100 °C for 1 wt% TiO_2. Further increases in TiO_2 content resulted in a more pronounced LFD/EP effect, with ϵ'_r exceeding that of pure epoxy for a given temperature (above T_g). In the epoxy-Al_2O_3 nanocomposites, the opposite was observed, and the nanocomposite with 5 wt% Al_2O_3 exhibited the weakest LFD/EP effect. This effect suggests that the charge transport (or the motion of the free charge carriers) is inhibited in the nanocomposites with a high Al_2O_3 or low TiO_2 content, whereas no such phenomenon occurs in the epoxy-SiO_2. Maity et al. [162] reported that any differences in the permittivity of pure epoxy and epoxy-Al_2O_3 nanocomposites were minimized at elevated temperatures, and became negligible over 70 °C for unfunctionalized nanoparticles. However, nanocomposites containing functionalized nanoparticles also exhibited reductions in ϵ'_r at higher temperatures. Nelson and Fothergill [5] also showed a decrease in ϵ'_r from that of pure epoxy in epoxy-TiO_2 nanocomposites (with 10 wt% TiO_{20}) at 120 °C. It appears that the functionalization, composition, and particle morphology play an important role in determining the dielectric properties of these nanocomposites above the glass transition.

5.5.3 Electrical treeing resistance

The resistance against tree propagation or growth in both the epoxy-TiO_2 and the epoxy-Al_2O_3 nanocomposites was significantly higher than in pure epoxy at 10 kV. Trees were initiated and grown at 15 kV in additional samples of pure epoxy to allow comparisons with the trees grown in the epoxy-TiO_2 and epoxy-Al_2O_3 nanocomposites. Figure 5.24 compares two of the trees grown in pure epoxy at 15 kV, with growth speeds of 0.11 mm min^{-1} in Figure 5.24a and 0.16 mm min^{-1} in Figure 5.24b.

In comparison, the growth rates for the trees in epoxy-Al_2O_3 nanocomposites were similar: 0.136, 0.179 and 0.092 mm min^{-1} for samples 10, 11, and 12,

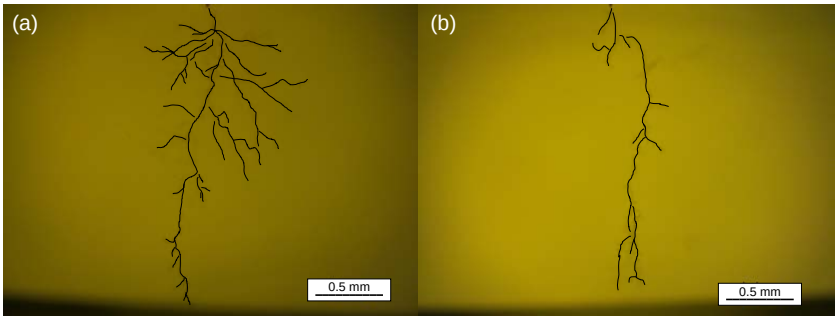

Figure 5.24. Electrical trees grown at 15 kV in pure epoxy. The tree growth speed in **(a)** was 0.11 mm min^{-1}, and in **(b)** was 0.16 mm min^{-1}. Unedited images of the trees are shown in Figure B.8

respectively (Table 5.5). The epoxy-TiO_2 sample (Sample 4) grown at 15 kV exhibited a significantly slower growth rate of 0.022 mm min^{-1} (Table 5.4). Therefore, with the increase in voltage the growth speed increased by several orders of magnitude in the epoxy-Al_2O_3 nanocomposites, whereas the epoxy-TiO_2 nanocomposite exhibited a relatively small increase. A similar behaviour was reported by Tanaka et al. [156] where epoxy-Al_2O_3 nanocomposites showed slower tree growth at 10 kV, and significantly faster growth at 20 kV. They attributed this to the formation of selective channel formation at high fields.

The partial discharge patterns shown in Figures 5.15 to 5.17 were consistent with the lengths of the corresponding trees, and showed similar developments as observed in pure epoxy earlier (Figure 4.30). The short trees grown at 10 kV in the epoxy-Al_2O_3 exhibited primarily wing-like PD throughout the entire period (left and center images in Figure 5.16), with the magnitude of the PD steadily increasing up to 0.04 nC with increasing tree length. The PD activity was quite low due to the limited growth of the tree. Since there was mostly wing-like PD and comparatively little turtle-like PD even after ~90 min, the trees remain non-conducting at 10 kV in the epoxy-Al_2O_3 nanocomposites. In contrast, the trees grown at 15 kV in epoxy-Al_2O_3 showed mostly turtle-like PD and few scatterings of discharges in a wing-like shape (right image in Figure 5.16), indicating that trees grown at 15 kV became conducting quite quickly. The transition from non-conducting to conducting trees occurred rapidly despite the low discharge activity and magnitude throughout the tree growth.

The trees grown in epoxy-TiO_2 exhibited a significantly higher discharge activity and magnitude (Figures 5.15 and 5.17). Like the pure epoxy and the epoxy-SiO_2 nanocomposites (as discussed in Chapter 4.3.3.2), the trees in epoxy-TiO_2 also

underwent the transition from conducting to non-conducting after ~30-45 min. However, the wing-like PD in the tree grown at 15 kV (Figure 5.17) did not cease, which his implies that either there are certain branches in the tree that remain non-conducting, or that the new branches forming tend to be non-conducting for a longer period even late into the tree growth.

5.5.4 Tensile properties of the epoxy-TiO_2 nanocomposites

While the UTS of the epoxy increased with increasing TiO_2 content (Figure 5.18b), the strain at failure was lower than that for pure epoxy at all filler contents (Figure 5.18c). Goyat et al. [133] observed a similar fracture surface morphology in *ex-situ* prepared epoxy-TiO_2 nanocomposites. They reported several additional toughening mechanisms for the epoxy, although those were not observed in the specimens produced in this work. They also reported the same trends in the UTS and strain at failure with increasing TiO_2 content. However, the reported values of the strength were significantly lower than those measured in this work (35-50 MPa), and the strain at failure was higher (10-14 %). Ozsoy et al. [241] demonstrated a similar increase in the tensile strength and decrease in the strain at failure with increasing TiO_2 content. However, the decrease in the strain at failure was more significant when micron-sized TiO_2 was used instead of nano-sized TiO_2.

The decrease in strain (and subsequent reduction in the plastic deformation) at failure implies that the epoxy-TiO_2 nanocomposites are more brittle. However, the roughness of the fracture surfaces (shown in Figures 5.19 to 5.21) indicate otherwise. The fracture origins in all the epoxy-TiO_2 nanocomposites were in the interior of the specimen, unlike the pure epoxy where the fracture originated on the edges. The voids seen in Figures 5.19 to 5.21 are air bubbles that remained in the specimens from casting, and are the most likely source of weakness in the materials. Despite these voids, the increase in the UTS can be attributed to other toughening mechanisms in the nanocomposites. The fracture surfaces also showed a mirror-mist-hackle pattern similar to that observed in epoxy-SiO_2 nanocomposites with 5 wt% SiO_2. The increased fracture surface roughness indicates a greater dissipation of energy as the crack acceleration slowed down. At 3 and 5 wt% TiO_2, there was an additional smooth region between the mist and hackle regions in some specimens (highlighted in Figures 5.20 and 5.21). These regions were observed where the cracks bent perpendicularly, showing that these regions have increased toughening. The formation of parabolic lines (Figure 5.21b and c) corresponds to the formation of secondary cracks in front of the primary crack in the region of fast crack propagation [224], which also contributes to dissipation of energy. Some of the smaller voids observed may

correspond to debonding between epoxy and the larger TiO_2 particles. The debonding can lead to particle pull-out, which creates hemi-spherical holes or cavities on one surface, and exposed particles coated in epoxy on the other surface [133]. The energy spent in particle pullouts can also contribute to increased crack resistance. It is therefore possible that the presence of the TiO_2 nanoparticles limits the plastic deformation by increasing the rigidity of the polymer chains (which is also reflected in the increased T_g). Simultaneously, the TiO_2 can limit the acceleration of cracks via the particle pull-outs and formation of secondary crack fronts, thereby improving the tensile strength and creating a rough fracture surface.

6 Dielectric breakdown strength

The dielectric breakdown strength is an important parameter in the selection of materials for high voltage insulation, as it determines the limitations of the voltage in the application, as well as the design specifications for the chosen material. Increased dielectric breakdown strengths are desired, as this will allow either the use of higher voltages in applications, or a thinner layer of insulation. Several works have performed measurements of the breakdown strength on pure epoxy and *ex-situ* epoxy nanocomposites using different approaches or experimental designs. However, none have been found that have investigated the breakdown strengths of epoxy nanocomposites with *in-situ* synthesized nanoparticles.

It is important that the experiment is designed to test as large an area of the sample as possible during the measurement of the breakdown strength, as it is a stochastic property. Some authors [130,142,143,160,242–244] have measured the breakdown strength using spherical or hemispherical electrodes, where there is a single point of contact between the electrodes and the sample. A disadvantage of this setup is that only that point in the sample is probed and exposed to the highest electric field strength, and therefore the strength of the material may be misrepresented. Therefore, the choice was made to use cylindrical electrodes so that a larger volume of the sample was exposed to a uniform electric field.

However, several challenges were faced during the performance of these measurements, and an accurate estimate of the breakdown strength of pure epoxy could not be obtained. Consequently, the breakdown strengths of the *in-situ* nanocomposites were not tested. This chapter discusses the results of the experiments on pure epoxy, and the strategies used to tackle the challenges that arose. A key factor in these measurements is the electric field strength in the transformer oil, which was evaluated using COMSOL simulations of the different experimental setups used in the measurements (listed in Table 3.3). In addition, recommendations are made for further work in measuring the breakdown strength of pure epoxy and the *in-situ* nanocomposites.

6.1 Breakdown measurements using different setups

6.1.1 Electrodes encased in epoxy

Using Setup 1 in Table 3.3, dielectric breakdowns occurred in pure epoxy at 20-22 kV. For a sample thickness of 0.5 mm, this corresponded to an electric field strength of 40-44 kV mm^{-1}. The breakdowns took place at the edges of the electrodes at the interface between the brass and the epoxy casing, as shown in Figure 6.1. Some damage was always observed on the electrode at the point of breakdown, as shown by the yellow arrows in Figure 6.1a-c, which necessitated polishing of the electrodes between measurements. Figure 6.1c and d shows an example of extreme damage from the breakdown to both the electrode and the sample, respectively. In some cases, electrical trees were also observed to grow close to the centre of the sample (Figure 6.1d), most likely forming prior to the breakdown as they were disconnected from the breakdown point.

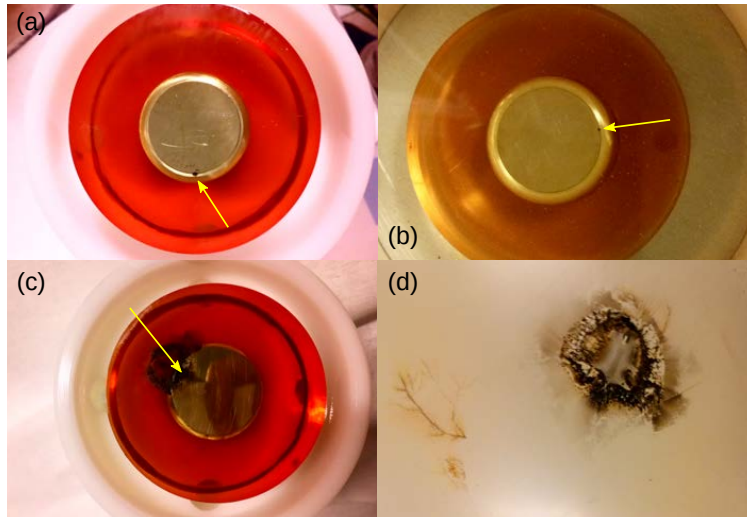

Figure 6.1. **(a,b)** The HV electrode surface after a breakdown was performed on two different samples of pure epoxy. The yellow arrow showing the damage to the electrode from discharges. **(c)** Severe damage to the HV electrode after a measurement. **(d)** The damage to the pure epoxy sample from carbonization due to the breakdown (same breakdown shown in **(c)**).

6.1.2 Bare electrodes

No changes in the breakdown strength were observed in pure epoxy when the bare brass electrodes were used without an epoxy casing (Setup 2 in Table 3.3). Breakdowns occurred at 20-22 kV, but the location of the breakdown was changed. Instead of at the edge of the flat face of the electrode, the breakdown occurred on a position in the sample that corresponded with the curved edge of the electrode. The difference is illustrated in Figure 6.2. Figure 6.3a and b show the position of the breakdown on the electrodes and the subsequent damage to them. Figure 6.3c and d show the regions of pure epoxy where cracks have formed radiating from the point of breakdown. Certain parts of the crack were sharp edged, while other parts appeared melted and rubbery (highlighted by the red and blue arrows, respectively, in Figure 6.3c and d). Some of the cracks can also be observed mirrored in the electrode, as seen by the line stretching across the flat surface in Figure 6.1a.

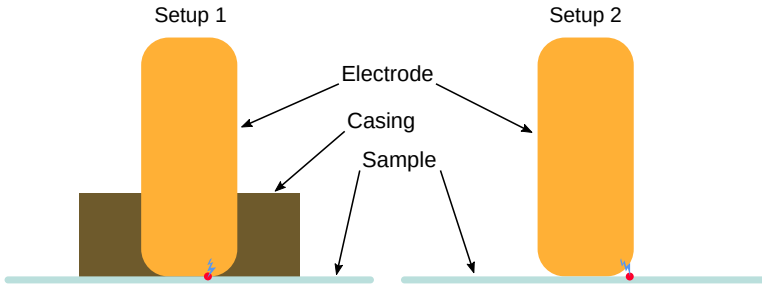

Figure 6.2. Illustration of the location of the breakdown in the pure epoxy in the two measurement setups (Setup 1 and Setup 2 from Table 3.3). The red dot with the blue lightning mark shows where the breakdown occurred in the two setups.

An additional incidence that was observed during the measurements after the epoxy casings were removed from the electrodes was the presence of a hissing noise above 18 kV. The transformer oil was also "cloudy" in appearance after each measurement, compared to previous experiments.

6.1.3 Pressurized oil and thinner samples

Pressurized oil was used to limit the discharges in the oil (Setup 3 in Table 3.3). The pure epoxy exhibited an increase in the breakdown strength, as the breakdown occurred at 26-27 kV (52-54 kV mm^{-1}). In addition, the hissing noise was no longer present. However, the breakdowns were still positioned on the curved edge of the electrodes (shown for Setup 2 in Figure 6.2).

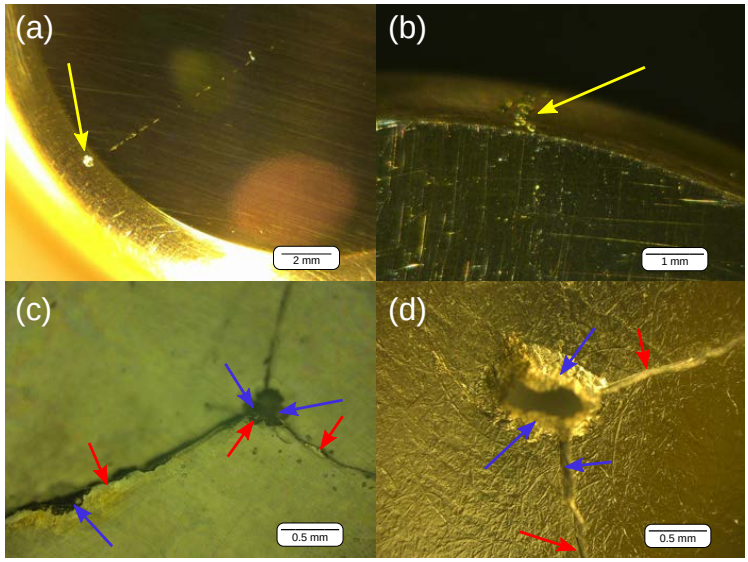

Figure 6.3. The breakdowns and the subsequent damage to **(a,b)** the electrodes and **(c,d)** the pure epoxy samples in two different measurements. The yellow arrows point to the electrode damage from the discharge during breakdown. The red and blue arrows indicate regions in the epoxy samples where the damage from the discharges resulted in either sharp cracks or melting/rubbery deformations, respectively.

The final set of measurements were performed on samples of pure epoxy with thicknesses between 0.25 and 0.3 mm, which were cured under N_2 pressurization (Setup 4 in Table 3.3). The breakdowns occurred at 20-21 kV, but due to the lower sample thicknesses this corresponded to a breakdown strength of 100-105 kV mm^{-1}. Despite the increase in the breakdown strength, the position of the breakdowns remained unchanged on the electrode edge.

6.1.4 Discussion

The occurrence of the breakdown at the interfaces between the electrode and the epoxy in Setup 1 can be attributed to delamination of the epoxy casing. A delamination introduces voids at the triple points between the casing, the electrode, and the sample. The electric field strength is amplified in the voids due to the lower relative permittivity of air (~1) compared to epoxy (~4), therefore acting as defects and a source for partial discharges. The partial discharges can erode the epoxy, making certain regions weaker and more susceptible to premature breakdown. Severe delaminations may result in significant damage

to the electrodes during the breakdown (shown in Figure 6.1c and d), as the discharges are increased significantly at the interfaces with many voids.

Removal of the epoxy casings, however, introduced a different problem. The hissing noise and the appearance of the oil was due to significant partial discharges in the oil prior to breakdown, resulting in the oil heating up and the formation of gas bubbles. Discharges in the oil are undesirable, as they can cause erosions in the epoxy sample, thereby weakening the material and making it more suspect to breakdowns at lower electric field strengths. In addition, the breakdown always taking place on the curved edge of the electrode is challenging, as the electric field strength in the sample underneath the edge is dependent on the curvature of the electrode. Usually the field strength at that location should also be lower than in the part of the sample that is between the flat surfaces of the electrode. Therefore, the exact field strength at the point of breakdown is unknown.

Despite these issues, the measured AC breakdown strengths were not too dissimilar from those reported in literature. Singha and Thomas [4] reported a breakdown strength of ~52.3 kV mm^{-1} in pure epoxy, using bare cylindrical electrodes with curved edges. Preetha and Thomas [245] performed similar measurements and reported bubbling in the oil and the breakdown taking place at a similar location. Liang and Wong [143] reported slightly lower breakdown strengths for pure epoxy (33 kV mm^{-1}), measured using spherical electrodes. Nascimento et al. [139] showed a breakdown strength of 47 mm^{-1} with a cylindrical electrode. However, the samples in that study were significantly thinner (50-80 μm).

Since the breakdown strength increased for pure epoxy when the transformer oil was pressurized, the breakdowns were not due to the failure of the epoxy samples, but failure in the transformer oil. The oil used, Midel 7131, has a minimum breakdown voltage of 75 kV (using the IEC 60156 standard) [246], which corresponds to a minimum breakdown strength of 30 kV mm^{-1}. Studies by Martin and Wang [247] and Jing et al. [248] reported that the breakdown strength of Midel 7131 lies between 45 and 55 kV mm^{-1}. The breakdowns in the experiments performed in this work occurred at similar electric field strengths. Combined with the fact that the breakdowns always occurred at the curved edge of the electrodes where they were exposed to the transformer oil, it is certain that the breakdown is measured not in the epoxy samples but in the oil instead. This would mean that the breakdown strength of the pure epoxy is possibly higher than 50 kV mm^{-1}. Pressurization of the oil minimizes the sizes of air bubbles in the oil, thereby increasing the breakdown strength of the oil.

In addition to pressurizing the oil, reducing the sample thickness also exhibited a significant increase in the breakdown strength. It is expected that even lower voltages would be required for breakdown to occur, as the field strength is increased significantly for a given voltage. However, the breakdowns still occurred at 20-21 kV, which exceeded the reported field strength of Midel 7131 significantly. The increased breakdown strength in Midel could be attributed to the presence of fewer air bubbles due to both the pressurization of the oil, as well as a smaller gap between the electrodes. Studies have shown how the breakdown strength of materials increased significantly for decreased sample thicknesses or gaps between electrodes [245, 249]. Since the breakdown is still occurring in the oil, the breakdown strength of pure epoxy exceeds at least 100 kV mm^{-1}. Several studies have reported similarly high (or even higher values) for breakdowns in pure epoxy. Bell et al. [70] and Virtanen et al. [141] both reported a breakdown strength of 185 kV mm^{-1} using recessed sample geometries for testing. Yeung and Vaughan showed similar values of 182 kV mm^{-1} in 70 µm thick samples tested with spherical electrodes. Heid et al. [160] reported 160 kV mm^{-1} in samples with an average thickness of 0.233 mm. Therefore, the correct experimental setup is important in determining the actual breakdown strength of pure epoxy, and subsequently the nanocomposites.

6.2 Simulations of the electric field

The electric fields around the sample and the electrodes with different configurations were simulated using the multiphysics simulation software COMSOL, as presented in Figure 6.4. Such simulations can be used to determine the appropriate electrode and sample geometries for measurements of the breakdown strength.

The simulations revealed that due to the lower relative permittivity of the oil (~3.15 [250]) compared to the pure epoxy and the shape of the electrodes, the electric field strength is slightly higher in the oil at the onset of the electrode edge. This is shown by the red arrows in the magnified image of the electrode edge in Figure 6.4a. Figure 6.4b shows that when electrodes with sharp edges are used, the electric field is amplified at the part of the sample closest to the edge of the ground electrode. If rounded edges are used with a sample with a diameter smaller than the electrode diameter (Figure 6.4c), then no amplification of the electric field is observed. The strongest field is then in the uniform part through the sample that is between the two electrodes, and becomes uniformly weaker at further distances. If a larger ground electrode is used (as was the case in the experiments when the epoxy casing was removed), then the electric field

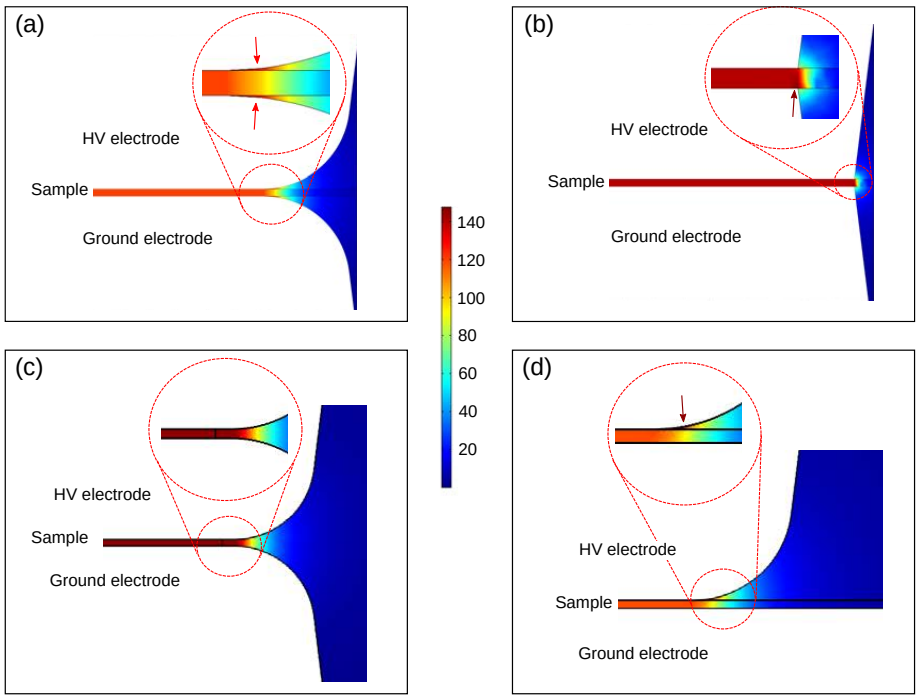

Figure 6.4. The simulated electric fields for different testing setups for the breakdown experiments: **(a)** electrodes with Rogowski profiles; **(b)** electrodes with sharp edges; **(c)** electrodes with Rogowski profile and sample diameter smaller than electrode diameter; **(d)** electrodes with Rogowski profile, and ground electrode with larger diameter than HV electrode. The red arrows indicate regions with a higher electric field strength.

strength is again amplified in the oil at the triple point interface between the HV electrode, the sample, and the oil, as seen in Figure 6.4d.

Based on the COMSOL simulations, changes in the sample shape or size, or changes in the electrode design can prevent the higher field strength in the oil. However, new challenges may arise for each option. If sharp electrode edges are used (Figure 6.4b), the electric field will be amplified close to the edge of the ground electrode instead of in the oil. Breakdowns are more likely to occur at that spot instead of in the region between the electrodes with a uniform electric field. This will add uncertainty to the measurements as the exact field strength at the breakdown point will not be known. Another alternative is to use a sample with a shorter diameter than the flat face of the electrode, so that the triple point between the electrode, oil, and the sample is not a curved surface (Figure 6.4c).

However, due to the short distance between the two electrodes, there is a high chance of surface discharges. The oil is used to negate such discharges over the sample surface but it would be ineffective if the distance between the electrodes over the surface is reduced so drastically. A third option would be to change the insulating fluid to a different oil, either with a permittivity higher than (but close to) that of the epoxy samples, or with a higher dielectric breakdown strength.

6.3 Recommendations for future measurements

A different solution to the challenge of breakdown in the insulating oil would be to remove the oil from the setup, and to use a different type of sample. Mohanty and Srivastava [251] performed breakdown measurements using a needle-plate configuration similar to that used for the electrical treeing measurements. One disadvantage with this approach, however, is that it is difficult to calculate the electric field strength around the high voltage needle accurately. This method also probes a smaller volume of material, since the electric field is uneven around the needle, and the highest field strength the sample will be exposed to will be only at the tip of the needle.

Another possible solution is to design the sample itself in the Rogowski profile that is used for the electrodes. The sample may be cast as a hollow "Rogowski cup" with an inner layer of a deposited electrode that is connected to the high voltage electrode, as shown in Figure 6.5. The Rogowski profile of the sample will prevent concentration of the electric field at the edges or in any one area, while maintaining a uniform electric field in a large volume of the flat face of the sample. The COMSOL simulations shown in Figure 6.5 show that in such a design there is no region where the electric field strength is larger than in the flat region between the two electrodes. Surface flashovers will also be prevented due to the shape of the sample, thereby eliminating the necessity for insulating oil. The primary challenge with such a design is in the casting of samples without defects, especially the removal of any air bubbles that may be introduced during casting.

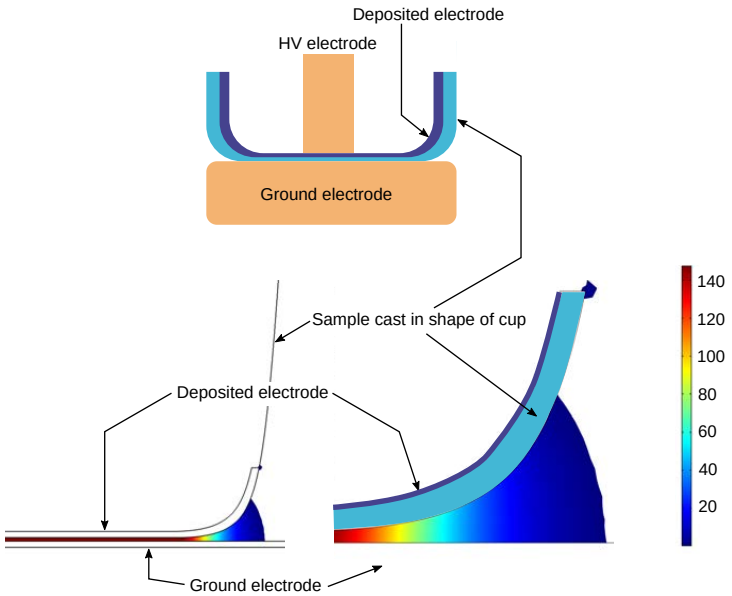

Figure 6.5. Illustration of the "Rogowski cup" design for the sample, and the COMSOL simulation of the electric field in a setup employing this cup with deposited electrodes.

7 Structure-property relations of the epoxy nanocomposites

The *in-situ* synthesized inorganic oxides in the different nanocomposites all have varying structures and morphologies, resulting from the different synthesis conditions and reactions of the alkoxide precursors. The interactions between the particles and the epoxy are affected by various factors, such as the type of inorganic oxide, the morphology and structure of the particle clusters and their state of dispersion, or the amount of coupling agent used. Increasing the knowledge of how these interactions are changed in the different nanocomposites will lead to increased understanding of the structure-property relations in these hybrid materials. In this chapter, selected properties of the nanocomposites with different types of inorganic oxide fillers are first compared. The glass transition behaviours, the complex permittivity, and the electrical treeing properties are emphasized. Explanations for these properties, based on the the chemistry of the reactions, the structure of the nanoparticles, and the formation of the organic-inorganic network are proposed and discussed.

7.1 Assessment of the different nanocomposites

Table 7.1 summarizes the key properties that were investigated for the different *in-situ* nanocomposites in this work. In general, epoxy-SiO_2 nanocomposites prepared with sufficient APTES, at neutral conditions (pH 7), and with a high filler content (5 wt% SiO_2) exhibited increased T_g and thermal stability, decreased permittivity, lower dielectric losses (above 10^3 Hz), and an increased resistance to electrical tree propagation. However, both the ultimate tensile strength and resistance to tree initiation were significantly decreased, and charge transport effects above the glass transition were amplified compared to pure epoxy or a lower SiO_2 content. In addition, other variations of the synthesis conditions or lower SiO_2 contents may result in degradation in one or more of the properties of the nanocomposites.

Table 7.1. A summary of the changes in selected properties of the *in-situ* epoxy nanocomposites, compared to pure epoxy, that are important for their application as materials in high voltage insulation.

Filler	Property		Description
SiO_2	Thermal	T_g	Initial decrease then increase with increasing SiO_2 content. Dependent on amount of SCA.
		Stability	Increased.
	Mechanical [a]	Elastic moduli	Initial decrease, then increase with increasing SiO_2 content.
		UTS	Decreased with increasing SiO_2 content.
		Strain at failure	Increased at higher SiO_2 content.
	Dielectric [b]	ϵ'_r (25 °C)	Dependent on synthesis conditions. Lower than pure epoxy for 5 wt% SiO_2 at all frequencies.
		tan δ (25 °C)	Dependent on synthesis conditions. Lower than pure epoxy for 5 wt% SiO_2 above 10^3 Hz, and higher below that frequency.
		ϵ'_r (above T_g)	Significantly higher independent of SiO_2 content. Increase in ϵ'_r occurs at lower temperatures for lower SiO_2 content.
	Treeing [c]	Initiation voltage	Lower than pure epoxy. Decrease dependent on synthesis conditions.
		Growth speed	Dependent on synthesis conditions. Slower growth at 10 kV for nanocomposites prepared at pH 7 with more APTES.
TiO_2	Thermal	T_g	Increased for all TiO_2 contents.
		Stability	Increased with increasing TiO_2 content °C.

Continued on next page

Table 7.1. continued

Filler	Property		Description
TiO_2	Mechanical	Elastic moduli	Increase with increasing TiO_2 content.
		UTS	Increased with increasing TiO_2 content.
		Strain at failure	Initially large decrease, then small increase with increasing TiO_2 content.
	Dielectric[b]	ϵ'_r (25 °C)	Lower than pure epoxy at 3 wt% TiO_2. At 5 wt% TiO_2, ϵ'_r is greater than that of pure epoxy above ~10^5 Hz.
		tan δ (25 °C)	Lower than pure epoxy above 10^3 Hz, and higher below that frequency.
		ϵ'_r (above T_g)	Lower than pure epoxy for 1 wt% TiO_2. Increased with increasing TiO_2 content.
	Treeing [c]	Initiation voltage	Generally lower than pure epoxy.
		Growth speed	Slower than in pure epoxy when trees are grown at both 10 and 15 kV.
Al_2O_3	Thermal	T_g	Higher for most filler contents.
	Dielectric [b]	ϵ'_r (25 °C)	Decreased with increasing Al_2O_3 content at all frequencies.
		tan δ (25 °C)	Slightly lower than pure epoxy above 10^2 Hz.
		ϵ'_r (above T_g)	Lower than pure epoxy for 5 wt% Al_2O_3. Decreased with increasing Al_2O_3 content.
	Treeing [c]	Initiation voltage	Similar to pure epoxy.
		Growth speed	Slower than in pure epoxy when trees are grown at 10 kV. Slightly faster than in pure epoxy when trees are grown at 15 kV.

[a] Measured only for the epoxy-SiO_2 nanocomposites prepared at pH 7 with APTES:DGEBA mass ratio of 1:10
[b] ϵ'_r and tan δ at 25 °C are compared over the entire frequency range. ϵ'_r above T_g is compared only at low frequencies (< 1 Hz).
[c] Treeing measurements were performed only for nanocomposites with 5 wt% filler content.

The epoxy-TiO_2 nanocomposites with 5 wt% TiO_2 displayed significant increases in T_g and the ultimate tensile strength, increased thermal stability, lower dielectric losses (above 10^3 Hz), and increased resistance to tree growth at both 10 and 15 kV. Charge transport effects were subdued in the nanocomposites with low TiO_2 content. The resistance to tree initiation, however, was decreased in these nanocomposites. Nanocomposites with 3 wt% TiO_2 exhibited a lower permittivity than pure epoxy, whereas at 5 wt% TiO_2 the permittivity was lower below 10^5 Hz, and higher above that frequency.

The epoxy-Al_2O_3 nanocomposites exhibited increases in T_g, but the increase in T_g was lower than in the epoxy-TiO_2 nanocomposites. Similar decreases in the permittivity and dielectric losses were observed as in the epoxy-SiO_2 nanocomposites. The strongest advantage of the epoxy-Al_2O_3 nanocomposites is that the resistance to tree initiation is comparable to that of pure epoxy, and the tree growth is negligible at 10 kV. However, at 15 kV the tree growth is similar to pure epoxy.

7.2 Interactions between the particles and the epoxy

The mobility of the epoxy chains determines several properties of the nanocomposites, including the glass transition behaviour. Piscitelli et al. [100] proposed an explanation for how the structure of the *in-situ* synthesized SiO_2 can affect T_g. In their work T_g decreased up to 3 wt% SiO_2, and then remained constant up to 12 wt% SiO_2. The decrease was attributed to the formation of flexible and linear siloxane species, and the constant T_g above 3 wt% SiO_2 was explained by the segregation of larger siloxane domains into a continuous phase. In this work, a similar mechanism is proposed, taking into account the interactions at the interfaces that can strongly influence the chain mobility.

In the *in-situ* synthesized nanocomposites, the primary form of interaction at the interfaces is the chemical bond between the particles and the epoxy chains via the APTES. Figure 7.1 illustrates the proposed interactions between SiO_2, with mass and surface fractal structures, and the epoxy chains for low and high SiO_2 contents, respectively. Table 7.2 compares the T_g for the different nanocomposites (Figure 4.38a and Figure 5.5a). APTES cannot cross-link four DGEBA molecules the way POPDA does due to the single amine group ($-NH_2$). The inclusion of APTES therefore leads to a reduction in the cross-linking degree in the cured epoxy, which is expected to decrease T_g. This decrease was observed in the epoxy-SiO_2 nanocomposites with low SiO_2 contents (< 4 wt%), as shown in Figure 4.38a and Table 7.2. T_g increased for higher SiO_2 content, which can be explained by the increasing size of SiO_2 and the evolution from mass to surface fractals in the structure.

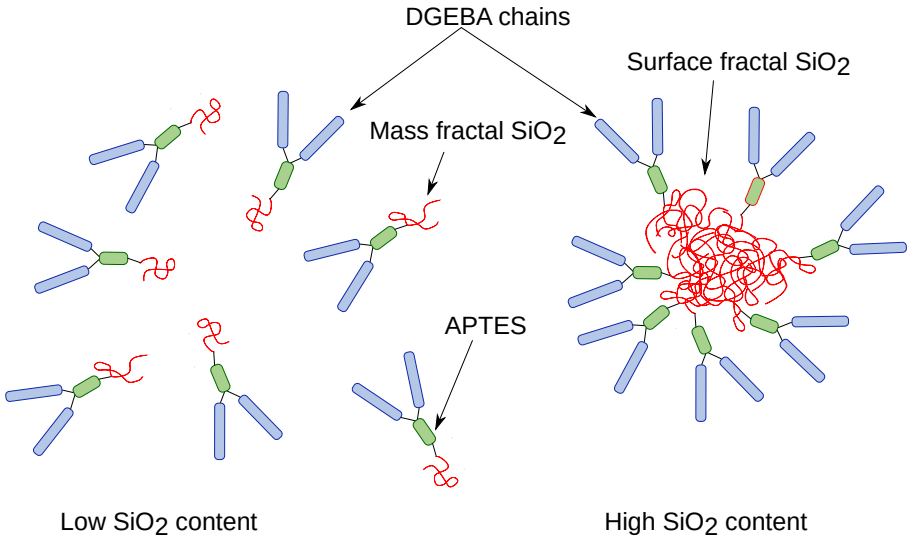

Figure 7.1. Illustration showing the proposed mechanism for how the SiO_2 structures interact with APTES and the DGEBA molecules at low and high SiO_2 content, and the resulting effect on the cross-linking degree of the DGEBA chains.

The cluster-cluster growth at low SiO_2 contents (Figure 4.12) results in mass fractal structures that are polymer-like and not interconnected. When attached to two DGEBA molecules via the APTES, the resulting molecule is long and flexible with no cross-links, and therefore exhibits a plasticizing effect on the neighbouring epoxy chains. This effect contributes to the decrease in T_g [100].

The likelihood of a SiO_2 cluster attaching to two or more APTES molecules is low due to the small size of the clusters. This situation is represented in Figure 7.1a. As the SiO_2 content is increased, the growth mechanism switches to monomer-cluster, which results in the formation of a networked surface-fractal structure that is more rigid. In addition, the increasing size of the SiO_2 clusters increases the likelihood of multiple APTES molecules connecting the epoxy chains to these clusters. It is also possible that several SiO_2 clusters, each attached to APTES, can start forming a network. If more than two APTES molecules are attached to a SiO_2 cluster (Figure 7.1b), then the cross-linking degree of the DGEBA molecules is greater than it would have been if they were cross-linked with POPDA. Therefore, T_g is increased and exceeds that of pure epoxy.

When the amount of APTES used is reduced (from an APTES:DGEBA mass ratio of 1:10 to 1:30), T_g increased. With fewer APTES molecules, there are fewer DGEBA molecules that are connected to one rather than three other DGEBA molecules (as is the case when cross-linked with POPDA). Thus the cross-linking degree is not significantly reduced. Simultaneously, the presence of larger clusters and agglomerates (as observed in Figure 4.1e and Figure 4.9) means that the cross-linking degree can even be increased further, since the agglomerates can connect several DGEBA chains that are attached to APTES. These two combined factors results in the epoxy-SiO_2 nanocomposites having a higher T_g for a lower APTES:DGEBA mass ratio at a given SiO_2 content. The preceding arguments can be used to also explain the changes in T_g in the epoxy-Al_2O_3 nanocomposites (listed in Table 7.2). Both the epoxy-TiO_2 and the epoxy-Al_2O_3 nanocomposites were prepared with the lower amount of APTES. Despite this, the Al_2O_3 clusters are large enough to bond with several APTES molecules, which can increase the cross-linking degree in the nanocomposites compared to pure epoxy.

The epoxy-TiO_2 nanocomposites, however, exhibited the largest increase in T_g among all the *in-situ* nanocomposites, despite having generally smaller structures than both the SiO_2 and the Al_2O_3. One possible reason could be the formation of a large number of titanium polyalkoxide clusters, with size of 3-5 nm (Figure 5.3). Due to the small size of these clusters (which are not part of a larger, hierarchical structure as in the case of the SiO_2), the interfacial volume will be much larger than in the other nanocomposites. The interactions between the epoxy chains and the particles are not limited to the bonds via the APTES, but can also be other physical bonds such as van der Waal's or hydrogen bonds. A larger interfacial volume would mean that more of the epoxy chains can have physical interactions with the inorganic clusters. Therefore, even if the degree of cross-linking is not increased, a larger interfacial volume will increase the number of physical interactions that can restrict the motion of the polymer chains, thus increasing T_g. The precipitation of larger particles, which occurs more

Table 7.2. Comparison of T_g between epoxy nanocomposites with SiO_2, TiO_2, and Al_2O_3 nanoparticles.

Filler	**Content [wt%]**	**APTES:DGEBA mass ratio**	**T_g [°C]**
None	-	-	83
SiO_2, pH 7	1	1:10	72
	3		75
	5		87
SiO_2, pH 11	5	1:10	82
		1:30	93
TiO_2, pH 7	1	1:30	103
	3		105
	5		89
Al_2O_3, pH 7	1	1:30	82
	3		93
	5		87

frequently for a larger TiO_2 content, will reduce the interfacial volume due to the lower ratio of surface area to volume for the larger particles. Hence, T_g decreased upon increasing the TiO_2 content to 5 wt%. Sajjad et al. [252] proposed that smaller nanoparticles do not hinder the development of the epoxy network during curing, whereas larger particles can act as barricades. Several authors have proposed that the free volume of the polymer increases for particles exceeding a certain size or filler content, which leads to a decrease in T_g [18,88,89,252]. This might explain why a decrease in T_g is observed for 5 wt% TiO_2 and Al_2O_3, compared to 3 wt% of the same fillers.

A final consideration is the shape and structure of the inorganic particles formed. The TiO_2 forms structures with a sharp, defined boundary, in contrast to the clusters of SiO_2 with a more diffuse boundary. The smaller titanium polyalkoxide clusters are also not as flexible as the linear siloxane mass fractals. These differences can be attributed to the faster hydrolysis and condensation reactions of TIP, compared to the TEOS and AIP, resulting in a more condensed TiO_2 product. The SiO_2 (and to some extent, the Al_2O_3) structures exhibit more open fractal features, and condensed particles are present only at higher filler contents. The shape of the nanoparticles is known to significantly affect the interfacial volume [253], and therefore the interactions with the epoxy chains. The diffuse, fractal structures in the epoxy-SiO_2 nanocomposites may allow closer interac-

tions between the particles and the epoxy chains (compared to the condensed TiO_2 particles). As a result, the free volume of the polymers may not be affected as much by the larger SiO_2 clusters at higher SiO_2 contents. In addition, the formation of open fractal structures in the SiO_2 allows interpenetration of the inorganic networks by the epoxy chains, which is illustrated in Figure 7.2. The ability of the epoxy chains to penetrate the larger inorganic network means that the free volume is not significantly decreased for larger clusters in the epoxy-SiO_2 nanocomposites. Hence, T_g does not decrease when the cluster size increases at higher filler contents.

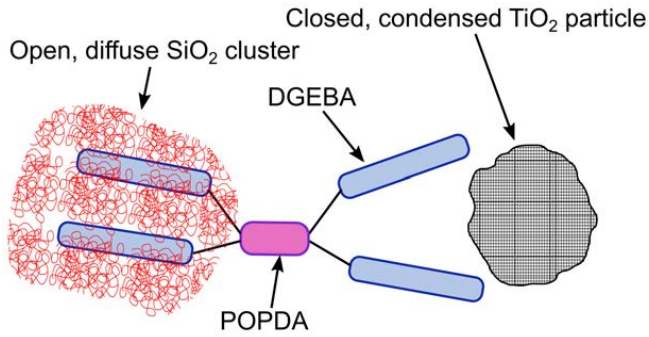

Figure 7.2. Illustration of the difference in the interactions of the DGEBA molecules in cured epoxy with the open fractal structures in SiO_2 and with the closed, condensed particles of TiO_2.

Therefore, there are several factors that can influence the structure of the organic-inorganic network in the *in-situ* epoxy nanocomposites. The most important of these appear to be how the cross-linking degree is affected by the APTES, the shape and structure of the inorganic networks (whether they are open and fractal, or closed and condensed), and the size of the inorganic domains. Features that control the glass transition of the nanocomposites, such as the chain mobilities, polymer-particle interactions, interfacial volume, and interpenetration of the two networks, are also expected to affect the other properties of the materials, including its behaviour in an electric field.

7.3 Effects of the interactions on the permittivity

The interactions between the epoxy chains and the inorganic oxide networks are most evident in the changes to the β-relaxation, as well as the overall decrease in the real relative permittivities. Figure 7.3 shows a comparison of ϵ_r' and tan

δ for the different *in-situ* nanocomposites (with 5 wt% filler content) prepared in this work. The *ex-situ* nanocomposite (with 0.5 wt% SiO_2) is also included. The regions in both ϵ'_r and tan δ that correspond to the β-relaxation and the new relaxation associated with the nanoparticles (referred to as NP relaxation in Figure 7.3) are highlighted.

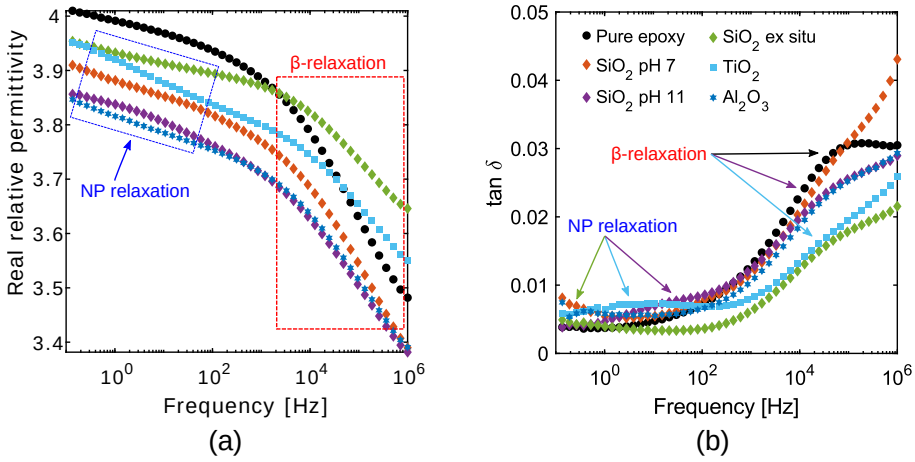

Figure 7.3. The **(a)** real permittivity and **(b)** tan δ of pure epoxy and different nanocomposites. The *in-situ* nanocomposites were all prepared with an APTES:DGEBA mass ratio of 1:30 and have a filler content of 5 wt%. The *ex-situ* SiO_2 however only contains 0.5 wt% SiO_2.

The overall decrease in the permittivity observed in most of the nanocomposites shows that the epoxy becomes less polarizable in general in the presence of inorganic oxide nanoparticles. Kochetov et al. [140] stated that this means fewer dipole groups on the epoxy chains respond to the electric field, and attributed it to the formation of an interfacial polymer layer with immobilized chains. This model is similar to the aligned chain model proposed by Andritsch et al. [59] (Figure 2.9d), and describes a situation akin to that shown in Figure 7.1b where multiple DGEBA molecules are bonded directly to the SiO_2 cluster via the APTES. Yeung and Vaughan [142] argued that these interactions should affect the glass transition primarily, as observed in this work, and not necessarily the polarizability of the system below T_g since the mobility of the entire chain is negligible below the glass transition. Alhabil et al. [214] attributed the decrease in ϵ'_r observed in the work by Kochetov et al. [140] to changes in the stoichiometry of the epoxy and the curing agent. However, these studies were performed on *ex-situ* nanocomposites, where pre-synthesized, condensed particles were used. In

this work, the *in-situ* nanocomposites containing SiO_2 and Al_2O_3 both exhibited open, fractal inorganic networks that can be penetrated by the organic network prior to curing. The interpenetration of DGEBA molecules into the inorganic oxide clusters (illustrated in Figure 7.2) will not only restrict the mobility of the whole chain, but also the mobility of dipole groups on the chains. Therefore, the *in-situ* nanocomposites exhibit a lower degree of polarization, and subsequently a lower ϵ'_r compared to pure epoxy.

Upon comparing the change in ϵ'_r in Figure 7.3a, the decrease in ϵ'_r is not even at all frequencies. The larger decrease in ϵ'_r at lower frequencies suggests that fewer O-H dipoles are participating in the β-relaxation in the nanocomposites. These dipoles can become more restricted due to the formation of hydrogen bonds with unreacted -OH groups in the open inorganic oxide networks, thus becoming less responsive to the switching electric field. However, the interactions of the O-H dipoles will change if the particles are more closed and condensed structures. Subsequently, the β-relaxation is significantly different in the *in-situ* epoxy-TiO_2 and *ex-situ* epoxy-SiO_2 nanocomposites, showing the lowest values of tan δ (Figure 7.3b). The larger decrease in tan δ in these nanocomposites might suggest that there are even fewer participating O-H dipoles, but this is misleading. In such a case, ϵ'_r would still be lower than in pure epoxy at high frequencies, not higher (as seen in Figure 7.3a). It is possible that the O-H dipoles can interact with the surface -OH groups on the particles. However, the agglomeration of the *ex-situ* SiO_2 and the larger spacing between the *in-situ* synthesized TiO_2 clusters means that these interactions are not ubiquitous, which could result in the formation of numerous and fragmented dipole clusters [240]. It is also unknown what kind of interactions may exist between the O-H dipoles and the smaller titanium polyalkoxide clusters, since the exact structure of such alkoxides in these nanocomposites are unknown.

Other questions remain regarding the new relaxation between 1 and 100 Hz in the nanocomposites. This relaxation is mostly insignificant in the *in-situ* epoxy-Al_2O_3 and *ex-situ* epoxy-SiO_2 nanocomposites, but is stronger in the *in-situ* epoxy-SiO_2 and epoxy-TiO_2 nanocomposites. Yeung and Vaughan [142] suggested that the relaxation is caused by adsorbed water on the particle surface, and reported that increasing the amount of SCA resulted in a less apparent relaxation. This is unlikely to be the cause of the relaxation in the *in-situ* nanocomposites, as the only exposure to water for the nanoparticle surfaces would be unreacted water from the synthesis. In addition, changing the amount of APTES did not result in a significant difference in the relaxation, showing that it is not absorbed water that is responsible for the relaxation. Since the relaxation occurs in the frequency region where interfacial polarization mechanisms are prevalent, it is assumed that the new relaxation is associated with dipoles

forming at the interfaces between the polymer and the particles. This assumption is consistent with how the strength of the new relaxation changes with the interfacial volume in the different nanocomposites. The *ex-situ* nanocomposite contains agglomerated SiO_2 and a low SiO_2 content, and therefore a low interfacial volume. Subsequently the new relaxation is weak and present at a lower frequency. At the opposite end, the *in-situ* epoxy-TiO_2 nanocomposites contain some condensed particles (10-50 nm) that are precipitated from a large number of small titanium polyalkoxide clusters. The interfacial volume in these nanocomposites is therefore the largest, and subsequently presents the strongest relaxation (and highest peak in tan δ). However, further studies are required to determine what kind of interactions at the interfaces are responsible for the dipoles associated with this relaxation.

7.4 Proposed models for the electrical treeing

Several models have been proposed to explain the increased resistance to electrical treeing in nanocomposites. Tanaka et al. [156] attributed the slower tree growth to the formation of tortuous zig-zag paths through the nanocomposite, illustrated in Figure 7.4. Due to the higher permittivity of the inorganic oxides than the epoxy matrix, the electrical field is reduced in the particles. Consequently, the difference in the electrical field strength is higher at the interfaces. The local enhancement of the electrical field gradient means that the tree channels will be directed towards the nanoparticles. However, due to the higher discharge resistance of the inorganic oxides, the tree channel will propagate around the particle surface before it exits the interfacial region and into the epoxy matrix. The channel then is directed towards the next particle interface.

The model assumes that the tip of the tree must be in the same size scale as the filler particles. The observed tree channels are usually 2-5 μm in width and the inorganic nanoparticles typically form clusters smaller than 300 nm. Therefore it is possible that the tip of the trees are initially thinner, and are only observed when they grow wider with time as they erode the epoxy. One limitation of this model is that it cannot explain why the tree growth speed increased in the *in-situ* epoxy-SiO_2 nanocomposites when the amount of APTES was decreased. Despite the poorer dispersion and larger cluster sizes, the presence of the SiO_2 in epoxy should still obstruct the tree growth in a similar way. Instead, the growth rate was faster than in pure epoxy. Chen et al. [155] demonstrated how the treeing properties were improved in nanocomposites when the particles were surface treated to improve the dispersion, compared to no surface treatment.

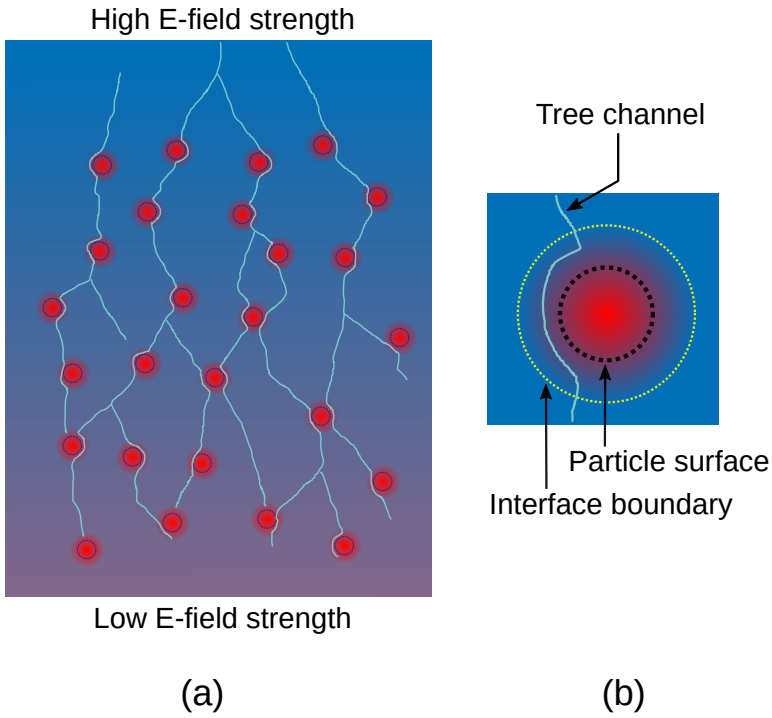

Figure 7.4. **(a)** Illustration of one proposed mechanism explaining the slower tree growth in nanocomposites with well dispersed nanoparticles, showing how the tree channels are directed towards the particle interfaces with a steeper electric field gradient. The blue areas represent high electric field strength, and the red areas low electric field strength. **(b)** A magnification of the region around a nanoparticle, showing the change in the electric field strength over the interface, and the propagation of a tree channel around the particle surface through the interface.

However, even without surface treatment, the nanocomposites exhibited better electrical treeing properties than pure epoxy. Nakamura et al. [154] proposed that the internal stresses in epoxy creates regions of the polymer that are weaker, and therefore more susceptible to tree propagation. These internal stresses usually arise during the curing of the epoxy resin due to shrinkage and mismatch in thermomechanical properties [254], and can be amplified due to inadequate interfacial adhesion [255]. Reducing the amount of APTES may therefore have led to poorer interfacial adhesion between the SiO_2 and the epoxy, contributing to increases in the internal stresses compared to when no fillers are used.

The zig-zag treeing model can explain why the tree growth is significantly faster in the epoxy-TiO_2 and epoxy-Al_2O_3 nanocomposites than in the epoxy-SiO_2 nanocomposites. SiO_2 has a permittivity of ~3.9 [256], which is very close to that of epoxy, whereas the permittivities of Al_2O_3 and TiO_2 are much higher at ~9.4 and ~100, respectively [1, 256]. Hence, the electrical field gradient will not be as steep around the SiO_2 nanoparticles. In addition, despite TiO_2 having a higher permittivity, the tree growth was significantly slower in the epoxy-Al_2O_3 nanocomposites. Therefore, there must be additional mechanisms which determine the propagation speed of the tree channels.

An alternative model for explaining tree growth in nanocomposites is the presence of carrier traps in the nanoparticles. Usually charge carriers can be captured by carrier traps in the polymer, which limits the carrier mobility and density, thus limiting the tree propagation [257–259]. The addition of nanoparticles can introduce deep level traps or change the trap density, thereby increasing resistance to electrical tree growth compared to pure epoxy. Zhang et al. [260] proposed that a potential well forms between the epoxy matrix and the "bound" interfacial region (described in the layered model by Tanaka et al. [53]) which traps the charge carriers. Smith et al. [259] stated that the charge layer that develops between the inorganic oxide and the polymer is critical for the trapping mechanism. Therefore, changes in the interfaces via the SCAs can also alter the traps or the charge mobility. Since the SCAs affect the bonding and interaction of the nanoparticles with the polymer, they can affect the Coulombic interactions at the nanoparticle surface. Agglomeration of the nanoparticles, as is the case when the amount of APTES is reduced, and a subsequent reduction in the interfacial volume will naturally reduce the number of deep traps introduced by the nanoparticles. Zhang et al. [260] showed using thermally stimulated currents and pulsed electro-acoustic measurements that the number of shallow traps increased in agglomerated Al_2O_3 nanoparticles. The traps introduced by the nanoparticles may also be dependent on the type of inorganic oxide. In their particle interphase model (Figure 2.9e), Alhabil et al. [60] described how defects on the particle surface can generate new localized energy levels, which can form charge traps if they lie in the band gap. If the traps are sufficiently deep and far from each other, they will contribute to decreasing charge movement. Alternatively, the generated energy levels may be deeper in the conduction or valence band, thereby widening the band gap and creating an energy barrier for charge movement through the interphase. It is therefore likely that the trap density and trap depth varies in the different nanocomposites depending on the type of nanoparticle used, the morphology of the particles, and the surface functionalization.

Generally, the voltage at which the tree initiates depends on the charge build-up from injection and extraction of electrons, or when other charge carriers are accelerated by the electric field and gain sufficient kinetic energy to cause chain scissions [124, 258]. Therefore, the presence of charge traps in the nanoparticles will also affect the initiation voltage. Based on the initiation voltages and the tree growth behaviours at 10 and 15 kV, it can be assumed that traps in the epoxy-Al_2O_3 nanocomposites are more numerous than in the epoxy-TiO_2 nanocomposites, but the traps in the epoxy-TiO_2 nanocomposites are deeper. The large number of traps means a larger number of charge carriers need to be accelerated to initiate and propagate the trees in the epoxy-Al_2O_3 nanocomposites. Since the traps are shallow, a higher voltage might be sufficient to excite the charge carriers out of these traps, but not the deep traps in the epoxy-TiO_2 nanocomposites. Therefore, the tree growth rate remains slow in the epoxy-TiO_2 nanocomposites at 15 kV, but not in the epoxy-Al_2O_3 nanocomposites. Another factor that may influence the initiation voltages in the nanocomposites is the presence of extra charge carriers (e.g. ions) from the *in-situ* synthesis process. This could explain why the epoxy-SiO_2 nanocomposites prepared at pH 11, which is achieved by the addition of ammonia solution, have the lowest initiation voltages. The inclusion of NH_4^+ and OH^- in the epoxy from the ammonia used is therefore detrimental to its treeing resistance. Any other unreacted chemicals from the *in-situ* synthesis of the inorganic oxides, or even by-products that have not been completely removed such as ethanol or 2-propanol, can contribute to the lowering of the initiation voltage.

7.5 Summary of structure-property relations

The various differences in the properties of the *in-situ* epoxy nanocomposites in this work are attributed to a combination of the composition of the materials (the content and the type of inogranic oxide), the morphology and structure of the filler particles, and the degree of dispersion of the particles. The structure and morphology of the particles can affect the cross-linking of the epoxy chains, the volume of the interfacial region, and the degree of interpenetration between the organic and inorganic networks. These factors can influence the glass transition behaviour and dielectric properties. At the same time, the choice of the inorganic oxide filler (TiO_2, Al_2O_3, SiO_2, or even other oxides not investigated in this work) can also be important. The different electronic structures and band gaps of the various oxides will influence the charge trap levels and densities, thereby affecting the electrical treeing properties and partial discharge resistance. The treeing may also be affected by the inherent permittivities of the inorganic oxides. In addition, the morphology of the particles is also dependent on the filler

content in the *in-situ* nanocomposites. Hence, both the filler morphology (size, shape, and structure) and the filler composition (type of oxide, and amount) are important to consider when evaluating the desired properties for applications.

The epoxy-Al_2O_3 and epoxy-TiO_2 nanocomposites exhibited the best dielectric and thermal properties among the three types of *in-situ* nanocomposites prepared in this work. Due to the higher resistance to electrical tree initiation and tree growth observed in the epoxy-Al_2O_3 nanocomposites, they may be suitable for use in insulation where electrical stress from partial discharges are prominent. The decrease in permittivity, compared to pure epoxy, at higher temperatures may also make epoxy-Al_2O_3 nanocomposites attractive for high-temperature dielectrics, which are required in generators or compact transformers [1]. The decrease in PD observed in the epoxy-Al_2O_3 nanocomposites can extend their lifetime as components in barriers and bushings [261], or in motor windings and power generators [262]. The epoxy-TiO_2 nanocomposites, on the other hand, could be more suitable in applications where mechanical and thermal stresses are higher. Their improved tensile strength, significantly higher T_g, lower permittivity, increased resistance to tree growth, and increased thermal stability are desirable for gas insulated switchgear, bushings, cable joints, or other outdoor insulation [261]. The epoxy-SiO_2 nanocomposites demonstrate slight improvements in resistance towards electrical tree growth and a lower permittivity, depending on the synthesis conditions used. However, their poorer mechanical properties make them less desirable for outdoor applications. They might be suitable for use as packaging materials or encapsulations for power electronic devices (e.g. power converters or insulated-gate bipolar transistors) [263, 264]. The predicted improvements in the thermal conductivity of the epoxy-SiO_2 nanocomposites from the MD simulations make them an attractive option in insulation where heat transfer from the conductors is important [265].

8 Further work

The *in-situ* approach has proven to be a reliable and robust method for preparing epoxy nanocomposites with a good dispersion of the inorganic oxide filler particles, thereby negating the challenge of producing well-dispersed nanocomposites via *ex-situ* methods. The next step towards applications of the *in-situ* nanocomposites as nanodielectrics is to explore how the synthesis conditions can be used to tune the structure, morphology, and the dispersion of the particles, and subsequently control the dielectric, mechanical, and thermal properties.

As observed from the higher permittivities at low frequencies above the glass transition and the lower initiation voltages for trees in the epoxy-SiO_2 and epoxy-TiO_2 nanocomposites, the aqueous sol-gel method for preparing nanoparticles *in situ* has disadvantages, despite the excellent dispersion of the particles. Therefore, a non-aqueous sol-gel approach should be considered. Several works have demonstrated similar morphologies of SiO_2 synthesized *in situ* in epoxy using the non-aqueous approach with BF_3MEA as the catalyst [21, 90, 91]. However, there have been no investigations of the dielectric properties of nanocomposites prepared using non-aqueous methods. It would therefore be interesting to investigate the complex permittivity and electrical treeing properties in these materials, and to check if the use of different catalysts and the removal of water from the synthesis would be less or more detrimental to the properties. An additional synthesis parameter that can be investigated is the type of SCA used. Several other SCAs such as 3-(isocyanatopropyl) triethoxysilane (IPTES) or 3-(aminopropyl) trimethoxysilane (APTMS) could be employed. APTMS may also be hydrolysed in organic solvents without water due to the increased reactivity of the methoxy groups [266], making it suitable for non-aqueous sol-gel routes.

Further improvements to the models used in the MD simulations can allow improved predictions of different thermoelastic properties of the nanocomposites systems. The incorporation of interfacial interactions between the SiO_2 nanoparticle in Model I and the epoxy chains, for example by including SCAs, is recommended. Equivalent models for other nanoparticles, such as TiO_2, Al_2O_3, MgO, or ZnO, should also be built and used to predict the properties of those nanocomposites. MD can therefore be a versatile tool for deciding which nanocomposite systems should be selected for experimental investigations. Experimental verification of the thermal conductivities of the epoxy-SiO_2 nanocomposites predicted by the MD simulations can be useful, as nanodielectrics with higher thermal conductivities are desirable.

Additional characterization of the dielectric properties of the nanocomposites is strongly recommended. The dielectric breakdown strength is a critical parameter for nanodielectrics, and should be investigated for the *in-situ* nanocomposites and compared to that of pure epoxy. As discussed in Chapter 6, performing accurate measurements in the transformer oil is difficult due to the lower breakdown strength of the oil. Therefore, the use of test samples shaped into Rogowski cups is recommended for these experiments. One challenge that is expected in this approach is that the sample preparation will be comparatively more time consuming and difficult, as the samples should be cast without defects (e.g. air bubbles). In addition, the current flow at breakdown should be limited using either a resistor, or a faster disconnecting circuit, to reduce the damage to the electrodes. The effect of the filler content of the different inorganic oxides on the breakdown strength of the nanocomposites will be highly informative of the performances of these materials as high voltage insulation.

While the complex permittivities of the nanocomposites with different fillers were investigated at multiple filler contents between 1 and 5 wt%, the treeing properties were investigated only for the nanocomposites with 5 wt% filler. Investigating how the treeing resistance (in terms of initiation voltage, or tree growth rate, or tree morphology) varies with the filler contents of SiO_2, TiO_2, and Al_2O_3 could be beneficial. A combination of the treeing measurements with additional techniques, such as electroluminescence, thermally stimulated currents, pulsed electro-acoustic and space charge measurements, can provide deeper insight into the processes occurring at tree initiation (e.g. characterizing trap densities and levels). 3D imaging techniques, such as X-ray computed tomography (XCT) [220, 267] can provide a better visual representation of the trees, allowing additional characterization of the tree structure. XCT can also enable characterization of trees in more opaque materials, which will be useful for investigating trees formed in nanocomposites with a poorer dispersion or a higher filler content.

9 Conclusions and outlook

Nanoparticles of SiO_2, TiO_2, and (pseudo-)Al_2O_3 were synthesized *in situ* in epoxy using an aqueous sol-gel procedure with APTES as a coupling agent. The *in-situ* synthesis of the inorganic oxides was established as a versatile and efficient method for consistently achieving a satisfactory state of dispersion of the filler nanoparticles. Nanocomposites with up to 5 wt% filler content were prepared with well dispersed nanoparticle clusters, compared to the *ex-situ* nanocomposite with 0.5 wt% SiO_2 with micron-sized agglomerates. Variations in the morphologies and structures of the *in-situ* synthesized nanoparticles were related to differences in the growth mechanisms and the chemistry of the precursors. The changes in the glass transition temperatures of the nanocomposites were attributed to the changes in the structure with filler content, and the effect of including the APTES on the cross-linking degree of the epoxy chains. Generally, at high filler contents (5 wt%) the glass transition temperatures of the nanocomposites were increased compared to pure epoxy. The epoxy-SiO_2 nanocomposites had a lower tensile strength than pure epoxy. The opposite was observed in the epoxy-TiO_2 nanocomposites, showing increased strength with increasing TiO_2 content. Both the epoxy-SiO_2 and epoxy-TiO_2 nanocomposites exhibited a higher tensile modulus than pure epoxy for 5 wt% filler content. MD simulations of the nanocomposite, modelling the SiO_2 as both a particle and as molecular units, predicted the glass transition and elastic moduli of the nanocomposites well, compared to the measured data. The model representing the SiO_2 as a particle predicted a thermal conductivity that was closer to values reported in literature.

The real relative permittivity at room temperature was lower in all nanocomposites with 5 wt% filler. The decrease in permittivity corresponds to a lower degree of polarization of the epoxy, which was attributed to both the interaction of the dipoles with the nanoparticles, and the interpenetration of the organic and inorganic network. The interfacial interactions between the epoxy chains and the nanoparticles resulted in an additional dielectric relaxation, generally between 1 and 100 Hz. The strength of this relaxation was observed to be correlated with the state of dispersion of the nanoparticles. The presence of the nanoparticles had a strong influence on the O-H dipoles in the β-relaxation, as all the nanocomposites with 5 wt% filler exhibited a lower dielectric loss than pure epoxy above 10^3 Hz. Above the glass transition, the charge transport effects in pure epoxy were usually amplified in the nanocomposites due to the presence of additional ions and by-products from the *in-situ* sol-gel process.

These by-products also contributed to the lower voltages required for initiation of electrical trees in the nanocomposites, compared to pure epoxy. However, the epoxy-TiO_2 and epoxy-Al_2O_3 nanocomposites both exhibited a significant resistance to electrical tree growth at 10 kV. The epoxy-SiO_2 nanocomposites displayed both slower and faster tree growth than pure epoxy, depending on the amount of APTES used. At 15 kV, the electrical tree growth rate was comparable for the pure epoxy and epoxy-Al_2O_3 nanocomposites, whereas the epoxy-TiO_2 nanocomposites still possessed a higher resistance to tree propagation. Two possible factors for the improved resistance to electrical tree growth were proposed and discussed: The higher inherent permittivities of the TiO_2 and Al_2O_3 compared to pure epoxy, and the increased number and depth of carrier traps in the inorganic oxides. The formation of these traps is also dependent on the morphology and surface chemistry of the particles, which may explain the variation in treeing properties of the epoxy-SiO_2 nanocomposites with different amounts of APTES.

The increased resistance to electrical tree propagation, lower permittivities, and increased thermal stabilities of the *in-situ* nanocomposites demonstrates the potential of the *in-situ* synthesis route in preparing these hybrid materials in high quality. However, for this method to be used for high voltage insulation nanocomposites on an industrial scale, the complete parameter space must be understood. New challenges may also emerge in scaling up the *in-situ* procedure, especially considering the use of chemicals such as TEOS, which is flammable, and TIP, which hydrolyses easily with moisture. With an increasing focus on a green shift in industry, further investigations should be performed on the sustainability of both *in-situ* and *ex-situ* formed epoxy nanocomposites. It is worth remembering that many of the improvements in properties demonstrated by the *in-situ* nanocomposites can be useful in applications other than nanodielectrics. While a lower permittivity is desirable in electrical insulation, higher permittivities can be attractive for capacitors [262, 265]. Thus, the *in-situ* synthesis of other inorganic fillers, such as $BaTiO_3$, that are known to increase the permittivity of the nanocomposites can be explored as well. Control of the permittivity in the material can also allow development of functionally graded materials, enabling control over the distribution of the electric field [264, 265]. An improved understanding and overview of the *in-situ* synthesis route can enable the preparation of several different inorganic oxides simultaneously in epoxy, with control over the structures of the different oxides. The use of two or more different types of fillers in epoxy nanocomposites can lead to the development of novel materials for nanodielectrics.

Bibliography

[1] J. K. Nelson. *Dielectric polymer nanocomposites*. Springer, New York, USA, 2010.

[2] I. Plesa, P. V. Notingher, S. Schlögl, C. Sumereder, and M. Muhr. Properties of Polymer Composites Used in High-Voltage Applications. *Polymers*, 8(173), 2016.

[3] K. N. Mathes. A brief history of development in electrical insulation. In *Proceedings of the Electrical/Electronics Insulation Conference*, Boston, MA, USA, 1991. IEEE.

[4] S. Singha and M. J. Thomas. Dielectric properties of epoxy nanocomposites. *IEEE Transactions on Dielectrics and Electrical Insulation*, 15(1):12–23, 2008.

[5] J. K. Nelson and J. C. Fothergill. Internal charge behaviour of nanocomposites. *Nanotechnology*, 15(5):586–595, 2004.

[6] M. M. Adnan, E. G. Tveten, J. Glaum, M.-H. G. Ese, S. Hvidsten, W. Glomm, and M.-A. Einarsrud. Epoxy-Based Nanocomposites for High-Voltage Insulation: A Review. *Advanced Electronic Materials*, 5(2):1800505, 2019.

[7] C. Calebrese, L. Hui, L. S. Schadler, and J. K. Nelson. A Review on the Importance of Nanocomposite Processing to Enhance Electrical Insulation. *IEEE Transactions on Dielectrics and Electrical Insulation*, 18(4):938–945, 2011.

[8] H. Gu, C. Ma, J. Gu, J. Guo, X. Yan, J. Huang, Q. Zhang, and Z. Guo. An overview of multifunctional epoxy nanocomposites. *Journal of Materials Chemistry C*, 4:5890–5906, 2016.

[9] M. M. Adnan, A. R. M. Dalod, M. H. Balci, J. Glaum, and M.-A. Einarsrud. In situ synthesis of hybrid inorganic-polymer nanocomposites. *Polymers*, 10(10), 2018.

[10] P. H. C. Camargo, K. G. Satyanarayana, and F. Wypych. Nanocomposites: Synthesis, Structure, Properties and New Application Opportunities. *Materials Research*, 12(1):1–39, 2009.

[11] C. Sanchez, B. Julián, P. Belleville, and M. Popall. Applications of hybrid organic–inorganic nanocomposites. *Journal of Materials Chemistry*, 15(35-36):3559, 2005.

[12] G. Schottner. Hybrid Sol-Gel-Derived Polymers: Applications of Multifunctional Materials. *Chem.Mater*, 13:3422–3435, 2001.

[13] F. L. Jin, X. Li, and S. J. Park. Synthesis and application of epoxy resins: A review. *Journal of Industrial and Engineering Chemistry*, 29:1–11, 2015.

[14] C. J. Brinker and G. W. Scherer. *Sol-Gel Science: The Physics and Chemistry of Sol–Gel Processing*. Academic Press, Inc., 1990.

[15] A. R. M. Dalod. *In situ synthesis of titania and titanium based organic-inorganic nanomaterials*. PhD thesis, Norwegian University of Science and Technology (NTNU), Norway, 2017.

[16] W. D. Callister Jr., D. G. Rethwisch, and R. Balsubramaniam. *Callister's Materials Science and Engineering*. Wiley India, India, 8th edition, 2010.

[17] A. Serra, X. Ramis, and X. Fernández-Francos. Epoxy sol-gel hybrid thermosets. *Coatings*, 6:8, 2016.

[18] M. Perchacz, H. Beneš, A. Zhigunov, M. Serkis, and E. Pavlova. Differently-catalyzed silica-based precursors as functional additives for the epoxy-based hybrid materials. *Polymer*, 99:434–446, 2016.

[19] W. Yu, J. Fu, X. Dong, L. Chen, H. Jia, and L. Shi. Highly populated and nearly monodispersed nanosilica particles in an organic medium and their epoxy nanocomposites. *ACS Applied Materials and Interfaces*, 5(18):8897–8906, 2013.

[20] C. C. Wu and S. L. C. Hsu. Preparation of epoxy/silica and epoxy/titania hybrid resists via a sol-gel process for nanoimprint lithography. *Journal of Physical Chemistry C*, 114(5):2179–2183, 2010.

[21] S. Ponyrko, L. Kobera, J. Brus, and L. Matějka. Epoxy-silica hybrids by nonaqueous sol-gel process. *Polymer*, 54:6271–6282, 2013.

[22] P. Judeinstein and C. Sanchez. Hybrid organic–inorganic materials: a land of multidisciplinarity. *J. Mater. Chem.*, 6(4):511–525, 1996.

[23] G. Kickelbick. Hybrid Materials – Past, Present and Future. *Hybrid Materials*, 1(1), 2014.

[24] C. Sanchez and F. Ribot. Design of Hybrid Organic-Inorganic Materials Synthesized Via Sol-Gel Chemistry. *New Journal of Chemistry*, 18(10):1007–1047, 1994.

[25] T. Tanaka, G. C. Montanari, and R. Mulhaupt. Polymer Nanocomposites as Dielectrics and Electrical Insulation-perspectives for Processing Technologies, Material Characterization and Future Applications. *IEEE Transactions on Dielectrics and Electrical Insulation*, 11(5):763–784, 2004.

[26] International Organization for Standardization 80004-1:2015, ISO/TS, 2015.

[27] J. Jeevanandam, A. Barhoum, Y. S. Chan, A. Dufresne, and M. K. Danquah. Review on nanoparticles and nanostructured materials: history, sources, toxicity and regulations. *Beilstein J. Nanotechnol*, 9:1050–1074, 2018.

[28] M. Imteyaz Ahmad and S. S. Bhattacharya. Size effect on the lattice parameters of nanocrystalline anatase. *Appl. Phys. Lett*, 95:191906, 2009.

[29] H. Zhang and J. F. Banfield. Thermodynamic analysis of phase stability of nanocrystalline titania. *Journal of Materials Chemistry*, 8(9):2073–2076, 1998.

[30] F. Font and T. G. Myers. Spherically symmetric nanoparticle melting with a variable phase change temperature. *Journal of Nanoparticle Research*, 15:2086, 2013.

[31] E. Roduner. Size matters: Why nanomaterials are different. *Chemical Society Reviews*, 35(7):583–592, 2006.

[32] O. G. Grendal, I. Nylund, A. B. Blichfeld, S. Tominaka, K. Ohara, S. M. Selbach, T. Grande, and M. Einarsrud. Controlled Growth of $Sr_xBa_{1-x}Nb_2O_6$ Hopper- and Cube-Shaped Nanostructures by Hydrothermal Synthesis. *Chemistry – A European Journal*, 26:1–9, apr 2020.

[33] T. Gholami, M. Salavati-Niasari, M. Bazarganipour, and E. Noori. Synthesis and characterization of spherical silica nanoparticles by modified Stöber process assisted by organic ligand. *Superlattices and Microstructures*, 61:33–41, 2013.

[34] A. R. M. Dalod, O. G. Grendal, S. L. Skjærvø, K. Inzani, S. M. Selbach, L. Henriksen, W. van Beek, T. Grande, and M.-A. Einarsrud. Controlling Oriented Attachment and in Situ Functionalization of TiO_2 Nanoparticles During Hydrothermal Synthesis with APTES. *The Journal of Physical Chemistry C*, 121:11897–11906, 2017.

[35] N. Sui, Y. Duan, X. Jiao, and D. Chen. Large-Scale Preparation and Catalytic Properties of One-Dimensional α / β-MnO_2 Nanostructures. *J. Phys. Chem. C*, 113:8560–8565, 2009.

[36] N. R. Keskar and J. R. Chelikowsky. Structural properties of nine silica polymorphs. *Physical Review B*, 46(1):46, 1992.

[37] H. Zhang, D. R. Dunphy, X. Jiang, H. Meng, B. Sun, D. Tarn, M. Xue, X. Wang, S. Lin, Z. Ji, R. Li, F. L. Garcia, J. Yang, M. L. Kirk, T. Xia, J. I. Zink, A. Nel, and C. J. Brinker. Processing pathway dependence of amorphous silica nanoparticle toxicity: Colloidal vs pyrolytic. *Journal of the American Chemical Society*, 134:15790–15804, 2012.

[38] A. Mulderig, G. Beaucage, K. Vogtt, H. Jiang, and V. Kuppa. Quantification of branching in fumed silica. *Journal of Aerosol Science*, 109:28–37, 2017.

[39] H. Zhang and J. F. Banfield. Structural characteristics and mechanical and thermodynamic properties of nanocrystalline TiO_2. *Chemical Reviews*, 114(19):9613–9644, 2014.

[40] H. H. Pham and L. W. Wang. Oxygen vacancy and hole conduction in amorphous TiO_2. *Physical Chemistry Chemical Physics*, 17:541–550, 2015.

[41] B. Prasai, B. Cai, M. K. Underwood, J. P. Lewis, and D. A. Drabold. Properties of amorphous and crystalline titanium dioxide from first principles. *Journal of Materials Science*, 47:7515–7521, 2012.

[42] K. Momma and F. Izumi. VESTA 3 for three-dimensional visualization of crystal, volumetric and morphology data. *Journal of Applied Crystallography*, 44:1272–1276, 2011.

[43] C. J. Howard, T. M. Sabine, and F. Dickson. Structural and Thermal Parameters for Rutile and Anatase. *Acta Crystallographica*, B47:462–468, 1991.

[44] S. Sun, P. Song, J. Cui, and S. Liang. Amorphous TiO_2 nanostructures: Synthesis, fundamental properties and photocatalytic applications. *Catalysis Science and Technology*, 9:4198–4215, 2019.

[45] J. F. Shackelford and W. Alexander. *CRC Materials Science and Engineering Handbook*. CRC Press, 2001.

[46] I. Levin and D. Brandon. Metastable alumina polymorphs: Crystal structures and transition sequences. *Journal of the American Ceramic Society*, 81(8):1995–2012, 1998.

[47] X. L. Wang, C. R. Hubbard, K. B. Alexander, P. F. Becher, J. A. Fernandez-Baca, and S. Spooner. Neutron Diffraction Measurements of the Residual Stresses in Al_2O_3-ZrO_2 (CeO_2) Ceramic Composites. *Journal of the American Ceramic Society*, 77(6):1569–1575, 1994.

[48] X. Bokhimi, J. Sánchez-Valente, and F. Pedraza. Crystallization of sol-gel boehmite via hydrothermal annealing. *Journal of Solid State Chemistry*, 166:182–190, 2002.

[49] Y. K. Park, E. H. Tadd, M. Zubris, and R. Tannenbaum. Size-controlled synthesis of alumina nanoparticles from aluminum alkoxides. *Materials Research Bulletin*, 40:1506–1512, 2005.

[50] F. Mirjalili, H. Mohamad, and L. Chuah. Preparation of Nano-scale α Al_2O_3 Powder by the Sol-Gel Method. *Ceramics*, 55(4):378–383, 2011.

[51] M. G. Z. Khorasani, D. Silbernagl, D. Platz, and H. Sturm. Insights into nano-scale physical and mechanical properties of epoxy/boehmite nanocomposite using different AFM modes. *Polymers*, 11:235, 2019.

[52] T. Tanaka. Dielectric Nanocomposites with Insulating Properties. *IEEE Transactions on Dielectrics and Electrical Insulation*, 12(5):914–928, 2005.

[53] T. Tanaka, M. Kozako, N. Fuse, and Y. Ohki. Proposal of a Multi-core Model for Polymer Nanocomposite Dielectrics. *IEEE Transactions on Dielectrics and Electrical Insulation*, 12(4):669–681, 2005.

[54] S. Raetzke and J. Kindersberger. Role of interphase on the resistance to high-voltage arcing, on tracking and erosion of silicone/SiO_2 nanocomposites. *IEEE Transactions on Dielectrics and Electrical Insulation*, 17(2):607–614, 2010.

[55] S. Raetzke and J. Kindersberger. The effect of interphase structures in nanodielectrics. *IEEJ Transactions on Fundamentals and Materials*, 126(11):1044–1049, 2006.

[56] T. J. Lewis. Nanometric Dielectrics. *IEEE Transactions on Dielectrics and Electrical Insulation*, 5(1):812–825, 1994.

[57] G. Tsagaropoulos and A. Eisenberg. Dynamic Mechanical Study of the Factors Affecting the Two Glass Transition Behavior of Filled Polymers. Similarities and Differences with Random Ionomers. *Macromolecules*, 28:6067–6077, 1995.

[58] C. Zou, J. C. Fothergill, and S. W. Rowe. The Effect of Water Absorption on the Dielectric Properties of Epoxy Nanocomposites . *IEEE Transactions on Dielectrics and Electrical Insulation*, 15(1):106–117, 2008.

[59] T. Andritsch, R. Kochetov, P. H. Morshuis, and J. J. Smit. Proposal of the polymer chain alignment model. In *Annual Report - Conference on Electrical Insulation and Dielectric Phenomena, CEIDP*, 2011.

[60] F. N. Alhabill, R. Ayoob, T. Andritsch, and A. S. Vaughan. Introducing particle interphase model for describing the electrical behaviour of nanodielectrics. *Materials and Design*, 158:62–73, 2018.

[61] D. H. Everett. Basic Principles of Colloid Science. In *Basic Principles of Colloid Science*. Royal Society of Chemistry, London, UK, 1988.

[62] V. P. Swapna, V. S. Abhisha, and R. Stephen. Polymer/polyhedral oligomeric silsesquioxane nanocomposite membranes for pervaporation. In S. Thomas, S. C. George, and T. Jose, editors, *Polymer Nanocomposite Membranes for Pervaporation*, chapter 9, pages 201–229. Elsevier, 2020.

[63] M. Alcoutlabi and G. B. Mckenna. Effects of confinement on material behaviour at the nanometre size scale. *Journal of Physics Condensed Matter*, 17:461–524, 2005.

[64] I. Y. Jeon and J. B. Baek. Nanocomposites derived from polymers and inorganic nanoparticles. *Materials*, 3(6):3654–3674, 2010.

[65] Q. Guo, P. Zhu, G. Li, J. Wen, T. Wang, D. D. Lu, R. Sun, and C. Wong. Study on the effects of interfacial interaction on the rheological and thermal performance of silica nanoparticles reinforced epoxy nanocomposites. *Composites Part B: Engineering*, 116:388–397, 2017.

[66] S. Kango, S. Kalia, A. Celli, J. Njugana, Y. Habibi, and R. Kumar. Surface modification of inorganic nanoparticles for development of organic–inorganic nanocomposites—A review. *Progress in Polymer Science*, 38:1232–1261, 2013.

[67] E. P. Plueddemann. *Silane Coupling Agents*. Springer-Verlag US, Boston, MA, USA, 2nd edition, 1991.

[68] S. Mallakpour and M. Madani. A review of current coupling agents for modification of metal oxide nanoparticles. *Progress in Organic Coatings*, 86:194–207, 2015.

[69] S. Siddabattuni, T. P. Schuman, and F. Dogan. Dielectric Properties of Polymer-Particle Nanocomposites Influenced by Electronic Nature of Filler Surfaces. *ACS Applied Materials and Interfaces*, 5:1917–1927, 2013.

[70] M. Bell, T. Krentz, J. K. Nelson, L. Schadler, K. Wu, C. Breneman, S. Zhao, H. Hillborg, and B. Benicewicz. Investigation of dielectric breakdown in silica-epoxy nanocomposites using designed interfaces. *Journal of Colloid and Interface Science*, 495:130–139, 2017.

[71] L. Matějka, J. Pleštil, and K. Dušek. Structure evolution in epoxy–silica hybrids: sol–gel process. *Journal of Non-Crystalline Solids*, 226(1-2):114–121, 1998.

[72] D. Morselli, F. Bondioli, M. Sangermano, and M. Messori. Epoxy Networks Reinforced With TiO_2 Generated by Nonhydrolytic Sol–Gel Process: A Comparison Between In Situ and Ex Situ Syntheses to Obtain Filled Polymers. *Polymer Engineering and Science*, 55(7):1689–1697, 2015.

[73] D. Liu, G. He, X. Zeng, D. Sun, and X. Li. Preparation of SiO_2/epoxy nanocomposite via reverse microemulsion in situ polymerization. *Polymer Composites*, 35(7):1388–1394, 2014.

[74] H. Zhang, R. Qi, M. Tong, Y. Su, and M. Huang. In Situ Solvothermal Synthesis and Characterization of Transparent Epoxy/TiO_2 Nanocomposites. *Journal of Applied Polymer Science*, 125:1152–1160, 2012.

[75] A. Dalod, O. Grendal, A. Blichfeld, V. Furtula, J. Pérez, L. Henriksen, T. Grande, and M.-A. Einarsrud. Structure and Optical Properties of Titania-PDMS Hybrid Nanocomposites Prepared by In Situ Non-Aqueous Synthesis. *Nanomaterials*, 7(12):460, 2017.

[76] C. Lü and B. Yang. High refractive index organic–inorganic nanocomposites: design, synthesis and application. *Journal of Materials Chemistry*, 19:2884–2901, 2009.

[77] J. Wen and G. L. Wilkes. Organic/Inorganic Hybrid Network Materials by the Sol-Gel Approach. *Chemistry of Materials*, 8:1667–1681, 1996.

[78] V. Bounor-Legaré and P. Cassagnau. In situ synthesis of organic-inorganic hybrids or nanocomposites from sol-gel chemistry in molten polymers. *Progress in Polymer Science*, 39(8):5050–5056, 2014.

[79] A. D. Pomogailo. Polymer sol-gel synthesis of hybrid nanocomposites. *Colloid Journal*, 67(6):658–677, 2005.

[80] G. Kickelbick. The search of a homogeneously dispersed material—the art of handling the organic polymer/metal oxide interface. *Journal of Sol-Gel Science and Technology*, 46:281–290, 2008.

[81] J. Livage and C. Sanchez. Sol-gel chemistry. *Journal of Non-Crystalline Solids*, 145:11–19, 1992.

[82] H. Zou, S. Wu, and J. Shen. Polymer/Silica Nanocomposites: Preparation, Characterization, Properties, and Applications. *Chemical Reviews*, 108(9):3893–3957, 2008.

[83] J. N. Hay and H. M. Raval. Synthesis of organic-inorganic hybrids via the non-hydrolytic sol-gel process. *Chemistry of Materials*, 13(10):3396–3403, 2001.

[84] T. Ogoshi and Y. Chujo. Organic-inorganic polymer hybrids prepared by the sol-gel method. *Composite Interfaces*, 11(8-9):539–566, 2005.

[85] B. J. Bauer, D. W. Liu, C. L. Jackson, and J. D. Barnes. Epoxy/SiO_2 interpenetrating polymer networks. *Polymers for Advanced Technologies*, 7(4):333–339, 1996.

[86] L. Matějka, K. Dušek, J. Pleštil, J. Kříž, and F. Lednický. Formation and structure of the epoxy-silica hybrids. *Polymer*, 40(1):171–181, 1999.

[87] L. Matejka, O. Dukh, and J. Kolařík. Reinforcement of crosslinked rubbery epoxies by in-situ formed silica. *Polymer*, 41(4):1449–1459, 2000.

[88] A. Afzal and H. M. Siddiqi. A comprehensive study of the bicontinuous epoxy-silica hybrid polymers: I. Synthesis, characterization and glass transition. *Polymer*, 52(6):1345–1355, 2011.

[89] T. Nazir, A. Afzal, H. M. Siddiqi, Z. Ahmad, and M. Dumon. Thermally and mechanically superior hybrid epoxy-silica polymer films via sol-gel method. *Progress in Organic Coatings*, 69(1):100–106, 2010.

[90] T. M. Lee and C. C. M. Ma. Nonaqueous synthesis of nanosilica in epoxy resin matrix and thermal properties of their cured nanocomposites. *Journal of Polymer Science, Part A: Polymer Chemistry*, 44:757–768, 2006.

[91] R. K. Donato, M. Perchacz, S. Ponyrko, K. Z. Donato, H. S. Schrekker, H. Beneš, and L. Matějka. Epoxy–silica nanocomposite interphase control using task-specific ionic liquids via hydrolytic and non-hydrolytic sol–gel processes. *RSC Adv.*, 5(111):91330–91339, 2015.

[92] D. Morselli, F. Bondioli, M. Sangermano, and M. Messori. Photo-cured epoxy networks reinforced with TiO_2 in-situ generated by means of non-hydrolytic solegel process. *Polymer*, 53:283–290, 2012.

[93] S. Yano, T. Ito, K. Shinoda, H. Ikake, T. Hagiwara, T. Sawaguchi, K. Kurita, and M. Seno. Properties and microstructures of epoxy resin/TiO_2 and SiO_2 hybrids. *Polymer International*, 54:354–361, 2005.

[94] A. Ghosal and S. Ahmad. High performance anti-corrosive epoxy-titania hybrid nanocomposite coatings. *New Journal of Chemistry*, 41:4599–4610, 2017.

[95] J. Jiao, P. Liu, and Y. Cai. One-step synthesis of improved silica/epoxy nanocomposites with inorganic-organic hybrid network. *Journal of Polymer Research*, 20(202), 2013.

[96] R. K. Donato, M. Lavorgna, P. Musto, K. Z. Donato, A. Jager, P. Štěpánek, H. S. Schrekker, and L. Matějka. The role of ether-functionalized ionic liquids in the sol-gel process: Effects on the initial alkoxide hydrolysis steps. *Journal of Colloid and Interface Science*, 447:77–84, 2015.

[97] R. K. Donato, L. Matějka, H. S. Schrekker, J. Pletil, A. Jigounov, J. Brus, and M. Slouf. The multifunctional role of ionic liquids in the formation of epoxy-silica nanocomposites. *Journal of Materials Chemistry*, 21(36):13801–13810, 2011.

[98] R. K. Donato, K. Z. Donato, H. S. Schrekker, and L. Matějka. Tunable reinforcement of epoxy-silica nanocomposites with ionic liquids. *Journal of Materials Chemistry*, 22(19):9939–9948, 2012.

[99] M. Ochi and T. Matsumura. Thermomechanical properties and phase structure of epoxy/silica nano-hybrid materials constructed from a linear silicone oligomer. *Journal of Polymer Science, Part B: Polymer Physics*, 43(13):1631–1639, 2005.

[100] F. Piscitelli, M. Lavorgna, G. G. Buonocore, L. Verdolotti, J. Galy, and L. Mascia. Plasticizing and reinforcing features of siloxane domains in amine-cured epoxy/silica hybrids. *Macromolecular Materials and Engineering*, 298:896–909, 2013.

[101] C.-F. Yang, L.-F. Wang, S.-M. Wu, and C.-C. Su. Characterization and Curing Kinetics of Epoxy/Silica Nano-Hybrids. *Materials*, 8:7032–7040, 2015.

[102] Y.-T. Bi, Z.-J. Li, and W. Liang. Preparation and characterization of epoxy/SiO_2 nanocomposites by cationic photopolymerization and sol–gel process. *Polymers for Advanced Technologies*, 25:173–178, 2013.

[103] M. Sangermano, G. Matucelli, E. Amerio, R. Bongiovanni, A. Priola, A. Di Gianni, B. Voit, and G. Rizza. Preparation and characterization of nanostructured TiO_2/epoxy polymeric films. *Macromolecular Materials and Engineering*, 291(5):517–523, 2006.

[104] E. Tuncer, G. Polizos, I. Sauers, D. R. James, A. R. Ellis, and K. L. More. Epoxy nanodielectrics fabricated with in situ and ex situ techniques. *Journal of Experimental Nanoscience*, 7(3):274–281, 2012.

[105] C. Guan, C. L. Lü, Y. F. Liu, and B. Yang. Preparation and characterization of high refractive index thin films of TiO_2/epoxy resin nanocomposites. *Journal of Applied Polymer Science*, 102(2):1631–1636, 2006.

[106] R. Tilley. *Understanding Solids; The Science of Materials*. Wiley, 2 edition, 2013.

[107] C. Zou. *The effect of humidity and surface functionalisation on the dielectric properties of nanocomposites*. Thesis, University of Leicester, 2007.

[108] A. K. Jonscher. Dielectric relaxation in solids. *Journal of Physics D: Applied Physics*, 32:57–70, 1999.

[109] A. Vassilikou-Dova and I. M. Kalogeras. Dielectric Analysis (DEA). In J. D. Menczel and R. B. Prime, editors, *Thermal Analysis of Polymers: Fundamentals and Applications*, chapter 6, pages 497–613. Wiley, 2009.

[110] M. F. García-Sánchez, J. C. M'Peko, A. R. Ruiz-Salvador, G. Rodríguez-Gattorno, Y. Echevarría, F. Fernández-Gutierrez, and A. Delgado. An elementary picture of dielectric spectroscopy in solids: Physical basis. *Journal of Chemical Education*, 80(9):1062–1073, 2003.

[111] S. Havriliak and S. Negami. A complex plane analysis of α-dispersions in some polymer systems. *Journal of Polymer Science Part C: Polymer Symposia*, 14:99–117, 1966.

[112] A. K. Jonscher. The 'universal' dielectric response. *Nature*, 267:673–679, 1977.

[113] A. K. Jonscher. The "Universal" Dielectric Response: Part I. *IEEE Electrical Insulation Magazine*, 6(2):16–22, 1990.

[114] L. A. Dissado and R. M. Hill. A cluster approach to the structure of imperfect materials and their relaxation spectroscopy. *Proceedings of The Royal Society of London, Series A: Mathematical and Physical Sciences*, 390:131–180, 1983.

[115] Y. Gao, X. Liang, L. A. Dissado, S. J. Dodd, and N. M. Chalashkanov. Dielectric response of filled high temperature vulcanized silicone rubber. *IEEE Transactions on Dielectrics and Electrical Insulation*, 23(6):3683–3695, 2016.

[116] A. K. Jonscher. The "Universal" Dielectric Response: Part II. *IEEE Electrical Insulation Magazine*, 6(3):24–28, 1990.

[117] F. Palumbo, C. Wen, S. Lombardo, S. Pazos, F. Aguirre, M. Eizenberg, F. Hui, and M. Lanza. A Review on Dielectric Breakdown in Thin Dielectrics: Silicon Dioxide, High-k, and Layered Dielectrics. *Advanced Functional Materials*, 30(18):1900657, 2020.

[118] W. Weibull. A Statistical Distribution Function of Wide Applicability. *Journal of Applied Mechanics*, 18:293–297, 1951.

[119] C. Chauvet and C. Laurent. Weibull Statistics in Short-term Dielectric Breakdown of Thin Polyethylene Films. *IEEE Transactions on Electrical Insulation*, 28(1):18–29, 1993.

[120] H. Fröhlich. Dielectric breakdown in solids. *Reports on Progress in Physics*, 6(1):411–430, 1939.

[121] X. Huang and C. Zhi, editors. *Polymer Nanocomposites - Electrical and Thermal Properties*. Springer International Publishing, Cham, 2016.

[122] A. Eigner and K. Rethmeier. An overview on the current status of partial discharge measurements on AC high voltage cable accessories. *IEEE Electrical Insulation Magazine*, 32(2):48–55, 2016.

[123] J. Fuhr and T. Aschwanden. Identification and localization of PD-sources in power-transformers and power-generators. *IEEE Transactions on Dielectrics and Electrical Insulation*, 24(1):17–30, 2017.

[124] L. A. Dissado. Understanding electrical trees in solids: From experiment to theory. *IEEE Transactions on Dielectrics and Electrical Insulation*, 9(4):483–497, 2002.

[125] H. Illias, Teo Soon Yuan, A. H. A. Bakar, H. Mokhlis, G. Chen, and P. L. Lewin. Partial discharge patterns in high voltage insulation. In *2012 IEEE International Conference on Power and Energy*, 2012.

[126] Z. Lv, S. M. Rowland, S. Chen, H. Zheng, and I. Iddrissu. Evolution of partial discharges during early tree propagation in epoxy resin. *IEEE Transactions on Dielectrics and Electrical Insulation*, 24(5):2995–3003, 2017.

[127] I. Iddrissu, S. M. Rowland, H. Zheng, Z. Lv, and R. Schurch. Electrical tree growth and partial discharge in epoxy resin under combined AC and DC voltage waveforms. *IEEE Transactions on Dielectrics and Electrical Insulation*, 25(6):2183–2190, 2018.

[128] H. Zheng, S. M. Rowland, I. Iddrissu, and Z. Lv. Electrical treeing and reverse tree growth in an epoxy resin. *IEEE Transactions on Dielectrics and Electrical Insulation*, 24(6):3966–3973, 2017.

[129] T. Imai, F. Sawa, T. Nakano, T. Ozaki, T. Shimizu, M. Kozako, and T. Tanaka. Effects of nano- and micro-filler mixture on electrical insulation properties of epoxy based composites. *IEEE Transactions on Dielectrics and Electrical Insulation*, 13(1):319–326, 2006.

[130] G. Iyer, R. S. Gorur, R. Richert, A. Krivda, and L. E. Schmidt. Dielectric Properties of Epoxy based Nanocomposites for High Voltage Insulation. *IEEE Transactions on Dielectrics and Electrical Insulation*, 18(3):659–666, 2011.

[131] N. Domun, H. Hadavinia, T. Zhang, T. Sainsbury, G. H. Liaghat, and S. Vahid. Improving the fracture toughness and the strength of epoxy using nanomaterials-a review of the current status, 2015.

[132] B. Wetzel, F. Haupert, and M. Q. Zhang. Epoxy nanocomposites with high mechanical and tribological performance. *Composites Science and Technology*, 63:2055–2067, 2003.

[133] M. S. Goyat, S. Rana, S. Halder, and P. K. Ghosh. Facile fabrication of epoxy-TiO_2 nanocomposites: A critical analysis of TiO_2 impact on mechanical properties and toughening mechanisms. *Ultrasonics - Sonochemistry*, 40:861–873, 2018.

[134] H. Zhang, Z. Zhang, K. Friedrich, and C. Eger. Property improvements of in situ epoxy nanocomposites with reduced interparticle distance at high nanosilica content. *Acta Materiala*, 54:1833–1842, 2006.

[135] S. G. Prolongo, M. R. Gude, and A. Ureña. Water uptake of epoxy composites reinforced with carbon nanofillers. *Composites Part A: Applied Science and Manufacturing*, 43:2169–2175, 2012.

[136] R. Kochetov, T. Andritsch, U. Lafont, P. H. F. Morshuis, S. J. Picken, and J. J. Smit. Thermal Behaviour of Epoxy Resin Filled with High Thermal

Conductivity Nanopowders. *IEEE Electrical Insulation Conference*, pages 524–528, 2009.

[137] Q. Xie, Y. Cheng, S. Chen, G. Wu, Z. Wang, and Z. Jia. Dielectric and thermal properties of epoxy resins with TiO_2 nanowires. *Journal of Materials Science: Materials in Electronics*, Published, 2017.

[138] S. Singha and M. J. Thomas. Permittivity and Tan Delta Characteristics of Epoxy Nanocomposites in the Frequency Range of 1 MHz–1 GHz. *IEEE Transactions on Dielectrics and Electrical Insulation*, 15(1):2–11, 2008.

[139] E. do Nascimento, A. Ramos, D. Windmoller, P. Reig Rodrigo, R. Teruel Juanes, A. Ribes Greus, V. Amigó Borrás, and L. A. F. Coelho. Breakdown, free-volume and dielectric behavior of the nanodielectric coatings based on epoxy/metal oxides. *Journal of Materials Science: Materials in Electronics*, 27:9240–9254, 2016.

[140] R. Kochetov, T. Andritsch, P. H. F. Morshuis, and J. J. Smit. Anomalous Behaviour of the Dielectric Spectroscopy Response of Nanocomposites. *IEEE Transactions on Dielectrics and Electrical Insulation*, 19(1):107–117, 2012.

[141] S. Virtanen, T. Krentz, J. K. Nelson, L. Schadler, M. Bell, B. Benicewicz, H. Hillborg, and S. Zhao. Dielectric Breakdown Strength of Epoxy Bimodal-polymer-Brush-Grafted Core Functionalized Silica Nanocomposites. *IEEE Transactions on Dielectrics and Electrical Insulation*, 21(2), 2014.

[142] C. Yeung and A. S. Vaughan. On the Effect of Nanoparticle Surface Chemistry on the Electrical Characteristics of Epoxy-Based Nanocomposites. *Polymers*, 8(126), 2016.

[143] M. Liang and K. L. Wong. Electrical performance of epoxy resin filled with micro particles and nanoparticles. *Energy Procedia*, 110:162–167, 2017.

[144] T. Andritsch, R. Kochetov, P. H. F. Morshuis, and J. J. Smit. Short term DC Breakdown and Complex Permittivity of Al_2O_3- and MgO-Epoxy Nanocomposites. In *Annual Report Conference on Electrical Insulation and Dielectric Phenomena*, 2010.

[145] Z. Li, K. Okamoto, Y. Ohki, and T. Tanaka. Effects of Nano-filler Addition on Partial Discharge Resistance and Dielectric Breakdown Strength of Micro-Al_2O_3/Epoxy Composite. *IEEE Transactions on Dielectrics and Electrical Insulation*, 17(3):653–661, 2010.

[146] Y. Li, M. Tian, Z. Lei, and J. Zhang. Effect of nano-silica on dielectric properties and space charge behavior of epoxy resin under temperature gradient. *Journal of Physics D: Applied Physics*, 51:125309, 2018.

[147] P. Marx, A. J. Wanner, Z. Zhang, H. Jin, I. A. Tsekmes, J. J. Smit, W. Kern, and F. Wiesbrock. Effect of interfacial polarization and water absorption on the dielectric properties of epoxy-nanocomposites. *Polymers*, 9:195, 2017.

[148] G. Yang, J. Cui, Y. Ohki, D. Wang, Y. Li, and K. Tao. Dielectric and relaxation properties of composites of epoxy resin and hyperbranched-polyester-treated nanosilica. *RSC Advances*, 8:30669–30677, 2018.

[149] S. Alapati and M. J. Thomas. Influence of nano-fillers on electrical treeing in epoxy insulation. *IET Science, Measurement and Technology*, 6(1):21–28, 2012.

[150] C. Nyamupangedengu and D. R. Cornish. Time-evolution phenomena of electrical tree partial discharges in Magnesia, Silica and Alumina epoxy nanocomposites. *IEEE Transactions on Dielectrics and Electrical Insulation*, 23(1):85–94, 2016.

[151] T. Imai, F. Sawa, T. Ozaki, Y. Inoue, T. Shimizu, and T. Tanaka. Comparison of Insulation Breakdown Properties of Epoxy Nanocomposites under Homogeneous and Divergent Electric Fields. In *IEEE Conference on Electrical Insulation and Dielectric Phenomena*, pages 306–309, Kasnsas City, MO, USA, 2006.

[152] Y. Chen, T. Imai, Y. Ohki, and T. Tanaka. Tree initiation phenomena in nanostructured epoxy composites. *IEEE Transactions on Dielectrics and Electrical Insulation*, 17(5):1509–1515, 2010.

[153] S. Raetzke, Y. Ohki, T. Imai, T. Tanaka, and J. Kindersberger. Tree initiation characteristics of epoxy resin and epoxy/clay nanocomoposite. *IEEE Transactions on Dielectrics and Electrical Insulation*, 16(5):1473–1480, 2009.

[154] S. Nakamura, A. Kumada, K. Hidaka, H. Hirai, T. Imai, T. Nakamura, and T. Yoshimitsu. Effects of temperature on electrical treeing and partial discharges in epoxy/silica nanocomposites. *IEEE Transactions on Dielectrics and Electrical Insulation*, 27(4):1169–1177, 2020.

[155] S. Chen, S. Rowland, J. Carr, M. Storm, K. L. Choy, and A. J. Clancy. The importance of particle dispersion in electrical treeing and breakdown in nano-filled epoxy resin. *International Journal of Electrical Power and Energy Systems*, 129:106838, jul 2021.

[156] T. Tanaka, A. Matsunawa, Y. Ohki, M. Kozako, M. Kohtoh, and S. Okabe. Treeing phenomena in epoxy/alumina nanocomposite and interpretation by a multi-core model. *IEEJ Transactions on Fundamentals and Materials*, 126(11):1128–1135, 2006.

[157] J. M. Pochan, R. J. Gruber, and D. F. Pochan. Dielectric relaxation phenomena in a series of polyhydroxyether copolymers of bisphenol-A—endcapped polyethylene glycol with epichlorohydrin. *Journal of Polymer Science: Polymer Physics Edition*, 19:143–149, 1981.

[158] Y. Huang, D. Min, S. Li, X. Wang, and S. Lin. Dielectric relaxation and carrier transport in epoxy resin and its microcomposite. *IEEE Transactions on Dielectrics and Electrical Insulation*, 24(5):3083–3091, 2017.

[159] F. Tian and Y. Ohki. Charge transport and electrode polarization in epoxy resin at high temperatures. *Journal of Physics D: Applied Physics*, 47:045311, 2014.

[160] T. Heid, M. Fréchette, and E. David. Epoxy/BN micro- and submicrocomposites: Dielectric and thermal properties of enhanced materials for high voltage insulation systems. *IEEE Transactions on Dielectrics and Electrical Insulation*, 22(2):1176–1185, 2015.

[161] W. Yang, R. Yi, S. Hui, Y. Xu, and X. Cao. Analysis of the dielectric spectroscopy of an epoxy-ZnO nanocomposite using the universal relaxation law. *Journal of Applied Polymer Science*, 127(5):3891–3897, 2013.

[162] P. Maity, P. K. Poovamma, S. Basu, V. Parameswaran, and N. Gupta. Dielectric spectroscopy of epoxy resin with and without nanometric alumina fillers. *IEEE Transactions on Dielectrics and Electrical Insulation*, 16(5):1481–1488, 2009.

[163] P. Dittanet and R. A. Pearson. Effect of silica nanoparticle size on toughening mechanisms of filled epoxy. *Polymer*, 53:1890–1905, 2012.

[164] E. Lizundia, I. Serna, E. Axpe, and J. L. Vilas. Free-volume effects on the thermomechanical performanceof epoxy–SiO_2 nanocomposites. *Journal of Applied Polymer Science*, 134:45216, 2017.

[165] T. Nazir, A. Afzal, H. M. Siddiqi, S. Saeed, and M. Dumon. The influence of temperature and interface strength on the microstructure and performance of sol-gel silica-epoxy nanocomposites. *Polymer Bulletin*, 67:1539–1551, 2011.

[166] S. Zhao, L. S. Schadler, R. Duncan, H. Hillborg, and T. Auletta. Mechanisms leading to improved mechanical performance in nanoscale alumina filled epoxy. *Composites Science and Technology*, 68:2965–2975, 2008.

[167] F. Piscitelli, G. G. Buonocore, M. Lavorgna, L. Verdolotti, S. Pricl, G. Gentile, and L. Mascia. Peculiarities in the structure - Properties relationship of epoxy-silica hybrids with highly organic siloxane domains. *Polymer*, 2015.

[168] A. Afzal, H. M. Siddiqi, S. Saeed, and Z. Ahmad. Exploring resin viscosity effects in solventless processing of nano-SiO_2/epoxy polymer hybrids. *RSC Advances*, 3:3885–3892, 2013.

[169] P. K. Ghosh, A. Pathak, M. S. Goyat, and S. Halder. Influence of nanoparticle weight fraction on morphology and thermal properties of epoxy/TiO_2 nanocomposite. *Journal of Reinforced Plastics and Composites*, 31(17):1180–1188, 2012.

[170] C. Alzina, N. Sbirrazzuoli, and A. Mija. Epoxy-Amine Based Nanocomposites Reinforced by Silica Nanoparticles. Relationships between Morphologic Aspects, Cure Kinetics, and Thermal Properties. *J. Phys. Chem. C*, 115:22789–22795, 2011.

[171] Y. L. Liang and R. A. Pearson. Toughening mechanisms in epoxy–silica nanocomposites (ESNs). *Polymer*, 50:4895–4905, 2009.

[172] B. B. Johnsen, A. J. Kinloch, R. D. Mohammed, A. C. Taylor, and S. Sprenger. Toughening mechanisms of nanoparticle-modified epoxy polymers. *Polymer*, 48:530–541, 2007.

[173] S. A. Hollingsworth and R. O. Dror. Molecular Dynamics Simulation for All. *Neuron*, 99(6):1129–1143, 2018.

[174] M. E. Tuckerman and G. J. Martyna. Understanding Modern Molecular Dynamics: Techniques and Applications. *Journal of Physical Chemistry B*, 104(2):159–178, 2000.

[175] M. González. Force fields and molecular dynamics simulations. *École thématique de la Société Française de la Neutronique*, 12:169–200, 2011.

[176] J. A. Harrison, J. D. Schall, S. Maskey, P. T. Mikulski, M. T. Knippenberg, and B. H. Morrow. Review of force fields and intermolecular potentials used in atomistic computational materials research. *Applied Physics Reviews*, 5(3):031104, 2018.

[177] P. H. Lin and R. Khare. Molecular simulation of cross-linked epoxy and epoxy-POSS nanocomposite. *Macromolecules*, 42(12):4319–4327, 2009.

[178] J. Choi, S. Yu, S. Yang, and M. Cho. The glass transition and thermoelastic behavior of epoxy-based nanocomposites: A molecular dynamics study. *Polymer*, 52(22):5197–5203, 2011.

[179] H. B. Fan and M. M. Yuen. Material properties of the cross-linked epoxy resin compound predicted by molecular dynamics simulation. *Polymer*, 48(7):2174–2178, 2007.

[180] J. Li, J. Chen, M. Zhu, H. Song, and H. Zhang. Interfacial Characteristics of Boron Nitride Nanosheet/Epoxy Resin Nanocomposites: A Molecular Dynamics Simulation. *Applied Sciences*, 9(14):2832, 2019.

[181] V. Varshney, S. S. Patnaik, A. K. Roy, and B. L. Farmer. A molecular dynamics study of epoxy-based networks: Cross-linking procedure and prediction of molecular and material properties. *Macromolecules*, 41(18):6837–6842, 2008.

[182] Q. Xie, K. Fu, S. Liang, B. Liu, L. Lu, X. Yang, Z. Huang, and F. Lü. Micro-structure and thermomechanical properties of crosslinked epoxy composite modified by nano-SiO_2: A molecular dynamics simulation. *Polymers*, 10:801, 2018.

[183] S. Yu, S. Yang, and M. Cho. Multi-scale modeling of cross-linked epoxy nanocomposites. *Polymer*, 50(3):945–952, 2009.

[184] Z. Wang, Q. Lv, S. Chen, C. Li, S. Sun, and S. Hu. Effect of Interfacial Bonding on Interphase Properties in SiO_2/Epoxy Nanocomposite: A Molecular Dynamics Simulation Study. *ACS Applied Materials and Interfaces*, 8(11):7499–7508, 2016.

[185] J. Fankhänel, B. Arash, and R. Rolfes. Elastic interphase properties of nanoparticle/epoxy nanocomposites: A molecular dynamics study. *Composites Part B: Engineering*, 176:107211, 2019.

[186] X. Zhang, H. Wen, and Y. Wu. Computational thermomechanical properties of silica-epoxy nanocomposites by molecular dynamic simulation. *Polymers*, 9:430, 2017.

[187] H. S. Khare and D. L. Burris. A quantitative method for measuring nanocomposite dispersion. *Polymer*, 51:719–729, 2010.

[188] G. Beaucage. Approximations Leading to a Unified Exponential/Power-Law Approach to Small-Angle Scattering. *Journal of Applied Crystallography*, 28:717–728, 1995.

[189] G. Beaucage. Combined Small-Angle Scattering for Characterization of Hierarchically Structured Polymer Systems over Nano-to-Micron Meter: Part I Experiments. In K. Matyjaszewski and M. Möller, editors, *Polymer Science: A Comprehensive Reference, 10 Volume Set*, volume 2, pages 399–409. Elsevier B.V., 2012.

[190] G. Beaucage. Small-angle scattering from polymeric mass fractals of arbitrary mass-fractal dimension. *Journal of Applied Crystallography*, 29(2):134–146, 1996.

[191] A. Y. Cherny, E. M. Anitas, V. A. Osipov, and A. I. Kuklin. Scattering from surface fractals in terms of composing mass fractals. *J. Appl. Cryst*, 50:919–931, 2017.

[192] J. Als-Nielsen and D. McMorrow. *Elements of Modern X-ray Physics: Second Edition*. Wiley, West Sussex, UK, 2 edition, 2011.

[193] S. Brunauer, P. H. Emmett, and E. Teller. Adsorption of Gases in Multimolecular Layers. *Journal of the American Chemical Society*, 60(2):309–319, 1938.

[194] N. G. Trinh. Electrode design for testing in uniform field gaps. *IEEE Transactions on Power Apparatus and Systems*, PAS-99(3):1235–1242, 1980.

[195] W. L. Jorgensen, D. S. Maxwell, and J. Tirado-Rives. Development and testing of the OPLS all-atom force field on conformational energetics and properties of organic liquids. *Journal of the American Chemical Society*, 118(45):11225–11236, 1996.

[196] W. L. Jorgensen and J. Tirado-Rives. Potential energy functions for atomic-level simulations of water and organic and biomolecular systems. *Proceedings of the National Academy of Sciences of the United States of America*, 102(19):6665–6670, 2005.

[197] L. S. Dodda, I. C. De Vaca, J. Tirado-Rives, and W. L. Jorgensen. LigParGen web server: An automatic OPLS-AA parameter generator for organic ligands. *Nucleic Acids Research*, 45(W1):W331–W336, 2017.

[198] L. S. Dodda, J. Z. Vilseck, J. Tirado-Rives, and W. L. Jorgensen. 1.14*CM1A-LBCC: Localized Bond-Charge Corrected CM1A Charges for Condensed-Phase Simulations. *Journal of Physical Chemistry B*, 121(15):3864–3870, 2017.

[199] A. P. Thompson, H. M. Aktulga, R. Berger, D. S. Bolintineanu, W. M. Brown, P. S. Crozier, P. J. in't Veld, A. Kohlmeyer, S. G. Moore, T. D. Nguyen, R. Shan, M. J. Stevens, J. Tranchida, C. Trott, and S. J. Plimpton. LAMMPS - a flexible simulation tool for particle-based materials modeling at the atomic, meso, and continuum scales. *Computer Physics Communications*, 271:108171, 2022.

[200] F. S. Emami, V. Puddu, R. J. Berry, V. Varshney, S. V. Patwardhan, C. C. Perry, and H. Heinz. Force field and a surface model database for silica to simulate interfacial properties in atomic resolution. *Chemistry of Materials*, 26(8):2647–2658, 2014.

[201] J. Shen, J. Liu, Y. Gao, X. Li, and L. Zhang. Elucidating and tuning the strain-induced non-linear behavior of polymer nanocomposites: A detailed molecular dynamics simulation study. *Soft Matter*, 10(28):5099–5113, 2014.

[202] S. H. Jamali, L. Wolff, T. M. Becker, M. De Groen, M. Ramdin, R. Hartkamp, A. Bardow, T. J. Vlugt, and O. A. Moultos. OCTP: A Tool for On-the-Fly Calculation of Transport Properties of Fluids with the Order- n Algorithm in LAMMPS. *Journal of Chemical Information and Modeling*, 59(4):1290–1294, 2019.

[203] P. Ganguly and N. F. Van Der Vegt. Convergence of sampling Kirkwood-Buff integrals of aqueous solutions with molecular dynamics simulations. *Journal of Chemical Theory and Computation*, 9(3):1347–1355, 2013.

[204] M. G. González, J. C. Cabanelas, and J. Baselga. Applications of FTIR on Epoxy Resins - Identification, Monitoring the Curing Process, Phase Separation and Water Uptake. In T. Theophile, editor, *Infrared Spectroscopy - Materials Science, Engineering and Technology*, chapter 13, pages 261–284. InTech, 2012.

[205] P. J. Launer and B. Arkles. Infrared analysis of organosilicon compounds: spectra-structure correlations. In B. Arkles and G. L. Larson, editors, *Silicon Compounds: Silanes and Silicones*, chapter 1, pages 177–180. Gelest, Inc., Morrisville, PA, 3 edition, 2013.

[206] G. Socrates. *Infrared and Raman Characteristic Group Frequencies*. John Wiley and Sons, West Sussex, UK, third edition, 2001.

[207] T. Arunkumar and S. Ramachandran. Surface coating and characterisation of polyurea for liquid storage. *International Journal of Ambient Energy*, 38(8):781–787, 2017.

[208] L. B. Capeletti, I. M. Baibich, I. S. Butler, and J. H. Dos Santos. Infrared and Raman spectroscopic characterization of some organic substituted hybrid

silicas. *Spectrochimica Acta - Part A: Molecular and Biomolecular Spectroscopy*, 133:619–625, 2014.

[209] H. Aguiar, J. Serra, P. González, and B. León. Structural study of sol-gel silicate glasses by IR and Raman spectroscopies. *Journal of Non-Crystalline Solids*, 355(8):475–480, 2009.

[210] K. Mackenzie and M. Smith. *Multinuclear Solid-State NMR of Inorganic Materials*. Elsevier Science Ltd., Oxford, UK, first edition, 2002.

[211] D. Hoebbel, M. Nacken, and H. Schmidt. On the Existence and Hydrolytic Stability of Titanosiloxane Bonds in the System: Glycidoxypropyltrimethoxysilane-Water-Titaniumtetraethoxide. *Journal of Sol-Gel Science and Technology*, 1998.

[212] M. M. Adnan, I.-E. Nylund, A. Jaworski, S. Hvidsten, M.-H. G. Ese, J. Glaum, and M.-A. Einarsrud. The Structure, Morphology, and Complex Permittivity of Epoxy Nanodielectrics with In Situ Synthesized Surface-Functionalized SiO2. *Polymers*, 13(9):1469, 2021.

[213] E. A. Lysenkov, N. G. Leonova, and S. V. Zhiltsova. Effect of the Silicon-Containing Phase on the Hierarchy of the Structure of Epoxy–Silica Nanocomposites. *Theoretical and Experimental Chemistry*, 55(4):250–257, 2019.

[214] F. N. Alhabill, R. Ayoob, T. Andritsch, and A. S. Vaughan. Influence of filler/matrix interactions on resin/hardener stoichiometry, molecular dynamics, and particle dispersion of silicon nitride/epoxy nanocomposites. *Journal of Materials Science*, 53(6):4144–4158, 2018.

[215] T. Fuqiang, Z. Lin, Z. Junliang, and P. Xiao. Space charge and dielectric behavior of epoxy composite with SiO_2-Al_2O_3 nano-micro fillers at varied temperatures. *Composites Part B: Engineering*, 114:93–100, 2017.

[216] L. A. Dissado and R. M. Hill. Anomalous low-frequency dispersion. Near direct current conductivity in disordered low-dimensional materials. *Journal of the Chemical Society, Faraday Transactions 2: Molecular and Chemical Physics*, 80(3):291–319, 1984.

[217] T. Fuqiang and O. Yoshimichi. Electric Modulus Powerful Tool for Analyzing Dielectric Behavior. *IEEE Transactions on Dielectrics and Electrical Insulation*, 21(3):929–931, 2014.

[218] J. C. Pandey and N. Gupta. Study of treeing in epoxy-alumina nanocomposites using electroluminescence. *IEEE Transactions on Dielectrics and Electrical Insulation*, 26(2):648–654, 2019.

[219] Y. Fan, D. Zhang, and J. Li. Study on the fractal dimension and growth time of the electrical treeing degradation at different temperature and moisture. *Advances in Materials Science and Engineering*, 2018:601926, 2018.

[220] R. Schurch-Brandt. *Three-Dimensional Imaging and Analysis of Electrical Trees*. Thesis, University of Manchester, 2014.

[221] J. V. Champion and S. J. Dodd. Systematic and reproducible partial discharge patterns during electrical tree growth in an epoxy resin. *Journal of Physics D: Applied Physics*, 29(3):862–868, 1996.

[222] K. Wu, Y. Suzuoki, T. Mizutani, and H. Xie. A novel physical model for partial discharge in narrow channels. *IEEE Transactions on Dielectrics and Electrical Insulation*, 6(2):181–190, 1999.

[223] S. J. Dodd, N. M. Chalashkanov, and J. C. Fothergill. Partial discharge patterns in conducting and non-conducting electrical trees. In *Proceedings of the 2010 IEEE International Conference on Solid Dielectrics, ICSD 2010*, 2010.

[224] W. J. Cantwell and H. H. Kausch. Fracture behaviour of epoxy resins. In *Chemistry and Technology of Epoxy Resins*, chapter 5, pages 144–174. Springer, Dordrecht, 1993.

[225] A. Zotti, S. Zuppolini, M. Zarrelli, and A. Borriello. Fracture Toughening Mechanisms in Epoxy Adhesives. In *Adhesives - Applications and Properties*, chapter 10. IntechOpen, 2016.

[226] R. Kochetov, A. V. Korobko, T. Andritsch, P. H. F. Morshuis, S. J. Picken, and J. J. Smit. Modelling of the thermal conductivity in polymer nanocomposites and the impact of the interface between filler and matrix. *Journal of Physics D: Applied Physics*, 44:395401, 2011.

[227] T. Yamane, N. Nagai, S. I. Katayama, and M. Todoki. Measurement of thermal conductivity of silicon dioxide thin films using a 3ω method. *Journal of Applied Physics*, 91(12):9772–9776, 2002.

[228] W. Zhu, G. Zheng, S. Cao, and H. He. Thermal conductivity of amorphous SiO_2 thin film: A molecular dynamics study. *Scientific Reports*, 8(1):10537, 2018.

[229] A. Kinaci, J. B. Haskins, and T. Çağn. On calculation of thermal conductivity from Einstein relation in equilibrium molecular dynamics. *Journal of Chemical Physics*, 137(1):014106, 2012.

[230] R. Parra, M. S. Góes, M. S. Castro, E. Longos, P. R. Bueno, and J. A. Varela. Reaction pathway to the synthesis of anatase via the chemical modification of titanium isopropoxide with acetic acid. *Chemistry of Materials*, 20(1):143–150, 2008.

[231] M. T. Colomer, M. J. Velasco, and J. R. Jurado. Synthesis and thermal evolution of TiO_2-RuO_2 xerogels. *Journal of Sol-Gel Science and Technology*, 39(3):211–222, 2006.

[232] V. A. Zeitler and C. A. Brown. The infrared spectra of some Ti-O-Si, Ti-O-Ti and Si-O-Si compounds. *Journal of Physical Chemistry*, 61(9):1174–1177, 1957.

[233] L. Rozes, N. Steunou, G. Fornasieri, and C. Sanchez. Titanium-oxo clusters, versatile nanobuilding blocks for the design of advanced hybrid materials, 2006.

[234] M. E. Simonsen and E. G. Søgaard. Sol-gel reactions of titanium alkoxides and water: Influence of pH and alkoxy group on cluster formation and properties of the resulting products. *Journal of Sol-Gel Science and Technology*, 53(3):485–497, 2010.

[235] A. Soloviev and E. G. Søgaard. Application of electro-spray ionization mass spectrometry for characterization of titanium polyoxoalkoxides in sol-gel processes. *Journal of Materials Science*, 41(18):6159–6161, 2006.

[236] A. Soloviev, R. Tufeu, C. Sanchez, and A. V. Kanaev. Nucleation stage in the $Ti(OPr^i)_4$ sol-gel process. *Journal of Physical Chemistry B*, 105(19):4175–4180, 2001.

[237] L. Rozes and C. Sanchez. Titanium oxo-clusters: Precursors for a Lego-like construction of nanostructured hybrid materials. *Chemical Society Reviews*, 40(2):1006–1030, 2011.

[238] B. E. Yoldas. Alumina gels that form porous transparent Al_2O_3. *Journal of Materials Science*, 10(11):1856–1860, 1975.

[239] B. E. Yoldas. Hydrolysis of aluminium alkoxides and bayerite conversion. *Journal of Applied Chemistry and Biotechnology*, 23(11):803–809, 1973.

[240] L. A. Dissado and R. M. Hill. The fractal nature of the cluster model dielectric response functions. *Journal of Applied Physics*, 66(6):2511–2524, 1989.

[241] I. Ozsoy, A. Demirkol, A. Mimaroglu, H. Unal, and Z. Demir. The Influence of Micro- and Nano-Filler Content on the Mechanical Properties of Epoxy Composites. *Strojniški vestnik - Journal of Mechanical Engineering*, 61(10):601–609, 2015.

[242] Z. Li, K. Okamoto, Y. Ohki, and T. Tanaka. The role of nano and micro particles on partial discharge and breakdown strength in epoxy composites. *IEEE Transactions on Dielectrics and Electrical Insulation*, 18(3):675–681, 2011.

[243] M. Donnay, S. Tzavalas, and E. Logakis. Boron nitride filled epoxy with improved thermal conductivity and dielectric breakdown strength. *Composites Science and Technology*, 110:152–158, 2015.

[244] Z. Wang, T. Iizuka, M. Kozako, Y. Ohki, and T. Tanaka. Development of epoxy/BN composites with high thermal conductivity and sufficient dielectric breakdown strength part II-breakdown strength. *IEEE Transactions on Dielectrics and Electrical Insulation*, 18(6):1973–1983, 2011.

[245] P. Preetha and M. J. Thomas. AC breakdown characteristics of epoxy nanocomposites. *IEEE Transactions on Dielectrics and Electrical Insulation*, 18(5):1526–1534, 2011.

[246] Midel 7131 Product Brochure. Available online: https://www.midel.com/app/uploads/2018/05/MIDEL-71. Accessed 29.09.2021.

[247] D. Martin and Z. D. Wang. Statistical analysis of the AC breakdown voltages of ester based transformer oils. *IEEE Transactions on Dielectrics and Electrical Insulation*, 15(4):1044–1050, 2008.

[248] Y. Jing, I. V. Timoshkin, M. P. Wilson, M. J. Given, S. J. Macgregor, T. Wang, and J. Lehr. Dielectric properties of natural ester, synthetic ester midel 7131 and mineral oil diala D. *IEEE Transactions on Dielectrics and Electrical Insulation*, 21(2):644–652, 2014.

[249] D. Martin. *Evaluation of the Dielectric Capability of Ester Based Oils for Power Transformers*. Thesis, The University of Manchester, 2008.

[250] T. G. Aakre, T. A. Ve, and Ø. L. Hestad. Conductivity and permittivity of midel 7131: Effect of temperature, moisture content, hydrostatic pressure and electric field. *IEEE Transactions on Dielectrics and Electrical Insulation*, 23(5):2957–2964, 2016.

[251] A. Mohanty and V. K. Srivastava. Dielectric breakdown performance of alumina/epoxy resin nanocomposites under high voltage application. *Materials and Design*, 47:711–716, 2013.

[252] M. Sajjad, B. Feichtenschlager, S. Pabisch, J. Svehla, T. Koch, S. Seidler, H. Peterlik, and G. Kickelbick. Study of the effect of the concentration, size and surface chemistry of zirconia and silica nanoparticle fillers within an epoxy resin on the bulk properties of the resulting nanocomposites. *Polymer International*, 61(2):274–285, 2012.

[253] H. Liu and L. C. Brinson. Reinforcing efficiency of nanoparticles: A simple comparison for polymer nanocomposites. *Composites Science and Technology*, 68(6):1502–1512, 2008.

[254] Y. Eom, L. Boogh, V. Michaud, and J. A. Månson. Internal stress control in epoxy resins and their composites by material and process tailoring. *Polymer Composites*, 23(6):1044–1056, 2002.

[255] C. Zilg, R. Thomann, J. Finter, and R. Mülhaupt. The influence of silicate modification and compatibilizers on mechanical properties and morphology of anhydride-cured epoxy nanocomposites. *Macromolecular Materials and Engineering*, 280-281:41–46, 2000.

[256] L. Fumagalli, D. Esteban-Ferrer, A. Cuervo, J. L. Carrascosa, and G. Gomila. Label-free identification of single dielectric nanoparticles and viruses with ultraweak polarization forces. *Nature Materials*, 11(9):808–816, 2012.

[257] W. Wang, D. Min, and S. Li. Understanding the conduction and breakdown properties of polyethylene nanodielectrics: Effect of deep traps. *IEEE Transactions on Dielectrics and Electrical Insulation*, 23(1):564–572, 2016.

[258] B. Du, J. Su, M. Tian, T. Han, and J. Li. Understanding Trap Effects on Electrical Treeing Phenomena in EPDM/POSS Composites. *Scientific Reports*, 8(1):8481, 2018.

[259] R. C. Smith, C. Liang, M. Landry, J. K. Nelson, and L. S. Schadler. The mechanisms leading to the useful electrical properties of polymer nanodielectrics. *IEEE Transactions on Dielectrics and Electrical Insulation*, 15(1):187–196, 2008.

[260] B. Zhang, W. Gao, P. Chu, Z. Zhang, and G. Zhang. Trap-modulated carrier transport tailors the dielectric properties of alumina/epoxy nanocomposites. *Journal of Materials Science: Materials in Electronics*, 29(3):1964–1974, 2018.

[261] G. C. Stevens and A. S. Vaughan. Nanodielectrics and their role in power transmission applications. In *Electricity Transmission, Distribution and Storage Systems*, pages 206–241. Woodhead Publishing, 2013.

[262] T. Tanaka and A. S. Vaughan, editors. *Tailoring of Nanocomposite Dielectrics*. Pan Stanford Publishing, New York, USA, 1 edition, 2016.

[263] F. Richardeau, Z. Dou, E. Sarraute, J. M. Blaquiere, and D. Flumian. Comparison of IGBT short-circuit failure "ohmic mode": Epoxy molded package versus silicone gel module for new fail-safe and interruptible power converters. In *Microelectronics Reliability*, volume 51, pages 1919–1926. Pergamon, 2011.

[264] E. A. Cherney. Nanodielectrics applications-today and tomorrow. *IEEE Electrical Insulation Magazine*, 29(6):59–65, 2013.

[265] L. S. Schadler and J. K. Nelson. Polymer nanodielectrics - Short history and future perspective. *Journal of Applied Physics*, 128(12):120902, 2020.

[266] J. J. Gooding and Y. Zhu. Modifying porous silicon with self-assembled monolayers for biomedical applications. In *Porous Silicon for Biomedical Applications*, pages 81–103. Woodhead Publishing, 2014.

[267] S. Iwata. Study on three-dimensional structural analysis method for electrical tree. In *Proceedings of the IEEE International Conference on Properties and Applications of Dielectric Materials*, pages 236–239. Institute of Electrical and Electronics Engineers Inc., 2015.

Appendices

A Published papers

The following articles are reproduced with permission under the Creative Commons Attribution 4.0 International License.

Adnan, M.M., Tveten, E.G., Miranti, R., Hvidsten, S., Ese, M.-H.G., Glaum, J., Einarsrud, M.-A. In situ synthesis of epoxy nanocomposites with hierarchical surface-modified SiO_2 clusters. *J Sol-Gel Sci Technol* **95**, 783–794 (2020). https://doi.org/10.1007/s10971-020-05220-3

Adnan, M.M., Nylund, I.-E., Jaworski, A., Hvidsten, S., Ese, M.-H.G., Glaum, J., Einarsrud, M.-A. The structure, morphology, and complex permittivity of epoxy nanodielectrics with in situ synthesized surface-functionalized SiO_2. *Polymers* **13**(9), 1469 (2021). https://doi.org/10.3390/polym13091469

Journal of Sol-Gel Science and Technology
https://doi.org/10.1007/s10971-020-05220-3

ORIGINAL PAPER: SOL-GEL AND HYBRID MATERIALS FOR DIELECTRIC, ELECTRONIC, MAGNETIC AND FERROELECTRIC APPLICATIONS

In situ synthesis of epoxy nanocomposites with hierarchical surface-modified SiO_2 clusters

Mohammed Mostafa Adnan[1] · Erlend Grytli Tveten[2] · Rany Miranti[1] · Sverre Hvidsten[2] · Marit-Helen Glomm Ese[2] · Julia Glaum[1] · Mari-Ann Einarsrud[1]

Received: 3 October 2019 / Accepted: 7 January 2020

Abstract

Polymer nanocomposites are often produced using in situ approaches where an inorganic filler (as the dispersed phase) is synthesized directly in an organic matrix. Such an approach generally leads to improved dispersion and reduced agglomeration of the filler material. Epoxy-based nanocomposites have demonstrated promising properties for application as high-voltage insulation materials. In this work, a sol–gel based method has been adapted to synthesize surface-functionalized SiO_2 in situ in epoxy. The synthesized SiO_2 moieties were dispersed in clusters of 10–80 nm, and formed chemical bonds with the epoxy monomers via a silane coupling agent. Raman spectra show the formation of four-membered D_1 rings, which may be part of a cage-like structure similar to that of polyhedral oligomeric silsesquioxanes (POSS). SAXS measurements indicate that the SiO_2 clusters consist of a hierarchical structure with an increasing fractal dimension with increasing SiO_2 content. The nanocomposites displayed improved thermal stability, while the glass transition behavior varied depending on the structure and content of the SiO_2 moieties. While the relative permittivity showed no significant changes from that of pure epoxy, the onset of the dielectric relaxation changed with the SiO_2 structure and content, similar to the behavior observed for the glass transition.

Graphical Abstract

The synthesis of surface-functionalized SiO_2 in situ in an epoxy resin (DGEBA) resulted in a good dispersion and limited agglomeration of the SiO_2 in the nanocomposite, with little deviation in the dielectric properties (i.e., complex permittivity). The SiO_2 is suspected to have a hierarchical structure based on the SAXS measurements, with the primary structural level consisting of POSS-like cages, and an evolution in the structure from inorganic chains to cross-linked clusters with increasing SiO_2 content.

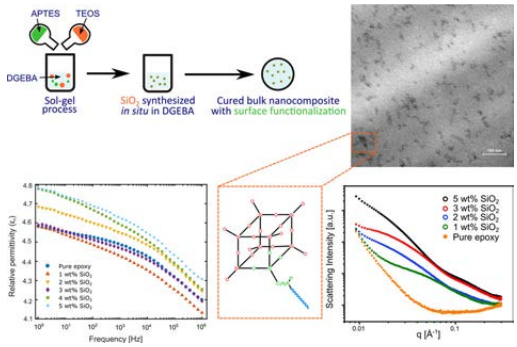

✉ Mari-Ann Einarsrud
mari-ann.einarsrud@ntnu.no

[1] Department of Materials Science and Engineering, NTNU Norwegian University of Science and Technology, Trondheim, Norway

[2] SINTEF Energy Research AS, Trondheim, Norway

Published online: 30 January 2020

Keywords Sol–gel · Nanocomposites · Epoxy · Silica · Dielectric properties

Highlights

- Surface-modified SiO_2 clusters of 10–80 nm synthesized in situ in epoxy using a sol–gel method.
- Raman spectra show the formation of four-membered SiO rings (D_1 breathing mode).
- SAXS indicates the presence of a hierarchical structure within the SiO_2 clusters.
- The glass transition and the dielectric relaxation varies with the structure and content of SiO_2.
- No significant changes in relative permittivity.

1 Introduction

Epoxy-based nanocomposites, containing inorganic oxide nanoparticles as filler, are often used as nanodielectrics in high-voltage insulation materials or microelectromechanical systems due to the novel properties exhibited by these hybrid materials [1–3]. Several studies have presented the advantages of adding nanoparticles of SiO_2, TiO_2, MgO, ZnO, BN, etc. to the epoxy matrix, such as higher dielectric breakdown strengths, reduced complex permittivity, decreased accumulation of space charge, greater mechanical strength and fracture toughness, increased thermal stability, and higher glass transition temperatures [4–11]. However, there is a large spread in the reported results, likely due to the difficulty in consistently achieving a homogeneous and stable dispersion of nanoparticles in epoxy. A poor dispersion quality can result in a deterioration of the desired dielectric properties [12]. The use of surface modifiers for the nanoparticles, such as silane coupling agents (SCAs) or organophosphate ligands, have been shown to improve the properties of epoxy nanocomposites [13]. These surface modifiers allow chemical bonds to form at the interfaces between the nanoparticles and the polymer chains, facilitating the dispersion of the nanoparticles [14], thereby increasing the interfacial area. The interfacial region between the nanoparticles and the polymer chains is thought to play a key role in determining the properties of these nanocomposites. Tanaka et al. [15] proposed a multicore model to describe the interfacial region, suggesting three distinct layers around the nanoparticles. The strength of the bonds between the polymer chains and the nanoparticle surface varied in each layer, thus affecting the mobility and chain conformation. Earlier studies of the dielectric properties of epoxy nanocomposites have primarily applied an ex situ blending method in the preparation of the materials, which involves mechanically mixing presynthesized nanoparticles into the uncured epoxy resin. The high viscosity of the epoxy resin makes it difficult to disperse the nanoparticles during a physical mixing procedure, which also does not always break up any existing agglomerates. The use of ultrasonication has shown to improve the dispersion quality to a certain degree [16]. However, even with the use of surface-functionalized nanoparticles, the use of ex situ techniques makes it challenging to obtain a homogeneous dispersion of nonagglomerated nanoparticles in the epoxy.

An alternative approach to improve the dispersion quality is in situ synthesis of the inorganic oxide directly in the epoxy using the sol–gel method [17]. One of the advantages of this method is the ability to control the size and morphology of the inorganic moieties formed by adjusting the synthesis parameters, e.g., precursor concentration, temperature, pH, as well as type and amount of catalyst [18]. SCAs may also be applied to form stronger interactions between the organic and inorganic components, resulting in the formation of class II hybrid materials [19]. Several studies have investigated the in situ formation of SiO_2 networks in epoxy using sol–gel methods and the resulting changes in the structure, as well as the mechanical and thermal properties of the hybrid materials. Matějka et al. [20, 21] showed variations in the fractal dimension of the SiO_2 structures formed, depending on whether a single-step procedure or a two-step procedure (with prehydrolyzed tetraethylorthosilicate (TEOS) as the SiO_2 precursor) was used in the synthesis. Nazir et al. [22] and Afzal and Siddiqi [18] reported improvements in the dispersion quality, the storage modulus, and a higher glass transition temperature (T_g) when a two-step procedure with SCAs was used. Yu et al. [23] found an improved dispersion quality and higher flexural moduli and impact strengths for in situ prepared nanocomposites. However, to the best of our knowledge, no studies have reported the dielectric properties such as the complex permittivity and dielectric breakdown strength of epoxy-SiO_2 nanocomposites synthesized using an in situ sol–gel method. These are critical properties for applications of these hybrid materials, for example as nanodielectrics in high-voltage power insulation systems and components.

Hence, the objective of this work is to develop a synthesis route to epoxy-SiO_2 nanocomposites with a homogeneous dispersion of the SiO_2, by nucleating surface-functionalized SiO_2 nanoparticles in situ in silanized epoxy. The structure of the hybrid materials and their thermal stability, glass transition, and complex permittivity have been investigated and an improved understanding of the structure–property relations has been developed. This

provides a solid basis for optimization of the synthesis route to tailor the functional properties of nanocomposites, and eventually improve the dielectric properties.

2 Experimental

2.1 Materials

Diglycidyl ether of bisphenol-A (DGEBA, molar mass of 340.41 g mol^{-1}, epoxide equivalent weight of 170.2 g/eq epoxy) was used as the epoxy monomer. Poly(propylene glycol) bis(2-aminopropyl ether) (molar mass of 230 g mol^{-1}, and amine-hydrogen equivalent weight of 57.5 g/eq amine) was the curing agent for the system. TEOS was used as the precursor for the SiO_2, and 3-(aminopropyl) triethoxysilane (APTES) was employed as the coupling agent between the SiO_2 and the epoxy chains. Distilled water, brought to pH 2 using concentrated HCl (37%), was the catalyst for the hydrolysis reaction. All chemicals were obtained from Merck.

2.2 Preparation of samples

2.2.1 Pure epoxy samples

As a reference, samples of pure epoxy (containing no SiO_2 or APTES) were prepared by mixing DGEBA with the curing agent (1:1 ratio of epoxide to amine-hydrogen groups) in a beaker for 15 min at room temperature using a mechanical stirrer. The mixture was degassed in vacuum (<10 mbar pressure) for 15–20 min to remove entrapped gas and air bubbles introduced during the stirring. Two different types of samples were prepared for different characterization methods. Bulk samples (30 mm diameter, thickness varying between 3 and 15 mm) were formed by pouring the resins into cylindrical Teflon molds. The walls of the molds were waxed lightly with high-vacuum silicone grease to allow the samples to be more easily ejected from the molds after curing. The samples were cured at 100 °C for 5 h. Thin disc-shaped samples (10 cm in diameter, 0.5 mm thick) were also prepared by mixing the resin and curing agent, and then injecting the resin using 700 mbar of air pressure into a stainless steel mold under vacuum. Frekote NC-150 (Henkel) was used as the release agent for this mold. The mold was then kept under vacuum (<10 mbar pressure) for 30 min to remove any air bubbles remaining in the resin before curing at 100 °C for 5 h.

2.2.2 Epoxy-SiO_2 nanocomposites

The chronological two-step procedure employed by Afzal and Siddiqi [18] is adapted in this study for the preparation of the nanocomposite samples. Table 1 shows the reactants and amounts used in the synthesis of the materials with different SiO_2 contents. The sample names in Table 1 are used to identify the different materials investigated in this work.

DGEBA was initially heated to 80 °C under reflux in a round-bottomed flask on a heating mantle to reduce the viscosity and enable easier stirring. APTES was added to the DGEBA (in a weight ratio of 1:10 for APTES:DGEBA) and mixed with a magnetic stirrer for 1 h at 80 °C. Afterward TEOS was added to the mixture, which was stirred for another hour at 60 °C. The amount of TEOS was varied corresponding to a SiO_2 content between 0 and 5 wt% of the total mass. Water (in the ratio 2:1 for water to TEOS and 1.5:1 for water to APTES), brought to pH 2 using concentrated HCl, was then added to catalyze the hydrolysis of TEOS. The mixture was stirred for 4 h at 60 °C, and then 1 h at 80 °C to allow the hydrolysis and condensation reactions to be completed. The mixture was then poured into a beaker, and stirred for 15–18 h at 80 °C overnight to evaporate any unreacted water or alcohol byproducts. The resin was then mixed with the curing agent, casted in the molds, and cured using the same procedures as described above. All the samples are identified based on the SiO_2 content that originated from the TEOS added. Figure 1 displays a flow chart for the preparation of the nanocomposites.

2.3 Characterization

Fourier transform infrared (FTIR) spectroscopy was performed on the thin disc samples using a Bruker Vertex 80 v spectrophotometer equipped with a Bruker Platinum attenuated total reflectance (ATR) diamond. For each sample, 32 scans were recorded at a resolution of 1 cm^{-1}. For the in situ measurements, a drop of the reactant mixture from

Table 1 Compositions of the reactants used in the synthesis of epoxy nanocomposites with varying SiO_2 content

Sample name	Epoxy (g)	APTES (g)	TEOS (g)	Water (g)	Curing agent (g)	Nominal amount of SiO_2 formed from TEOS (wt%)
EAS0	30	0	0	0	10.13	0
EAS1		3	1.51	0.63		1
EAS2			3.06	0.89		2
EAS3			4.63	1.17		3
EAS4			6.24	1.44		4
EAS5			7.88	1.73		5

each synthesis step was placed on the ATR diamond. For the measurements on the cured samples, 0.5 mm films were pressed down on top of the diamond.

Raman spectroscopy was also performed on the disc samples using a WITec Alpha 300R using a monochromatic diode laser ($\lambda = 532$ nm) at 10 mW power. The spectra were measured with three accumulations collected over an integration time of 60 s for each accumulation.

Small angle X-ray scattering (SAXS) measurements were performed on a Bruker NanoSTAR instrument with a Cu microsource and Våntex-2000 detector, operating at 50 kV and 600 µA. Both the disc and the bulk samples, which were cut to 1 mm thickness using a diamond saw, were used. The scattering vector (q) range was from 0.009 to 0.3 $Å^{-1}$, and a glassy carbon standard was used to obtain an absolute scale for the scattering intensities. All the intensities were corrected for the scattering from the empty sample compartment. The measurements were analyzed using both model-independent methods (Guinier and Porod laws), and the unified exponential/power-law fitting model developed by Beaucage (for hierarchical structures) [24] to characterize the inorganic structures after subtraction of the background scattering from the pure epoxy matrix. The software SasView 4.2.0 was used to obtain the fits to the unified model.

Transmission electron microscopy (TEM) was performed using a JEOL JEM 2100F with an accelerating voltage of 200 kV. The samples were prepared from the bulk samples using an ultramicrotome to cut ~50–100 nm thin slices.

Differential scanning calorimetry (DSC) was performed on a Netzsch DSC 214 Polyma instrument. Five to ten milligrams sized pieces were cut from the bulk samples and used for the measurements. The samples were cycled four times between 0 and 200 °C at 10 °C/min rates (both heating and cooling), with N_2 gas flow at 40 mL/min. The glass transition temperature was determined from the local maxima in the heat capacity measured in the final cycle. Thermogravimetric analysis (TGA) was carried out on a Netzsch STA 449C using an alumina crucible and synthetic air (30 mL/min gas flow). The samples were first held at 120 °C for 30 min, before being heated to 900 °C at 10 °C/min.

Dielectric spectroscopy was performed using a Novocontrol Spectrometer with an Alpha Beta dielectric analyzer and a BDS1200 sample cell. The cylindrical bulk samples were grinded with SiC paper (#800, #1200, and #2000 grade) and dried in a vacuum oven at 120 °C for 2 h, before gold electrodes were sputtered onto the top and bottom surfaces. An electric field of 0.1 V/mm was used, and the spectroscopy was performed between 1 and 10^6 Hz at room temperature. Measurements were performed on four to five samples for each nanocomposite with SiO_2 and for pure epoxy.

3 Results

3.1 Structure and morphology of the nanocomposites

The prepared nanocomposite and pure epoxy samples were transparent and clear. No visual indication of phase separation of the inorganic filler from the epoxy matrix was observed. The dispersion of the in situ prepared SiO_2 nanoparticles was observed from the representative TEM and STEM images in Fig. 2. The SiO_2 nanoparticles are arranged in irregularly shaped clusters varying in size

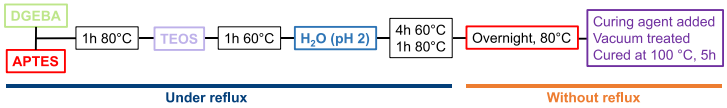

Fig. 1 Flow chart outlining the synthesis procedure for the preparation of nanocomposites

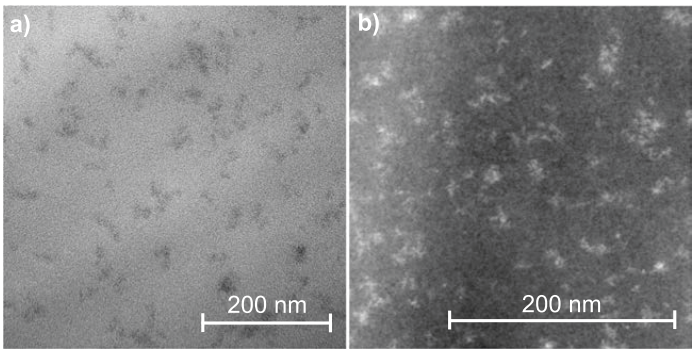

Fig. 2 **a** TEM image of the nanocomposite EAS5, and **b** STEM dark-field image of the nanocomposite EAS2

between 10 and 20 nm for the EAS2 sample, and between 20 and 50 nm with some larger clusters up to 80 nm for the EAS5 sample.

Figure 3a shows the development of the FTIR spectra during the in situ synthesis. Figure 3b, c magnify the regions in which important changes occur as the reaction proceeds. The strong characteristic bands from Si–O–C bonds (1070–1105 cm^{-1}) and the ethyl groups (940–970 cm^{-1}), present in both APTES and TEOS, are observed [25]. These bands are strongest upon addition of TEOS, but as the reaction proceeds they become relatively weaker (compared with the band at 1036 cm^{-1} assigned to the aromatic C–O–C group in the DGEBA [26]). The band originating from the oxirane ring at 915 cm^{-1} [26] is also weaker upon reaction with APTES (shown by the dotted red lines). The broad band between 3300 and 3600 cm^{-1} corresponds to O–H groups, which becomes stronger at later stages of the reaction. The characteristic band from the N–H bonds in APTES at 1620 cm^{-1} is difficult to distinguish due to overlap with the C = C aromatic band in DGEBA [26]. The spectra of the pure epoxy (EAS0) and nanocomposite epoxy film (EAS4) after curing are shown in Fig. 4. The broad band from the O–H groups is more intense due to the opening of all the oxirane rings in DGEBA by the curing agent, which results in a significant decrease in the characteristic band at 915 cm^{-1}. The O–Si–O rocking band is observed at 450 cm^{-1} in the nanocomposite. The more characteristic fingerprint of inorganic Si–O–Si networks is observed at 1080–1100 cm^{-1} [27, 28] for the nanocomposite sample containing SiO_2, shown in the inset. The pure epoxy also exhibits a band in the same range, which is attributed to the C–O stretching (1089 cm^{-1}) from the curing agent [29]. A considerable

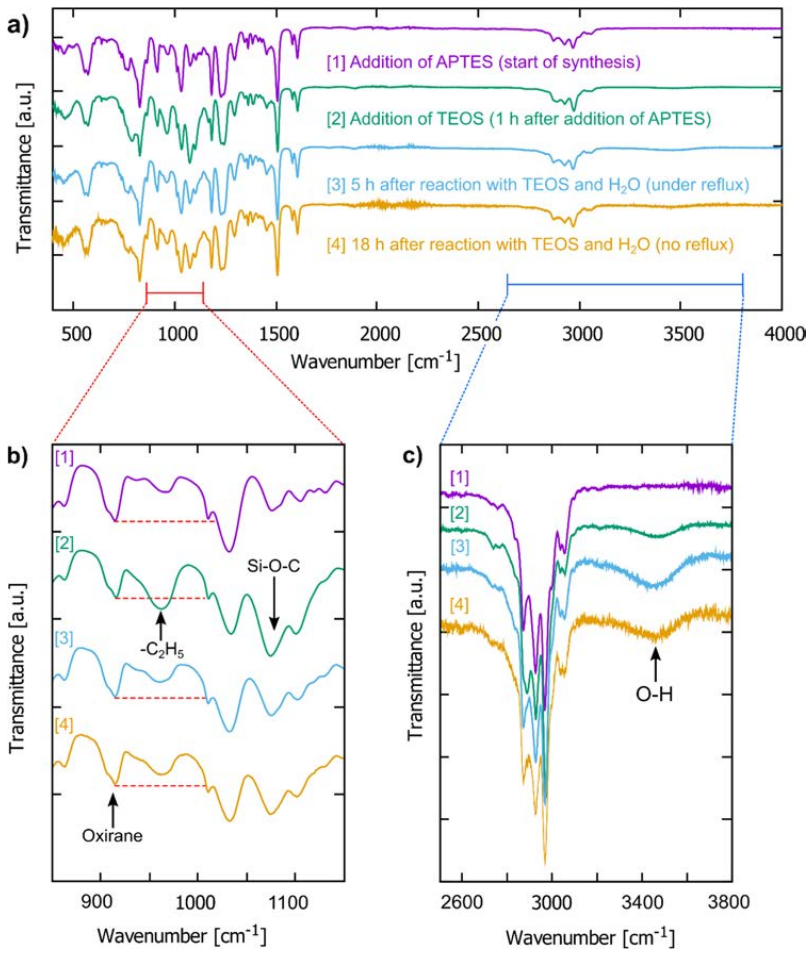

Fig. 3 **a** FTIR spectra of the reactant mixture during the in situ synthesis at four stages of the reaction process: after the addition of APTES to DGEBA (1), after the addition of TEOS (2), 5 h after the addition of water (3), and upon completion of the reaction (18 h without reflux) (4). Magnified spectra are shown in the (**b**) 800–1200 cm^{-1} range, and the (**c**) 2500–3800 cm^{-1} range as the reaction proceeds

overlap between these two bands is observed in the cured nanocomposite samples containing SiO_2.

In the Raman spectra, shown in Fig. 5, the band from the four-membered SiO rings is observed at 483 cm^{-1} (D_1^*) in the EAS3 sample. A broad Raman peak in the range of 470–510 cm^{-1} is detected for samples with a larger SiO_2 content (EAS4 and EAS5). This peak can be identified as an overlap of two Raman modes, D_1^* mode at 484 cm^{-1} and D_1 at 493 cm^{-1}. For pure epoxy (EAS0) these bands are absent in this region, as expected due to the lack of any SiO_2, while for small amounts of SiO_2 (EAS1 and EAS2) they were weaker and difficult to detect.

Figure 6a displays the SAXS profiles of pure epoxy as well as nanocomposites with varying SiO_2 content. The scattering intensity increased with the amount of SiO_2. All the materials exhibit a broad knee feature in a q range

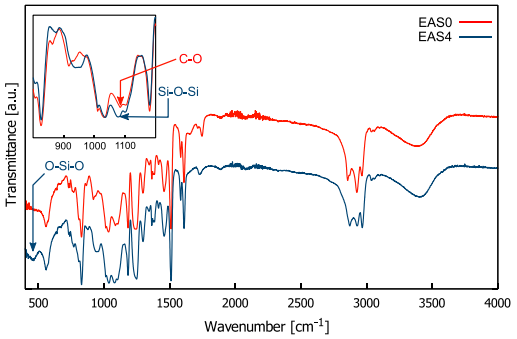

Fig. 4 FTIR spectra of cured films of pure epoxy (EAS0) and epoxy nanocomposite with SiO2 (EAS4). The inset shows a magnified part of the low frequency region of the spectra, exhibiting the difference in the spectra

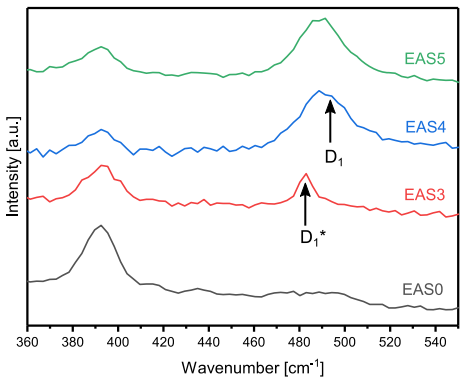

Fig. 5 Raman spectra of pure cured epoxy (EAS0) and epoxy nanocomposites with different SiO2 contents (EAS3, EAS4, and EAS5). The Raman shift for the different four-membered SiO rings (D_1 and D_1*) are indicated

between 0.02 and 0.07 $Å^{-1}$, which shifts to lower q values with increasing SiO_2 content. The nanocomposites with higher SiO_2 content (EAS3 and EAS5) possess an additional knee at higher q values (between 0.1 and 0.2 $Å^{-1}$) that can be attributed to inorganic domains with higher electron density [30]. These features in the scattering may be attributed to inorganic nanoparticles arranged in hierarchical structures at different size scales [31]. The scattering data for all the samples were analyzed using model-independent methods. At low q values below 0.02 $Å^{-1}$, Guinier analysis was performed to calculate the radius of gyration, R_g, for the nanoparticles. Assuming that the scattering objects are spherical, the size of the inorganic domains (d) was calculated using as

$$d = 2R_g\sqrt{\frac{5}{3}}. \quad (1)$$

The slopes of the linear regions of a log–log plot (log(I) vs log(q)) at intermediate q values ($0.03 < q < 0.13$), where the best linear fit for each plot could be obtained, were calculated to obtain the power-law scaling of the scattering by the inorganic structures (fractal dimension, D). Both the model-independent analysis and the fitting to the unified model were performed after subtraction of the background scattering from the pure epoxy matrix, so that the calculations represent the SiO_2 only and do not include scattering effects from the epoxy.

The fits of the SAXS data with the unified model [24] using two structural levels for the EAS3 and EAS5 samples in the q range 0.015–025 $Å^{-1}$ are shown in Fig. 6b. The first structural level was assumed to consist of perfectly spherical nanoparticles (with size d^1), which are then arranged in clusters (of size d^2) to form the second structural level. Acceptable fits were not obtained for the samples containing a lower amount of SiO_2, since they do not exhibit the scattering feature at higher q. From these fits, the radius of gyration for the two structural levels (R_g^1 and R_g^2), the particle size and cluster size (d^1 and d^2, respectively), and the fractal dimension for the clusters in the second structural level (D^2) were obtained. The fractal dimension for the first structural level was fixed to a value of 4, assuming that the spherical nanoparticles have perfectly smooth surfaces.

Table 2 shows the calculated parameters from the model-independent Guinier and Porod laws and from the unified model. Using both analysis methods, an increase in the SiO_2 content resulted in an increasing R_g (and therefore an increasing particle or cluster size) and an increase in the fractal dimension. The increase in R_g indicates the formation of larger inorganic domains. The calculated size of these structures is comparable with the sizes observed from the TEM images. The increase in the fractal dimension may also represent an evolution of the network structure of the SiO_2 — the samples with a lower SiO_2 content (EAS1,

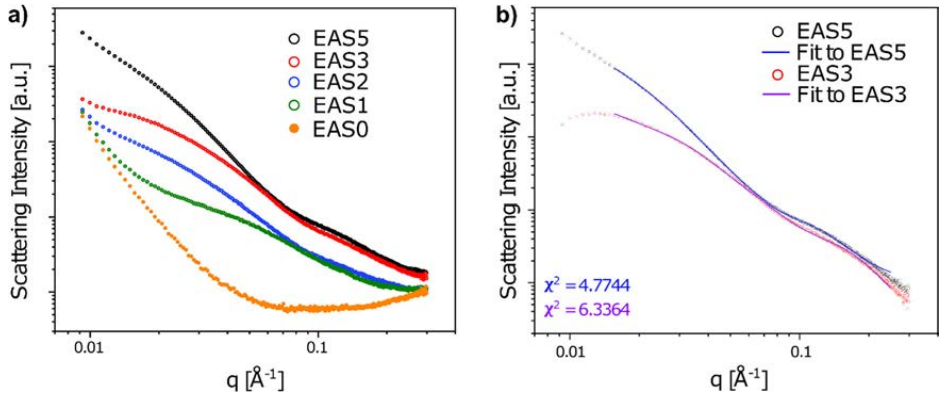

Fig. 6 **a** SAXS profiles of pure epoxy (EAS0) and epoxy nanocomposites with different SiO_2 contents (EAS1, EAS2, EAS3, and EAS5), and **b** the unified model fit to the scattering data, as shown by the solid lines, for the EAS3 and EAS5 samples. The reduced χ^2 values for the two fits are also shown

Table 2 Calculated structural parameters of the epoxy-SiO_2 nanocomposites calculated from the model-independent Guinier and Porod laws, and from the unified model fits

Sample	Guinier and Porod laws			Unified model				
	R_g (nm)	d (nm)	D	R_g^1 (nm)	d^1 (nm)	R_g^2 (nm)	d^2 (nm)	D^2
EAS5	12	31	3.06	2.8	7	13	34	3.48
EAS3	6	16	2.47	2.1	5	11	28	2.91
EAS2	7	18	2.33	–	–	–	–	–
EAS1	4	10	1.94	–	–	–	–	–

The superscripts 1 and 2 indicate the first and second levels in the hierarchical structures

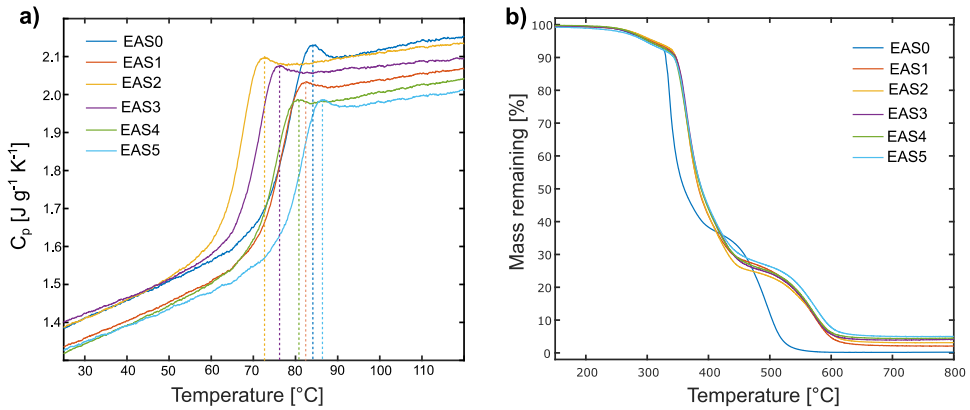

Fig. 7 **a** Variations in the heat capacity, and **b** thermogravimetric analysis of the nanocomposites with different SiO_2 contents. The dotted lines indicate the glass transition temperature (T_g)

EAS2, and EAS3) are more likely to consist of inorganic chains, representing a mass fractal structure ($D < 3$), while for a higher SiO_2 content (EAS5) the chains are coiled up and cross-linked into a more compact structure, representing a surface fractal ($3 < D < 4$).

3.2 Properties of the nanocomposites

The glass transition temperatures (T_g) of the nanocomposites were determined from the local maxima in the heat capacity as shown in Fig. 7a, and the measured values are

shown in Table 3. The incorporation of SiO_2 in epoxy resulted in an initial decrease of T_g to ~73 °C for 2 wt% SiO_2, followed by an increase to 87 °C for 5 wt% SiO_2. Figure 7b shows the TGA of the nanocomposites, displaying the increased thermal stability of the nanocomposites compared with pure epoxy at temperatures above 325 °C. Above 330 °C, the pure epoxy experiences a rapid drop in mass as it decomposes. The nanocomposites do not degrade until ~350 °C. The pure epoxy is completely decomposed before 600 °C, while in the nanocomposites the decomposition is delayed to 650 °C. The remaining mass beyond 650 °C corresponds to the amount of SiO_2 in the sample. The measured values of the temperatures for the initial decomposition (10% mass loss) from the TGA are included in Table 3.

Figure 8 shows the results from the dielectric spectroscopy measurements, i.e., the relative permittivity (or dielectric constant) and the dielectric loss tangent (tan δ) of pure epoxy and epoxy-SiO_2 nanocomposites. The permittivity curves and dielectric loss tangents were averaged over at least four different samples for each composition. The addition of SiO_2 does not significantly affect the complex permittivity. The real relative permittivity differed between 0.2 and 0.4 from the values of pure epoxy across all frequencies measured. The nanocomposites exhibited a larger dielectric loss than the pure epoxy below 500 Hz, although the losses for all the samples were generally quite low (below 1%) at 50 Hz.

Table 3 also contains the permittivity and loss tangent (tan δ) at 50 Hz for each material, as well as the frequency for the onset of the dielectric relaxation exhibited by all the materials. This frequency was determined by the intersection of two linear regression lines from the two regions, as demonstrated in the inset in Fig. 8.

Table 3 Thermal and dielectric properties of pure epoxy and epoxy-SiO_2 nanocomposites

Sample	T_g [°C]	T_{10}[a] [°C]	Permittivity[b]	tan δ[b]	Relaxation frequency[c] [Hz]
EAS0	83	330	4.53	0.0049	2630
EAS1	82	347	4.50	0.0086	2874
EAS2	73	347	4.61	0.0069	11501
EAS3	76	347	4.52	0.0067	6391
EAS4	81	343	4.68	0.0097	5648
EAS5	86	343	4.70	0.0076	4531

[a]Temperature at which 10% of mass has thermally decomposed

[b]Average values measured at 50 Hz

[c]Frequency at the onset of the dielectric relaxation

4 Discussion

4.1 Reaction pathway and resulting structure of the inorganic component

A schematic showing the proposed pathway for the reaction, based on the changes observed in the FTIR spectra, is shown in Fig. 9. The decrease in the band from the oxirane ring, the emergence of the O–H band, and the absence of the N–H band confirm that the DGEBA monomers have been silanized with the APTES. Upon addition of TEOS and the subsequent reaction with water, no further changes are observed in the oxirane ring band. However, the O–H band increases over time, which can be attributed to the hydrolysis of the TEOS and subsequent formation of surface O–H (silanol) groups after the SiO_2 clusters have formed. The band for the Si–O–C groups is present in the initial mixture (due to the APTES) and is seen to increase after addition of TEOS, as expected. The initial decrease in this signal over the first few hours is attributed to the

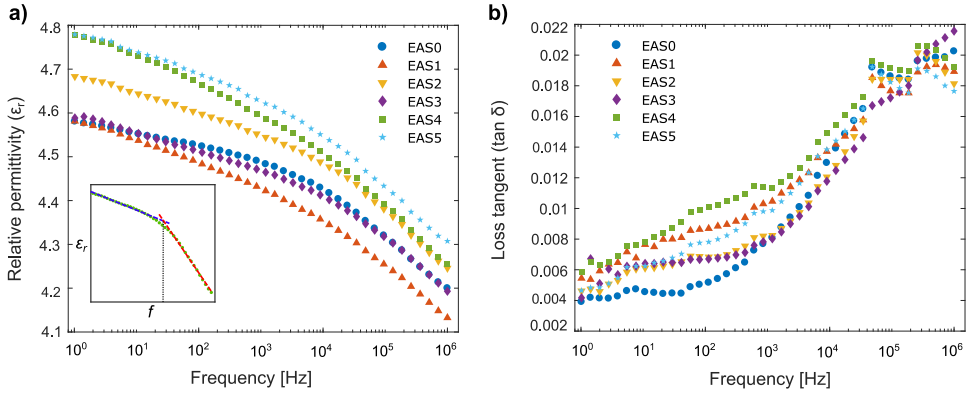

Fig. 8 **a** Real relative permittivities (ε), and **b** the loss tangent (tan δ) of pure epoxy (EAS0) and epoxy nanocomposites (EAS1, EAS2, EAS3, EAS4, and EAS5) as a function of frequency (*f*). The inset in **a** demonstrates how the frequency for the start of the dielectric relaxation was determined. The standard deviation in the average permittivity values is <0.05 for all the samples, except the EAS3 sample where the standard deviation is 0.25. The standard deviation in the average tan δ values is <0.003

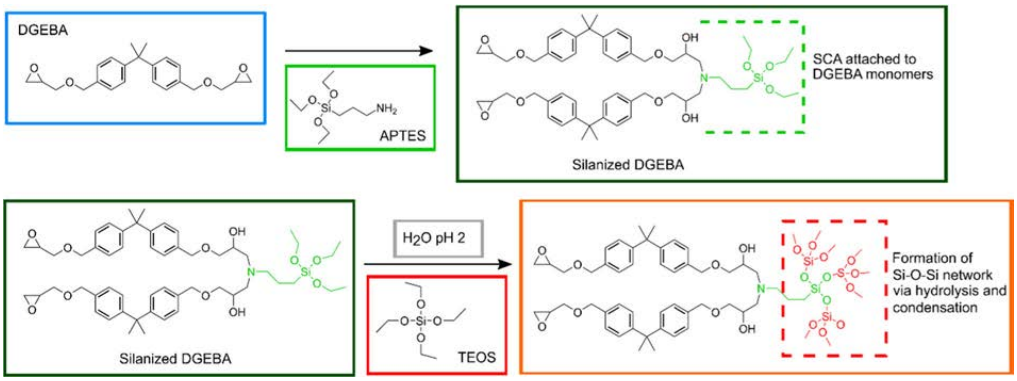

Fig. 9 Schematic of the possible reaction pathway during the in situ synthesis of SiO_2 nanoparticles from hydrolysis and condensation of TEOS in the epoxy resin

breaking of the Si–O–C bond during hydrolysis. However, the subsequent formation of Si–O–Si bonds (which are characterized by a band in the same region) by the condensation reactions results in no further changes over the remainder of the reaction.

As seen in the Raman spectra (Fig. 5), the D_1 breathing mode at 495 cm^{-1} is shifting between 484 and 503 cm^{-1} depending on the organic groups that are attached to the Si [32]. The shift to D_1* in samples containing SiO_2 can therefore be attributed to the surface functionalization, where one of the Si in the four-membered rings originates from the APTES and is connected to a carbon chain instead of oxygen. Due to the presence of the D_1* mode only for the nanocomposite with 3 wt% of SiO_2, it is likely that all of the SiO_2 structures formed are chemically bonded directly to the epoxy, while for higher SiO_2 contents (4 and 5 wt%) both types of four-membered rings are formed. Therefore, some of these rings are originating from the APTES (as demonstrated in Fig. 9) and the others are formed from the hydrolysis and condensation of isolated TEOS molecules with no covalent attachment to the epoxy.

In addition, the features observed by SAXS of these nanocomposites are similar to those observed for the epoxy nanocomposites containing silsesquioxanes structures [30, 33, 34]. The size of the primary structure level (5 nm and 7 nm for 3 wt% and 5 wt% SiO_2, respectively) is close to that reported for polyhedral oligomeric silsesquioxanes (1–3 nm) [35, 36]. Combined with the observations from Raman, it is therefore likely that the SiO_2 domains in the nanocomposites in the present work consist of particles built from oligomeric silsesquioxanes units, consisting of a cage structure with four-membered SiO rings on each face, as exemplified in Fig. 10. These structures may contain SiO rings with or without attachment to the APTES (resulting in the D_1* and D_1 bands in the Raman spectra).

The model-independent analysis of the SAXS measurements only provides limited information from a certain q range, since Guinier's law is only applied at $q < 0.02$. As seen in Fig. 6a, the scattering from the samples shows more complex behavior, particularly for higher SiO_2 content, with multiple Guinier regions (represented by the broad features, or knees) separated by a power-law (Porod) region. The data for the samples with 3 and 5 wt% SiO_2 (EAS3 and EAS5) showed a reasonable fit to the unified model developed by Beaucage [24], which describes hierarchical systems that show multiple Guinier and Porod regions in the scattering. These hierarchical systems consist of multiple structure levels, where each structure level is composed by an arrangement of the previous smaller level. The model could not provide good fits for the samples with 1 and 2 wt% SiO_2 (EAS1 and EAS2). The calculated parameters (R_g^2 and d^2) for the EAS5 sample are closer to the equivalent parameters calculated using the Guinier and Porod laws (R_g and d), while for the EAS3 sample there is a larger difference between them. The unified model also predicts higher fractal dimensions than using Porod's law. However, it should be noted that while the term fractal dimension is used to describe the inorganic structure, it is not necessarily expected that the clusters demonstrate fractal organization over multiple length scales. This is because the fractal dimensions were calculated from the slope in a narrow q range, since the power-law regime displays structural limits due to the Guinier features. However, this is a still useful qualitative descriptor for the type of structure (chains in the case of mass fractals, or a cross-linked network in the case of surface fractals) present in the clusters.

The size of the SiO_2 clusters calculated from the SAXS measurements are comparable with those measured by TEM, as seen for the EAS5 sample where the SAXS calculations predict an average cluster size between 31 and

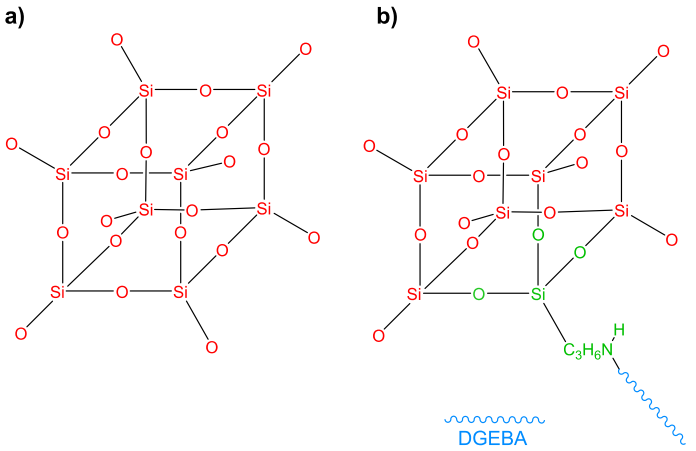

Fig. 10 Representation of the possible cage-like silsesquioxane structure with four-membered SiO rings on each face of the cage. The O atoms attached to the Si on the corners may be attached to other cages or terminated as surface O–H groups

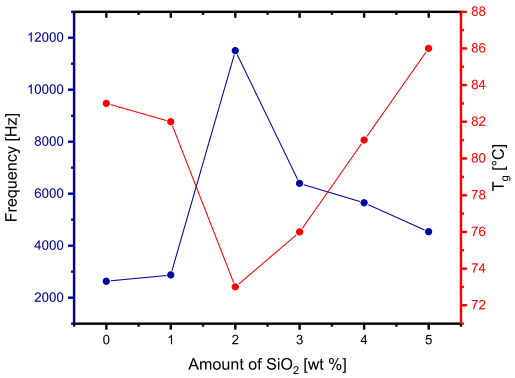

Fig. 11 Comparison of the changes in the glass transition temperature and the dielectric relaxation frequency with the amount of SiO_2 in the nanocomposites

34 nm, and the TEM shows clusters between 20 and 50 nm. A similar comparison can be made for the EAS2 sample. However, it is more difficult to determine from the TEM if the SiO_2 is organized as a mass or surface fractal network, as predicted by the SAXS.

4.2 Properties of the nanocomposites

The thermal analysis of the nanocomposites displays an interesting effect of the incorporated SiO_2 on the glass transition temperature of the epoxy, as shown in Fig. 11. The initial decrease in T_g for lower SiO_2 contents may be attributed to the mass fractal structure of the SiO_2, with polymer-like chains of silsesquioxanes, exhibiting a plasticizing effect on the surrounding resin [33]. With higher SiO_2 content, the inorganic domains form more clustered structures, as evidenced by the increase in fractal dimension from the SAXS measurements. In addition, there are more nanoparticles chemically bonded to the polymer chains for the higher SiO_2 content. The nanoparticles and the interfacial regions subsequently become more rigid, hindering the free motion of the polymer chains, thereby leading to an increase in T_g. The thermal stability of the materials is also improved by the incorporation of SiO_2. The initial degradation temperature is increased by 13–17 °C compared with pure epoxy, and is independent of the amount of SiO_2 added. The plateau in the polymer decomposition was also observed by Bauer et al. [37], and was attributed to char formation where the samples are carbonized. The increased thermal stability of the nanocomposites may be explained by the inorganic nanodomains of SiO_2 acting as a barrier to the decay of the organic components, with higher temperatures needed to break the chemical bonds at the interfaces. A closer observation of the morphology of the SiO_2 remaining after the pyrolysis of the epoxy shows a skeletal SiO_2 network with a shape similar to that of the original sample but slightly smaller in size, suggesting the formation of a continuous inorganic network as the epoxy is burnt off during the degradation.

Another effect of the SiO_2 is the shift in the dielectric relaxation observed around 10^3–10^4 Hz (Fig. 8). This is classified as a β-relaxation, which is attributed to the relaxations caused by O–H groups in the chain [5, 38]. The onset of the relaxation is observed to shift to a higher frequency initially for samples with a low SiO_2 content, or to a lower frequency for samples with a higher SiO_2 content, as shown in Table 3 and in Fig. 11. This behavior mimics the changes observed for the T_g in the opposite pattern, and may be explained with a similar reasoning. The samples with 1 and 2 wt% SiO_2 have polymer-like inorganic chains, where the dipoles in the O–H groups are more free to move and reorient themselves. These dipoles can therefore keep up

with the alternating electric field up to higher frequencies, delaying the dielectric relaxation. However, the inorganic domains are more compact and clustered (with higher fractal dimension) in the samples with higher SiO_2 content, and the dipoles cannot reorient themselves as quickly. The increased rigidity in the nanodomains results in the dielectric relaxation occurring at lower frequencies.

Tanaka et al. proposed that the presence of inorganic nanofillers possessing strong chemical bonds to the polymer matrix would lead to lower relative permittivity and loss factors [15]. However, despite the dispersion of the in situ grown SiO_2 nanodomains, there is no significant influence of the filler content on the permittivity or losses of the materials. Most of the studies reporting a decreased complex permittivity of epoxy nanocomposites have employed spherical nanoparticles that are dispersed. It is therefore possible that the fractal-like network structure of the inorganic nanodomains produced in the present work may be responsible for the absence of any significant changes in the relative permittivity from that of pure epoxy. Thus, it is of interest to vary the parameters of the in situ sol–gel synthesis that are known to affect the reaction kinetics in order to form different nanostructures of the inorganic oxide component.

5 Conclusion

The use of an adapted sol–gel method to synthesize and grow SiO_2 nanoparticles directly in the epoxy matrix is shown to be a successful approach in obtaining a well dispersed inorganic filler phase in the prepared nanocomposites. The nanoparticles were found to consist of cage-like four-membered SiO rings, which may then be arranged in fractal-like clusters (either as inorganic chains or a cross-linked network, depending on the SiO_2 content). The resulting epoxy-SiO_2 nanocomposites have improved thermal stability compared with pure epoxy, while the complex permittivity does not show significant deviation from that of pure epoxy. The presence of SiO_2 as more mobile chains causes a softening effect on the surrounding polymer, resulting in a lower glass transition and a delay in the dielectric relaxation. On the other hand, when the SiO_2 is present as a cross-linked network, it results in an increased rigidity of the surrounding polymer and an associated increase in the glass transition temperature and earlier onset of the dielectric relaxation. These findings show the influence of the inorganic filler morphology and structure on the properties of the final nanocomposite material.

Acknowledgements The authors would like to acknowledge support from the Research Council of Norway through the Norwegian Center for Transmission Electron Microscopy, NORTEM (197405/F50), and the use of the Norwegian national resource centre for X-ray diffraction and scattering (RECX). The authors would also like to thank Prof. Tor Grande for discussions regarding the thermal analysis, Dr Ragnhild Sæterli for her help in performing the TEM measurements, and Dr Matthias Amman for his help in performing the SAXS measurements. This work benefited from the use of the SasView application, originally developed under NSF award DMR-0520547 (http://www.sasview.org). Open Access funding provided by NTNU Norwegian University of Science and Technology (incl St. Olavs Hospital - Trondheim University Hospital).

Funding This study was funded by The Research Council of Norway through the project "Stipendiatstillinger til SINTEF Energi AS" (project no. 259866).

Compliance with ethical standards

Conflict of interest The authors declare that they have no conflict of interest.

References

1. Plesa I, Notingher PV, Schlögl S et al. (2016) Properties of polymer composites used in high-voltage applications. Polymers 8:173
2. Tanaka T, Montanari GC, Mulhaupt R (2004) Polymer nanocomposites as dielectrics and electrical insulation-perspectives for processing technologies, material characterization and future applications. IEEE Trans Dielectr Electr Insul 11:763–784
3. Adnan MM, Tveten EG, Glaum J et al. (2019) Epoxy-based nanocomposites for high-voltage insulation: a review. Adv Electron Mater 5:1800505
4. Singha S, Thomas MJ (2008) Dielectric properties of epoxy nanocomposites. IEEE Trans Dielectr Electr Insul 15:12–23
5. Singha S, Thomas MJ (2008) Permittivity and tan delta characteristics of epoxy nanocomposites in the frequency range of 1 MHz–1 GHz. IEEE Trans Dielectr Electr Insul 15:2–11
6. Nelson JK, Fothergill JC (2004) Internal charge behaviour of nanocomposites. Nanotechnology 15:586–595
7. Goyat MS, Rana S, Halder S, Ghosh PK (2018) Facile fabrication of epoxy-TiO2 nanocomposites: a critical analysis of TiO2 impact on mechanical properties and toughening mechanisms. Ultrason Sonochem 40:861–873
8. Kochetov R, Andritsch T, Morshuis PHF, Smit JJ (2012) Anomalous behaviour of the dielectric spectroscopy response of nanocomposites. IEEE Trans Dielectr Electr Insul 19:107–117
9. Andritsch T, Kochetov R, Morshuis PHF, Smit JJ (2010) Short term DC breakdown and complex permittivity of Al2O3 - and MgO-epoxy nanocomposites. Annu Rep Conf Electr Insul Dielectr Phenom. https://doi.org/10.1109/CEIDP.2010.5723960
10. Mohanty A, Srivastava VK (2013) Dielectric breakdown performance of alumina/epoxy resin nanocomposites under high voltage application. Mater Des 47:711–716
11. Ozsoy I, Demirkol A, Mimaroglu A et al. (2015) The influence of micro- and nano-filler content on the mechanical properties of epoxy composites. Strojniški Vestn 61:601–609

12. Calebrese C, Hui L, Schadler LS, Nelson JK (2011) A review on the importance of nanocomposite processing to enhance electrical insulation. IEEE Trans Dielectr Electr Insul 18:938–945
13. Bell M, Krentz T, Nelson JK et al. (2017) Investigation of dielectric breakdown in silica-epoxy nanocomposites using designed interfaces. J Colloid Interface Sci 495:130–139
14. Caseri WR (2014) In situ synthesis of polymer-embedded nanostructures. In: Nicolais L, Catotenuto G (eds) Nanocomposites: in situ synthesis of polymer-embedded nanostructures. John Wiley and Sons, Hoboken, NJ, USA, p 45–72
15. Tanaka T, Kozako M, Fuse N, Ohki Y (2005) Proposal of a multi-core model for polymer nanocomposite dielectrics. IEEE Trans Dielectr Electr Insul 12:669–681
16. Kurimoto M, Okubo H, Kato K et al. (2010) Permittivity characteristics of epoxy/alumina nanocomposite with high particle dispersibility by combining ultrasonic wave and centrifugal force. IEEE Trans Dielectr Electr Insul 17:1268–1275
17. Zou H, Wu S, Shen J (2008) Polymer/silica nanocomposites: preparation, characterization, properties, and applications. Chem Rev 108:3893–3957
18. Afzal A, Siddiqi HM (2011) A comprehensive study of the bicontinuous epoxy-silica hybrid polymers: I. Synthesis, characterization and glass transition. Polymer 52:1345–1355
19. Judeinstein P, Sanchez C (1996) Hybrid organic-inorganic materials: a land of multidisciplinarity. J Mater Chem 6:511–525
20. Matějka L, Pleštil J, Dušek K (1998) Structure evolution in epoxy–silica hybrids: sol–gel process. J Non Cryst Solids 226:114–121
21. Matějka L, Dušek K, Pleštil J et al. (1999) Formation and structure of the epoxy-silica hybrids. Polymer 40:171–181
22. Nazir T, Afzal A, Siddiqi HM et al. (2010) Thermally and mechanically superior hybrid epoxy-silica polymer films via sol-gel method. Prog Org Coatings 69:100–106
23. Yu W, Fu J, Dong X et al. (2013) Highly populated and nearly monodispersed nanosilica particles in an organic medium and their epoxy nanocomposites. ACS Appl Mater Interfaces 5:8897–8906
24. Beaucage G (1995) Approximations leading to a unified exponential/power-law approach to small-angle scattering. J Appl Crystallogr 28:717–728
25. Smith AL (1960) Infrared spectra-structure correlations for organosilicon compounds. Spectrochim Acta 16:87–105
26. González MG, Cabanelas JC, Baselga J (2012) Applications of FTIR on epoxy resins - identification, monitoring the curing process, phase separation and water uptake. In: Infrared spectroscopy - materials science, engineering and technology. InTech, Rijeka, Croatia, p 261–284
27. Rubio F, Rubio J, Oteo JL (1998) A FT-IR study of the hydrolysis of tetraethylorthosilicate (TEOS). Spectrosc Lett 31:199–219
28. Launer PJ, Arkles B (2013) Infrared analysis of organosilicon compounds: spectra-structure correlations. In: Arkles B, Larson GL (eds) Silicon compounds: silanes and silicones, 3rd edn. Gelest, Inc., Morrisville, PA, p 177–180
29. Arunkumar T, Ramachandran S (2017) Surface coating and characterisation of polyurea for liquid storage. Int J Ambient Energy 38:781–787
30. Perchacz M, Beneš H, Zhigunov A et al. (2016) Differently-catalyzed silica-based precursors as functional additives for the epoxy-based hybrid materials. Polymer 99:434–446
31. Beaucage G (2012) Combined small-angle scattering for characterization of hierarchically structured polymer systems over nano-to-micron meter: part II theory. In: Matyjaszewski K, Möller M (eds) Polymer science: a comprehensive reference, vol 2. Elsevier B.V., Amsterdam, Netherlands, p 399–409
32. Capeletti LB, Baibich IM, Butler IS, Dos Santos JHZ (2014) Infrared and Raman spectroscopic characterization of some organic substituted hybrid silicas. Spectrochim Acta 133:619–625
33. Piscitelli F, Lavorgna M, Buonocore GG et al. (2013) Plasticizing and reinforcing features of siloxane domains in amine-cured epoxy/silica hybrids. Macromol Mater Eng 298:896–909
34. Ponyrko S, Kobera L, Brus J, Matějka L (2013) Epoxy-silica hybrids by nonaqueous sol-gel process. Polymer 54:6271–6282
35. Kuo S-W, Chang F-C (2011) POSS related polymer nanocomposites. Prog Polym Sci 36:1649–1696
36. Ayandele E, Sarkar B, Alexandridis P et al. (2012) Polyhedral oligomeric silsesquioxane (POSS)-containing polymer nanocomposites. Nanomaterials 2:445–475
37. Bauer BJ, Liu DW, Jackson CL, Barnes JD (1996) Epoxy/SiO2 interpenetrating polymer networks. Polym Adv Technol 7:333–339
38. Pochan JM, Gruber RJ, Pochan DF (1981) Dielectric relaxation phenomena in a series of polyhydroxyether copolymers of bisphenol-A—endcapped polyethylene glycol with epichlorohydrin. J Polym Sci Polym Phys Ed 19:143–149

polymers

MDPI

Article

The Structure, Morphology, and Complex Permittivity of Epoxy Nanodielectrics with In Situ Synthesized Surface-Functionalized SiO_2

Mohammed Mostafa Adnan [1], Inger-Emma Nylund [1], Aleksander Jaworski [2], Sverre Hvidsten [3], Marit-Helen Glomm Ese [3], Julia Glaum [1] and Mari-Ann Einarsrud [1,*]

[1] Department of Materials Science and Engineering, NTNU Norwegian University of Science and Technology, 7491 Trondheim, Norway; mohammed.m.adnan@ntnu.no (M.M.A.); inger-emma.nylund@ntnu.no (I.-E.N.); julia.glaum@ntnu.no (J.G.)
[2] Department of Materials and Environmental Chemistry, Stockholm University, 106 91 Stockholm, Sweden; aleksander.jaworski@mmk.su.se
[3] SINTEF Energy Research AS, 7034 Trondheim, Norway; Sverre.Hvidsten@sintef.no (S.H.); marit-helen.ese@sintef.no (M.-H.G.E.)
* Correspondence: mari-ann.einarsrud@ntnu.no; Tel.: +47-48136521

Abstract: Epoxy nanocomposites have demonstrated promising properties for high-voltage insulation applications. An in situ approach to the synthesis of epoxy-SiO_2 nanocomposites was employed, where surface-functionalized SiO_2 (up to 5 wt.%) is synthesized directly in the epoxy. The dispersion of SiO_2 was found to be affected by both the pH and the coupling agent used in the synthesis. Hierarchical clusters of SiO_2 (10-60 nm) formed with free-space lengths of 53–105 nm (increasing with pH or SiO_2 content), exhibiting both mass and surface-fractal structures. Reducing the amount of coupling agent resulted in an increase in the cluster size (~110 nm) and the free-space length (205 nm). At room temperature, nanocomposites prepared at pH 7 exhibited up to a 4% increase in the real relative permittivity with increasing SiO_2 content, whereas those prepared at pH 11 showed up to a 5% decrease with increasing SiO_2 content. Above the glass transition, all the materials exhibited low-frequency dispersion effect resulting in electrode polarization, which was amplified in the nanocomposites. Improvements in the dielectric properties were found to be not only dependent on the state of dispersion, but also the structure and morphology of the inorganic nanoparticles.

Keywords: nanocomposites; electrical insulation; dielectric properties; filler dispersion; in situ synthesis; sol–gel

Citation: Adnan, M.M.; Nylund, I.-E.; Jaworski, A.; Hvidsten, S.; Ese, M.-H.G.; Glaum, J.; Einarsrud, M.-A. The Structure, Morphology, and Complex Permittivity of Epoxy Nanodielectrics with In Situ Synthesized Surface-Functionalized SiO_2 *Polymers* **2021**, *13*, 1469. https://doi.org/10.3390/polym13091469

Academic Editor: Keon-Soo Jang

Received: 7 April 2021
Accepted: 28 April 2021
Published: 1 May 2021

1. Introduction

Nanodielectrics, which are often defined as polymer composites containing filler particles smaller than 100 nm, have attracted interest for applications in high-voltage insulation due to their potentially higher dielectric breakdown strengths and lower complex permittivities, compared to unfilled polymers [1–3]. These benefits have been primarily attributed to the inclusion of nano-sized particles and the subsequent increase in interfacial regions between the organic matrix and inorganic filler [4]. However, the improvements in dielectric properties of nanocomposites is inconsistent across multiple studies [1], which is most likely due to variations in material processing and the resulting dispersion of the incorporated nanoparticles [5]. Dispersion of inorganic nanoparticles in an organic matrix is a challenging aspect of the processing, as the particles tend to agglomerate to reduce the high surface energy. This surface energy can be reduced by improving the

compatibility between the inorganic and organic components, which is usually done using coupling agents, ligands, or other types of surface modifiers [6]. Therefore, understanding the interactions in the interfacial regions is important for explaining the properties of the nanocomposite materials.

Among such materials, epoxy resin-based composites are commonly used in power equipment (cast-resin transformers, rotating machines, switchgear insulators, bushings, terminations, etc.) as high-voltage insulation, as well as other electrical applications, such as printed circuit boards [1,2,7]. Epoxy possesses good chemical resistance, high thermal stability, high tensile strength and toughness [6], making it suitable for such applications where the insulation is subjected not only to electrical stresses, but also thermal and mechanical stress from equipment operations [8].

Dielectric materials require a high dielectric strength as well as low power loss for applications in high-voltage apparatus. Since the power loss is proportional to both the real and imaginary parts (dielectric loss tangent) of the permittivity, the complex permittivity should also be low. Nelson and Fothergill [9] were among the first to demonstrate improvements in the dielectric properties of epoxy with the incorporation of inorganic nanoparticles. Since then, several others have reported similar results with a variety of different nanoparticles. Singha and Thomas presented reduced permittivities in epoxy-TiO_2 nanocomposites. Kochetov et al. [10] demonstrated similar improvements in epoxy nanocomposites containing AlN, MgO, or Al_2O_3. Virtanen et al. [11], Bell et al. [12], and Yeung and Vaughan [13] all reported improved short term dielectric breakdown strengths in epoxy-SiO_2 nanocomposites with various organic surface modifications. However, to the best of our knowledge, most studies investigating the dielectric properties of epoxy-based nanocomposites have used an ex situ processing route, where pre-synthesized nanoparticles (which may be surface-functionalized) are added to the epoxy resin and dispersed by physical methods (high shear mixing, blending, or sonication). Control of the state of dispersion of the nanoparticles, which is believed to be critical to the dielectric properties of the nanocomposites [5], is more difficult in such an approach, which often leads to agglomeration and degradation of the dielectric properties [1,5].

Alternative techniques can be employed in the preparation of the nanocomposites to improve the state of dispersion. In situ sol–gel processes can be applied to synthesize nanoparticles directly in the polymer matrix [14]. The sol–gel method is typically used for the synthesis of inorganic oxides (e.g., SiO_2, TiO_2, Al_2O_3) from the hydrolysis and polycondensation of metal alkoxide precursors [15]. Parameters such as the pH, length of the alkyl chains, solvent, and chelating agents, can be used to adjust the size and morphology of the inorganic network formed by controlling the hydrolysis and condensation reactions. The use of silane coupling agents (SCA) in the sol–gel process can result in the formation of Class II hybrid materials, where strong chemical bonds are present between the inorganic and organic components, resulting in an improved compatibility between the hydrophobic polymer and hydrophilic filler [16].

Matějka et al. [17,18] prepared epoxy-SiO_2 nanocomposites using both one- and two-stage sol–gel processes resulting in branched polysiloxane clusters and aggregated clusters, respectively. The use of both acid- and base-catalysis resulted in different SiO_2 morphologies. Nazir et al. [19] and Afzal et al. [20] adapted the former methods in a two-step chronological sol–gel process with acid catalysis and the incorporation of SCA. The use of SCA led to improved dispersion of the in situ formed SiO_2. Donato et al. [21,22] prepared similar epoxy-SiO_2 nanocomposites, but with the aid of ionic liquids instead of SCA for improving the dispersion further.

Although many such variations of the sol–gel method have been used in several studies to prepare epoxy-SiO_2 nanocomposites, none of them, to the best of our knowledge, have investigated the dielectric properties of the materials prepared in this way. Additionally, very few works have employed the use of quantitative methods for characterizing the state of dispersion, which is a useful tool for limiting subjective interpretations of the degree of dispersion [5]. Various statistical methods, such as the interparticle distance,

quadrat-based particle counting, and free-space length have been proposed, each with their own advantages and disadvantages [5,23].

Therefore, the purpose of this study was to investigate if epoxy nanocomposites fabricated using the in situ route presents reduced permittivity and dielectric loss, compared to nanocomposites fabricated using more conventional ex situ methods as reported in the literature. In the present work, epoxy-SiO_2 nanocomposites were prepared based on a sol–gel route described in our previous study [24], using different synthesis conditions (pH, SCA amount, and type). The morphology and structure of the inorganic network and the resulting complex permittivity of the nanocomposites were characterized. Additionally, the state of dispersion was quantitatively described by applying the free-space length method. An important aspect of the work is to increase the understanding of the structure-property relations in these materials. This will allow one to tune the properties as required, such as decreasing the dielectric loss or real permittivity, or increasing the dielectric strength for high-voltage insulation materials, by tailoring the structure via alteration of the synthesis conditions.

2. Materials and Methods

The epoxy resin was prepared using diglycidyl ether of bisphenol-A (DGEBA) as the epoxy monomer and poly(propylene glycol) bis(2-aminopropyl ether) as the curing agent. Tetraethyl orthosilicate (TEOS) was used as the precursor for the SiO_2 in the sol–gel reaction. 3-(aminopropyl) triethoxysilane (APTES) and 3-(glycidyloxypropyl) trimethoxysilane (GPTMS) were the silane coupling agents used to create the interfacial link between the in situ formed SiO_2 nanoparticles and the epoxy chains. Ammonia solution (35%) and HCl (36%) was used to alter the pH of the distilled water used for the hydrolysis and condensation of tetraethyl orthosilicate. All chemicals had a purity of >98% and were obtained from Merck Life Science AS, Oslo, Norway.

Pure epoxy samples were prepared by mixing stoichiometric amounts of DGEBA and the curing agent in a PET beaker at room temperature. This was performed under vacuum to remove all the air bubbles present in the mixture. The resin mixture was injected into a stainless-steel mold (for disc-shaped samples with 1 mm thickness and 40 mm diameter) under vacuum. The mold was placed in a pressure chamber at 100 °C for 5 h with 10 bars of N_2 pressurization to collapse any remaining air bubbles. Leftover resin was casted in Teflon cups without pressurization to prepare bulk samples (over 5 mm in thickness).

The composites were prepared using the procedure outlined in our previous work [24] and is illustrated in Scheme 1. DGEBA was heated to 80 °C in a round bottom flask mounted with a reflux condenser. The silane coupling agent, either APTES or GPTMS, was mixed with the DGEBA for 1 h (at 80 °C) using a magnetic stirrer (mass ratio of SCA:DGEBA was equal to either 1:10 or 1:30), followed by mixing the required amount of TEOS for 1 h (60 °C). Distilled water was then added to initiate the TEOS hydrolysis, and the mixture was stirred for a further 4 h at 60 °C, then 1 h at 80 °C. Composites were prepared using water with pH 2, pH 7 (neutral) and pH 11. Afterwards, the reaction mixture was poured into a beaker and stirred overnight (15–18 h) at 80 °C to remove alcohol byproducts. Finally, the curing agent was added to the mixture and the samples were casted using the aforementioned procedure. Table 1 shows an overview of the compositions of the various samples investigated.

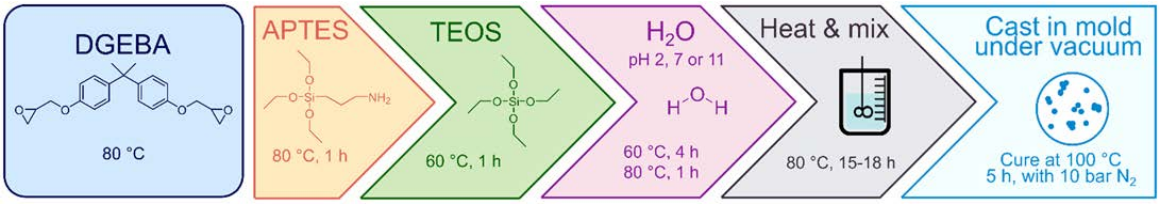

Scheme 1. An outline of the sol–gel procedure used in the in situ synthesis of SiO_2 functionalized with APTES in epoxy.

Table 1. Compositions of the epoxy-SiO_2 nanocomposites prepared via the in situ sol–gel method

Filler content	pH	SCA:DGEBA mass ratio	SCA
1–5 wt%	2 [1]	1:10	APTES
1, 2, 3, and 5 wt%	7		
1,2 and 5 wt%	11		
5 wt%	11	1:30	
2, 3, 4, and 5 wt%	2	1:10	GPTMS

[1] Prepared previously in [24].

Fourier transform infrared (FTIR) spectroscopy was performed using a Bruker Vertex 80v spectrophotometer with an attenuated total reflectance (ATR) diamond cell (Bruker Corporation, Billerica, Massachusetts, USA). Each sample was scanned 32 times at a resolution of 1 cm^{-1}. Small angle X-ray scattering (SAXS) measurements were performed with a Bruker NanoSTAR instrument with a Cu micro-source (Bruker Corporation, Billerica, Massachusetts, USA), operating at 50 kV and 600 μA (scattering vector (q) range of 0.009–0.3 $Å^{-1}$). The data from the SAXS was analyzed using software SasView 5.0.1 (http://www.sasview.org), and fitted to the unified exponential/power-law model [25]. The Porod exponents, also known as fractal dimension (D), for each structural level in the model were obtained from the slopes of the linear regions after each feature. From the fits, the radii of gyration (R_g) for each structural level were obtained, from which the inorganic domain size was calculated (assuming spherical domains), using:

$$2\sqrt{5/3}(R_g). \quad (1)$$

The correlation length (ζ) between inorganic structures or domains was estimated using [26]:

$$\zeta = \frac{2\pi}{q}, \quad (2)$$

where q is the scattering vector for the peak or feature.

Transmission electron microscopy (TEM) was performed using a JEOL JEM 2100F (JEOL Ltd., Tokyo, Japan), at 200 kV accelerating voltage, on 50–100 nm slices of the samples cut using an ultramicrotome. Energy-dispersive X-ray spectroscopy (EDS) was performed using an Oxford X-Max 80 SDD detector (Oxford Instruments, Abingdon, UK) attached to the TEM instrument. Particle cluster sizes were determined visually from the TEM images. The quantitative analysis of the dispersion of the nanoparticles was performed using MATLAB 202a (Mathworks, Portola Valley, CA, USA) and the code and methodology provided by Khare and Burris [23]. The TEM images were processed into the binary images required for the analysis using ImageJ 1.52a.

A Netzsch DSC 214 Polyma (NETZSCH-Gerätebau GmbH, Selb, Germany) was used to perform differential scanning calorimetry (DSC) between 0 and 200 °C in N_2 atmosphere (4 cycles, 10 °C/min heating and cooling rates, 40 mL/min gas flow). The glass transition temperature (T_g) was obtained from the local maxima during the increase in the heat capacity.

$^{1}H \rightarrow ^{29}Si$ cross-polarization magic-angle spinning (CPMAS) NMR spectra were collected on a Bruker Avance-III NMR spectrometer (Bruker Corporation, Billerica, MA, USA) at a magnetic field strength of 14.1 T (Larmor frequencies of 600.1 and 119.2 MHz for ^{1}H and ^{29}Si, respectively) using 7.0 mm zirconia rotors at a MAS rate of 5.00 kHz. Acquisitions involved proton 90° excitation pulse of 4 μs and matched spin-lock fields of ν_H = 60 kHz and ν_C = 40 kHz. Contact time of 5 ms was used and SPINAL-64 proton decoupling at 60 kHz. Between 16384 and 28672 signal transients with 4 s relaxation delays were collected per sample. Chemical shifts were referenced with respect to neat tetramethylsilane (TMS). Peak deconvolution was performed using Origin 2018b (OriginLab Corporation, Northhampton, MA, USA), and the degrees of condensation for Q and T species were calculated from the peak areas using **(3)** and **(4)**, respectively:

$$[\alpha_{Si}]_Q = \frac{\sum iQ_i}{4}, \quad (3)$$

$$[\alpha_{Si}]_T = \frac{\sum iT_i}{3}. \quad (4)$$

Broadband dielectric spectroscopy was conducted using a Novocontrol Spectrometer with an Alpha Beta dielectric analyzer (Montabaur, Germany). A BDS1200 sample cell with 1 V/mm electric field was used to measure the samples' dielectric response between 10^{-2} and 10^{6} Hz over 5 °C intervals from 25 to 120 °C, and 20 °C intervals from 140 to 200 °C.

3. Results

3.1. Dispersion and Morphology of the In Situ Synthesized Nanoparticles

The primary motivation for the use of the in situ approach in the synthesis of the nanocomposites was to ensure that the nanoparticles formed were well dispersed with limited agglomeration. The composites prepared with APTES as the SCA were transparent for the composites casted both with and without N_2 pressurization, as shown in Figure 1, indicating high degree of dispersion.

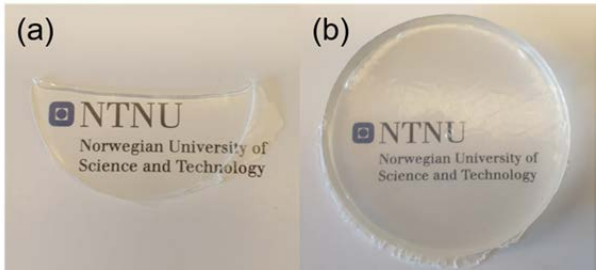

Figure 1. Representative images of transparent epoxy-SiO_2 nanocomposites (5 wt.% SiO_2 with APTES at pH 11) after casting. (a) A 1 mm thick sample casted under N_2 pressurization. (b) A thick sample (> 5 mm) casted without N_2 pressurization.

The scarcity of SiO_2 agglomerates, defined in this work as particle clusters larger than 100 nm, was confirmed by TEM. Figure 2 shows representative bright field TEM and high-angle annular dark field scanning TEM (HAADF-STEM) images of the nanocomposites (all with 5 wt.% SiO_2) prepared with APTES at pH 7 and 11, and with GPTMS at pH 2. The SiO_2 particles form randomly dispersed clusters. For the composites prepared at pH 11 several large agglomerates (100–150 nm) consisting of multiple smaller particles (Figure 2c) were formed, compared to composites prepared using pH 2 and 7 where fewer or almost no such agglomerates were present. HAADF-STEM was used to image the smaller clusters in the nanocomposites as it provided better contrast (Figure 2a) and was also used

to verify that the particle composition was SiO_2 using energy-dispersive X-ray spectroscopy (EDS, see Figure S1). The samples prepared with GPTMS, however, showed poor dispersion of the SiO_2, forming agglomerates in the micron range as shown in Figure 2d.

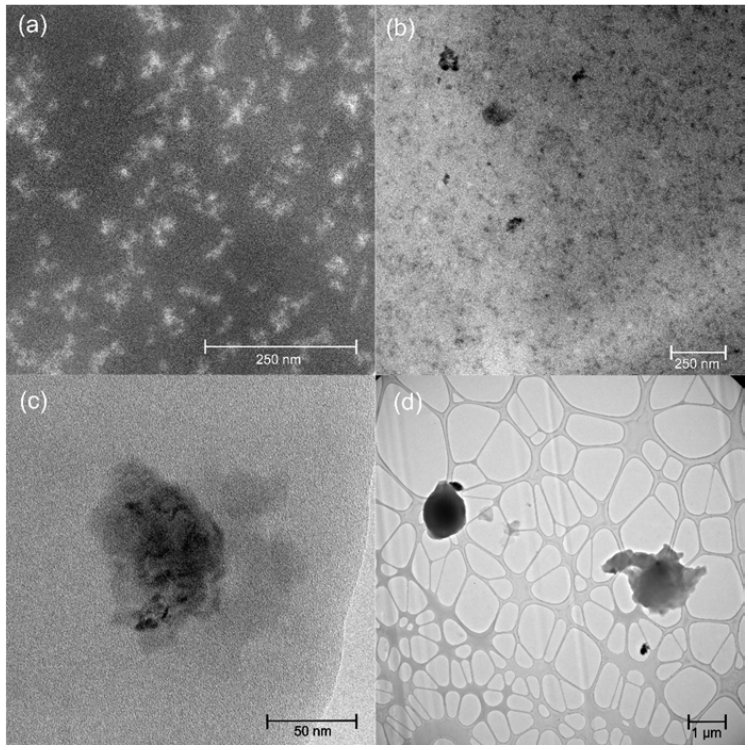

Figure 2. (a) Representative HAADF-STEM image of epoxy nanocomposite (5 wt.% SiO_2) prepared using pH 7 and APTES. **(b)** Representative TEM image of epoxy nanocomposite (5 wt.% SiO_2) prepared using pH 11 and APTES. **(c)** A single SiO_2 agglomerate consisting of smaller particles in the composite prepared at pH 11 (5 wt.% SiO_2). **(d)** Epoxy nanocomposite (5 wt.% SiO_2) prepared using GPTMS, exhibiting large SiO_2 agglomerates.

Figure 3 shows the changes in free-space length (L_f) with variations in filler content and pH during synthesis. The calculation of L_f from the TEM images is described in the supplementary material (Figures S1 and S2, and Table S1). An increase in pH (for a given filler and SCA content) resulted in an increase in L_f. An increase in the filler content also had the same effect. The cluster sizes were affected by the changes in pH and filler content as well. At pH 2, the clusters increased in average size with the increasing amount of SiO_2. At pH 11, increasing amount of SiO_2 led to a partly bimodal distribution of particle clusters, which were smaller on average than at lower SiO_2 contents, and agglomerates of 100–150 nm, which were not as frequent or completely absent at lower SiO_2 contents. A reduction in the amount of SCA, however, resulted in the most noticeable difference in the dispersion quality, with a doubling in the cluster sizes as well as the L_f.

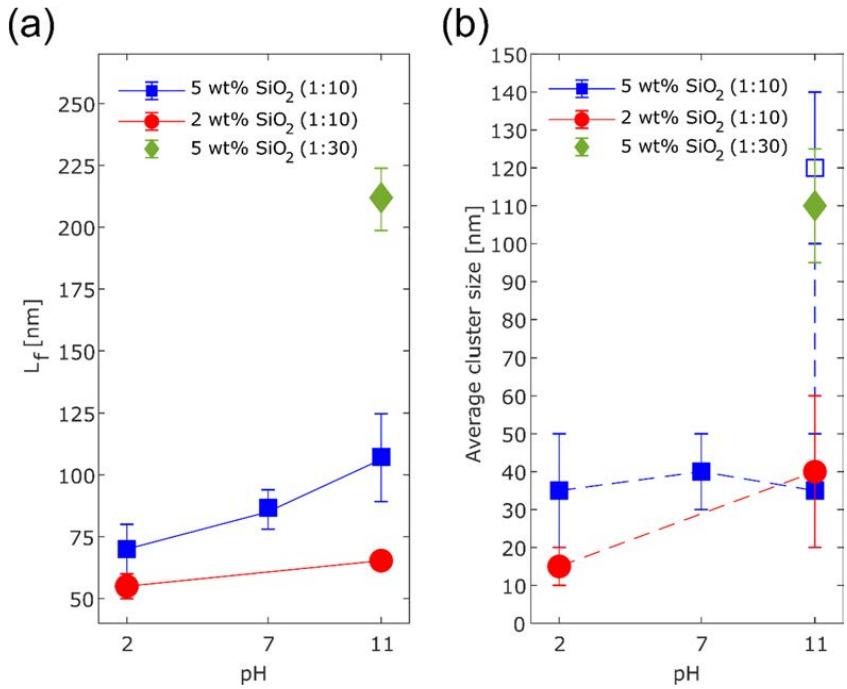

Figure 3. Changes in the dispersion quality with variations in pH, filler content, and amount of SCA (shown as the ratio of APTES:DGEBA in parentheses in the legend) used in the synthesis. The **(a)** L_f and **(b)** average cluster sizes are shown for composites prepared with 2 and 5 wt.% SiO_2 (● and ■ respectively) and 1:10 of APTES:DGEBA at different pH. The ◆ indicates the composite prepared at pH 11 with 1:30 APTES:DGEBA and 5 wt.% SiO_2. In **(b)**, the □ indicates the average size of the agglomerates observed in the composite with 5 wt.% SiO_2 (1:10 APTES:DGEBA, pH 11).

The SAXS profiles of the nanocomposites prepared at pH 7 and 11 presented in Figure 4 show increased scattering from the epoxy-SiO_2 nanocomposites compared to pure epoxy. The emergence of broad features (often referred to as Guinier knees) in the scattering profile are indicated by the arrows. These knee-like features become more prominent with increasing SiO_2 content and appear in the q range 0.07–0.24 $Å^{-1}$ and 0.01–0.03 $Å^{-1}$ for samples with 2 and 5 wt.% SiO_2 at pH 7. For the sample with 1 wt.% SiO_2 at pH 7, it appears that only one broad feature is present between 0.024 and 0.15 $Å^{-1}$. For the nanocomposites prepared at pH 11, those with 1 and 2 wt.% of SiO_2 also show a single broad feature between 0.02 and 0.15 $Å^{-1}$, and the "peak" for the feature at low q for the 5 wt.% SiO_2 is below the measured q range (< 0.009 $Å^{-1}$). The 5 wt.% SiO_2 sample prepared with reduced APTES (1:30 of APTES:DGEBA) at pH 11 does not exhibit the second feature at higher q, and a more linear region of scattering is observed. In all nanocomposites, the scattering appears to increase further at q lower than the measured range.

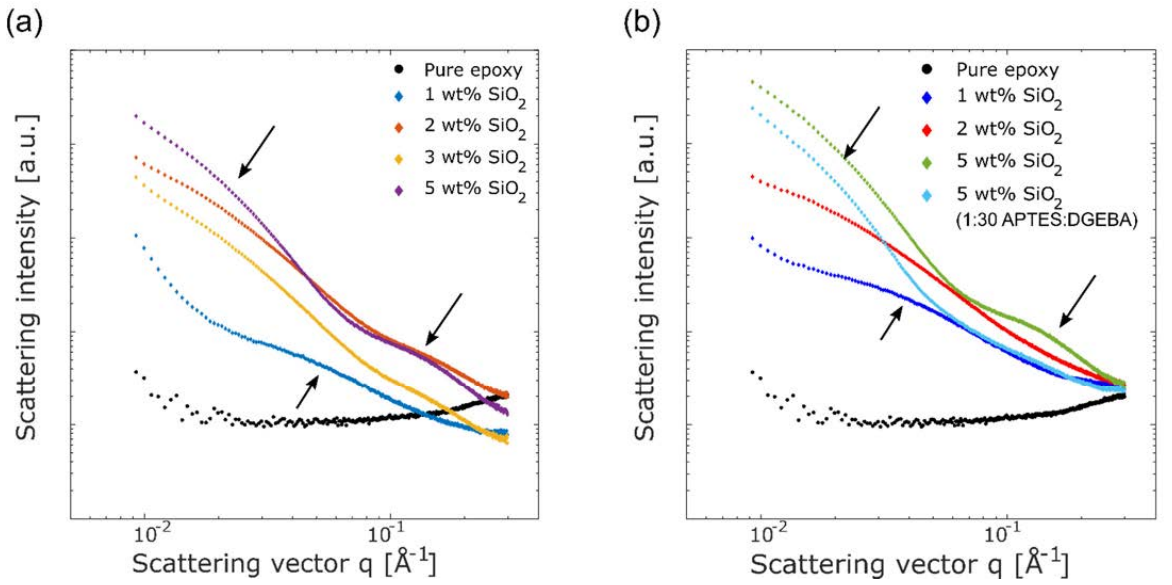

Figure 4. SAXS profiles for pure epoxy and epoxy-SiO_2 nanocomposites with APTES synthesized with **(a)** pH 7 and **(b)** pH 11. The sample prepared with an APTES:DGEBA ratio of 1:30 at pH 11 is also included in **(b)**. The features in the scattering pattern for the nanocomposites (shown by the arrows) indicate a hierarchical structure in the SiO_2.

The presence of multiple features indicates a hierarchical structure of the SiO_2, which is described by the unified exponential/power-law model by Beaucage [25]. The model describes complex morphology over wide q ranges using structural levels—a structural level in scattering is reflected by a knee and a linear region on a log-log plot of scattering, representing Guinier's law and a structurally limited power law, respectively [27]. A fit of this model with two structural levels was applied to the data where two broad features were observed. Table 2 shows the fractal dimension (D) (measured from the slopes of the linear regions after each feature) and the calculated radii of gyration (R_g) and structure sizes (d) for the inorganic domains (obtained from the fits to the unified exponential/power-law model). The sizes of the SiO_2 domains in the second structural level increased with increasing SiO_2 content for nanocomposites prepared at pH 7. At the primary level, the changes were inconsistent. A similar comparison could not be made for the samples prepared at pH 11, since no suitable fits were obtained for the nanocomposites with 1 and 2 wt.% SiO_2 at pH 11.

Table 2. Structural parameters (radius of gyration R_g) obtained from fitting the SAXS data to the unified exponential/power-law model with two structural levels. The inorganic domain size d was calculated using Equation 4. The fractal dimension D was measured from the linear slopes of the plots in Figure 4.

Sample		Structural level	D	R_g (nm)	d (nm)
pH	Filler Content (wt.%)				
7	1 [1]	1	1.3	-	-
	2	1	1.5	3.3 ± 0.1	8.5
		2	2.2	11.6 ± 0.9	30.0
	3	1	1.6	4.1 ± 0.4	10.6
		2	2.4	12.1 ± 1.0	31.2
	5	1	1.9	3.3 ± 0.1	8.5
		2	3.1	13.3 ± 1.7	34.3

11	1 [1]	1	1.5	-	-
	2 [1]	1	2	-	-
	5	1	1.9	3.3 ± 0.1	8.5
		2	3.3	14.7 ± 1.8	38.0
	5 [1,2]	1	1.2	-	-
		2	3.5	-	-

[1] No suitable fit was obtained with the unified model. [2] Reduced amount of APTES (APTES:DGEBA = 1:30).

The fractal dimension, which describes the power-law dependence of the scattering intensity [28], increased in all the samples with increasing SiO_2 content at both the primary and secondary structural levels. At the primary level, $1 < D < 2$, indicating a mass-fractal structure—in other words, the SiO_2 clusters (8–10 nm) consist of coiled polymeric chains (with Si-O-Si links). At the secondary level, $D > 2$ for all samples, and increased with increasing SiO_2 content. In nanocomposites containing 5 wt.% SiO_2, $3 < D < 4$. This indicates the formation of increasingly interconnected polymer chains forming a clustered network, and eventually the formation of particles with a rough surface (a surface-fractal structure).

3.2. Structure of the Inorganic Components

FTIR and ^{29}Si solid-state NMR provided further information on the bonds formed in the nanocomposites. Figure 5 shows the IR spectra of pure epoxy and the epoxy-SiO_2 nanocomposite with 5 wt.% SiO_2 (pH 7), both normalized for the band at 1500 cm^{-1} (not shown in the figure). The features specific for the nanocomposite spectrum are the presence of the O-Si-O rocking band around 450 cm^{-1}, the band at 940–970 cm^{-1} for the ethyl (-C_2H_5) groups from unreacted precursors and coupling agents, and a broader band at 1080–1100 cm^{-1} assigned to the Si-O-Si and Si-O-C stretching [29]. A more detailed description of the progress of the in situ sol–gel reactions and formation of the inorganic domains is provided in our previous work [24].

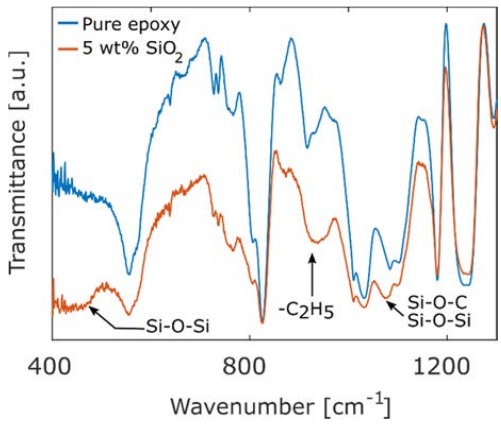

Figure 5. FTIR spectra of pure epoxy and epoxy-SiO_2 nanocomposite with 5 wt.% SiO_2 at pH 7. The relevant differences in the spectra are marked.

^{29}Si NMR was used to ascertain the degree of condensation of the Si-O network. Figure 6 shows the NMR spectra of the nanocomposites prepared at different pH and using different SCAs, along with the deconvolution of the peaks. Each peak corresponds to either a T^x or Q^y signal ($0 \le x \le 3$ and $0 \le y \le 4$), where x and y indicate the number of alkyl or -OH groups that have been replaced by an -O-Si bond on a central Si atom in the SCA or TEOS, respectively. The Q^3 and Q^4 signals are prominent, while the Q^0, Q^1, and Q^2 signals are much weaker. For the APTES, the T^0 peak is the most prominent, with weaker T^1

and T^3 peaks. For the nanocomposite containing GPTMS, however, the NMR spectra shows stronger T^2 and T^3 peaks and a weaker T^0 peak, accompanied with the presence of Q^1, Q^3, and Q^4 peaks. The degree of condensation of Q and T species, $[\alpha_{Si}]_Q$ and $[\alpha_{Si}]_T$, were calculated to be 0.77 and 0.17, respectively, for nanocomposites prepared with APTES. For the nanocomposites prepared with GPTMS, $[\alpha_{Si}]_Q$ and $[\alpha_{Si}]_T$ were calculated to be 0.77 and 0.59, respectively. The fractions of the structural units Q_i and T_i were obtained from the area under the peaks. No significant differences were observed between samples prepared at different pH (for a given SCA).

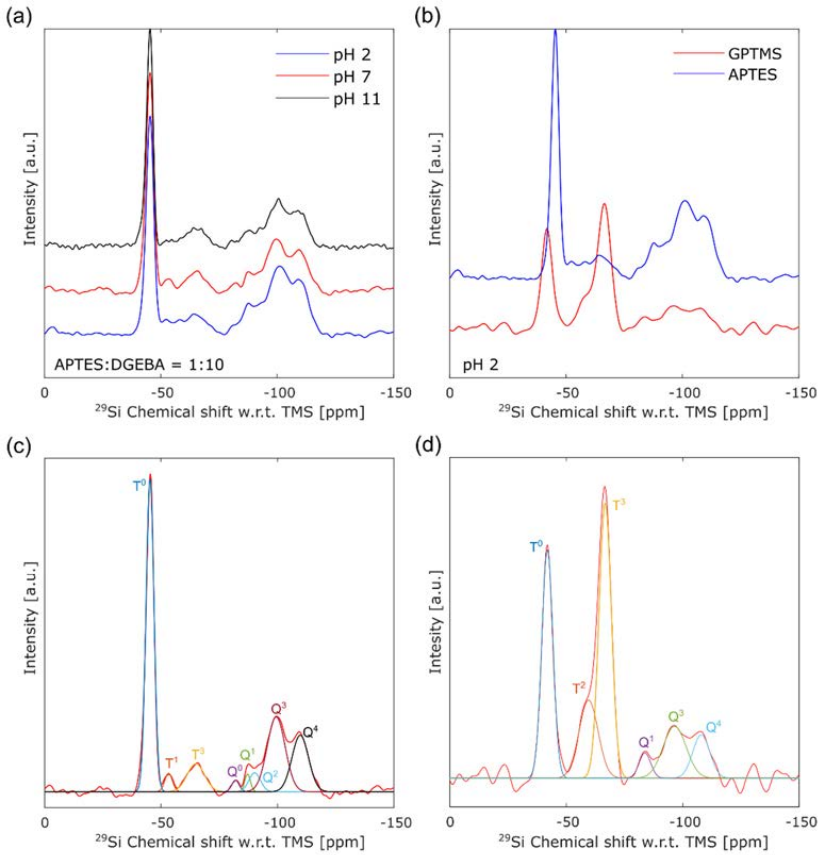

Figure 6. ^{29}Si NMR (CP-MAS) spectra of epoxy-SiO_2 nanocomposites. **(a)** Nanocomposites prepared with APTES (APTES:DGEBA = 1:10) at different pH. **(b)** Comparison of nanocomposites prepared with APTES and with GPTMS (both at pH 2). **(c)** Deconvolution of the peaks in the spectra for nanocomposites prepared with APTES. **(d)** Deconvolution of the peaks for nanocomposites prepared with GPTMS.

Figure 7 displays the glass transition temperatures (T_g) for the various nanocomposites compared to epoxy. In the composites prepared with APTES, the initial addition of SiO_2 resulted in a decrease in T_g from that of pure epoxy (83 °C). In the composites prepared at pH 2, T_g continues to decrease until the SiO_2 content is above 2 wt.%, after which T_g increases again with further increases in SiO_2 content. In the composites prepared at pH 7, the drop in T_g is much more drastic at 1 wt.% SiO_2, but it again increases rapidly with increasing SiO_2 content, and exceeds the T_g of pure epoxy. The changes in T_g for the composites prepared at pH 11 are comparatively less drastic, and even at 5 wt.% SiO_2 the T_g is less than that of pure epoxy. However, the sample with 5 wt.% SiO_2 prepared with

less APTES (APTES:DGEBA of 1:30) exhibited quite a high T_g (93 °C). The nanocomposites prepared with GPTMS on the other hand show the opposite behavior, and T_g is seen to increase steadily with SiO_2 content and exhibits the highest T_g of all the composites (up to 95 °C).

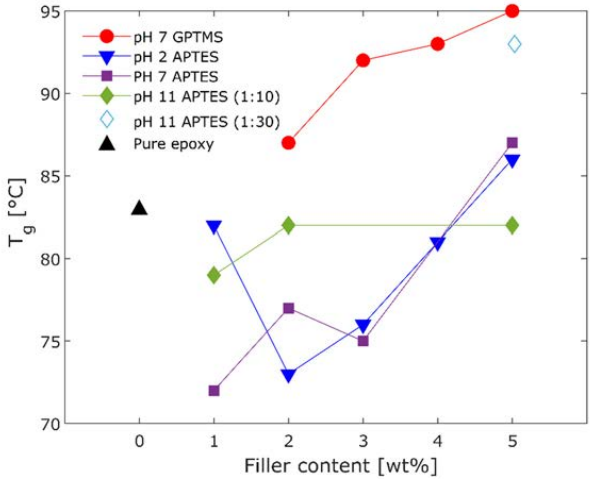

Figure 7. Changes in the glass transition for the epoxy-SiO_2 nanocomposites with varying filler content prepared using APTES (with APTES:DGEBA of 1:10 and 1:30) and GPTMS with different pH conditions, compared to that of pure epoxy (0 wt.% filler content). The error in the measurements is ±2 °C. The data for the pH 2 APTES samples were taken from [24].

3.3. Complex Permittivity of the Nanocomposites

The room temperature complex permittivities of pure epoxy and the in situ nanocomposites prepared with APTES are shown in Figure 8. The real part of the relative permittivity exhibited a small increase with increasing SiO_2 content for the nanocomposites prepared at pH 7. On the contrary, for the nanocomposites prepared at pH 11, the permittivity decreased with increasing SiO_2 content. Additionally, the sample with 5 wt.% SiO_2 prepared at pH 11 and with a lower amount of APTES (APTES:DGEBA = 1:30) exhibited the lowest real relative permittivity.

The dielectric loss tangent (tan δ) for pure epoxy displays a peak at $1 \cdot 10^5$–$2 \cdot 10^5$ Hz, which is henceforth called the β-relaxation peak. The nanocomposites exhibit small differences in the loss tangent, with the most noticeable being the emergence of a new feature with a much smaller peak height, between 1 and 10^3 Hz (indicated by the left arrow in the inset in Figure 8b). Another feature is observed at frequencies above the β-relaxation peak (10^5–10^6 Hz), and the β-relaxation appears as a shoulder on this new relaxation, which has its peak beyond the measurement range. The nanocomposites show small increases in the dielectric loss with increasing SiO_2 content for the new relaxation at 1–10^3 Hz. Near the β-relaxation peak, the dielectric loss is decreased for nanocomposites at frequencies below 10^5 Hz, but at higher frequencies the dielectric loss increased (due to the new relaxation that had emerged). An exception to this behavior was observed in nanocomposites prepared at pH 11, where the dielectric loss at high frequencies decreased significantly compared to pure epoxy (as indicated by the right arrow in the inset in Figure 8b), especially for higher SiO_2 contents. The peak for tan δ is lower, but it remains a shoulder on the new relaxation.

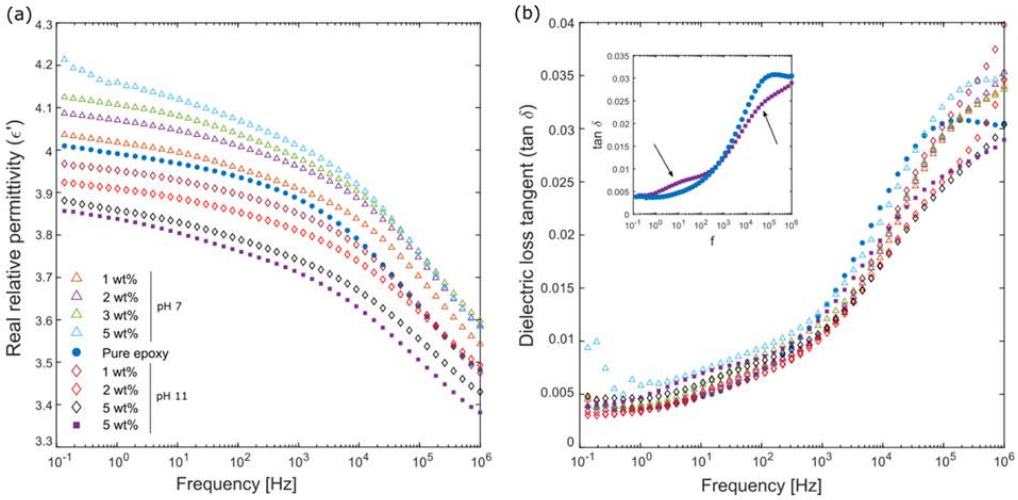

Figure 8. The complex permittivity of pure epoxy and epoxy nanocomposites with varying amounts of SiO_2 at room temperature. △ indicates samples prepared with pH 7 and ◇ indicates samples prepared with pH 11 (both with 1:10 of APTES:DGEBA), while ■ indicates the sample prepared with pH 11 and 1:30 of APTES:DGEBA. **(a)** The real relative permittivity (ε′). **(b)** The dielectric loss tangent (tan δ). The inset in **(b)** shows the same data for pure epoxy and epoxy-SiO_2 nanocomposite, with the arrows highlighting the different features in tan δ. The legend in **(a)** is common for both figures.

Figure 9 displays the real relative permittivities (ε′) of pure epoxy and selected nanocomposites from 25 to 200 °C, and Figure 10 shows the corresponding imaginary permittivities (ε′′) over the same temperature range. As the temperature is increased, the permittivity increased and the β-relaxation around 10^5 Hz shifted to higher frequencies for all the samples. This is observed more clearly from the peak positions in the imaginary permittivity. As the glass transition was approached (between 60 and 90 °C), a new relaxation shifted into the measurement range at low frequencies. This occurred at lower temperatures for the nanocomposites (60 °C) than for the pure epoxy (80 °C). Additionally, this relaxation was observed at higher frequencies as the temperature increased, which is similar to the behavior shown by the β-relaxation. Beyond T_g, the permittivity increased exponentially at low frequencies to very high values. For the nanocomposites, this development is more severe than for the pure epoxy, starting at lower temperatures and reaching higher values (above 10^3). At low frequencies and high temperatures, ε′′ becomes linear with a slope between -0.9 and -1. This linear region extends to higher frequencies as the temperature is increased further. Above 140 °C the slope of ε′ was approximately -1.

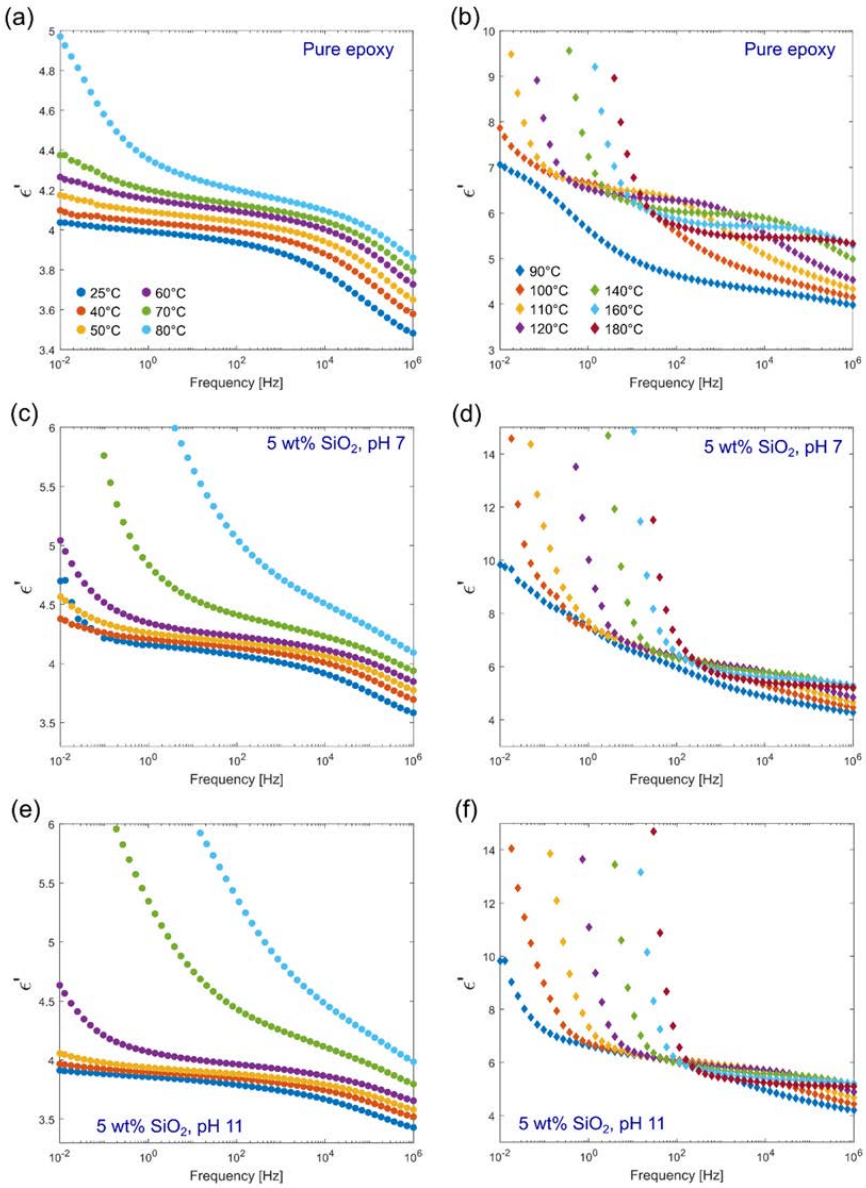

Figure 9. The real relative permittivities (ε′) for **(a,b)** pure epoxy, and epoxy nanocomposites prepared with 5 wt.% SiO_2 at **(c,d)** pH 7, and **(e,f)** pH 11. The plots on the left **(a,c,e)** show the permittivities below 80 °C, while the plots on the right **(b,d,f)** show the permittivities above 80 °C.

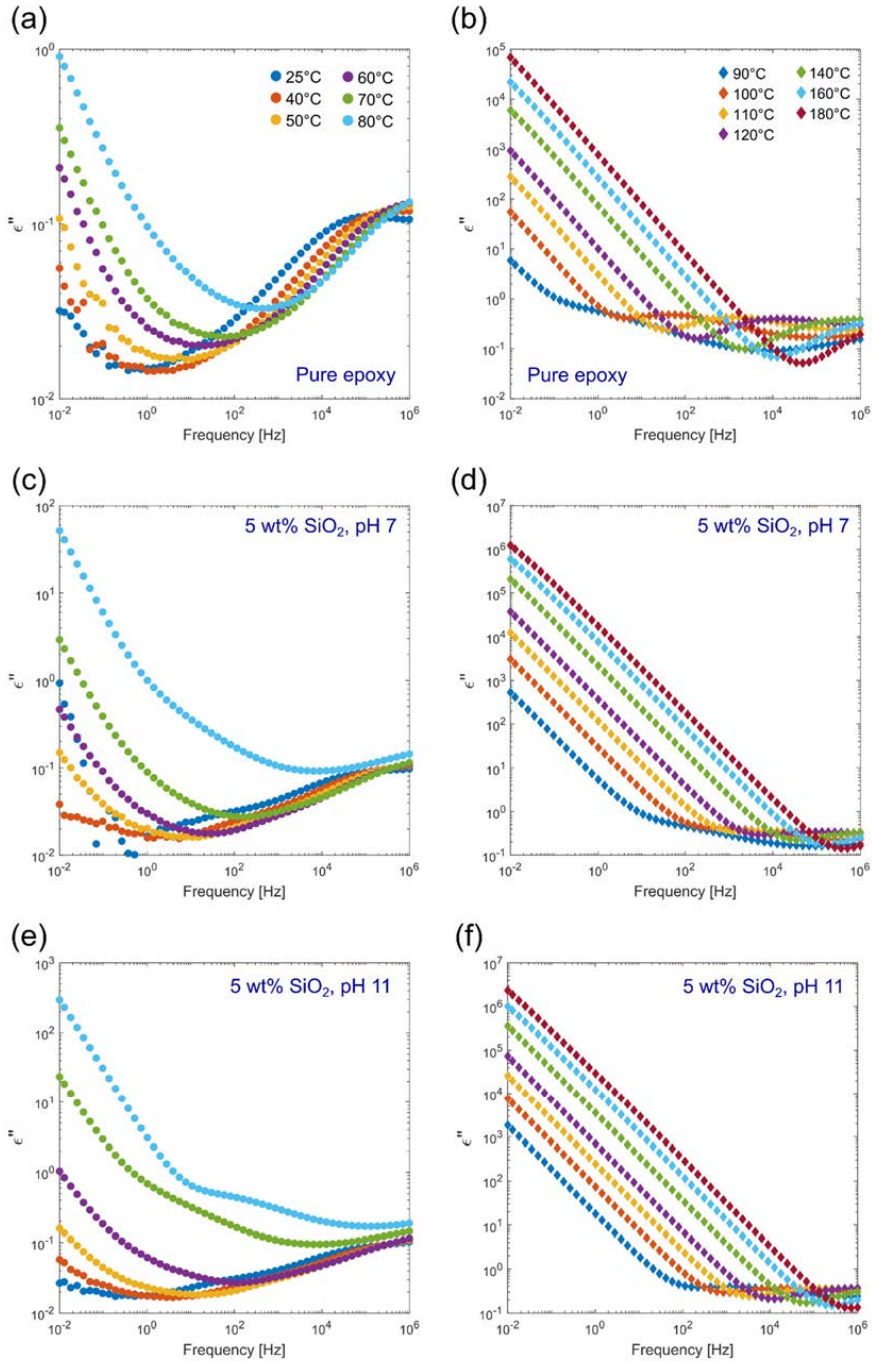

Figure 10. The imaginary permittivities (ε′′) for **(a,b)** pure epoxy, and epoxy nanocomposites prepared with 5 wt.% SiO_2 at **(c,d)** pH 7, and **(e,f)** pH 11. The plots on the left **(a,c,e)** show the permittivities below 80 °C, while the plots on the right **(b,d,f)** show the permittivities above 80 °C.

4. Discussion

4.1. The Effect of the SCA on the State of Dispersion

The reaction mechanisms for the formation of SiO_2 are different when APTES or GPTMS is used as the SCA. This can be attributed to the structures of the SCAs and how they interact with the DGEBA, as shown schematically in Figure 11. APTES contains a -NH_2 group, which is capable of bonding directly with DGEBA and forming cross-links [24]. GPTMS on the other hand contains epoxide groups, and, therefore, cannot bond with DGEBA directly. The connections to the epoxy chains are formed after the addition of the curing agent, which also contains -NH_2 groups that form the cross-links between DGEBA as well as between DGEPA and GPTMS. Therefore, in the synthesis procedure followed in this work, APTES can immediately link with the DGEBA monomers when it is initially mixed, attaching to the ends of various DGEBA chains and forming multiple sites for the SiO_2 to anchor to. GPTMS is unable to do this, as the curing agent is not added until the final stage of the synthesis.

The T^0 signal from the NMR spectra (Figure 6) is observed at a chemical shift of -45 instead of the expected -40 to -43 [30,31]. Hoebbel et al. [30] reported that the T^0 chemical shift becomes larger (more negative) with fewer -OH and more -OC_2H_5 groups attached to the Si in the SCA, thus indicating that some of the APTES is not completely hydrolyzed. This is also verified by the presence of Si-O-C_2H_5 groups as shown in the FTIR spectrum (Figure 5). It is, therefore, likely that APTES shows less self-condensation due to the anchoring to the DGEBA first. Piscitelli et al. [31,32] reported fully condensed GPTMS and SiO_2 (from TEOS) when prepared using a similar aqueous sol–gel method at pH 6 and the use of a condensation catalyst (dibutyltindilaurate). The use of such a condensation catalyst may help in ensuring that all the SiO_2 formed is connected to the APTES as it will be fully condensed, but also increases the chance of self-condensation of APTES. From the TEM images (Figure 2), it is seen that in all the samples prepared with APTES the SiO_2 is randomly distributed in well-dispersed nanoparticle clusters, with only some agglomeration at pH 11. A reduction in the amount of APTES by a third affects the dispersion quality noticeably, resulting in doubling the average cluster size and free-space length (L_f) (Figure 3). Figure 12 shows the differences in the state of dispersion when the mass ratio of APTES:DGEBA is changed (from 1:10 to 1:30). More discrete particle clusters with a larger average distance between the clusters (larger L_f of approximately 205 nm) form with a reduced amount of APTES. With fewer APTES molecules and fewer binding spots to the DGEBA chains, the SiO_2 subsequently forms structures that are larger, but fewer in number (in contrast to the multitude of smaller structures) and spread much further apart.

With GPTMS, however, the SCA self-condensates alongside TEOS, as observed from the higher degree of condensation $[\alpha_{Si}]_T$ for the T species in GPTMS (Figure 6b). Due to this and the inability of GPTMS to anchor to the DGEBA chains without the curing agent, the samples prepared with GPTMS form large agglomerates of SiO_2 over 1 μm (Figure 2d).

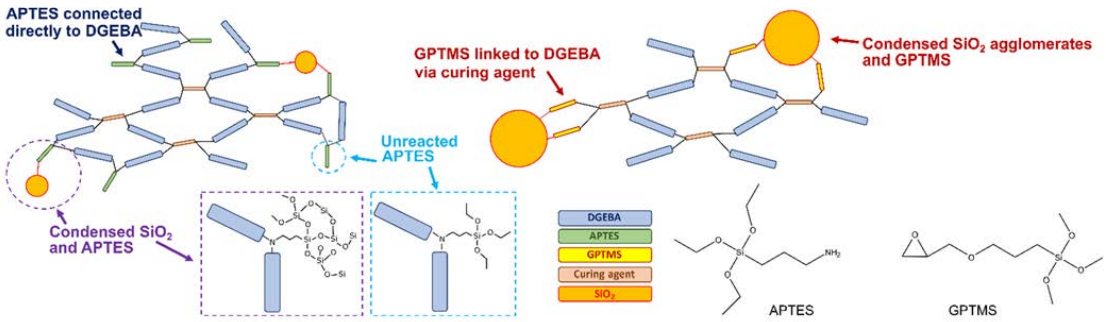

Figure 11. Schematic showing the structure of the two SCAs used and how they form a chemical link between the inorganic and organic components in the nanocomposites.

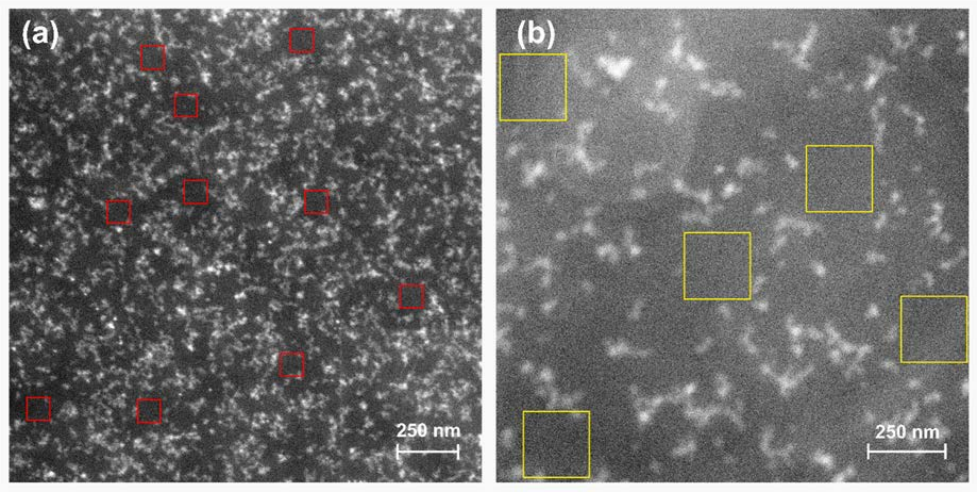

Figure 12. Comparison of the state of dispersion and morphology between SiO_2 prepared at pH 11 with an APTES:DGEBA ratio of **(a)** 1:10 and **(b)** 1:30, both at filler load of 5 wt.%. The red and yellow boxes visualize the size of the free-space lengths (L_f) in each composition (~ 105 and 205 nm, respectively).

Pre-synthesized SiO_2 nanoparticles, typically spherical or with a defined particle shape, have been found to be difficult to disperse in epoxy in traditional ex situ methods of preparation [1]. The in situ approach used in this work can consistently prepare nanocomposites with a homogeneous dispersion of the SiO_2 formed when APTES is used as the coupling agent, and the dispersion can be controlled by the synthesis parameters, as seen from the consistent changes in L_f with pH, filler content, and amount of APTES. However, unlike the pre-synthesized nanoparticles, the structures formed by SiO_2 in this in situ sol–gel route show greater variance, with the formation of an inorganic network instead of discretely shaped particles.

4.2. The Structure of the In Situ Synthesized SiO_2

The morphology and organization of the SiO_2 structures formed in the epoxy is quite different from when ex situ nanocomposites are prepared. From the SAXS measurements (Figure 4) it is seen that at higher SiO_2 contents, the SiO_2 domains have formed two structural levels in a hierarchical organization: the first level consisting of clusters consisting of polymeric chains of Si-O-Si links, formed from the hydrolysis of TEOS, exhibiting a mass-fractal structure; the second structural level consists of larger, networked clusters consist-

ing of several of these mass-fractal chains. The exact correlation lengths between the clusters could not be determined as the "peaks" of these features are difficult to identify, but they were estimated to be approximately 4.2–6.3 nm and 25–42 nm for the primary and secondary structural levels (or inorganic domains), respectively. For samples exhibiting just a single broad feature, the correlation length was estimated to be in the range 9–15 nm. For samples with 5 wt.% SiO_2 prepared at pH 11, the peak for the secondary structural level was not resolved within the resolution limits (as seen from the scattering profile at low q), so the correlation length between the inorganic domains must be larger than 70 nm. The calculated correlation lengths of 25–42 nm are much smaller than the calculated free-space lengths (L_f) (53–120 nm, as seen in Table S1). The discrepancy highlights one of the limitations of using quantitative methods in characterizing the dispersion quality from two-dimensional images. However, such techniques are still useful for highlighting trends in the state of dispersion, and to independently corroborate the results from other measurements. In this case, from the calculated values of both the correlation lengths from SAXS and the free-space lengths from TEM images, the same effect is observed with increasing SiO_2 content: an increase in the distance between the larger SiO_2 domains (secondary structures), as well as a small increase in the sizes of the domains. It should also be noted that the scattering appears to be increasing at even lower q than measured. This suggests that there might be an additional structural level. From the TEM images in Figures 2 and 12, it can be assumed that the additional structural level may be an arrangement of the secondary particle clusters to form more mass-fractal structures (spanning above 50–100 nm), or in some cases larger (>200 nm) agglomerates. Additionally, reducing the amount of APTES is also seen to alter the scattering profile (Figure 4b) where the knee-like feature at higher q is replaced by a more linear region with a Porod slope of -1.2. The slope of the linear region at $q < 0.04$ Å^{-1} is 3.5. The absence of an obvious knee-shaped feature at $q > 0.05$ Å^{-1} may be indicative of a lack of hierarchical organization, and instead the presence of both mass-fractal and surface-fractal structures in the same size region (resulting in an overlap in the scattering profile).

The changes in the SiO_2 structure with the filler content indicate a possible evolution in the growth mechanism. From the NMR spectra (Figure 6), there are very few Q^0 groups observed in the nanocomposites, meaning that there are few unreacted TEOS monomers. This indicates that the primary growth mechanism in the initial stages is cluster-cluster, with a strong hydrolysis and slow condensation with limited monomers [15]. This mechanism results in the more open mass-fractal structures observed for low SiO_2 contents. This is also observed from the SAXS analysis, with $D < 3$ for both the primary and secondary structural levels (Table 2). As the SiO_2 content is increased, a larger amount of TEOS is required (meaning a larger number of monomers) and after the initial cluster-cluster reactions, a monomer-cluster mechanism steadily takes over the growth process, causing the SiO_2 structures to become more closed and compact with more surface fractals ($3 < D < 4$) [15]. The increase in D for both the primary and secondary structural levels in the inorganic domains represents an increase in the compactness and cross-linking of the structures formed. Figure 13 illustrates the change in structure of the SiO_2 from mass-fractal to surface-fractal with increasing fractal dimension. The growth mechanism is, of course, also affected by the pH of the system—classically, a lower pH would increase the rate of hydrolysis in a silica sol–gel reaction, while a higher pH would increase the rate of condensation [15]. However, this effect is less evident in the present samples as the $[\alpha_{Si}]_Q$ does not change significantly with pH (as seen in Figure 6a). The effect of the pH is more prominent when looking closer at the dispersion quality—the faster condensation at higher pH leads to more compact clusters that are spaced further apart and have a higher fractal dimension, along with more agglomerates, resulting in a larger L_f (Figure 3). Meanwhile, the faster hydrolysis at lower pH results in fewer agglomerates, and the primary clusters are more open and spaced closer to one another, leading to a smaller L_f and a lower fractal dimension.

Silica derived from alkoxides via a sol–gel process is known for generally possessing less dense non-colloidal particles with fractal arrangements [15]. Several studies have demonstrated fractal structures for SiO_2. Lysenkov et al. [33] performed a similar analysis of their corresponding SAXS measurements of in situ prepared SiO_2 in epoxy using the exponential model. In their work, however, the clusters and agglomerates formed at higher SiO_2 contents were much larger, and displayed varying hierarchies (e.g., mass to surface to mass fractals, or mass to mass to surface fractals), while in the present work only the evolution from a mass-fractal to a surface-fractal structure is observed with increasing SiO_2 content. These differences in the morphology might be attributed to the lack of any SCA or other surface modifiers in Lysenkov's study, as well as differences in the synthesis procedure. Ponyrko et al. [34] showed changes in the scattering profile depending on whether an aqueous or nonaqueous sol–gel method was employed, resulting either in compact aggregates of SiO_2 or more open and branched aggregates, respectively. Perchacz et al. [35] similarly reported the formation of either mass-fractal or surface-fractal SiO_2 in epoxy depending on the type of catalyst used (amine or tin-based, respectively) during the in situ synthesis, although a hierarchical structure was not evident from the flatter features in the corresponding SAXS profiles shown in their work.

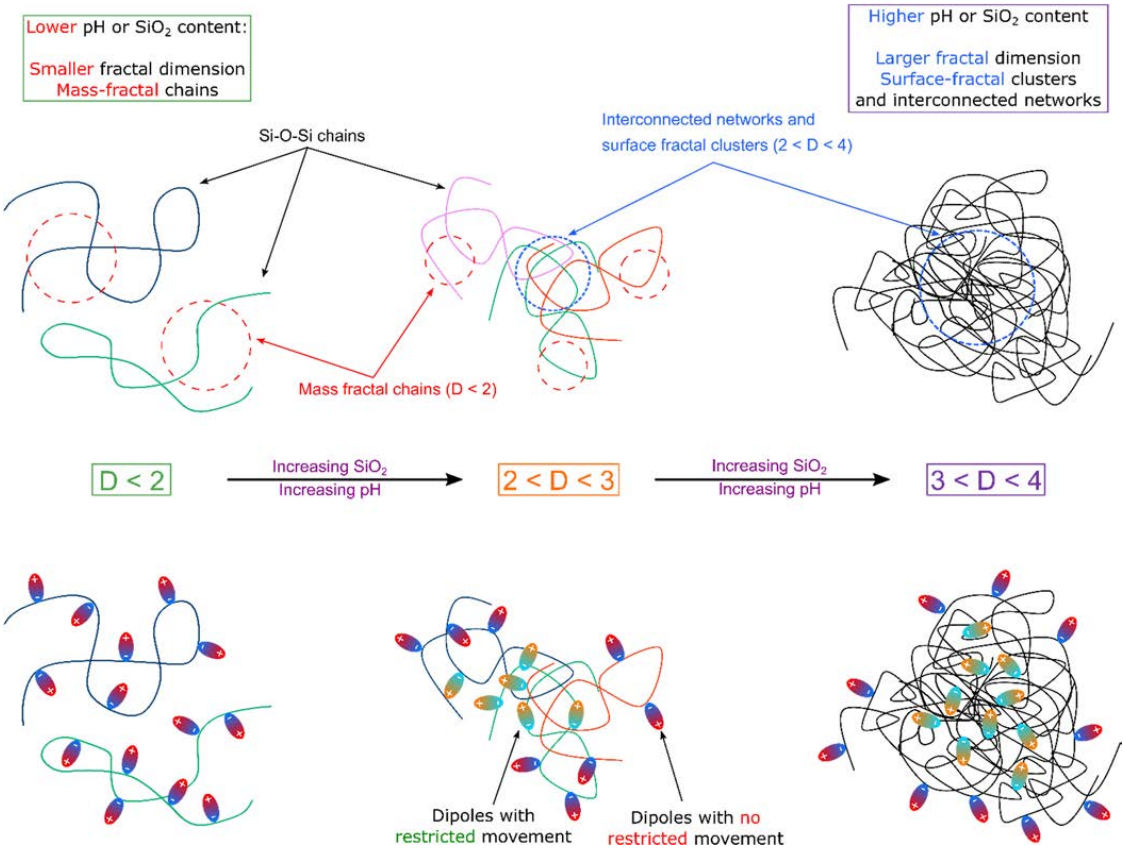

Figure 13. Illustration of the evolution of the SiO_2 structures forming in situ with increasing pH and SiO_2 content, from polymeric mass-fractal chains of Si-O-Si links to interconnected networks and rough particles with surface-fractal clusters. The resulting changes in the mobility of the chains and the freedom of the dipoles (-OH groups from hydrolysis of TEOS) to move and reorient in an electric field are shown as well.

4.3. The Effect of the SiO_2 on the Complex Permittivity at Room Temperature

The presence of SiO_2 is observed to affect the complex permittivity of epoxy differently depending on the synthesis conditions. One common feature present in all the nanocomposites is the emergence of a new dielectric relaxation that is associated with the SiO_2 (between 10^0 Hz and 10^3 Hz) as it is missing in pure epoxy (Figure 8b inset). This relaxation occurs at a lower frequency than the eminent β-relaxation, which is associated with the dipoles on the O-H groups in the epoxy chains (or possibly from any unreacted amine groups in the curing agent) [36,37]. The dipoles associated with this new relaxation are therefore 'stiffer' than the β-relaxation and are suspected to be related to interfacial polarization effects at the surfaces of the nanoparticle clusters that are formed. An additional effect is the change in the β-relaxation. In pure epoxy the tan δ peak for the β-relaxation (around 10^5 Hz) is asymmetrical, which indicates that there is a distribution in the relaxation times of the O-H dipoles, which is not unexpected due to the varying lengths and conformations of the cross-linked DGEBA chains. For the nanocomposites, the β-relaxation is altered—it appears as a shoulder (around 10^5 Hz) on another relaxation with a higher tan δ peak at a higher frequency (beyond the measured range). This can indicate one of two possibilities—either the inclusion of the nanoparticles has introduced a new relaxation occurring in the same region as the β-relaxation, or it has shifted a pre-existing relaxation to a lower frequency region which now overlaps with the β-relaxation. The latter is less likely given that the only other relaxations that have been reported for epoxy at higher frequencies are associated with localized intramolecular motions involving the epoxide groups [38], of which there should be very few (if not none) upon complete curing. The other alternative, a new relaxation, could be related to the amine groups of any unreacted APTES, or the N-H dipoles in the cross-links formed with APTES (in addition to those in the cross-linked formed with the curing agent, which contribute already to the existing β-relaxation). Additionally, for the samples prepared at pH 11, the strength of the β-relaxation is diminished, as seen from the lower dielectric loss at high frequency. This would indicate that the more compact, networked SiO_2 clusters formed at higher pH can restrict the mobility of the epoxy chains or the O-H dipoles more strongly than mass-fractal SiO_2 chains.

Apart from the changes observed in the tan δ that are related to the relaxations, the real relative permittivity (ε′) at room temperature shows small changes with the SiO_2 content and the pH used during synthesis. It is interesting to note that all the nanocomposites prepared at pH 11 show a small decrease in ε′, while those prepared at pH 7 show a small increase, compared to pure epoxy. This is likely related to the differences in structure and morphology in the SiO_2 domains that were discussed earlier—Figure 13 shows also the subsequent effects on the dipoles present in SiO_2 with the evolving structure. The presence of mass-fractal-like polymeric chains of SiO_2 with a plasticizing effect on the epoxy has been reported previously [24,32], and may explain the increase in ε′ as well—the dipoles in these loose chains (such as O-H groups from hydrolyzed TEOS or surface hydroxyls in SiO_2) can more easily and freely reorient themselves with the electric field. However, with more condensed, compact SiO_2 structures, the dipoles are unable to keep up with the electric field as they are more restricted in such clusters—further, the rigidity of these clusters may also impede the motion of the O-H dipoles on the epoxy chains instead, thereby decreasing ε′ and decreasing the strength of the β-relaxation (tan δ above 10^3 Hz). However, due to the new relaxation introduced by the SiO_2, the dielectric losses are higher than that of pure epoxy between 1 and 100 Hz. Interestingly, the lowest real permittivity and dielectric loss was observed in the sample with less APTES at pH 11, which had the largest free-space length between the SiO_2 clusters as well as larger cluster sizes and a different structural organization to the other nanocomposites. The restrictive effect of the SiO_2 domains in this nanocomposite on the mobility of the epoxy chains is also reflected in the increase in T_g (Figure 7), compared to other nanocomposites prepared with APTES.

4.4. The High Temperature Complex Permittivity

At higher temperatures more pronounced differences are observed between the different compositions. A common change for all the samples is the shift of the relaxations to higher frequencies with higher temperatures. This is due to the increased mobility of epoxy chains as the glass transition is approached, and movements along the chains are no longer restricted—the O-H dipoles can then keep up with the faster switching of the electrical field at higher frequencies. Although not visible in the range of frequencies measured, it is suspected that above the glass transition the β-relaxation will be entirely absent and the movement of the molecular segments will be the primary dielectric relaxation. This phenomenon is known as the α-relaxation, which is observed above 80 °C in pure epoxy at lower frequencies. With increasing temperatures, the α-relaxation is similarly shifted to subsequently higher frequencies as the molecular segments will find it easier to orient themselves with the electrical field.

The rapid increase in real permittivity at temperatures beyond the glass transition region is accompanied by a similar increase in the imaginary permittivity (Figure 10). The slope of -0.9 to -1 for ε'' indicates that the increase in ε'' can be due to charge transport [39]. However, this is unlike DC conductivity (involving free-charge carriers moving continuously through the material) where ε' would show no frequency dependence, and does not lead to charge storage [40]. The simultaneous increase in ε' and ε'' is instead reminiscent of the low-frequency dispersion (LFD) effect, where a strong increase in the susceptibility χ' (and therefore the permittivity ε') at low frequencies implies a finite and reversible storage of charge at interfaces [41]. The LFD effect occurs in carrier dominated systems and may appear similar to DC conduction—therefore it is sometimes referred to as quasi-DC (QDC) [42]. The origin of the LFD in this case is possibly due to an electrode polarization (EP) effect caused by ion blockage at the electrode-sample interface. The ions responsible for this are the residual Na^+ and Cl^- ions from the synthesis of DGEBA, which accumulate at the electrodes at high temperatures [39]—this is enabled by the increased ion mobility once the epoxy becomes rubbery above the glass transition.

One problem that arises with this electrode polarization is that it is difficult to isolate the α-relaxation from the real and imaginary permittivities, especially since the corresponding peak in the imaginary permittivity is often obscured by the increase in ε'' at low frequencies. This necessitates the use of the complex moduli instead of the permittivity, as the relaxations move to a higher frequency in the modulus spectra compared to the permittivity spectra [43], and so are less obscured by the electrode polarization (which also manifests as peaks in the imaginary moduli, M'' instead of an increase in ε''). Figure 14 shows the evolution of the α-relaxation in in M'' for pure epoxy and different nanocomposites (5 wt.% SiO_2 prepared at pH 7 and 11). The α- and β-relaxations show the same trend observed in the permittivity, with shifts to higher frequencies at higher temperatures, and the α-relaxation appearing at lower temperatures in the nanocomposites. This is consistent with the changes in the glass transition behavior observed in nanocomposites prepared with APTES (Figure 7), which is also attributed to the increased mobility of the polymeric mass-fractal structures of SiO_2, especially at low SiO_2 content [24].

The electrode polarization (EP), and the corresponding increases in ε' and ε'', is more significant in the nanocomposites than in pure epoxy. The peak for EP in M'' in the nanocomposites is shifted to higher frequencies at the same temperature than the corresponding peak in pure epoxy—in other words, the EP appears at much lower T in the nanocomposites than in the pure epoxy. Additionally, the increase in ε'' is between one and two orders of magnitude larger in the nanocomposites than the pure epoxy for a given temperature. This is most likely due to an increased number of charge carriers, such as ions, from the precursors used for the in situ synthesis of the nanoparticles. Yang et al. [44] have demonstrated similar behavior in ε'' at temperatures above 100 °C when pre-synthesized SiO_2 (modified with APTES and hyperbranched polyesters) was used in the nanocomposites. However, in that work, at lower temperatures the SiO_2 was observed to inhibit the EP/LFD effect instead. Yeung and Vaughan [13] also reported increasing values for ε' and

ε'' above the glass transition for epoxy nanocomposites with pre-synthesized SiO_2 functionalized with GPTMS, although in their work the nanocomposites exhibited a more prominent EP/LFD effect. They attributed this partly to adsorbed water molecules at the interface between the epoxy and the SiO_2, and the effect was seen to diminish with increasing amount of GPTMS used for the surface modification. However, in this work the opposite effect is observed. Figure 15 shows that the EP/LFD effect is less prominent in nanocomposites prepared with less APTES (APTES:DGEBA ratio of 1:30 instead of 1:10) at all temperatures, with lower values in both ε' and ε'' at 10^{-2} Hz. This implies that the EP/LFD effect is not caused by adsorbed water on the surfaces in this case (as suggested by Yeung and Vaughan), as the presence of fewer APTES molecules would mean more available sites for water to attach at the interfaces—this should amplify the increase in permittivity at high temperatures. Since the opposite is observed with a reduction in the amount of APTES, the corresponding decrease in the high temperature complex permittivity must instead be related to the changes in the structure and dispersion of the SiO_2 domains. It is possible that the increased interconnectivity of the SiO_2 clusters (for APTES:DGEBA of 1:10) facilitates charge transfer in the epoxy, resulting in the enhanced EP; whereas when the APTES is reduced, the increased distances between the clusters and the more limited connectivity of the network means that the charge transfer is less amplified, thereby limiting the increase in EP.

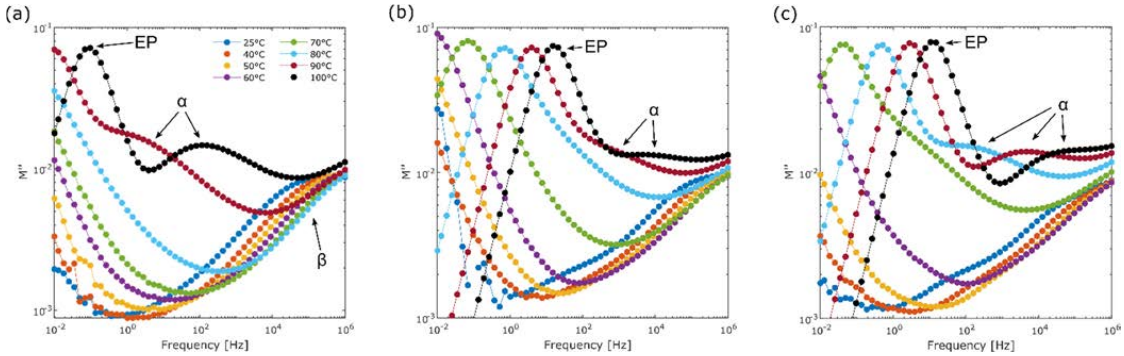

Figure 14. Imaginary moduli of **(a)** Pure epoxy, and nanocomposites with 5 wt.% SiO_2 prepared at **(b)** pH 7 and **(c)** pH 11, from 25–100 °C, showing the α and β relaxations as well as the electrode polarization (EP) effect.

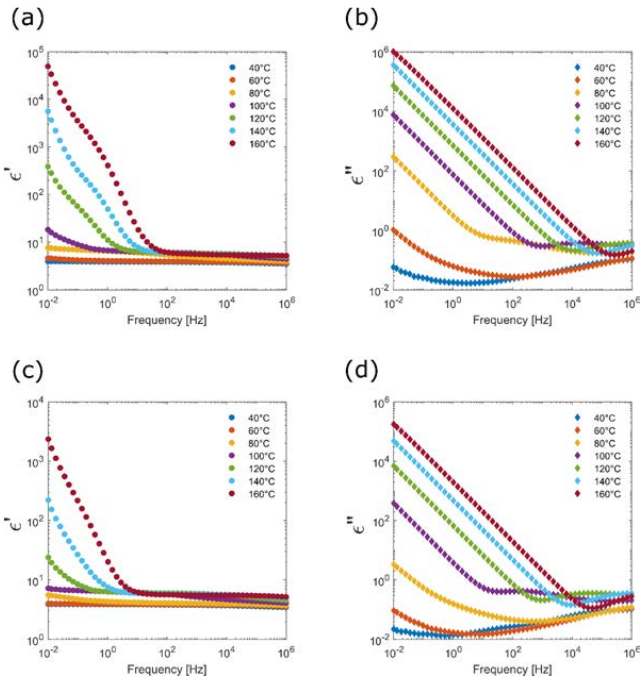

Figure 15. Comparison of the complex permittivities of epoxy-SiO_2 nanocomposite (5 wt.%, pH 11) with APTES:DGEBA mass ratios of **(a,b)** 1:10 and **(c,d)** 1:30. **(a)** and **(c)** display the real relative permittivities, while **(b)** and **(d)** and display the imaginary permittivities.

From the TEM and SAXS measurements, it is known that the structure, morphology, and dispersion of the SiO_2 in the nanocomposites change most significantly when the amount or type of SCA is altered, and this is also reflected in the dielectric properties. The state of dispersion of nanoparticle fillers has been highlighted as a key factor in the dielectric properties of nanocomposites [5], and agglomeration is observed to generally lead to increased permittivity and dielectric losses. The results in this work highlight the importance of the structure and morphology of the inorganic filler, in addition to the quality of dispersion, to the final properties of the material. In addition, the use of the in situ route may introduce unwanted ions from the reactants that contribute to the EP/LFD, which may be detrimental to the performance of the materials at higher temperatures.

5. Conclusions

The use of the sol–gel method to prepare surface-functionalized SiO_2 in epoxy is a promising alternate route in the preparation of nanocomposites with well-dispersed nanoparticles. The selection of the amount and type of coupling agent is critical, as seen by the differences in the state of dispersion between nanocomposites prepared with APTES and GPTMS, and with different amounts of APTES. The results from the dielectric spectroscopy indicate that the structure and morphology of the inorganic components of the hybrid material are quite important: the formation of polymeric structures with mass-fractal features (from faster hydrolysis at lower pH) are more likely to contribute to the mobility of the polymer chains, thereby increasing the permittivity. The formation of more compact, cross-linked SiO_2 domains with surface-fractal features (from faster condensation at higher pH), which more closely resembles particles with a defined shape, are more likely to inhibit the motions of the polymer chains instead, thereby reducing the permittivity. Therefore, the nanocomposites prepared at pH 11 with an APTES:DGEBA mass

ratio of 1:30 exhibited the most significant reduction in the real relative permittivity (by 5% at room temperature) and in the dielectric loss tangent above 10^3 Hz, compared to pure epoxy, which is a promising development for the use of these nanocomposites as high-voltage insulation. The next step towards such application would naturally be to investigate how the use of an in situ synthesis procedure that results in an improved dispersion of the nanoparticles, will affect the dielectric breakdown properties of the nanocomposites, in particular the inception and growth of electrical trees (pre-breakdown mechanism).

Supplementary Materials: The following are available online at www.mdpi.com/xxx/s1, Figure S1: Simultaneously acquired HAADF-STEM image and EDS maps of the nanocomposites, showing **(a)** the STEM image of the area mapped, and elemental maps for **(b)** silicon and **(c)** oxygen, Figure S2: **(a)** Procedure for processing of images for quantitative analysis and determination of the mean free-space length (L_f). **(b)** Histograms produced from the computation of L_f, showing the occurrences of a specific number of particle pixels found in each randomly placed box. The first histogram on the left was produced for the value of L_f computed automatically, while the middle and last histograms were produced from manually setting an undersized and oversized L_f, respectively, Table S1: Values of L_f computed from the TEM images for the different epoxy-SiO_2 nanocomposite samples, as well as the mean L_f values calculated from the computed values. The computation was run thrice for each image using 10 000 random boxes for each iteration of L_f.

Author Contributions: Conceptualization, M.M.A., M.-A.E., J.G., M.-H.G.E. and S.H.; methodology and investigation, M.M.A., I.-E.N. and A.J.; formal analysis, M.M.A.; visualization and writing—original draft preparation, M.M.A.; writing—review and editing, M.-A.E., J.G. S.H., and M.-H.G.E.; supervision, M.-A.E., J. G. and M.-H.G.E. All authors have read and agreed to the published version of the manuscript.

Funding: This work is funded by The Research Council of Norway through the project "Stipendiatstillinger til SINTEF Energi AS" (Project No. 259866).

Institutional Review Board Statement: Not applicable.

Informed Consent Statement: Not applicable.

Data Availability Statement: Data available upon request from the authors.

Acknowledgments: The authors would like to acknowledge support from the Research Council of Norway through the Norwegian Center for Transmission Electron Microscopy, NORTEM (197405/F50), and the use of the Norwegian national resource centre for X-ray diffraction and scattering (RECX).

Conflicts of Interest: The authors declare no conflict of interest.

References

1. Adnan, M.M.; Tveten, E.G.; Glaum, J.; Ese, M.-H.G.; Hvidsten, S.; Glomm, W.; Einarsrud, M.-A. Epoxy-Based Nanocomposites for High-Voltage Insulation: A Review. *Adv. Electron. Mater.* **2019**, *5*, 1800505, doi:10.1002/aelm.201800505.
2. Nelson, J.K.; Nelson, J.K. *Dielectric Polymer Nanocomposites*; Springer: New York, NY, USA, 2010; ISBN 978-1-4419-1590-0.
3. Plesa, I.; Notingher, P.V.; Schlögl, S.; Sumereder, C.; Muhr, M. Properties of Polymer Composites Used in High-Voltage Applications. *Polymers* **2016**, *8*, 173, doi:10.3390/polym8050173.
4. Lewis, T.J. Interfaces are the Dominant Feature of Dielectrics at the Nanometric Level. *IEEE Trans. Dielectr. Electr. Insul.* **2004**, *11*, 739–753.
5. Calebrese, C.; Hui, L.; Schadler, L.S.; Nelson, J.K. A Review on the Importance of Nanocomposite Processing to Enhance Electrical Insulation. *IEEE Trans. Dielectr. Electr. Insul.* **2011**, *18*, 938–945, doi:10.1109/TDEI.2011.5976079.
6. Adnan, M.M.; Dalod, A.R.M.; Balci, M.H.; Glaum, J.; Einarsrud, M.-A. In situ synthesis of hybrid inorganic-polymer nanocomposites. *Polymers* **2018**, *10*, 1129, doi:10.3390/polym10101129.
7. Gao, F. *Advances in Polymer Nanocomposites: Types and Applications*; Woodhead Publishing Limited: Cambridge, UK, 2012; ISBN 9781845699406.

8. Heid, T.; Fréchette, M.; David, E. Epoxy/BN micro- and submicro-composites: Dielectric and thermal properties of enhanced materials for high voltage insulation systems. *IEEE Trans. Dielectr. Electr. Insul.* **2015**, *22*, 1176–1185, doi:10.1109/TDEI.2015.7076820.
9. Nelson, J.K.; Fothergill, J.C. Internal charge behaviour of nanocomposites. *Nanotechnology* **2004**, *15*, 586–595, doi:10.1088/0957-4484/15/5/032.
10. Kochetov, R.; Andritsch, T.; Morshuis, P.H.F.; Smit, J.J. Anomalous Behaviour of the Dielectric Spectroscopy Response of Nanocomposites. *IEEE Trans. Dielectr. Electr. Insul.* **2012**, *19*, 107–117.
11. Virtanen, S.; Krentz, T.; Nelson, J.K.; Schadler, L.; Bell, M.; Benicewicz, B.; Hillborg, H.; Zhao, S. Dielectric Breakdown Strength of Epoxy Bimodal-polymer-Brush-Grafted Core Functionalized Silica Nanocomposites. *IEEE Trans. Dielectr. Electr. Insul.* **2014**, *21*, 563–570, doi:10.1109/TDEI.2014.004415.
12. Bell, M.; Krentz, T.; Nelson, J.K.; Schadler, L.; Wu, K.; Breneman, C.; Zhao, S.; Hillborg, H.; Benicewicz, B. Investigation of dielectric breakdown in silica-epoxy nanocomposites using designed interfaces. *J. Colloid Interface Sci.* **2017**, *495*, 130–139, doi:10.1016/j.jcis.2017.02.001.
13. Yeung, C.; Vaughan, A.S. On the Effect of Nanoparticle Surface Chemistry on the Electrical Characteristics of Epoxy-Based Nanocomposites. *Polymers* **2016**, *8*, 126, doi:10.3390/polym8040126.
14. Sanchez, C.; Ribot, F. Design of Hybrid Organic-Inorganic Materials Synthesized Via Sol-Gel Chemistry. *New J. Chem.* **1994**, *18*, 1007–1047, doi:10.4028/www.scientific.net/MSF.152-153.313.
15. Brinker, C.J.; Scherer, G.W. *Sol-Gel Science: The Physics and Chemistry of Sol–Gel Processing*; Academic Press, Inc.: Cambridge, MA, USA, 1990; ISBN 9780080571034.
16. Judeinstein, P.; Sanchez, C. Hybrid organic–inorganic materials: A land of multidisciplinarity. *J. Mater. Chem.* **1996**, *6*, 511–525, doi:10.1039/JM9960600511.
17. Matějka, L.; Dušek, K.; Pleštil, J.; Kříž, J.; Lednický, F. Formation and structure of the epoxy-silica hybrids. *Polymer* **1999**, *40*, 171–181, doi:10.1016/S0032-3861(98)00214-6.
18. Matějka, L.; Pleštil, J.; Dušek, K. Structure evolution in epoxy–silica hybrids: Sol–gel process. *J. Non. Cryst. Solids* **1998**, *226*, 114–121, doi:10.1016/S0022-3093(98)00356-1.
19. Nazir, T.; Afzal, A.; Siddiqi, H.M.; Ahmad, Z.; Dumon, M. Thermally and mechanically superior hybrid epoxy-silica polymer films via sol-gel method. *Prog. Org. Coatings* **2010**, *69*, 100–106, doi:10.1016/j.porgcoat.2010.05.012.
20. Afzal, A.; Siddiqi, H.M.; Saeed, S.; Ahmad, Z. Exploring resin viscosity effects in solventless processing of nano-SiO2/epoxy polymer hybrids. *RSC Adv.* **2013**, *3*, 3885–3892, doi:10.1039/c3ra21150a.
21. Donato, R.K.; Matějka, L.; Schrekker, H.S.; Pletil, J.; Jigounov, A.; Brus, J.; Slouf, M. The multifunctional role of ionic liquids in the formation of epoxy-silica nanocomposites. *J. Mater. Chem.* **2011**, *21*, 13801–13810, doi:10.1039/c1jm11752a.
22. Donato, R.K.; Donato, K.Z.; Schrekker, H.S.; Matějka, L. Tunable reinforcement of epoxy-silica nanocomposites with ionic liquids. *J. Mater. Chem.* **2012**, *22*, 9939–9948, doi:10.1039/c2jm30830d.
23. Khare, H.S.; Burris, D.L. A quantitative method for measuring nanocomposite dispersion. *Polymer* **2010**, *51*, 719–729.
24. Adnan, M.M.; Tveten, E.G.; Miranti, R.; Hvidsten, S.; Ese, M.-H.G.; Glaum, J.; Einarsrud, M.-A. In situ synthesis of epoxy nanocomposites with hierarchical surface-modified SiO2 clusters. *J. Sol-Gel Sci. Technol.* **2020**, *95*, 783–794, doi:10.1007/s10971-020-05220-3.
25. Beaucage, G. Approximations Leading to a Unified Exponential/Power-Law Approach to Small-Angle Scattering. *J. Appl. Crystallogr.* **1995**, *28*, 717–728, doi:10.1107/s0021889895005292.
26. Dalod, A.; Grendal, O.; Blichfeld, A.; Furtula, V.; Pérez, J.; Henriksen, L.; Grande, T.; Einarsrud, M.-A. Structure and Optical Properties of Titania-PDMS Hybrid Nanocomposites Prepared by In Situ Non-Aqueous Synthesis. *Nanomaterials* **2017**, *7*, 460, doi:10.3390/nano7120460.
27. Beaucage, G. Small-angle scattering from polymeric mass fractals of arbitrary mass-fractal dimension. *J. Appl. Crystallogr.* **1996**, *29*, 134–146, doi:10.1107/S0021889895011605.
28. Cherny, A.Y.; Anitas, E.M.; Osipov, V.A.; Kuklin, A.I. Scattering from surface fractals in terms of composing mass fractals. *J. Appl. Cryst* **2017**, *50*, 919–931, doi:10.1107/S1600576717005696.
29. Rubio, F.; Rubio, J.; Oteo, J.L. A FT-IR Study of the Hydrolysis of Tetraethylorthosilicate (TEOS). *Spectrosc. Lett.* **1998**, *31*, 199–219, doi:10.1080/00387019808006772.
30. Hoebbel, D.; Nacken, M.; Schmidt, H. On the Existence and Hydrolytic Stability of Titanosiloxane Bonds in the System: Glycidoxypropyltrimethoxysilane-Water-Titaniumtetraethoxide. *J. Sol-Gel Sci. Technol.* **1998**, *13*, 37–43, doi:10.1023/A:1008638918967.
31. Piscitelli, F.; Buonocore, G.G.; Lavorgna, M.; Verdolotti, L.; Pricl, S.; Gentile, G.; Mascia, L. Peculiarities in the structure—Properties relationship of epoxy-silica hybrids with highly organic siloxane domains. *Polymer* **2015**, *63*, 222–229, doi:10.1016/j.polymer.2015.03.012.
32. Piscitelli, F.; Lavorgna, M.; Buonocore, G.G.; Verdolotti, L.; Galy, J.; Mascia, L. Plasticizing and reinforcing features of siloxane domains in amine-cured epoxy/silica hybrids. *Macromol. Mater. Eng.* **2013**, *298*, 896–909, doi:10.1002/mame.201200222.
33. Lysenkov, E.A.; Leonova, N.G.; Zhiltsova, S.V. Effect of the Silicon-Containing Phase on the Hierarchy of the Structure of Epoxy–Silica Nanocomposites. *Theor. Exp. Chem.* **2019**, *55*, 250–257, doi:10.1007/s11237-019-09616-3.
34. Ponyrko, S.; Kobera, L.; Brus, J.; Matějka, L. Epoxy-silica hybrids by nonaqueous sol-gel process. *Polymer* **2013**, *54*, 6271–6282, doi:10.1016/j.polymer.2013.09.034.

35. Perchacz, M.; Beneš, H.; Zhigunov, A.; Serkis, M.; Pavlova, E. Differently-catalyzed silica-based precursors as functional additives for the epoxy-based hybrid materials. *Polymer* **2016**, *99*, 434–446, doi:10.1016/j.polymer.2016.07.053.
36. Alhabill, F.N.; Ayoob, R.; Andritsch, T.; Vaughan, A.S. Influence of filler/matrix interactions on resin/hardener stoichiometry, molecular dynamics, and particle dispersion of silicon nitride/epoxy nanocomposites. *J. Mater. Sci.* **2018**, *53*, 4144–4158, doi:10.1007/s10853-017-1831-x.
37. Pochan, J.M.; Gruber, R.J.; Pochan, D.F. Dielectric relaxation phenomena in a series of polyhydroxyether copolymers of bisphenol-A—endcapped polyethylene glycol with epichlorohydrin. *J. Polym. Sci. Polym. Phys. Ed.* **1981**, *19*, 143–149, doi:10.1002/pol.1981.180190112.
38. Vassilikou-Dova, A.; Kalogeras, I.M. Dielectric Analysis (DEA). In *Thermal Analysis of Polymers: Fundamentals and Applications*; Menczel, J.D., Prime, R.B., Eds.; Wiley, 2009; pp. 497–613, ISBN 9780471769170.
39. Fuqiang, T.; Lin, Z.; Junliang, Z.; Xiao, P. Space charge and dielectric behavior of epoxy composite with SiO_2-$Al2O_3$ nano-micro fillers at varied temperatures. *Compos. Part B Eng.* **2017**, *114*, 93–100, doi:10.1016/j.compositesb.2017.01.062.
40. García-Sánchez, M.F.; M'Peko, J.C.; Ruiz-Salvador, A.R.; Rodríguez-Gattorno, G.; Echevarría, Y.; Fernández-Gutierrez, F.; Delgado, A. An elementary picture of dielectric spectroscopy in solids: Physical basis. *J. Chem. Educ.* **2003**, *80*, 1062–1073, doi:10.1021/ed080p1062.
41. Jonscher, A.K. Dielectric relaxation in solids. *J. Phys. D. Appl. Phys.* **1999**, *32*, 57–70, doi:10.1088/0022-3727/32/14/201.
42. Gao, Y.; Liang, X.; Dissado, L.A.; Dodd, S.J.; Chalashkanov, N.M. Dielectric response of filled high temperature vulcanized silicone rubber. *IEEE Trans. Dielectr. Electr. Insul.* **2016**, *23*, 3683–3695, doi:10.1109/TDEI.2016.006057.
43. Fuqiang, T.; Yoshimichi, O. Electric Modulus Powerful Tool for Analyzing Dielectric Behavior. *IEEE Trans. Dielectr. Electr. Insul.* **2014**, *21*, 929–931, doi:10.1109/TDEI.2014.004561.
44. Yang, G.; Cui, J.; Ohki, Y.; Wang, D.; Li, Y.; Tao, K. Dielectric and relaxation properties of composites of epoxy resin and hyperbranched-polyester-treated nanosilica. *RSC Adv.* **2018**, *8*, 30669–30677, doi:10.1039/C8RA05846F.

B Additional experimental details and results

B.1 Overview of synthesis parameters

Table B.1 shows the amounts of the different reagents (precursors, coupling agents, water) used in the synthesis of the various nanocomposites using the *in situ* procedures outlined above. All of the volumes were based on the use of 30 g of DGEBA and the required 10.13 g of POPDA, with molar ratios of 2:1 for H_2O:TEOS and H_2O:TIP, and 1.5:1 for H_2O:SCA and H_2O:AIP.

Table B.1. Synthesis parameters for all the *in situ* prepared nanocomposites in this work

Filler	Alkoxide	Filler content [wt%]	Precursor amount [mL]	SCA	SCA amount [mL]	Water amount [mL]	pH
SiO_2	TEOS	1	1.62	APTES	3.17	0.63	2, 7, 11
		2	3.28			0.89	
		3	4.96			1.17	
		4	6.69			1.44	
		5	8.45			1.73	
		5	8.06	APTES	1.06	1.42	7, 11
		1	1.62	GPTMS	2.8	0.6	2
		2	3.06			0.87	
		3	4.63			1.14	
		4	6.24			1.42	
		5	7.88			1.70	
TiO_2	TIP	1	1.54	APTES	1.06	0.31	7
		3	4.71			0.69	
		5	8.01			2.18	
Al_2O_3	AIP	1	0.8	APTES	1.06	0.23	7
		3	2.46			0.46	
		5	4.19			0.69	

B.2 Calculation of L_f

Table B.2 shows the values of L_f computed from different TEM images of the epoxy-SiO_2 nanocomposites, including the mean values of L_f which were used in Figure 4.3.

Table B.2. Overview of calculated values of L_f for epoxy-SiO_2 nanocomposites prepared with APTES under different pH conditions and APTES:DGEBA mass ratios. L_f was computed three times for each image.

pH	APTES:DGEBA mass ratio	Filler content [wt%]	Image No.	L_f [nm]	Mean L_f [nm]
2	1:10	2	1	53, 53, 53	57
			2	59, 60, 63	
		5	1	79, 81, 83	72
			2	61, 62, 65	
7	1:10	5	1	76, 79, 79	86
			2	84, 89, 91	
			3	91, 92, 93	
	1:30	5	1	118, 118, 119	156
			2	191, 192, 193	
			3	157, 158, 157	
11	1:10	2	1	63, 63, 66	65
			2	64, 66, 67	
		5	1	106, 106, 109	105
			2	118, 119, 125	
			3	103, 106, 107	
			4	86, 88, 89	
	1:30	5	1	199, 199, 200	205
			2	206, 212, 216	

B.3 EDS maps of the nanocomposites

Compositional maps obtained from energy-dispersive X-ray spectroscopy (EDS) to verify that the structures observed in the TEM were the expected inorganic oxides. Representative elemental maps for the SiO_2, Al_2O_3, and TiO_2 are shown in Figure B.1.

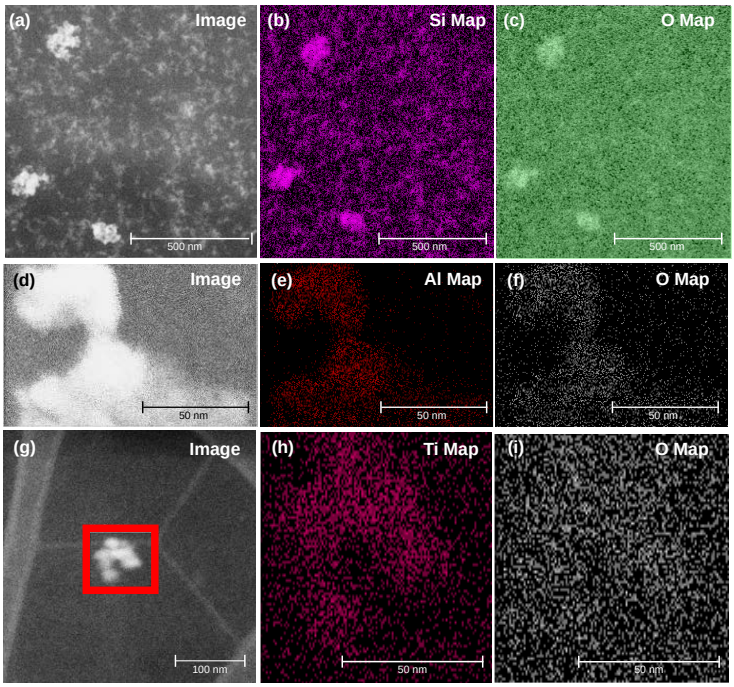

Figure B.1. Selected EDS maps of nanocomposites, alongside the STEM images of the regions that were mapped, for: **(a-c)** epoxy-SiO_2 nanocomposite prepared at pH 7 with an APTES:DGEBA mass ratio of 1:10, 5 wt% SiO_2; **(d-f)** epoxy-Al_2O_3 nanocomposite prepared with an APTES:DGEBA mass ratio of 1:30, 4 wt% Al_2O_3; **(g-i)** epoxy-TiO_2 nanocomposite prepared with an APTES:DGEBA mass ratio of 1:30, 5 wt% TiO_2. The region in the red square in **(g)** is shown in **(h)** and *(i)*.

The maps of the inorganic components (Si, Al, and Ti) overlapped consistently with the suspected particles or clusters. The maps for O showed that oxygen was more ubiquitous, which is expected due to its presence in both the DGEBA and POPDA molecules. Some Si was observed when mapping the epoxy-TiO_2 and epoxy-Al_2O_3 nanocomposites, due to the inclusion of APTES.

B.4 Permittivity of epoxy-SiO_2 nanocomposites prepared at pH 2

Figure B.2 shows the complex permittivity behaviour of the preliminary epoxy-SiO_2 nanocomposites prepared at pH 2 without N_2 pressurization during curing, and with an APTES:DGEBA mass ratio of 1:10. The values of ϵ'_r and tan δ were averaged over 3-5 samples. No trends in the permittivity with the SiO_2 filler content are evident. The nanocomposites with 1 and 3 wt% SiO_2 exhibited a slight decrease in the permittivity at certain frequencies, whereas those with 2, 4 or 5 wt% exhibited increases instead. The tan δ curves are also significantly noisier, but in general the nanocomposites exhibited a higher dielectric loss than pure epoxy between 1 and 10^4 Hz.

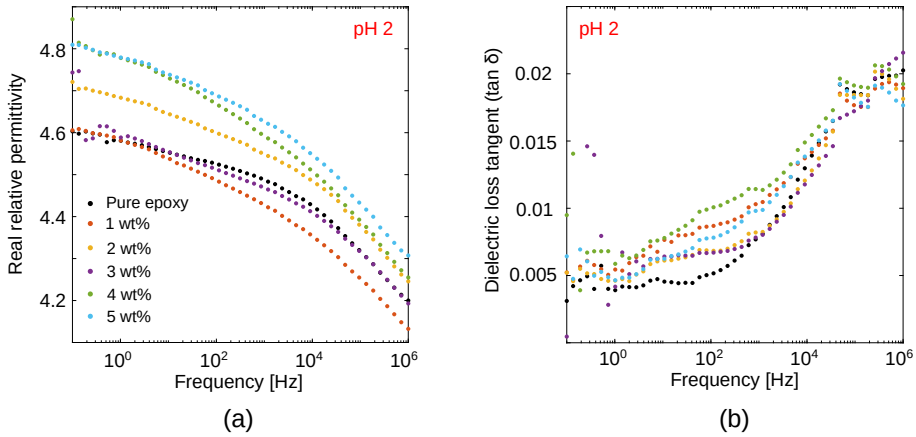

Figure B.2. The **(a)** real relative permittivities and **(b)** dielectric loss tangents of pure epoxy and epoxy-SiO_2 nanocomposites prepared under conditions of pH 2 and with a APTES:DGEBA mass ratio of 1:10.

B.5 Optical images of electrical trees

The optical images of the electrical trees included in this thesis were modified with additional lines to show the tree channels more clearly. The unmodified images are included in this section for comparison.

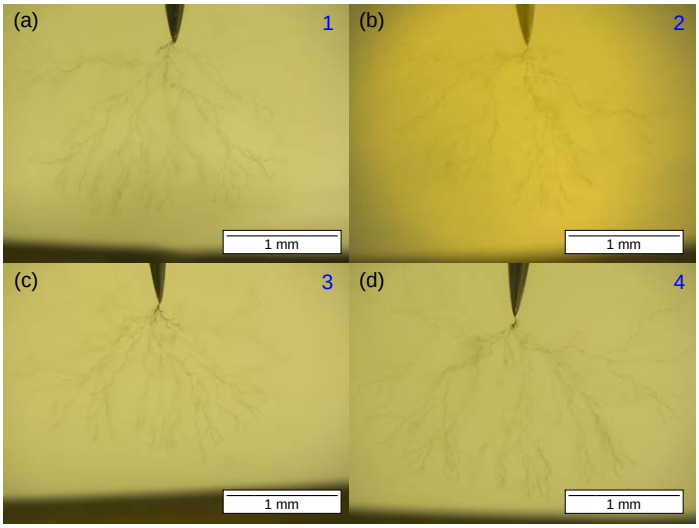

Figure B.3. Images of trees shown in Figure 4.24 with no lines drawn.

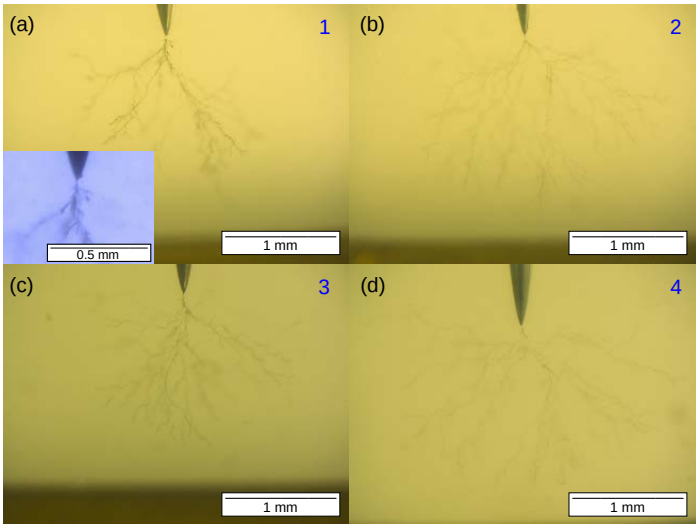

Figure B.4. Images of trees shown in Figure 4.25 with no lines drawn.

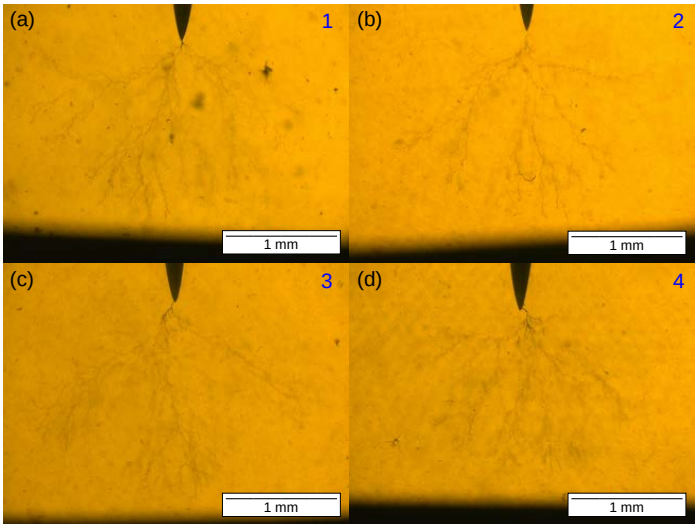

Figure B.5. Images of trees shown in Figure 4.26 with no lines drawn.

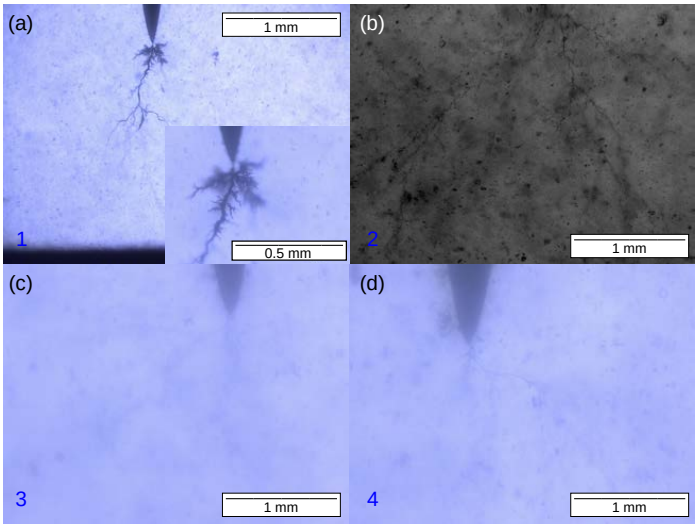

Figure B.6. Images of trees shown in Figure 4.27 with no lines drawn.

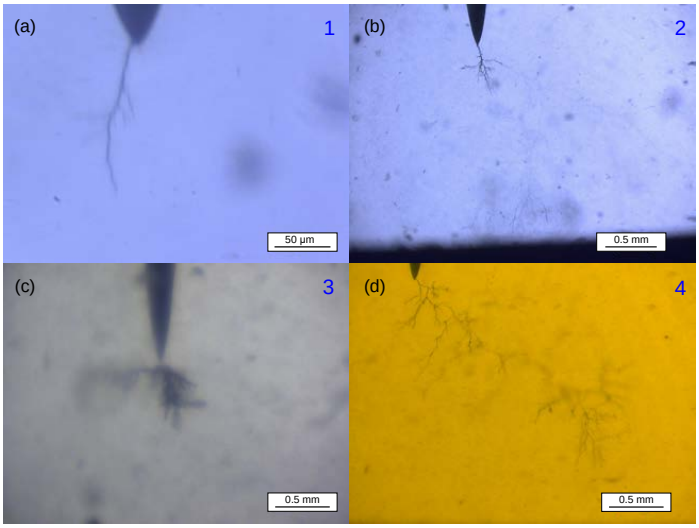

Figure B.7. Images of trees shown in Figure 5.12 with no lines drawn.

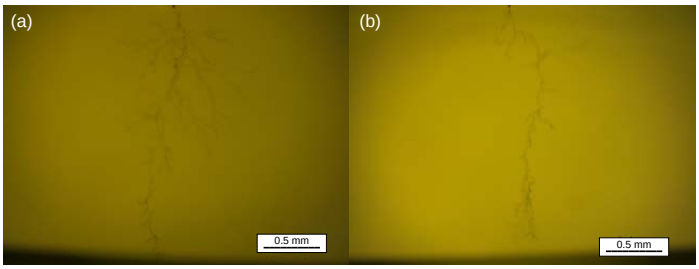

Figure B.8. Images of trees shown in Figure 5.24 with no lines drawn.

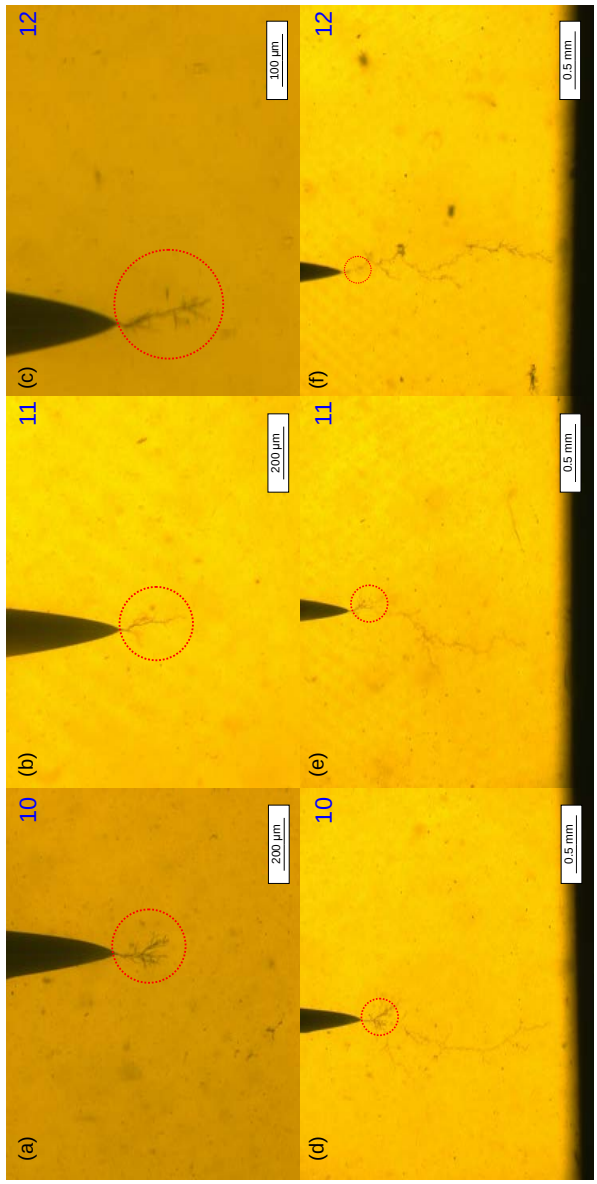

Figure B.9. Images of trees shown in Figure 5.14 with no lines drawn.

B.6 FTIR spectra of reactants

Figure B.10 shows the FTIR spectra of DGEBA and POPDA. Figure B.11 shows the FTIR spectra for the silanes used in the *in situ* syntheses of epoxy-SiO_2 nanocomposites, TEOS and APTES. Figure B.12 shows the FTIR spectrum for the TIP mixed in anhydrous 2-propanol, which was used in the synthesis of epoxy-TiO_2 nanocomposites. These spectra were used for identification of the bands observed in Figures 4.5 and 5.4.

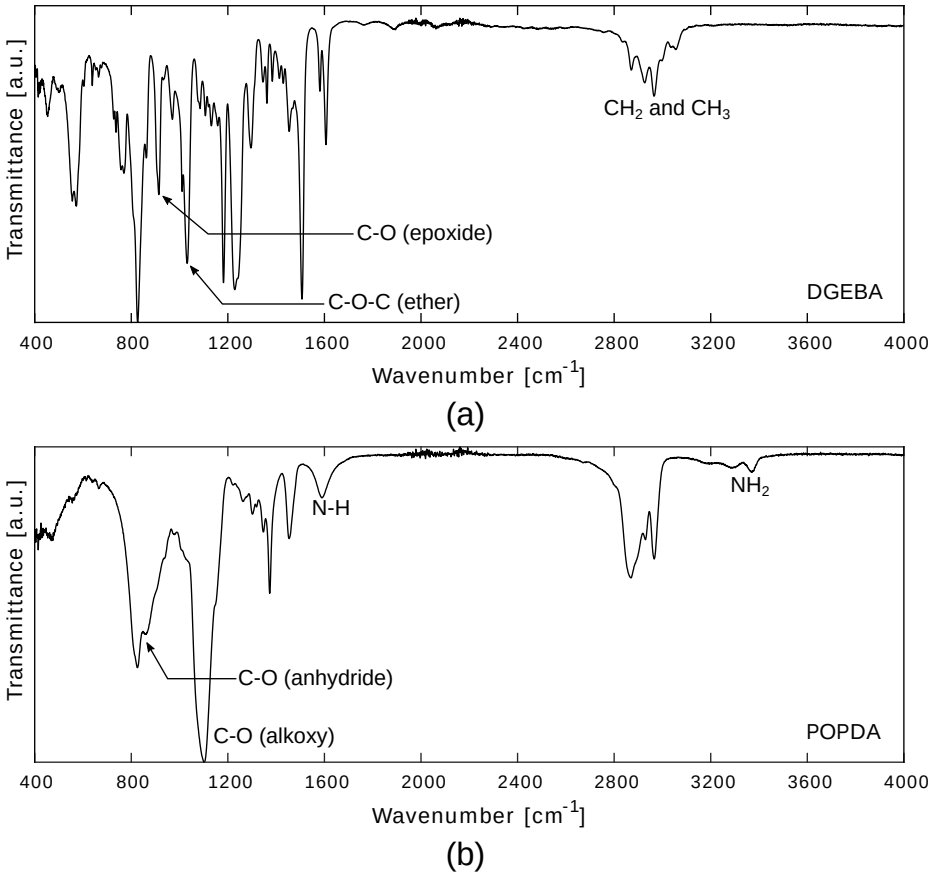

Figure B.10. FTIR spectra of **(a)** DGEBA (not cured), and **(b)** POPDA.

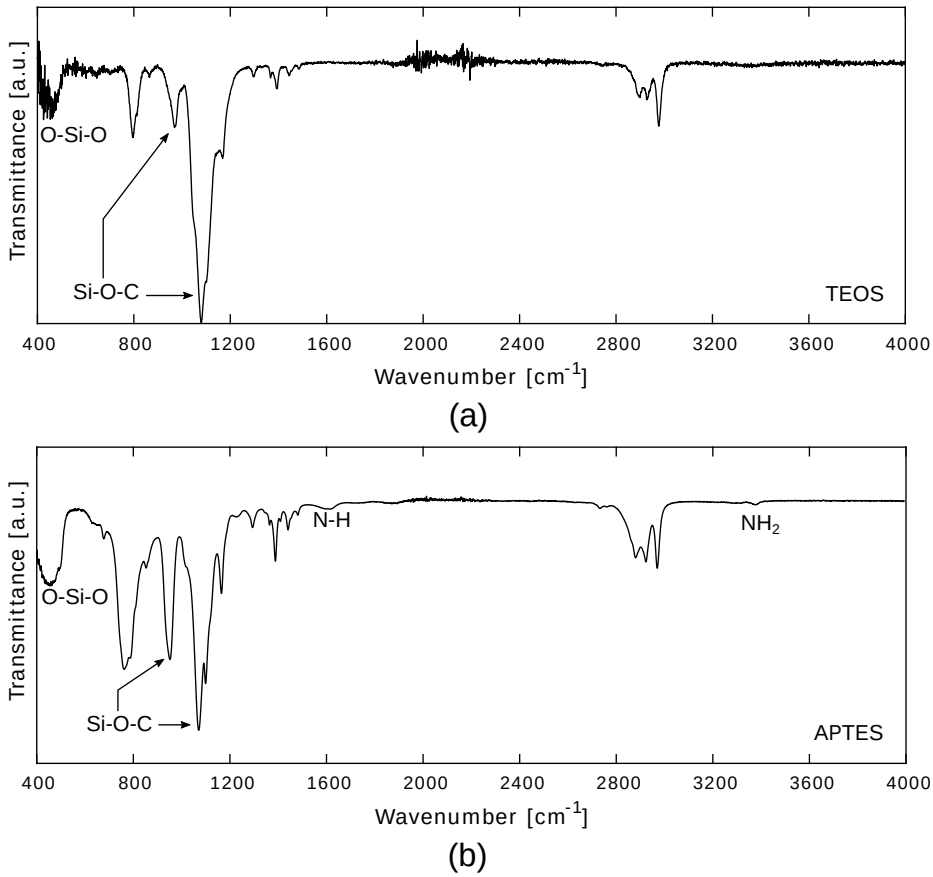

Figure B.11. FTIR spectra of **(a)** TEOS and **(b)** APTES.

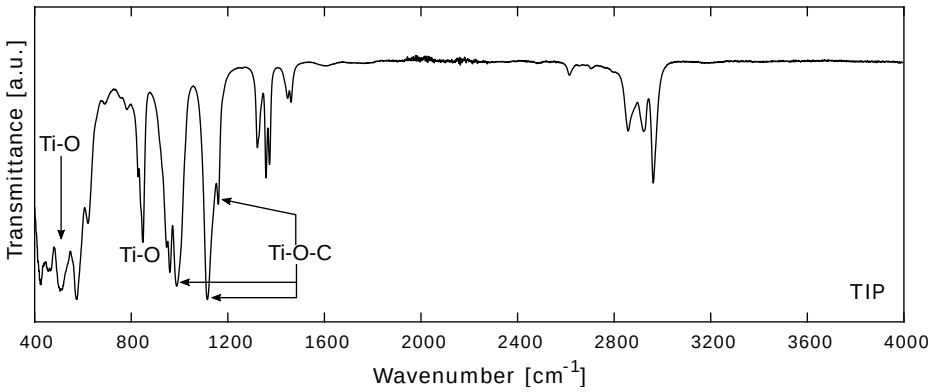

Figure B.12. FTIR spectra of TIP in anhydrous 2-propanol.

ISBN 978-82-326-6253-1 (printed ver.)
ISBN 978-82-326-5861-9 (electronic ver.)
ISSN 1503-8181 (printed ver.)
ISSN 2703-8084 (online ver.)

NTNU

Norwegian University of
Science and Technology